Developments on *Shell* and *Solid-Shell* Finite Elements Technology in Nonlinear Continuum Mechanics

---

Desenvolvimentos na Tecnologia de Elementos Finitos do Tipo *Casca* e *Sólido-Casca* na Mecânica dos Meios Contínuos Não-Linear

Robertt Angelo Fontes Valente

Universidade do Porto
Faculdade de Engenharia
FEUP

Julho de 2004

Developments on *Shell* and *Solid-Shell* Finite Elements Technology in Nonlinear Continuum Mechanics

Dissertation presented to the Faculty of Engineering, University of Porto, as a requirement to obtain the PhD Degree in Mechanical Engineering, and carried out under the supervision of Professor José Manuel de Almeida César de Sá, Associate Professor, Faculty of Engineering, University of Porto; Professor Renato Manuel Natal Jorge, Auxiliary Professor, Faculty of Engineering, University of Porto and José Joaquim de Almeida Grácio, Full Professor, Department of Mechanical Engineering, University of Aveiro.

Desenvolvimentos na Tecnologia de Elementos Finitos do Tipo *Casca* e *Sólido-Casca* na Mecânica dos Meios Contínuos Não-Linear

Dissertação apresentada à Faculdade de Engenharia da Universidade do Porto com vista à obtenção do grau de Doutor em Engenharia Mecânica, e realizada sob a orientação dos Professores José Manuel de Almeida César de Sá, Professor Associado, Faculdade de Engenharia, Universidade do Porto; Renato Manuel Natal Jorge, Professor Auxiliar, Faculdade de Engenharia, Universidade do Porto e José Joaquim de Almeida Grácio, Professor Catedrático, Departamento de Engenharia Mecânica, Universidade de Aveiro.

Research work supported by *Ministério da Ciência e do Ensino Superior* (FCT and FSE), Portugal, under PhD Scholarship PRAXIS XXI / BD / 21662 / 99

Investigação financiada pelo *Ministério da Ciência e do Ensino Superior* (FCT e FSE), Portugal, através da Bolsa de Doutoramento PRAXIS XXI / BD / 21662 / 99

Promete-me que, aconteça o que acontecer nesta vida,
nunca deixarás de procurar Deus.
Se fores derrubado, levanta-te no mesmo instante
com toda a tua força e desejo por Deus
e continua a caminhar!
Ora para que a vontade de Deus se una à tua,
tornando-a indomável,
e terás sucesso.
Cumprirás a vontade de Deus para ti,
nesta vida!
Deus abençoa-te agora pela tua jornada seguinte.
Paramahamsa Yogānanda

Os ousados começam, mas só os determinados terminam.
George Bernard Shaw

Agradecimentos

Longe de ser um trabalho puramente individual, o processo de investigação e desenvolvimento que uma tese de Doutoramento envolve depende, na minha opinião, de todo um sentido e espírito de grupo, sem o qual a discussão e questionamento científico simplesmente não existem.

Nesse contexto, e em primeiro lugar, os meus agradecimentos vão para o Professor José César de Sá (FEUP), orientador principal, pela oportunidade que me foi concedida de realizar este trabalho de investigação e por proporcionar todas as condições para a sua completa execução.

Ao Professor Renato Natal Jorge (FEUP), co-orientador, vão os meus mais sinceros agradecimentos pelo empenho, amizade e acompanhamento constante e incondicional proporcionado durante todo o Doutoramento. Simplesmente esta tese não existiria sem o seu apoio e dedicação. Por todas as horas de discussão e análise conjunta, por todas as linhas de código implementadas, revistas e corrigidas, e pelos incontáveis cafés tomados ao longo dos últimos anos, o meu muito obrigado e a minha amizade.

Ao Professor José Grácio (DEM-UA), co-orientador, o meu agradecimento pela forma como sempre apoiou e defendeu o meu trabalho de investigação e pela maneira como fui recebido no Departamento de Engenharia Mecânica da Universidade de Aveiro. O meu muito obrigado por todo o incentivo e pelas oportunidades oferecidas.

Ao colega, amigo (e companheiro de gabinete) Rui Cardoso (DEM-UA) a minha sincera gratidão pelas infindáveis horas de discussão científica, amizade constante e apoio nos momentos mais complicados deste trabalho. Muitas das linhas escritas nesta dissertação surgiram após intensos e produtivos debates, sem os quais esta tese não teria a mesma relevância.

Ao colega e amigo Ricardo Sousa (DEM-UA) o meu agradecimento por toda troca de ideias e amizade ao longo dos últimos anos. O seu sentido de companheirismo e constante bom humor proporcionaram-me um apoio adicional em muitos momentos difíceis. Obrigado!

To Dr. Jeong-Whan Yoon (ALCOA-USA) my sincere acknowledgement for the scientific and personal support demonstrated in several stages of the present work. His availability and expertise in the field of Finite Elements proved to be crucial in the implementation phase within Abaqus commercial code. More important, however, proved to be his friendship and constant words of encouragement.

Aos colegas professores do Departamento de Engenharia Mecânica da Universidade de Aveiro, em particular ao Professor Francisco Queirós de Melo, o meu agradecimento pelo acolhimento proporcionado e pelo incentivo pessoal muitas vezes demonstrado. Aos colegas bolseiros Gil Campos, Alexandre Cruz e Victor Neto o meu muito obrigado pelas palavras de apoio e amizade. Aos funcionários da secretaria, finalmente, o meu agradecimento pela eficaz resolução de problemas complexos, que de outra forma tomariam tempo a esta tese.

Aos Professores Lúcia Dinis, Pedro Ribeiro, Pedro Camanho, Marcelo Moura, António Ferreira, José Esteves, Carlos Magalhães Oliveira, Paulo Tavares de Castro e António Augusto Fernandes (DEMEGI - FEUP) o meu agradecimento pela amizade e pelas demonstrações de apoio prestadas durante este trabalho.

Aos colegas bolseiros de investigação do Departamento de Engenharia Mecânica (FEUP) Cassilda Tavares, André Roque, Pedro Martins, Carla Roque, Jorge Almeida, Jorge Belinha, David Recio, Pedro Bandeira e Pedro Portela o meu agradecimento pela amizade e excelente ambiente de investigação proporcionado. Um agradecimento especial, no entanto, vai para o meu colega e amigo Marco Parente, em particular pela paciência e entrega com que enfrentou a tarefa de encontrar erros nas minhas rotinas para o Abaqus. Muito obrigado e os meus votos pessoais de boa sorte em suas carreiras.

Ao colega e amigo Francisco Pires (University of Wales - Swansea) o meu agradecimento pela amizade e disponibilidade em providenciar cópias de artigos essenciais para a investigação envolvida neste trabalho.

Aos meus pais e irmão os meus profundos agradecimentos pela forma como sempre me apoiaram e incentivaram na minha carreira e vida pessoal. Sua presença constante foi fundamental para que esta tese chegasse ao fim.

Finalmente, agradeço à Sonia por todo o apoio, carinho e incentivo demonstrados de forma incondicional nesses últimos anos e ao longo da execução deste trabalho. Esta tese é a ela dedicada.

Resumo

Neste trabalho, são apresentadas novas formulações relativas ao desenvolvimento de elementos finitos do tipo ”casca” e ”sólido-casca”. A motivação principal deste estudo consiste na resolução de problemas estruturais não-lineares envolvendo componentes com reduzida espessura, através do Método dos Elementos Finitos. Em termos de aplicabilidade prática, é de realçar a possível utilização dos elementos finitos e procedimentos numéricos propostos e implementados em problemas industriais de conformação plástica em chapas finas.

Nesse sentido, foram desenvolvidos e implementados elementos finitos bilineares (tipo ”casca”) e trilineares (tipo ”sólido-casca”), cujos respectivos funcionais baseiam-se em variáveis de deslocamentos. Do ponto de vista da discretização do meio contínuo por meio de elementos finitos, são utilizados como variáveis primárias campos de deslocamentos nodais. Formulações desse gênero são reconhecidamente deficientes na análise de estruturas com reduzidos valores de espessura, devido ao aparecimento de fenómenos numéricos de retenção (*locking*), que se revelam através de uma sobre-estimação dos valores de rigidez associados a determinadas componentes de extensão. Para elementos do tipo ”casca”, de baixa ordem, surge predominantemente a retenção associada às componentes de extensão fora do plano (*transverse shear locking*). Para o caso dos elementos do tipo ”sólido-casca”, também de baixa ordem, surge adicionalmente a retenção associada aos termos de extensão linear (componentes directas do tensor das extensões), caracterizando o que ficou conhecido como retenção volumétrica (*volumetric locking*). Como resultado global, numa dada malha de elementos finitos, assiste-se a uma completa deterioração dos valores de deslocamentos obtidos como solução pelo método ou, nos casos mais favoráveis, a uma taxa de convergência muito baixa para a solução correcta, mesmo em problemas puramente lineares. Em qualquer desses cenários, uma utilização eficiente do elemento finito em causa torna-se inviável.

Na resolução dos fenómenos de retenção descritos foi utilizado o conceito de ”extensões acrescentadas” (*enhanced assumed strain method*), no qual cada elemento finito é ”enriquecido” com variáveis adicionais, sem significado físico, responsáveis por providenciar modos de deformação impossíveis de ser obtidos por uma formulação puramente

baseada em deslocamentos nodais. O número de variáveis internas a ser utilizado condiciona o desempenho computacional de um dado elemento, sendo muitas vezes escolhido de acordo com critérios empíricos de tentativa e erro. Neste trabalho, por outro lado, é utilizada uma filosofia de análise das bases dos subspaços de soluções admissíveis, para várias formulações publicadas na literatura especializada. Através dessa análise de bases, caracteriza-se o melhor ou pior comportamento de uma dada formulação e fundamenta-se assim a escolha quer do número de variáveis acrescentadas por elemento, quer das respectivas funções a elas associadas.

O resultado final consiste em uma nova classe de elementos finitos com um número óptimo de variáveis elementares (inferiores ao utilizado em proposas análogas por outros autores) e com bons desempenhos numa série de testes lineares e não-lineares (plasticidade, instabilidade e contacto). A implementação do método das extensões acrescentadas é feita de forma simplificada comparativamente a outras propostas na literatura, o que torna a tarefa de implementação numérica particularmente simples. A implementação de algoritmos para o tratamento de não-linearidades de material e geométrica é feita adoptando-se uma formulação co-rotacional a cada elemento finito, intuitiva no tratamento de problemas gerais envolvendo grandes (ilimitados) deslocamentos e rotações. Essa formulação co-rotacional permite, adicionalmente, o tratamento matemático objectivo de fenómenos envolvendo grandes deformações, com o aliciante de exigir uma implementação computacional relativamente simples e elegante. Não-linearidades relacionadas com problemas envolvendo situações de contacto, com ou sem atrito, foram resolvidas através da implementação dos elementos finitos propostos no código comercial *Abaqus* (*user-elements implementation*).

No fim do trabalho, é apresentada uma série de *benchmarks* numéricos, lineares e não-lineares, comumente adoptadas na literatura. Adicionalmente, é efectuado um estudo sobre um componente industrial (*S-Rail benchmark*), envolvendo plasticidade, grandes deformações e contacto com atrito, por forma a demonstrar a fiabilidade dos procedimentos implementados em problemas industriais. Os resultados obtidos atestam acerca robustez dos elementos finitos propostos, bem como dos algoritmos numéricos implementados.

Summary

In the present work, new formulations for *shell* and *solid-shell* finite elements are developed. The main goal of the present study is the correct numerical and computational analysis of nonlinear structural problems, involving components with reduced thickness values, and employing the Finite Element Method. In practical terms, it is interest to highlight the direct application of the proposed and implemented finite elements and numerical procedures to industrial sheet metal forming problems.

Within this scope, new bilinear shell type and trilinear solid-shell type finite elements were formulated and implemented, based on displacement variables. Going from the continuum media to the discretized finite element space, nodal displacement variables were taken into account. Displacement-based formulations are know to be affected by *locking* effects, characterized by an overestimation of determined stiffness. For the bilinear displacement-based shell elements, locking appearance is triggered mainly by the numerical treatment of low thickness values in the structure (*transverse shear locking*). For the specific case of low-order solid-shell displacement-based finite elements, and besides the locking referred before, *volumetric locking* is also prone to appear. The latter involves the direct components of the strain tensor, and is related to the numerical inability of a given formulation to automatically reproduce isochoric deformation paths. As a global result for a general finite element mesh, and for a deficient formulation, deterioration of displacement values numerically obtained occurs. In the most favorable case, the correct response might be obtained by the finite element model, but to the expense of a low convergence rate, even for fully linear behaviors.

In the treatment of locking, and now related to the line of research adopted in the present work, the *Enhanced Assumed Strain Method* was adopted, in the way that each finite element is improved by means of the use of internal variables, without physical meaning, and responsible for providing strain modes impossible to be obtained by a conventional formulation. The number of internal variables to be used per element influences the computational performance of the whole algorithm, and is a matter of crucial importance in the formulation. Sometimes their number is chosen according to specific problems to be solved, in a somewhat kind of "trial-and-error" basis. The present work, on the other side, intends to present a systematic and rational approach for the choice of the enhanced variables and functions, based on an analysis of the subspace bases for suitable solutions avoiding each specific class of locking patterns. The subspace bases study for well-established formulations in the literature turns clear the requirements that a fully displacement-based formulation might have, in order to overcome the transverse shear as well as the volumetric locking problems. As a result, an optimized number of internal variables are introduced into the formulation, when compared to similar proposals already published.

The final result is a new class of shell and solid-shell finite elements with improved results in a range of linear and nonlinear demanding benchmarks. The implementation of the Enhanced Assumed Strain Method is carried out in a simplified manner when compared with published proposals in the field, turning the coding effort straightforward. The implementation of algorithms for the modelling of geometric and material nonlinearities is carried out with the aid of a corotational approach, intuitive in the treatment of large displacement, rotations and deformations of shell structures. The use of a corotational formulation, furthermore, avoids considerations about the lack of objectivity in the rate type constitutive update of stress tensors. Nonlinearities involving contact and friction effects were dealt with by means of implementation of the proposed finite elements into the commercial package Abaqus.

Finally, and as a closure for the present research work, a set of numerical benchmarks is presented, involving demanding linear and nonlinear problems in the shell finite elements technology field. Additionally, it is taken into account an industrial problem involving the modelling and simulation of an automotive structural component (*S-Rail benchmark*), involving plasticity with large deformations, large displacements and rotations and frictional contact nonlinearities. The obtained results, in the general sense and for both the shell and solid-shell finite elements, infer about the reliability and accuracy of the new formulations and numerical algorithms implemented.

Résumé

Dans ce travail sont présentés des nouveaux développements des éléments finis de coque et solide-coque. La principale motivation de cette étude est l'application de la Méthode des Elements Finis pour la résolution des problèmes structurels non-linéaires avec components à faible épaisseur.

Au cours de ce travail, des nouveaux éléments finis bi-linéaire (de coque) e tri-linéaire (de solide-coque) sont proposés avec variables des déplacements dans les respectives functionnelles. Du point de vise de la descretization des milieux continus par les éléments finis, les champs des déplacements nodales sont utilises comme variables premières. L'application de ces formulations pour l'étude des problèmes structurels avec components à faible épaisseur est traditionnellement cause de problèmes numériques, spécialement l'apparition du connue phénomène de verrouillage (*locking*). Pour les éléments de coque, l'apparition du "transverse shear locking" est bien connue. L'application de la méthode des éléments finis au comportement incompressible, ou presque incompressible, avec des éléments tridimensionnelles est une cause de problème, spécialement l'apparition du verrouillage volumétrique (*volumetric locking*). Toutefois, les résultas obtenus avec ces éléments finis pour le champ des déplacements sont très mauvais, ou, la taxe de convergence est très faible.

En vue de la résolution de ces problèmes, dans ce travail on a utilise la méthode des déformations augmentées (*enhanced assumed strain method*). Dans cette méthode chaque élément finis est enrichisse avec variables additionnelles, sans significat physique, mais responsables pour l'obtention des modes de déformation, impossibles d'obtenir pour une formulation des déplacements nodales. Le nombre des variables additionnelles pour utiliser dans la méthode peut conditionner la performance d'un élément fini, être choisi pour critères empiriques de tentative-erreur. Dans ce travail l'analyse du sous-espace des solutions admissibles est effectuée. Cette philosophie, peut caractériser le comportement d'une formulation et peut permettre la définition du nombre de variables additionnelles.

Le résultat finale est une nouvelle classe d'élément finis avec un nombre optime de variables additionnelles (inférieur au nombre proposé par outres auteurs) qui montre

bonne performances en plusieurs exemples linéaire et non linéaire (plasticité, instabilité et contact). L'implémentation de la méthode des déformations augmentées est obtenu de forme simplifier. L'implémentation des algorithmes pour la résolution de problèmes non linéaires du matériel et géométrique est fait pour l'adoption d'une formulation co-rotacionnelle à chaque élément fini. Cette formulation co- rotacionnelle permettre le traitement mathématique objectif des phénomènes avec grandes déformations et avec une implémentation très simple et élégant. L'implémentation des nouveaux éléments finis dans le software Abaqus (user-elements implementation) on a permis la résolution des problèmes avec contact.

Dans le fin du travail est présenté un ensemble des benchmarks numériques, linéaire et non linéaire, usuellement utilisé dans la littérature. En plus, une étude est réalisée d'un component d'une voiture (*S-Rail benchmark*), avec déformations plastiques, grandes déformations et contact avec frottement, montrant la fiabilité des procédures implémentés en problèmes industriels. Les résultats obtenus montrent la robustesse des éléments finis proposés et des algorithmes numériques implémentés.

List of Symbols

(*in order of appearance in the text*)

$\mathcal{B}$	Element-wise region within $\mathbb{R}^3$
$\partial\mathcal{B}$	Boundary of region $\mathcal{B}$
$\mathcal{M}$	Reference (material) configuration within $\mathbb{R}^3$
$\mathcal{S}$	Current (spatial) configuration within $\mathbb{R}^3$
$\boldsymbol{\xi} \equiv \xi^i$	Convective set of coordinates ($i = 1, 2, 3$)
$\mathcal{P}$	Parametric configuration within $\mathbb{R}^3$
${}^{n}\mathbf{x}$	Position vector of a general point at state (n)
${}^{n}\mathbf{x}_k$	Position vector of a node (k) at state (n)
$\mathbf{N}_k$	Isoparametric shape functions for node (k)
${}^{n}a_k$	Thickness value calculated at node (k) and state (n)
${}^{n}\mathbf{v}_k^3$	Nodal normal vector at node (k) and state (n)
$\mathbf{e}_i$	Global set of coordinates ($i = 1, 2, 3$)
$\phi\left(\xi^1, \xi^2\right)$	Mid-surface representative function of convective ”in-plane” coordinates
$\mathbf{v}_k^i$	Nodal frame unit vectors ($i = 1, 2, 3$)
${}_{n}^{n+1}\mathbf{u}$	Displacement field between states (n) and ($n + 1$)
θ_k^i	Set of rotations d.o.f. for node (k) ($i = 1, 2$)
${}_{n}^{n+1}\boldsymbol{\Lambda}_k^i$	Iterative rotation matrix for node (k), at the i^{th} iteration between (n) and ($n + 1$)
$\boldsymbol{\Phi}_k^i$	Matrix of rotational d.o.f. for node (k) at iteration (i)
ϕ	Normalized (L_2) value of rotational d.o.f. at node (k)
${}_{n}^{i-1}\boldsymbol{\theta}_k$	Summated rotation vector for node (k), from converged state (n) until i^{th} iteration of ($n + 1$)
${}_{i-1}^{i}\boldsymbol{\theta}_k^a$	Iterative (additive) variation of the rotational d.o.f. at node (k)
$\mathbf{H}$	Non-additive to additive transformation matrix for the iterative rotational d.o.f.

${}^{n+1}\mathbf{g}_i$	Covariant base vectors $(i = 1, 2, 3)$
${}^{n+1}\mathbf{g}^i$	Contravariant base vectors $(i = 1, 2, 3)$
${}^{n+1}_{\ \ n}\mathbf{F}$	Deformation gradient tensor for deformation between states (n) and $(n + 1)$
${}^{n+1}_{\ \ n}\mathbf{E}^u$	Displacement-based Green-Lagrange strain tensor between states (n) and $(n + 1)$
$E^u_{\xi^i\xi^j}$	Displacement-based Green-Lagrange strain tensor convective components $(i, j = 1, 2, 3)$
$\mathbf{d}_k$	Degrees-of-freedom vector for node (k)
$\mathbf{u}_k \equiv u^i_k$	Translational d.o.f. components for node (k) $(i = 1, 2, 3)$
$\mathbf{M}^u$	Displacement-based strain-displacement matrix
$\mathbf{r}^i$	Local frame at a given point $(\boldsymbol{\xi})$ over an element $(i = 1, 2, 3)$
${}^{n+1}_{\ \ n}\mathbf{R}$	Relative rotation tensor for a deformation path between states (n) and $(n + 1)$
${}^{n+1}_{\ \ n}\mathbf{U}$	Relative right stretch tensor for a deformation path between (n) and $(n + 1)$
$\mathbf{T}$	Transformation (jacobian) matrix between the convective and global frames
$\mathbf{J}$	Transformation (jacobian) matrix between the global and convective frames
${}^l_c\mathbf{T}$	Linear map between tensors referred to the convective and local frames
${}^{n+1}_{\ \ n}\bar{\mathbf{E}}^u$	Incremental local displacement-based Green-Lagrange strain tensor
$\bar{\mathbf{M}}^u\big\rvert_{nl}$	Nonlinear displacement-based strain-displacement matrix on the local frame
$\mathbf{d}_e$	Degrees-of-freedom vector for a whole finite element (e)
$\mathbf{M}^u_s$	Convective, displacement-based, strain-displacement matrix accounting for out-of-plane shear strain components
$\mathcal{I}^s_h$	Subspace of admissible displacements granting a null transverse shear strain field
$\mathcal{U}$	Space of all displacements patterns
$\mathcal{U}_h$	Finite element approximation to the displacement space $\mathcal{U}$
$\mathbf{d}_h$	Finite element approximation to the element-based d.o.f. vector $\mathbf{d}_e$
$\mathcal{D}$	Isoparametric element-based space within $\mathbb{R}^2$
$\mathbf{d}_r$	”Reduced” nodal d.o.f. displacement vector
$\mathcal{I}^s_h\rvert_d$	Null transverse shear strain subspace for the *degenerated* formulation
$\mathbf{E}^{\mathrm{MITC}}$	Convective Green-Lagrange strain tensor coming from the *MITC* formulation
$\mathbf{M}^m_s$	Convective, *MITC*-based, strain-displacement matrix accounting for out-of-plane shear strain components
$\mathcal{I}^s_h\rvert_m$	Null transverse shear strain subspace for a *MITC*-based finite element formulation
$\mathbf{M}^r_s$	Convective, reduced integrated, strain-displacement matrix accounting for out-of-plane shear strain components
$\mathcal{I}^s_h\rvert_r$	Null transverse shear strain subspace for the 4 node *SRI* shell finite element
$\mathbf{E}^\alpha$	*EAS*-based Green-Lagrange strain tensor
$\mathbf{M}^\alpha$	Convective *EAS*-based strain-displacement matrix

$\boldsymbol{\alpha}$	Vector of *EAS* variables for out-of-plane strains
N_{α}^{2}	Two-dimensional bubble function
$\mathbf{M}^{\beta}$	Convective *EAS*-based strain-displacement matrix
$\boldsymbol{\beta}$	Vector of *EAS* variables for the in-plane strains
$\mathbf{x}_t$	Position vector over the top surface of a 3D element
$\mathbf{x}_b$	Position vector over the bottom surface of a 3D element
$\mathbf{x}_m$	Position vector over the mid-surface of a 3D element
$\mathcal{I}_h^v$	Subspace of admissible displacements granting volume conservation along deformation path
$\mathbf{K}_{uu}^{lg}$	Displacement-based linear geometric stiffness matrix
$\mathbf{Q}^v$	Coupling ”stiffness” matrix involving pressure and displacement fields
$\mathbf{p}_h$	Vector of (discrete) hydrostatic pressure field
$\mathbf{F}^e$	Vector of external forces
$\mathbb{V}_e$	Elemental finite volume
$\mathbf{E}^{\gamma}$	*EAS*-based Green-Lagrange strain tensor for volumetric locking
$\mathbf{M}^{\gamma}$	Convective *EAS*-based strain-displacement matrix for volumetric locking
N_{γ}^{3}	Three-dimensional bubble-function
$\mathbf{L}$	Velocity gradient tensor
$\boldsymbol{\Omega}$	Rotation rate tensor
$\boldsymbol{\sigma}$	Cauchy stress tensor
$\overset{\mathrm{G}}{\boldsymbol{\sigma}}$	Green-Naghdi-McInnis stress rate of the Cauchy stress tensor
$\mathbf{D}$	Spatial rate of deformation tensor
$\mathbf{D}^e$	Spatial rate of deformation tensor (elastic part)
$\mathbf{D}^p$	Spatial rate of deformation tensor (plastic part)
$\mathbf{W}$	Spin rate tensor
$\overset{\mathrm{J}}{\boldsymbol{\sigma}}$	Jaumann stress rate of the Cauchy stress tensor
$\bar{\mathbf{d}}$	Deformation rate rotated tensor
$\bar{\mathbf{d}}^e$	Deformation rate rotated tensor (elastic part)
$\bar{\mathbf{d}}^p$	Deformation rate rotated tensor (plastic part)
$\bar{\boldsymbol{\sigma}}$	Rotated Cauchy stress tensor
$\mathbf{c}$	Spatial constitutive tensor
$\bar{\mathbf{c}}$	Rotated constitutive tensor
$\bar{\mathbf{e}}$	Rotated total strain tensor (spatial)
$\bar{\mathbf{e}}^p$	Rotated plastic strain tensor (spatial)
$\bar{\mathbf{S}}$	Rotated 2^{nd} Piola-Kirchhoff stress tensor

W_s	Displacement-based strain energy
Π^{int}	Potential energy coming from internal forces
Π^{ext}	Potential energy coming from external forces
$\mathbf{t}$	Traction force vector
$\mathbf{b}$	Volume force vector
ρ	Density
$\hat{\mathbf{t}}$	Constrained value of traction force vector
$\hat{\mathbf{b}}$	Constrained value of volume force vector
$\mathbb{S}$	Elemental area (reference) for numerical integration
δ	Iterative (infinitesimal) operator for variations
Δ	Incremental (finite) operator for variations
$\mathcal{D}$	Directional derivative operator
$\mathbf{K}_{uu}^{lg}$	Displacement-based nonlinear geometric stiffness matrix
$\mathbf{K}_{u\alpha}$, $\mathbf{K}_{\alpha u}$	Coupled stiffness matrix coming from EAS and displacement variables
$\mathbf{K}_{\alpha\alpha}$	EAS-based stiffness matrix
Y	Elasto-plastic yield (loading) function
$\mathbf{P}$	Coefficients-based matrix for yield function
$\bar{\mathbf{s}}$	Deviatoric stress tensor in the local frame
δ_{ij}	Kronecker-delta operator
J_2	Second invariant of the deviatoric stress field
ν	Poisson's ratio
E	Young's modulus for elasticity
ϑ	Numerically integrated out-of-plane strain component in the local frame
$\bar{\mathbf{S}}^{trial}$	Elastic prediction of 2^{nd} Piola-Kirchhoff stress tensor
$\bar{\boldsymbol{\sigma}}^{trial}$	Elastic prediction of Cauchy stress tensor
Y^{trial}	Prediction of the yield function value based on a fully-elastic increment
ϵ^p	Equivalent plastic strain
σ_y	Isotropic hardening law based on the equivalent plastic strain
$\mathsf{H}_{\mathsf{iso}}$	Isotropic hardening linear parameter
λ	Plastic multiplier
$\bar{\mathbf{C}}$	Elastic constitutive modulus (material)
$\bar{\mathbf{C}}^a$	Algorithmic constitutive modulus (material)
$\bar{\mathbf{E}}^p$	Green-Lagrange plastic strain tensor
$\bar{\mathbf{C}}^p$	Consistent elasto-plastic constitutive operator
${}^n\rho$	Load factor at state (n)

$\delta\rho$	Iterative variation of load factor
${}^{n+1}_{n}\rho$	Incremental variation in the load factor between states (n) and $(n+1)$
$\mathbf{F}^i$	Internal force vector
$\mathbf{r}$	Residual vector
ψ	Weighting parameter for arc-length path following technique
l	Arc-length value
$\delta\mathbf{d}^*$	Auxiliary iterative displacement vector
$\delta\bar{\mathbf{d}}$	Auxiliary iterative displacement vector
a , b , c	Real coefficients for arc-length path following technique
l_{max}	Upper bound of the arc-length value
l_{min}	Lower bound of the arc-length value
σ_{y0}	Initial yield stress (scalar) for an e.p. evolution law
$\sigma_{y\infty}$	Saturation yield stress for an e.p. evolution law
n	Exponential hardening factor for an evolution e.p. law
C_i; m	Numerical constants for anisotropic criterion Yld'91 $(i = 1, \ldots, 6)$
μ	Friction coefficient

List of Tables

List of Figures

Contents

Chapter 1

Introduction

The present work is related to the study, development and implementation of numerical models and formulations within the Finite Element Method. The core point relies on the formulation of reliable and robust shell and solid-shell finite elements, suitable for the simulation of deformation processes on plate and shell structures.

If generality of applications is intended, then the proposed finite element formulation must inevitably lead to correct results either in linear and nonlinear ranges, thus encompassing large displacement, rotation and deformation problems. Numerical or physical instabilities arising from this class of problems must be correctly treated. Also, nonlinear material behavior must be taken into account, and specific algorithms dealing with computational plasticity must be implemented. Last but not least, distortion insensitivity is a desirable aspect, as problems coming from "real life" often involve irregular geometries.

Well-established shell and solid-shell finite element proposals in the literature sometimes lack one or more aspects of those referred before, and consequently developments in this specific area are always desirable. The present work aims to provide a contribution to this field, with the introduction and use of techniques not previously explored. The whole work was carried out over an "in-house" 2D finite element program, developed by P. Areias, former student of the Department of Mechanical Engineering, University of Porto. The shell and solid-shell finite element implementation, along with the Fortran 90 coding for nonlinear material and geometrical effects, including instabilities, were carried out in the aim of this Thesis. Nevertheless, results from Abaqus commercial finite element package are also provided when useful, for the sake of comparisons. Furthermore, some examples involving contact nonlinearities were also accounted for in the present work, taken advantage of the implementation of the developed finite elements as "user-elements" into Abaqus code.

Chronologically, this Thesis have started with the study and research over the concept behind degenerated shell elements for thin-shell applications. The main problem affecting this class of elements is the appearance of the transverse shear locking, a numerical pathology responsible for the overestimation of stiffness terms (and the consequent deterioration of results), when a conjunction of load, boundary and geometric conditions are attained.

From the analysis of common procedures dealing with this problem, such as the Mixed Interpolation of Tensorial Components (*MITC*) or the use of Reduced Integration (*RI*) techniques, the advantages and limitations of both techniques can be established . More important, it becomes patent why formulations entirely based on the displacement field are often affected by locking effects.

Being identified the problem to be solved, a new element formulation, based on the Enhanced Assumed Strain method, was then proposed, acting directly over the displacement-based (conventional) formulation. At the end, a new class of shell finite elements was obtained, with a sound and straightforward theoretical basis, in some cases with superior results when compared to *MITC* or *RI* based elements and, additionally, not including the physical instabilities of the latter. This subject, with all the steps undertaken, is the main topic of Chapter 2.

As more generality in the formulation and applications was needed, the research turned then to the development of the so-called ”solid-shell” type of finite elements, which have gained increasing interest along the last decade. Devoted to shell applications, but keeping a three-dimensional topology, these elements provide an elegant and straightforward alternative to shell elements. First of all, and compared to the latter, rotational degrees-of-freedom are not taken into account in the formulation, which remains entirely based on (additive) nodal translations, turning simulations in the nonlinear range simpler. Secondly, constitutive material models can be employed in its three-dimensional form, avoiding the (somewhat artificial) imposition of plane-stress conditions (characteristic of shell elements) and providing a natural way to account for through-thickness strain fields. Once again, the Enhanced Assumed Strain method is used to improve the performance of the conventional brick (8 node) solid element, which suffers from the before-mentioned transverse shear locking (for low thickness), but also from the volumetric locking pathology, arising when isochoric plasticity models are treated. As what happened with shell elements, the correct application of the *EAS* method turned to be sufficient in dealing with the mentioned locking effects, with no need to the inclusion of any other mixed approach into the formulation. The present work starts with the linear elastic *EAS* formulation for solid-shells initially developed by R. J. Alves de Sousa, then providing a proper extension in order to fully account for nonlinear geometric and material problems, including instabilities. The detailed description of the formulation, behind the presented solid-shell element, is carried out in Chapter 3.

Chapter 4 deals with the nonlinear theory and implementation aspects involved in the present work. The main idea is to provide the whole set of relevant information for subsequent users of the finite element code. The continuum mechanics aspects grounding the concept of a ”co-rotational” frame, constructed within each element and constituting the basis of the present work, are described in detail. The choice for this kind of description of the deformation process turned out to introduce a higher level of simplicity into the treatment of nonlinearities, when compared to other formulations. Nonlinear implementation aspects, specifically related to the Enhanced Assumed Strain method, are also detailed, along with the main guidelines in the computational inclusion of the elasto-plastic behavior. Finally in this Chapter, implementation details about the arc-length path-following technique are also detailed, providing the main basis for the treatment of numerical and physically-based instabilities along the load-displacement path.

In Chapter 5, an exhaustive set of numerical benchmarks, common in shell and solid-shell literature, is presented. The main motivation of such a large number of examples is to cover, as effectively as possible, all the ranges of solicitations, geometries, meshing distortion levels and boundary conditions available. Also, the chosen examples serve to show both the convergence and prediction capabilities of the developed Enhanced Assumed Strain shell and solid-shell formulations, within the nonlinear frame studied and implemented. The Chapter ends up with the analysis of an industrial component, whose simulation involves material, geometric and frictional contact nonlinearities.

Chapter 2

Enhanced Shell Finite Elements

In this chapter, the general guidelines for the implementation of a reliable Enhanced Assumed Strain (EAS) procedure, tackling the transverse shear locking problems in thin-shell finite elements, are developed. Details about the requirements and restrictions involved in the chosen enhanced shape functions are described. The analysis of the theoretical capabilities of well-known formulations for transverse shear locking-free elements is carried out. A new procedure, entirely based on the EAS method, is then introduced, remarkably improving the performance of the original degenerated four-node shell element.

2.1 State of the art

In the finite element analysis of shell structures, a landmark can be established with the work of Ahmad *et al.* (1970), leading to the so-called *degenerated shell element* concept. This formulation is obtained by judiciously imposing some *a priori* kinematic and mechanical assumptions on the three-dimensional continuum, circumventing the use of classical thin shell theories (Yang *et al.*, 2000). According to Bucalem and Bathe (1997), some key features of this class of elements are the applicability to any shell geometry, the use of $\left(C^0\right)$ conforming displacement-based formulations and the adoption of "engineering" degrees of freedom, such as displacements and rotations.

However, it is well known that degenerated formulations possess strong deficiencies in reproducing the behavior of thin-shell structures, leading to locking phenomena. For low order elements, like the four-node bilinear shell element entirely based on a displacement formulation, these effects are responsible for the complete deterioration of results coming from a finite element simulation. This *transverse shear locking* problem can be traced back to the fact that the *Kirchhoff-Love* hypotheses are not automatically reproduced by the displacement interpolations. The numerically calculated transverse shear strains cannot then vanish at all points in the element when it is subjected to a pure bending state (Kui *et al.*, 1985; Andelfinger and Ramm, 1993).

Amongst the approaches to overcome this problem, the simplest and earliest of all proposed was the use of *uniform* or *selective reduced integration*, as firstly reported by Hughes *et al.* (1978) and Zienkiewicz *et al.* (1979). Commonly, the *uniform reduced integration* (*URI*) procedure leads to spurious zero energy modes, even though for some cases a correct solution is obtained (Bucalem and Bathe, 1997). The *selective reduced integration* (*SRI*) technique, on the other hand, presents the same problems but usually on a smaller extent. In the specific case of plate elements, the work of Belytschko and Tsay (1983) pioneered a range of contributions using stabilization procedures for controlling the spurious modes arising from reduced formulations. Other techniques were proposed to alleviate the excess of stiffness coming from the onset of locking, most of them being classified as *hybrid*, *mixed* or *hybrid-mixed* methods. For these formulations, independent field assumptions for strains, stress and/or incompatible displacements can be assumed, and afterwards introduced into the corresponding functional. The additional fields may be discontinuous from element to element, so that the corresponding unknowns can be eliminated at the element level (Militello and Felippa, 1990; Andelfinger and Ramm, 1993).

These methods encomprise procedures such as the *Assumed Natural Strain* (*ANS*) approach (detailed for bilinear shell elements in the works of Hughes and Tezduyar (1981); MacNeal (1982); Dvorkin and Bathe (1984); Bathe and Dvorkin (1985) and for higher-order elements by Huang and Hinton (1986); Bathe and Dvorkin (1986); Bucalem and Bathe (1993)), and the *Enhanced Assumed Strain* (*EAS*) formulation (firstly introduced by Simo and Rifai (1990) and afterwards extended by Simo and Armero (1992) and Simo *et al.* (1993)). The *EAS* method was subsequently applied on shell elements by Andelfinger and Ramm (1993); Bischoff and Ramm (1997) and Huettel and Matzenmiller (1999), to name but a few. The key idea behind the *ANS* method is the replacement, in the minimum potential energy principle, of selected displacement-related strains by independently assumed strain fields in the element natural coordinates (Yunhua and Eriksson, 1999). A variational basis can be found, for example, in the work of Militello and Felippa (1990), and the performance of the elements derived from this formulation relies strongly in correctly choosing the sample strain positions within an element for the assumed (alternative) interpolation. However, deficiencies of results in the presence of irregular meshes can be pointed out (Andelfinger and Ramm, 1993). Nevertheless, the bilinear *MITC4* shell element of Dvorkin and Bathe (1984), based on this mixed interpolation of tensorial components, is amongst the most employed shell formulations, "which sometimes cause difficulties for other assumed strain techniques" (Stander *et al.*, 1989).

The *EAS* method, on the other hand, and as in the version firstly proposed by Simo and Rifai (1990), uses a three field mixed functional in terms of displacements, stresses and an *enhanced strain field*, relying on the *Hu-Washizu-de Veubeke* variational principle. As discussed in that reference, the total strain field is built up as a direct *summation* of the (compatible) symmetric gradient of the displacement and the enhanced strain fields. The latter is not subjected to any inter-element continuity requirement, and can be related to an *incompatible mode* field. A first consistent application of the enhanced techniques in shell analysis came shortly after in the work of Andelfinger and Ramm (1993), for the linear elastic range. The extension to nonlinear aspects was carried out in subsequent publications, such as, for instance, the works of Büchter *et al.* (1994), Roehl and Ramm (1996), Bischoff and Ramm (1997) and Eckstein and Basar (2000). Relating the low performance of *MITC4*, in the presence of distorted meshes, to in-plane formulation deficiencies, Andelfinger and Ramm (1993) introduced an enhanced membrane and bending strain field composed of seven internal (element-wise) parameters. Despite the improvements obtained, the procedure was not directly extended to the shear strain terms, once they have kept unaltered the assumed natural strain approach of Dvorkin and Bathe (1984) in attenuating transverse shear locking effects. In this sense, the problem of transverse shear locking in thin shell structures seemed to be "closed", with no completely distinct methodologies being proposed in the literature after that.

Within a distinct philosophy, the present work aims to introduce a new approach, suitable for the direct treatment of the transverse shear locking phenomenon for shell elements in the low-thickness limit. The methodology relies entirely on the Enhanced Assumed Strain formulation, and is applied over the formulation of the original degenerated four-node shell element. Following previous works of César de Sá and Owen (1986) and, subsequently, Natal Jorge (1998) and César de Sá and Natal Jorge (1999) for two-dimensional incompressible problems, shear locking appearance is related to the inability of a given basis of the null transverse shear strain subspace, implicitly defined by each finite element formulation, to accurately reproduce a set of required deformation patterns. A deep analysis of the *mixed interpolation of tensorial components* and the *selective reduced integration* procedures, thus leading to possible bases for their null transverse shear strain subspaces, reveals the missing terms on the respective basis for the *degenerated* formulation. Performing an enhancement over the covariant shear strain terms coming from this approach, an enlargement of its subspace is then obtained, leading to a new class of degenerated shell elements with improved behavior in the thin shell limit.

The specific analysis of the null transverse shear strain subspace carried out in this way was also helpful in revealing that the *MITC4* element itself lacks two missing components in any of its possible basis, when compared to *SRI*-based elements of the same order. These very same components are neither present in the basis of the *degenerated* element. In fact, in trying to reproduce the deformation pattern corresponding to one of those absent components, both elements' formulation reveals a strong deterioration of results. For this specific example, involving a single element, the *MITC4* and *degenerated* formulations provide the same numerical result, while the *SRI* approach shows no shear locking. Besides the improvements obtained by the *enhanced degenerated* shell element in what matters to the transverse shear locking, a further progress in the element's performance can be achieved with an additional enhancement over the original in-plane strain components. This modification leads to better results in some problems involving in-plane mesh distortion and membrane locking patterns.

Recently, deeper insight into locking phenomena affecting shell elements was brought forward by the work of Pitkäranta *et al.* (1995), Chapelle and Bathe (1998) and Malinen and Pitkäranta (2000) (and, after that, by Bathe *et al.* (2000); Chapelle and Bathe (2000); Bathe *et al.* (2003); Chapelle and Bathe (2003)). Based on a detailed analysis of bending and membrane-dominated problems, those authors developed a class of benchmark tests for the characterization of shell elements. In order to fully describe the behavior of the enhanced strain methodology and elements proposed in this work, this set of tests is carried out in Chapter 5, along with some classical problems in shell finite elements literature.

This Chapter is organized as follows. In Section 2.2, the basic equations for the kinematics of the degenerated shell element are shown, along with the respective equations for the Green-Lagrange strain tensor on the convective frame. The local axis system at each Gauss point level, providing a co-rotational space where nonlinear relations are expressed, is then introduced, along with the update procedure based on the deformation gradient tensor. In Section 2.3, subspace analyses for the degenerated, reduced integrated and assumed natural strain formulations are detailed, characterizing the ability of each approach to be affected (or not) by transverse shear locking effects. Section 2.4 introduces the developed Enhanced Assumed Strain procedure to deal with this locking in thin shells. Enhanced strain shell finite elements *S4E6P5*, *S4E6P7* and *MITC4–E2* are defined, along with their specific enhanced strain functions and variables. Finally, the extension of the referred points to account for nonlinearities is left to be carried out in Chapter 4.

2.2 Kinematics of shell displacement-based elements

In dealing with shell formulations directly derived from the *degenerated concept*, introduced by Ahmad *et al.* (1970), a starting point would be the assumption of the existence of a region $\mathcal{B} \subset \mathbb{R}^3$, with boundary $\partial\mathcal{B}$, which can be occupied by a given shell element. Considering the deformation of the continuum, it is also useful to invoke a *reference* (or *material*) and *current* (or *spatial*) configurations $\mathcal{M} \subset \mathbb{R}^3$ and $\mathcal{S} \subset \mathbb{R}^3$, respectively. In static analysis, these two configurations mimics successive deformation (loading) stages (n) and $(n+1)$ for a given body partition, without resorting to the time variable.

Departing from a given continuum body into a discretized one, finite elements can be described within a set of curvilinear (convective) coordinates

$$\boldsymbol{\xi} = (\xi^1, \xi^2, \xi^3) \equiv [-1, 1] \times [-1, 1] \times [-1, 1] \tag{2.1}$$

characterizing a parametric configuration $\mathcal{P} \subset \mathbb{R}^3$. Related to this parametric set, the position vector of any point $P \in \mathcal{B}$ of a shell element can then be defined by (Bathe, 1996; Chapelle and Bathe, 2003) in the form

$${}^n\mathbf{x}\left(\boldsymbol{\xi}\right) = \mathbf{N}_k {}^n\mathbf{x}_k + \frac{1}{2}\xi^3\, {}^n a_k\, \mathbf{N}_k\, {}^n\mathbf{v}_k^3 \tag{2.2}$$

for the configuration (n). In this equation, summation over indices k (nodes) is implicit. Nodes are assumed to rely on a (reference) mid-surface, being ${}^n\mathbf{x}_k$ (nodal) position vectors related to an external system of orthonormal vectors, forming a global triad $(\mathbf{e}_1, \mathbf{e}_2, \mathbf{e}_3)$. Also in equation (2.2), $\mathbf{N}_k = \mathbf{N}_k\left(\xi^1, \xi^2\right)$ are the matrices of two-dimensional isoparametric shape functions, ${}^n a_k$ are nodal thickness values and ${}^n\mathbf{v}_k^3$ represents a (unit) director vector, normal (at least in the initial state) to the reference surface, and defining the so-called "thickness direction".

In detail, for a mid-surface in the convective space, mapped onto $\mathcal{B}$ via a function (chart) $\phi\left(\xi^1, \xi^2\right)$, a couple of tangent vectors can be defined as (Chapelle and Bathe, 2003)

$$\mathbf{v}_l^\alpha = \frac{\partial\phi\left(\xi^1, \xi^2\right)}{\partial\xi^\alpha} \text{ , for } \alpha = 1, 2 \tag{2.3}$$

By assumption, these linearly independent vectors are candidates in forming a frame on the tangent plane to the mid-surface at each point (l). The director vector can then be explicitly defined as

$$\mathbf{v}_l^3 = \frac{\mathbf{v}_l^1 \times \mathbf{v}_l^2}{\left\|\mathbf{v}_l^1 \times \mathbf{v}_l^2\right\|} \tag{2.4}$$

However, in algorithmic terms and for a nodal point $(l = k)$ within a finite element, the nodal director vector can be defined, for instance, from the global coordinates of adjacent nodes or directly from the user input (ABAQUS, 2002a), in order to its direction coincide (or be close) to the fiber (thickness) direction (Hughes, 2000). Having the director being specified, the two auxiliary vectors on (2.3) can be stated with the aid of the global triad. In this sense, it is possible to enforce (Bathe, 1996) that

$$\mathbf{v}_k^1 = \frac{\mathbf{e}_2 \times \mathbf{v}_k^3}{\left\|\mathbf{e}_2 \times \mathbf{v}_k^3\right\|} \tag{2.5a}$$

$$\left(\text{if} \quad \mathbf{e}_2 \times \mathbf{v}_k^3 = \mathbf{0} \quad \text{then} \quad \mathbf{v}_k^1 \equiv \mathbf{e}_1\right) \tag{2.5b}$$

$$\mathbf{v}_k^2 = \mathbf{v}_k^3 \times \mathbf{v}_k^1 \tag{2.5c}$$

Unit vectors $\left(\mathbf{v}_k^1, \mathbf{v}_k^2, \mathbf{v}_k^3\right)$ on each node then introduce a unique nodal coordinate system at each configuration.

After deformation, the position of point P can be described in the final configuration $(n+1)$ as

$$^{n+1}\mathbf{x}\left(\boldsymbol{\xi}\right) = \mathbf{N}_k {}^{n+1}\mathbf{x}_k + \frac{1}{2}\,\xi^3\; {}^{n+1}a_k\,\mathbf{N}_k\; {}^{n+1}\mathbf{v}_k^3 \tag{2.6}$$

The displacement field of a given point $\left(\xi^1, \xi^2, \xi^3\right)$ between configurations (n) and $(n+1)$ now appears as

$$^{n+1}_{\ \ n}\mathbf{u}\left(\boldsymbol{\xi}\right) = {}^{n+1}\mathbf{x}\left(\boldsymbol{\xi}\right) - {}^{n}\mathbf{x}\left(\boldsymbol{\xi}\right) \tag{2.7}$$

Expansion of equation (2.7) gives rise to 5 nodal degrees-of-freedom, comprising three translations – related to the global frame $(\mathbf{e}_1, \mathbf{e}_2, \mathbf{e}_3)$ – plus two rotations – related to the nodal frame $\left(\mathbf{v}_k^1, \mathbf{v}_k^2, \mathbf{v}_k^3\right)$ – and coming from the general expression

$$^{n+1}_{\ \ n}\mathbf{u}\left(\boldsymbol{\xi}\right) = \mathbf{N}_k\, {}^{n+1}_{\ \ n}\mathbf{x}_k + \frac{1}{2}\,\xi^3\,\mathbf{N}_k\,\left({}^{n+1}a_k {}^{n+1}\mathbf{v}_k^3 - {}^{n}a_k {}^{n}\mathbf{v}_k^3\right) \tag{2.8}$$

In the present work, from configurations (n) to $(n+1)$, nodal thickness values are kept constant and equal to $a_k = {}^{n}a_k = {}^{n+1}a_k$. After the completion of iterations until the final stage $(n+1)$, thickness values at Gauss points are updated enforcing the plane-stress condition, which is usually assumed in this class of degenerated shell elements. Those Gaussian thickness values are subsequently extrapolated to the nodal points, and a new deformation stage is started with the corrected nodal thickness value (Yoon *et al.*, 1999; Cardoso *et al.*, 2002; Cardoso, 2002).

Apart from these considerations about nodal thickness values, nodal director variations in equation (2.8) can be explicitly described in the nodal frame $\left(\mathbf{v}_k^1, \mathbf{v}_k^2, \mathbf{v}_k^3\right)$ as

$$^{n+1}_{\ \ n}\mathbf{v}_k^3 = {}^{n+1}\mathbf{v}_k^3 - {}^{n}\mathbf{v}_k^3 = \theta_k^1\; {}^{n}\mathbf{v}_k^1 - \theta_k^2\; {}^{n}\mathbf{v}_k^2 - \frac{1}{2}\left[\left(\theta_k^1\right)^2 + \left(\theta_k^2\right)^2\right] {}^{n}\mathbf{v}_k^3 \tag{2.9}$$

where $\left(\theta_k^1, \theta_k^2\right)$ are the rotational degrees-of-freedom of director ${}^{n}\mathbf{v}_k^3$ about auxiliary vectors ${}^{n}\mathbf{v}_k^1$ and ${}^{n}\mathbf{v}_k^2$, respectively. Although valid for large incremental rotations, the contribution of the quadratic terms in equation (2.9) to the displacement-based geometric stiffness matrix is not accounted for in the present work, without prejudice of the overall convergence behavior and with benefit of the computational costs, in the same manner as stated by Saleeb *et al.* (1990).

The rotational degrees-of-freedom $\left(\theta_k^1, \theta_k^2\right)$ are also used in the construction of a rotation-based matrix, responsible for the update of the nodal triad $\left(\mathbf{v}_k^1, \mathbf{v}_k^2, \mathbf{v}_k^3\right)$ at each iteration between two successive load levels (n) and $(n+1)$.

Focusing on the current and converged directors at a node, it is possible to state that

$$ {}^{n+1}\mathbf{v}_k^3\big|^i = {}_{n}^{n+1}\boldsymbol{\Lambda}_k^i \; {}^{n}\mathbf{v}_k^3 \tag{2.10}$$

for a given iteration (i). The general form of the second-order transformation tensor adopted in this work follows the Rodrigues formula from rigid body dynamics (Basar and Weicher, 2000; Büchter and Ramm, 1992; Betsch *et al.*, 1998; Doyle, 2001)

$$ {}_{n}^{n+1}\boldsymbol{\Lambda}_k^i \equiv e^{\boldsymbol{\Phi}_k^i} = \mathbf{I}_2 + \frac{\sin(\phi)}{\phi}\,\boldsymbol{\Phi}_k^i + \frac{1-\cos(\phi)}{\phi^2}\,\boldsymbol{\Phi}_k^i\,\boldsymbol{\Phi}_k^i \tag{2.11}$$

for the second-order identity tensor $\mathbf{I}_2$. In the equation, $\boldsymbol{\Phi}_k^i$ contains a composition of the nodal rotational degrees of freedom θ_k^1 and θ_k^2, from (n) to the ith iteration up to $(n+1)$, in the form

$$ \left[\boldsymbol{\Phi}_k^i\right] = \begin{bmatrix} 0 & 0 & {}_{n}^{i}\theta_k^1 \\ 0 & 0 & -{}_{n}^{i}\theta_k^2 \\ -{}_{n}^{i}\theta_k^1 & {}_{n}^{i}\theta_k^2 & 0 \end{bmatrix} \text{ and with } \phi = \sqrt{\left({}_{n}^{i}\theta_k^1\right)^2 + \left({}_{n}^{i}\theta_k^2\right)^2} \tag{2.12}$$

once no drilling degrees-of-freedom are employed in the present formulation.

The converged director $\left({}^{n}\mathbf{v}_k^3\right)$ is taken as the reference one, being updated at each iteration (i), and leading to a "pseudo-converged" current director $\left({}^{n+1}\mathbf{v}_k^3\big|^i\right)$ with iterative character. This involves the knowledge of the total values of the rotational degrees-of-freedom $\left({}_{n}^{i}\theta_k^1, {}_{n}^{i}\theta_k^2\right)$ from the converged state (n) up to the current iteration (i), respectively. Since the degrees-of-freedom $\left(\theta_k^1, \theta_k^2\right)$ are, by definition, non-additive variables (even for a small deformation analysis), a special procedure to convert them into additive variables is employed, following the general guidelines of Crisfield (1997) and detailed in the following for the sake of completeness.

Consider the accumulated rotation vector (previously additively evaluated) from the converged state (n) until the previous iteration $(i-1)$ for a given node as

$$ {}_{n}^{i-1}\boldsymbol{\theta}_k = \sum_{j=1}^{i-1} {}_{j-1}^{j}\boldsymbol{\theta}_k^a = \begin{Bmatrix} {}_{n}^{i-1}\theta_k^1 \\ {}_{n}^{i-1}\theta_k^2 \\ 0 \end{Bmatrix}; \quad \text{summation over } j \text{ iterations} \tag{2.13}$$

where the index (a) enforces the additive character of the (transformed) rotations. If the iterative variation in the rotational variables corresponds to the vector $\left({}_{i-1}^{\;\;i}\boldsymbol{\theta}_k\right)$, it is possible to change its non-additive character into an additive one, represented by a new iterative rotation vector $\left({}_{i-1}^{\;\;i}\boldsymbol{\theta}_k^a\right)$, in the form

$$
{}_{i-1}^{\;\;i}\boldsymbol{\theta}_k^a = \left[\mathbf{H}\left({}^{i-1}_{\;\;n}\boldsymbol{\theta}_k\right)\right]^{-1} {}_{i-1}^{\;\;i}\boldsymbol{\theta}_k \tag{2.14}
$$

accounting for

$$
\mathbf{H}\left({}^{i-1}_{\;\;n}\boldsymbol{\theta}_k\right) = \frac{\sin(\phi)}{\phi}\mathbf{I}_2 + \frac{1}{\phi^2}\left(1 - \frac{\sin(\phi)}{\phi}\right){}^{i-1}_{\;\;n}\boldsymbol{\theta}_k \left[{}^{i-1}_{\;\;n}\boldsymbol{\theta}_k\right]^{\mathrm{T}} + \frac{1}{2}\left(\frac{\sin\left(\phi/2\right)}{\phi/2}\right)^2 \boldsymbol{\Phi}_k\left({}^{i-1}_{\;\;n}\boldsymbol{\theta}_k\right) \tag{2.15}
$$

and where the function $\boldsymbol{\Phi}_k\left({}^{i-1}_{\;\;n}\boldsymbol{\theta}_k\right)$ is evaluated according to equation (2.12). The updated incremental additive variation can now be directly employed in the director update expressions

$$
\left({}^{i-1}_{\;\;n}\boldsymbol{\theta}_k + {}_{i-1}^{\;\;i}\boldsymbol{\theta}_k^a\right) \xrightarrow{\text{equations (2.10),(2.11),(2.12)}} \left({}^{n+1}_{\;\;\;n}\boldsymbol{\Lambda}_k^i\right) \tag{2.16}
$$

The same procedure as detailed for the update of the director $\left({}^n\mathbf{v}_k^3\right)$ can be extended in order to obtain the updated triad $\left({}^{n+1}\mathbf{v}_k^1, {}^{n+1}\mathbf{v}_k^2, {}^{n+1}\mathbf{v}_k^3\right)$, at each iteration (i). After these considerations about the nodal frame in each node and configuration, the displacement-based strain tensor for this class of shell elements can be completely defined.

Taking again a deformation path between configurations (n) and $(n+1)$ (and dropping superscripts (i) for simplicity reasons), the Green-Lagrange strain tensor for a given point on the convective space $\left(\xi^1, \xi^2, \xi^3\right)$ can be defined in an explicit way. First it is necessary to establish a set of covariant base vectors from the partial derivatives of the position vectors (Bathe, 1996; Basar and Weicher, 2000)

$$
{}^{n+1}\mathbf{g}_l\left(\boldsymbol{\xi}\right) = \frac{\partial\, {}^{n+1}\mathbf{x}\left(\boldsymbol{\xi}\right)}{\partial \xi^l} \tag{2.17a}
$$

$$
{}^{n}\mathbf{g}_l\left(\boldsymbol{\xi}\right) = \frac{\partial\, {}^{n}\mathbf{x}\left(\boldsymbol{\xi}\right)}{\partial \xi^l} \tag{2.17b}
$$

each one directly related to its contravariant counterparts ${}^{n+1}\mathbf{g}^l$ and ${}^{n}\mathbf{g}^l$, respectively, and with $(l = 1, 2, 3)$. With the position vector for two successive configurations, it is also possible to evaluate the two-point relative deformation gradient tensor

$$
{}^{n+1}_{\;\;\;n}\mathbf{F}\left(\boldsymbol{\xi}\right) = \frac{\partial\, {}^{n+1}\mathbf{x}}{\partial\, {}^{n}\mathbf{x}} = {}^{n+1}\mathbf{g}_k \otimes {}^{n}\mathbf{g}^k \tag{2.18}
$$

The displacement-based Green-Lagrange strain tensor $\mathbf{E}^u$, as well as its components, can then be stated in the form

$$
{}^{n+1}_{\;\;\;n}\mathbf{E}^u = \frac{1}{2}\left({}^{n+1}_{\;\;\;n}\mathbf{F}^{\mathrm{T}}\ {}^{n+1}_{\;\;\;n}\mathbf{F} - \mathbf{I}_2\right) = E^u_{\xi^j\xi^l}\ {}^{n}\mathbf{g}^j \otimes {}^{n}\mathbf{g}^l \tag{2.19a}
$$

$$ {}^{n+1}_{\;\;n}E^{u}_{\xi^j\xi^l} = \frac{1}{2}\left(\underbrace{{}^{n}\mathbf{g}_j \cdot \frac{\partial\, {}^{n+1}_{\;\;n}\mathbf{u}}{\partial\, \xi^l} + \frac{\partial\, {}^{n+1}_{\;\;n}\mathbf{u}}{\partial\, \xi^j} \cdot {}^{n}\mathbf{g}_l}_{\text{linear part}} + \underbrace{\frac{\partial\, {}^{n+1}_{\;\;n}\mathbf{u}}{\partial\, \xi^j} \cdot \frac{\partial\, {}^{n+1}_{\;\;n}\mathbf{u}}{\partial\, \xi^l}}_{\text{non-linear part}} \right) \tag{2.19b} $$

The choice of the convective frame as the departure point for strain components evaluations is due to generality reasons and also because the enhanced transverse shear strain field used in this work is firstly defined in this referential, as will be detailed in the next section. The first two terms of the right hand side of equation (2.19b) lead to the linear strain-displacement and, subsequently, linear stiffness matrices. A degrees-of-freedom vector $\mathbf{d}_k$, gathering the translation and rotational components at each node point (k), is now introduced in the form

$$ \mathbf{d}_k = \left\{\; u^1 \quad u^2 \quad u^3 \quad \theta^1 \quad \theta^2 \;\right\}^{\mathrm{T}} \tag{2.20} $$

for $\mathbf{u}_k = \left\{u^1 \;\; u^2 \;\; u^3\right\}^{\mathrm{T}}$.

Considering the director cosines of the nodal vectors $\left(\mathbf{v}^1_k, \mathbf{v}^2_k, \mathbf{v}^3_k\right)$ as $\mathbf{v}^1_k = \left\{v^{11} \;\; v^{12} \;\; v^{13}\right\}^{\mathrm{T}}$, $\mathbf{v}^2_k = \left\{v^{21} \;\; v^{22} \;\; v^{23}\right\}^{\mathrm{T}}$, $\mathbf{v}^3_k = \left\{v^{31} \;\; v^{32} \;\; v^{33}\right\}^{\mathrm{T}}$, the components of the nodal position vector as $\mathbf{x}_k = \left\{x^1 \;\; x^2 \;\; x^3\right\}^{\mathrm{T}}$ – dropping the configurations indices (n) and $(n+1)$ – it is possible to formulate explicit expressions for the linear part of the convective components of the Green-Lagrange strain tensor (equation (2.19b)) in the form

$$ \begin{aligned} E^u_{\xi^1\xi^1} = {} & \left(\frac{\partial x^1}{\partial \xi^1}\frac{\partial N}{\partial \xi^1}\right) u^1 + \left(\frac{\partial x^2}{\partial \xi^1}\frac{\partial N}{\partial \xi^1}\right) u^2 + \left(\frac{\partial x^3}{\partial \xi^1}\frac{\partial N}{\partial \xi^1}\right) u^3 \\ & + \left(\frac{a}{2}\xi^3\frac{\partial N}{\partial \xi^1}\left(\frac{\partial x^1}{\partial \xi^1}v^{11} + \frac{\partial x^2}{\partial \xi^1}v^{12} + \frac{\partial x^3}{\partial \xi^1}v^{13}\right)\right)\theta^1 \\ & - \left(\frac{a}{2}\xi^3\frac{\partial N}{\partial \xi^1}\left(\frac{\partial x^1}{\partial \xi^1}v^{21} + \frac{\partial x^2}{\partial \xi^1}v^{22} + \frac{\partial x^3}{\partial \xi^1}v^{23}\right)\right)\theta^2 \end{aligned} \tag{2.21} $$

$$ \begin{aligned} E^u_{\xi^2\xi^2} = {} & \left(\frac{\partial x^1}{\partial \xi^2}\frac{\partial N}{\partial \xi^2}\right) u^1 + \left(\frac{\partial x^2}{\partial \xi^2}\frac{\partial N}{\partial \xi^2}\right) u^2 + \left(\frac{\partial x^3}{\partial \xi^2}\frac{\partial N}{\partial \xi^2}\right) u^3 \\ & + \left(\frac{a}{2}\xi^3\frac{\partial N}{\partial \xi^2}\left(\frac{\partial x^1}{\partial \xi^2}v^{11} + \frac{\partial x^2}{\partial \xi^2}v^{12} + \frac{\partial x^3}{\partial \xi^2}v^{13}\right)\right)\theta^1 \\ & - \left(\frac{a}{2}\xi^3\frac{\partial N}{\partial \xi^2}\left(\frac{\partial x^1}{\partial \xi^2}v^{21} + \frac{\partial x^2}{\partial \xi^2}v^{22} + \frac{\partial x^3}{\partial \xi^2}v^{23}\right)\right)\theta^2 \end{aligned} \tag{2.22} $$

$$ \begin{aligned} E^u_{\xi^3\xi^3} = {} & \left(\frac{a}{2}N\left(\frac{\partial x^1}{\partial \xi^3}v^{11} + \frac{\partial x^2}{\partial \xi^3}v^{12} + \frac{\partial x^3}{\partial \xi^3}v^{13}\right)\right)\theta^1 \\ & - \left(\frac{a}{2}N\left(\frac{\partial x^1}{\partial \xi^3}v^{21} + \frac{\partial x^2}{\partial \xi^3}v^{22} + \frac{\partial x^3}{\partial \xi^3}v^{23}\right)\right)\theta^2 \end{aligned} \tag{2.23} $$

$$\begin{aligned}2E^u_{\xi^1\xi^2} = {} & \left(\frac{\partial x^1}{\partial \xi^1}\frac{\partial N}{\partial \xi^2} + \frac{\partial x^1}{\partial \xi^2}\frac{\partial N}{\partial \xi^1}\right) u^1 + \left(\frac{\partial x^2}{\partial \xi^1}\frac{\partial N}{\partial \xi^2} + \frac{\partial x^2}{\partial \xi^2}\frac{\partial N}{\partial \xi^1}\right) u^2 + \left(\frac{\partial x^3}{\partial \xi^1}\frac{\partial N}{\partial \xi^2} + \frac{\partial x^3}{\partial \xi^2}\frac{\partial N}{\partial \xi^1}\right) u^3 + \\ & \left(\frac{a}{2}\xi^3\frac{\partial N}{\partial \xi^2}\left(\frac{\partial x^1}{\partial \xi^1}v^{11} + \frac{\partial x^2}{\partial \xi^1}v^{12} + \frac{\partial x^3}{\partial \xi^1}v^{13}\right) + \frac{a}{2}\xi^3\frac{\partial N}{\partial \xi^1}\left(\frac{\partial x^1}{\partial \xi^2}v^{11} + \frac{\partial x^2}{\partial \xi^2}v^{12} + \frac{\partial x^3}{\partial \xi^2}v^{13}\right)\right)\theta^1 - \\ & \left(\frac{a}{2}\xi^3\frac{\partial N}{\partial \xi^2}\left(\frac{\partial x^1}{\partial \xi^1}v^{21} + \frac{\partial x^2}{\partial \xi^1}v^{22} + \frac{\partial x^3}{\partial \xi^1}v^{23}\right) + \frac{a}{2}\xi^3\frac{\partial N}{\partial \xi^1}\left(\frac{\partial x^1}{\partial \xi^2}v^{21} + \frac{\partial x^2}{\partial \xi^2}v^{22} + \frac{\partial x^3}{\partial \xi^2}v^{23}\right)\right)\theta^2\end{aligned} \tag{2.24}$$

$$\begin{aligned}2E^u_{\xi^1\xi^3} = {} & \left(\frac{\partial x^1}{\partial \xi^1}\frac{\partial N}{\partial \xi^3} + \frac{\partial x^1}{\partial \xi^3}\frac{\partial N}{\partial \xi^1}\right) u^1 + \left(\frac{\partial x^2}{\partial \xi^1}\frac{\partial N}{\partial \xi^3} + \frac{\partial x^2}{\partial \xi^3}\frac{\partial N}{\partial \xi^1}\right) u^2 + \left(\frac{\partial x^3}{\partial \xi^1}\frac{\partial N}{\partial \xi^3} + \frac{\partial x^3}{\partial \xi^3}\frac{\partial N}{\partial \xi^1}\right) u^3 + \\ & \left(\frac{a}{2}\left(v^{11}\left(N\frac{\partial x^1}{\partial \xi^1} + \xi^3\frac{\partial N}{\partial \xi^1}\frac{\partial x^1}{\partial \xi^3}\right) + v^{12}\left(N\frac{\partial x^2}{\partial \xi^1} + \xi^3\frac{\partial N}{\partial \xi^1}\frac{\partial x^2}{\partial \xi^3}\right) + v^{13}\left(N\frac{\partial x^3}{\partial \xi^1} + \xi^3\frac{\partial N}{\partial \xi^1}\frac{\partial x^3}{\partial \xi^3}\right)\right)\right)\theta^1 - \\ & \left(\frac{a}{2}\left(v^{21}\left(N\frac{\partial x^1}{\partial \xi^1} + \xi^3\frac{\partial N}{\partial \xi^1}\frac{\partial x^1}{\partial \xi^3}\right) + v^{22}\left(N\frac{\partial x^2}{\partial \xi^1} + \xi^3\frac{\partial N}{\partial \xi^1}\frac{\partial x^2}{\partial \xi^3}\right) + v^{23}\left(N\frac{\partial x^3}{\partial \xi^1} + \xi^3\frac{\partial N}{\partial \xi^1}\frac{\partial x^3}{\partial \xi^3}\right)\right)\right)\theta^2\end{aligned} \tag{2.25}$$

$$\begin{aligned}2E^u_{\xi^2\xi^3} = {} & \left(\frac{\partial x^1}{\partial \xi^2}\frac{\partial N}{\partial \xi^3} + \frac{\partial x^1}{\partial \xi^3}\frac{\partial N}{\partial \xi^2}\right) u^1 + \left(\frac{\partial x^2}{\partial \xi^2}\frac{\partial N}{\partial \xi^3} + \frac{\partial x^2}{\partial \xi^3}\frac{\partial N}{\partial \xi^2}\right) u^2 + \left(\frac{\partial x^3}{\partial \xi^2}\frac{\partial N}{\partial \xi^3} + \frac{\partial x^3}{\partial \xi^3}\frac{\partial N}{\partial \xi^2}\right) u^3 + \\ & \left(\frac{a}{2}\left(v^{11}\left(N\frac{\partial x^1}{\partial \xi^2} + \xi^3\frac{\partial N}{\partial \xi^2}\frac{\partial x^1}{\partial \xi^3}\right) + v^{12}\left(N\frac{\partial x^2}{\partial \xi^2} + \xi^3\frac{\partial N}{\partial \xi^2}\frac{\partial x^2}{\partial \xi^3}\right) + v^{13}\left(N\frac{\partial x^3}{\partial \xi^2} + \xi^3\frac{\partial N}{\partial \xi^2}\frac{\partial x^3}{\partial \xi^3}\right)\right)\right)\theta^1 - \\ & \left(\frac{a}{2}\left(v^{21}\left(N\frac{\partial x^1}{\partial \xi^2} + \xi^3\frac{\partial N}{\partial \xi^2}\frac{\partial x^1}{\partial \xi^3}\right) + v^{22}\left(N\frac{\partial x^2}{\partial \xi^2} + \xi^3\frac{\partial N}{\partial \xi^2}\frac{\partial x^2}{\partial \xi^3}\right) + v^{23}\left(N\frac{\partial x^3}{\partial \xi^2} + \xi^3\frac{\partial N}{\partial \xi^2}\frac{\partial x^3}{\partial \xi^3}\right)\right)\right)\theta^2\end{aligned} \tag{2.26}$$

The last equations can be grouped in an equivalent (general) single equation in the form

$$\mathbf{E}^u = \mathbf{M}^u\left(\boldsymbol{\xi}\right)\left\{\begin{array}{c}\mathbf{d}_1 \\ \cdots \\ \mathbf{d}_k\end{array}\right\} \quad \text{for} \quad k = 1, \ldots, nnode \quad \text{and with} \quad nnode = 4 \tag{2.27}$$

leading to the linear convective strain-displacement differential matrix ($\mathbf{M}^u$) and, afterwards, to the linear displacement-based stiffness matrix. An analogous nodal discretization also applies to the nonlinear term in equation (2.19b), leading to the corresponding nonlinear strain-displacement matrix and, subsequently, the geometric (initial stress) displacement-based stiffness operator.

Due to the non-orthogonal character of the convective frame, the linear strain-displacement operator coming from equations (2.21)-(2.26) will now be projected onto a new orthonormal frame $\left(\mathbf{r}^1, \mathbf{r}^2, \mathbf{r}^3\right)$. This local (or "lamina", as referred by Hughes (2000)) coordinate system is used for the constitutive update and for the application of the plane-stress hypothesis. It is defined at each Gauss point over the undeformed mesh (being subsequently updated as deformation occurs, as will be described in the following sections).

There is not a unique way to choose the starting configuration for the local frame (Bathe, 1996; Hughes, 2000), and in this work the following straightforward algorithm was adopted:

$$\begin{aligned}
&1.\ \text{Let } \mathbf{r}^3 = \left\{ \frac{\partial x^1}{\partial \xi^1} \quad \frac{\partial x^2}{\partial \xi^1} \quad \frac{\partial x^3}{\partial \xi^1} \right\}^{\mathrm{T}} \times \left\{ \frac{\partial x^1}{\partial \xi^2} \quad \frac{\partial x^2}{\partial \xi^2} \quad \frac{\partial x^3}{\partial \xi^2} \right\}^{\mathrm{T}} \\
&2.\ \mathbf{r}^3 = \frac{\mathbf{r}^3}{\|\mathbf{r}^3\|} \\
&3.\ \text{Let } \mathbf{r}^1 = \left\{ \frac{\partial x^1}{\partial \xi^1} \quad \frac{\partial x^2}{\partial \xi^1} \quad \frac{\partial x^3}{\partial \xi^1} \right\}^{\mathrm{T}} \\
&4.\ \mathbf{r}^1 = \frac{\mathbf{r}^1}{\|\mathbf{r}^1\|} \\
&5.\ \mathbf{r}^2 = \mathbf{r}^3 \times \mathbf{r}^1
\end{aligned} \tag{2.28}$$

For the general case of anisotropic elasto-plastic behaviors, axes $\mathbf{r}^1$ and $\mathbf{r}^2$ can be initially taken coincident with the planar anisotropic axes (rolling and transverse direction, respectively), with $\mathbf{r}^3$ corresponding to the normal direction.

The local frame for each Gauss point is subjected to the rigid-body part of the relative deformation gradient, between configurations (n) and $(n+1)$. In fact, applying a polar decomposition on the relative deformation gradient of equation (2.18), it follows that

$$ {}^{n+1}_{\ \ n}\mathbf{F} = {}^{n+1}_{\ \ n}\mathbf{R} \ \ {}^{n+1}_{\ \ n}\mathbf{U} \tag{2.29}$$

where $\left({}^{n+1}_{\ \ n}\mathbf{R}\right)$ is the orthogonal relative rotation tensor and $\left({}^{n+1}_{\ \ n}\mathbf{U}\right)$ corresponds to the relative right stretch tensor. The decomposition in (2.29) can be easily carried out with, for instance, the algorithm introduced by Franca (1989) (see Box 4.1, in Chapter 4).

Once knowing the local coordinate system at stage (n) and the relative rotation tensor between stages (n) and $(n+1)$, it is possible to perform the update

$$\left[{}^{n+1}\mathbf{r}^1 \quad {}^{n+1}\mathbf{r}^2 \quad {}^{n+1}\mathbf{r}^3 \right] = {}^{n+1}_{\ \ n}\mathbf{R} \ \left[{}^{n}\mathbf{r}^1 \quad {}^{n}\mathbf{r}^2 \quad {}^{n}\mathbf{r}^3 \right] \tag{2.30}$$

In this way, the local coordinate system for a given point is then only affected by the rigid body component of the total deformation, characterizing this frame as a "co-rotational" one, with material strain (and stress) tensors being rotated as if frozen into the deformed continuum (Qin and Chen, 1988; Peng and Crisfield, 1992; Jiang and Chernuka, 1994a,b; Moita and Crisfield, 1996; Belytschko *et al.*, 2000).

As stated before, the local system is used for the imposition of the plane-stress conditions over the stress field and, afterwards, for the constitutive update (Chapter 4). The stress field is kept related to the local coordinate system during deformation, making the stress update procedure, in the presence of large elasto-plastic deformations, a direct extension of linear small deformation cases, as recently explored by Arif Masud and co-workers (Masud *et al.*, 2000; Masud and Tham, 2000).

The strain field, previously formulated in the convective frame, must therefore be transformed onto the local reference system. This can be achieved with the components of the director cosines matrix

$$\mathbf{T}(\xi^1,\xi^2,\xi^3) = \begin{bmatrix} (\xi^1,\mathbf{r}^1) & (\xi^2,\mathbf{r}^1) & (\xi^3,\mathbf{r}^1) \\ (\xi^1,\mathbf{r}^2) & (\xi^2,\mathbf{r}^2) & (\xi^3,\mathbf{r}^2) \\ (\xi^1,\mathbf{r}^3) & (\xi^2,\mathbf{r}^3) & (\xi^3,\mathbf{r}^3) \end{bmatrix} = \begin{bmatrix} \dfrac{\partial\xi^1}{\partial\mathbf{r}^1} & \dfrac{\partial\xi^2}{\partial\mathbf{r}^1} & \dfrac{\partial\xi^3}{\partial\mathbf{r}^1} \\ \dfrac{\partial\xi^1}{\partial\mathbf{r}^2} & \dfrac{\partial\xi^2}{\partial\mathbf{r}^2} & \dfrac{\partial\xi^3}{\partial\mathbf{r}^2} \\ \dfrac{\partial\xi^1}{\partial\mathbf{r}^3} & \dfrac{\partial\xi^2}{\partial\mathbf{r}^3} & \dfrac{\partial\xi^3}{\partial\mathbf{r}^3} \end{bmatrix} \tag{2.31}$$

which can be easily evaluated with the alternative expression

$$\mathbf{T}(\xi^1,\xi^2,\xi^3) = \begin{bmatrix} \mathbf{r}^1 & \mathbf{r}^2 & \mathbf{r}^3 \end{bmatrix}^{\mathrm{T}} (\mathbf{J})^{-1} \tag{2.32}$$

for a given configuration. In this equation, $(\mathbf{J})$ corresponds to the conventional Jacobian matrix, relating the global position coordinates to the convective frame in the form

$$\mathbf{J} = \begin{bmatrix} \dfrac{\partial x^1}{\partial\xi^1} & \dfrac{\partial x^2}{\partial\xi^1} & \dfrac{\partial x^3}{\partial\xi^1} \\ \dfrac{\partial x^1}{\partial\xi^2} & \dfrac{\partial x^2}{\partial\xi^2} & \dfrac{\partial x^3}{\partial\xi^2} \\ \dfrac{\partial x^1}{\partial\xi^3} & \dfrac{\partial x^2}{\partial\xi^3} & \dfrac{\partial x^3}{\partial\xi^3} \end{bmatrix} \tag{2.33}$$

The components (T_{ij}) of matrix $\mathbf{T}$ in equation (2.32) can be arranged in the form of a transformation matrix (mapping the convective frame to the local coordinate system) as

$${}^{l}_{c}\mathbf{T} = \begin{bmatrix} T_{11}T_{11} & T_{12}T_{12} & T_{13}T_{13} & T_{11}T_{12} & T_{11}T_{13} & T_{12}T_{13} \\ T_{21}T_{21} & T_{22}T_{22} & T_{23}T_{23} & T_{21}T_{22} & T_{21}T_{23} & T_{22}T_{23} \\ 2T_{11}T_{21} & 2T_{12}T_{22} & 2T_{13}T_{23} & (T_{11}T_{22})+(T_{21}T_{12}) & (T_{11}T_{23})+(T_{21}T_{13}) & (T_{12}T_{23})+(T_{22}T_{13}) \\ 2T_{11}T_{31} & 2T_{12}T_{32} & 2T_{13}T_{33} & (T_{11}T_{32})+(T_{31}T_{12}) & (T_{11}T_{33})+(T_{31}T_{13}) & (T_{12}T_{33})+(T_{32}T_{13}) \\ 2T_{21}T_{31} & 2T_{22}T_{32} & 2T_{23}T_{33} & (T_{21}T_{32})+(T_{31}T_{22}) & (T_{21}T_{33})+(T_{31}T_{23}) & (T_{22}T_{33})+(T_{32}T_{23}) \end{bmatrix} \tag{2.34}$$

where the (c) and (l) refer to the convective and local frames, respectively. The strain tensor components in the local frame can be finally obtained, from the convective strain tensor (2.19), simply by the relation

$${}^{n+1}_{\ \ n}\bar{\mathbf{E}}^u = {}^{n+1}_{\ \ n}\bar{\mathbf{E}}^u\left(\mathbf{r}^1,\mathbf{r}^2,\mathbf{r}^3\right) = {}^{l}_{c}\mathbf{T}\,{}^{n+1}_{\ \ n}\mathbf{E}^u \tag{2.35}$$

which obviously also applies to the linear strain-displacement matrices. The nonlinear (geometric or initial stress) strain-displacement matrix, on the other hand, can be directly referred to the updated local frame in the form (Bathe, 1996)

$$\left.\bar{\mathbf{M}}^u\right|_{nl} = \underbrace{\begin{bmatrix}
N_{\mathbf{r}^1} & 0 & 0 & \frac{a}{2}v^{11}\left(\xi^3 N_{\mathbf{r}^1} + \frac{\partial\xi^3}{\partial\mathbf{r}^1}N\right) & -\frac{a}{2}v^{21}\left(\xi^3 N_{\mathbf{r}^1} + \frac{\partial\xi^3}{\partial\mathbf{r}^1}N\right) \\
N_{\mathbf{r}^2} & 0 & 0 & \frac{a}{2}v^{11}\left(\xi^3 N_{\mathbf{r}^2} + \frac{\partial\xi^3}{\partial\mathbf{r}^2}N\right) & -\frac{a}{2}v^{21}\left(\xi^3 N_{\mathbf{r}^2} + \frac{\partial\xi^3}{\partial\mathbf{r}^2}N\right) \\
N_{\mathbf{r}^3} & 0 & 0 & \frac{a}{2}v^{11}\left(\xi^3 N_{\mathbf{r}^3} + \frac{\partial\xi^3}{\partial\mathbf{r}^3}N\right) & -\frac{a}{2}v^{21}\left(\xi^3 N_{\mathbf{r}^3} + \frac{\partial\xi^3}{\partial\mathbf{r}^3}N\right) \\
0 & N_{\mathbf{r}^1} & 0 & \frac{a}{2}v^{12}\left(\xi^3 N_{\mathbf{r}^1} + \frac{\partial\xi^3}{\partial\mathbf{r}^1}N\right) & -\frac{a}{2}v^{22}\left(\xi^3 N_{\mathbf{r}^1} + \frac{\partial\xi^3}{\partial\mathbf{r}^1}N\right) \\
0 & N_{\mathbf{r}^2} & 0 & \frac{a}{2}v^{12}\left(\xi^3 N_{\mathbf{r}^2} + \frac{\partial\xi^3}{\partial\mathbf{r}^2}N\right) & -\frac{a}{2}v^{22}\left(\xi^3 N_{\mathbf{r}^2} + \frac{\partial\xi^3}{\partial\mathbf{r}^2}N\right) \\
0 & N_{\mathbf{r}^3} & 0 & \frac{a}{2}v^{12}\left(\xi^3 N_{\mathbf{r}^3} + \frac{\partial\xi^3}{\partial\mathbf{r}^3}N\right) & -\frac{a}{2}v^{22}\left(\xi^3 N_{\mathbf{r}^3} + \frac{\partial\xi^3}{\partial\mathbf{r}^3}N\right) \\
0 & 0 & N_{\mathbf{r}^1} & \frac{a}{2}v^{13}\left(\xi^3 N_{\mathbf{r}^1} + \frac{\partial\xi^3}{\partial\mathbf{r}^1}N\right) & -\frac{a}{2}v^{23}\left(\xi^3 N_{\mathbf{r}^1} + \frac{\partial\xi^3}{\partial\mathbf{r}^1}N\right) \\
0 & 0 & N_{\mathbf{r}^2} & \frac{a}{2}v^{13}\left(\xi^3 N_{\mathbf{r}^2} + \frac{\partial\xi^3}{\partial\mathbf{r}^2}N\right) & -\frac{a}{2}v^{23}\left(\xi^3 N_{\mathbf{r}^2} + \frac{\partial\xi^3}{\partial\mathbf{r}^2}N\right) \\
0 & 0 & N_{\mathbf{r}^3} & \frac{a}{2}v^{13}\left(\xi^3 N_{\mathbf{r}^3} + \frac{\partial\xi^3}{\partial\mathbf{r}^3}N\right) & -\frac{a}{2}v^{23}\left(\xi^3 N_{\mathbf{r}^3} + \frac{\partial\xi^3}{\partial\mathbf{r}^3}N\right)
\end{bmatrix}}_{\text{for node } k} \tag{2.36}$$

where the subscript (nl) refers to its non-linear character and

$$N_{\mathbf{r}^j} = \frac{\partial N}{\partial \xi^i}\frac{\partial \xi^i}{\partial \mathbf{r}^j}, \text{ summation on } i \tag{2.37}$$

The basic block presented in equation (2.36) is repeated for each node (k) of an element, leading to a matrix $\left.\bar{\mathbf{M}}^u\right|_{nl}$, for the present shell elements, with a total of (9×20) components.

After detailing the strain field coming from an entirely displacement based formulation, it is time to define the enhanced strain field that will be simply *added* to the *linear* strain tensor in (2.19), in order to eliminate transverse shear locking and, simultaneously, improve the in-plane behavior of the original degenerated shell element. To this end, a lengthy verification of the subspace of null transverse shear strains will be carried out, as detailed in the following.

2.3 Bases for the subspace of null transverse shear strains

2.3.1 Overview

In the analysis of shear locking phenomena, attention is focused on the transverse components of the strain field, defined in the natural (convective) set of coordinates $\boldsymbol{\xi} = (\xi^1, \xi^2, \xi^3)$ – equation (2.1). Related to this system, the displacement dependent strain field components, for a given point within an element, can be represented in vector form as

$$\mathbf{E}^u \equiv \{E^u_{\xi^1\xi^1} \;\; E^u_{\xi^2\xi^2} \;\; E^u_{\xi^1\xi^2} \;\; E^u_{\xi^1\xi^3} \;\; E^u_{\xi^2\xi^3}\}^{\mathrm{T}} \tag{2.38}$$

with each strain component being defined by equations (2.21)–(2.26) and the plane-stress condition in the convective frame $\left(E^u_{\xi^3\xi^3}=0\right)$ being implicitly accounted for. Recalling equation (2.27), it is possible to relate the strain field to the nodal displacement variables, at the element level, in the form

$$\mathbf{E}^u = \mathbf{M}^u\left(\boldsymbol{\xi}\right)\left\{\begin{array}{c}\mathbf{d}_1\\ \cdots\\ \mathbf{d}_k\end{array}\right\} = \mathbf{M}^u\left(\boldsymbol{\xi}\right)\,\mathbf{d}_e$$

via the differential operator $(\mathbf{M}^u)$, grouping together contributions from each of the k nodal points.

The importance in starting with the convective strain field is related to the imposition of the Kirchhoff constraints for thin-shells, requiring that the transverse (out-of-plane) convective strain components must vanish as thickness values tends to zero. When applying the Mindlin-type formulations (characteristic of degenerated elements) this requirement cannot be simultaneously fulfilled in each point over a specified domain. However, dealing with an *energetic* approach, it is possible to formulate an analogous condition in the form (Huang, 1989)

$$\int_{\square} E^u_{\xi^1\xi^3}\,\mathrm{d}\xi^1\,\mathrm{d}\xi^2 = 0 \tag{2.39a}$$

$$\int_{\square} E^u_{\xi^2\xi^3}\,\mathrm{d}\xi^1\,\mathrm{d}\xi^2 = 0 \tag{2.39b}$$

at the elemental level and area $\left(\square \equiv \mathrm{d}\xi^1 \times \mathrm{d}\xi^2\right)$. The assumption that the shear strain field $\left(E^u_{\xi^1\xi^3}\right)$ is a linear function of $\left(\xi^1\right)$ and, in a similar manner, $\left(E^u_{\xi^2\xi^3}\right)$ is a linear function of $\left(\xi^2\right)$ – linear strain field – leads to the equations in the isoparametric space

$$\int_{-1}^{0} E^u_{\xi^1\xi^3}\,\mathrm{d}\xi^1 = 0 \tag{2.40a}$$

$$\int_{0}^{+1} E^u_{\xi^1\xi^3}\,\mathrm{d}\xi^1 = 0 \tag{2.40b}$$

$$\int_{-1}^{0} E^u_{\xi^2\xi^3}\,\mathrm{d}\xi^2 = 0 \tag{2.40c}$$

$$\int_{0}^{+1} E^u_{\xi^2\xi^3}\,\mathrm{d}\xi^2 = 0 \tag{2.40d}$$

Discrete imposition of these constraints directly over the Gauss points then leads to

$$\left\{\begin{array}{c}E^u_{\xi^1\xi^3}\\ E^u_{\xi^2\xi^3}\end{array}\right\} = \mathbf{M}^u_s\left(\boldsymbol{\xi}\right)\,\mathbf{d}_e = \mathbf{0} \tag{2.41}$$

where $(\mathbf{M}_s^u)$ is a sub-matrix of the total operator $(\mathbf{M}^u)$ – equation (2.27) – that is, corresponding to the last 2 lines of the latter.

A general displacement field obeying the constraint (2.41) can be then related to an algebraic subspace in the form

$$\mathcal{I}_h^s = \{\mathbf{d}_h \in \mathcal{U}_h : \mathbf{M}_s^u(\boldsymbol{\xi})\,\mathbf{d}_e = \mathbf{0}\} \tag{2.42}$$

where $\mathcal{I}_h^s$ is the subspace of possible deformations associated with a null transverse shear strain field, with $\mathcal{U}_h$ corresponding to an approximation of the linear space of all admissible solutions $\mathcal{U}$ (and coming from the finite element approximation $\mathbf{d}_h$ for the displacement field).

Benefiting from previous works in the field (César de Sá and Owen, 1986; César de Sá and Natal Jorge, 1999), it is possible to infer that, in order to avoid the onset of transverse shear locking, the discrete finite element solution $(\mathbf{u}_h \equiv \mathbf{d}_e)$ *must lie on the null space of* $\mathbf{M}_s^u$, thus avoiding the trivial solution $(\mathbf{u}_h \equiv \mathbf{0})$ to be the unique one. In other words, any required displacement solution must be a linear combination of the elements of a given basis of $\mathcal{I}_h^s$. If this is not the case, shear locking is therefore verified for the required displacement field.

Distinct finite element formulations, for a given mesh, will lead to distinct null transverse shear strain subspaces. In the next sections, analyses over the bilinear degenerated, mixed interpolated *MITC4* and bilinear selective reduced elements are performed, aiming to identify for each one of the elements their respective subspace $\mathcal{I}_h^s$ and, consequently, to clarify their ability (or not) to avoid locking behaviors.

2.3.2 Analysis of the *degenerated* formulation

Referring to equation (2.41), it is possible to enforce that, for a single element,

$$\left\{ \begin{array}{c} E^u_{\xi^1\xi^3} \\ E^u_{\xi^2\xi^3} \end{array} \right\} = \left\{ \begin{array}{c} \mathbf{M}^u_{\xi^1\xi^3} \\ \mathbf{M}^u_{\xi^2\xi^3} \end{array} \right\} \mathbf{d}_e = \mathbf{0} \tag{2.43}$$

where the former matrix $(\mathbf{M}_s^u)$ was further decomposed into the two sub-matrices $\left(\mathbf{M}^u_{\xi^1\xi^3}\right)$ and $\left(\mathbf{M}^u_{\xi^2\xi^3}\right)$.

In the following analysis, a square element placed in the OXY plane is considered. The normal to the surface of the element is taken coincident with the OZ axis, which is also responsible for thickness orientation. The element represents then a reference square in the two-dimensional natural coordinate space $\mathcal{D} \subset \mathbb{R}^2$, with representative dimensions

$$\mathcal{D} = [-1,+1] \times [-1,+1] = \left\{(\xi,\eta) \in \mathbb{R}^2; -1 \leq \xi,\eta \leq +1\right\} \tag{2.44}$$

Within this configuration, the in-plane components $\left(u^1\,,\,u^2\right)$ of the displacement nodal vector – equation (2.20) – do not interfere with the transverse shear strain field. It is obvious then that any deformation state in which only the in-plane degrees-of-freedom are active will inevitably belong to the $\mathcal{I}_h^s$ subspace, related only to the out-of-plane shear strain energy.

Therefore, and for the sake of simplicity, these degrees-of-freedom will be "removed" from the generalized nodal displacement vector ($\mathbf{d_e}$), leading to the "reduced" nodal degrees-of-freedom vector

$$\mathbf{d}_r = \left\{ \begin{array}{ccccccc} u^3_{k=1} & \theta^1_{k=1} & \theta^2_{k=1} & \ldots & u^3_{k=4} & \theta^1_{k=4} & \theta^2_{k=4} \end{array} \right\}^{\mathrm{T}} \tag{2.45}$$

specific to the bilinear element ($nnode = 4$) and associated with the condition

$$\left\{ \begin{array}{c} E^u_{\xi^1\xi^3} \\ E^u_{\xi^2\xi^3} \end{array} \right\} = \left\{ \begin{array}{c} \mathbf{M}^u_{\xi^1\xi^3} \\ \mathbf{M}^u_{\xi^2\xi^3} \end{array} \right\} \mathbf{d}_r = \mathbf{0} \tag{2.46}$$

in replacement of equation (2.43). The main goal in the following will be the search for reduced degrees-of-freedom vectors ($\mathbf{d}_r$) respecting condition (2.46) for a given finite element formulation.

The next step refers then to the extension of the latter equality over all the sample points used in the numerical integration. For the four-node bilinear shell element, with a complete 2×2 Gauss integration, 8 restrictions coming from (2.46) can be accounted for as

$$\left\{ \begin{array}{c} E^u_{\xi^1\xi^3}\left(\xi^1_I, \xi^2_I\right) \\ E^u_{\xi^1\xi^3}\left(\xi^1_{II}, \xi^2_{II}\right) \\ E^u_{\xi^1\xi^3}\left(\xi^1_{III}, \xi^2_{III}\right) \\ E^u_{\xi^1\xi^3}\left(\xi^1_{IV}, \xi^2_{IV}\right) \end{array} \right\} = \underbrace{\left[\begin{array}{c} \mathbf{M}^u_{\xi^1\xi^3}\left(\xi^1_I, \xi^2_I\right)^T \\ \mathbf{M}^u_{\xi^1\xi^3}\left(\xi^1_{II}, \xi^2_{II}\right)^T \\ \mathbf{M}^u_{\xi^1\xi^3}\left(\xi^1_{III}, \xi^2_{III}\right)^T \\ \mathbf{M}^u_{\xi^1\xi^3}\left(\xi^1_{IV}, \xi^2_{IV}\right)^T \end{array} \right]}_{4\times12} \mathbf{d}_r = \mathbf{0} \tag{2.47}$$

and

$$\left\{ \begin{array}{c} E^u_{\xi^2\xi^3}\left(\xi^1_I, \xi^2_I\right) \\ E^u_{\xi^2\xi^3}\left(\xi^1_{II}, \xi^2_{II}\right) \\ E^u_{\xi^2\xi^3}\left(\xi^1_{III}, \xi^2_{III}\right) \\ E^u_{\xi^2\xi^3}\left(\xi^1_{IV}, \xi^2_{IV}\right) \end{array} \right\} = \underbrace{\left[\begin{array}{c} \mathbf{M}^u_{\xi^2\xi^3}\left(\xi^1_I, \xi^2_I\right)^T \\ \mathbf{M}^u_{\xi^2\xi^3}\left(\xi^1_{II}, \xi^2_{II}\right)^T \\ \mathbf{M}^u_{\xi^2\xi^3}\left(\xi^1_{III}, \xi^2_{III}\right)^T \\ \mathbf{M}^u_{\xi^2\xi^3}\left(\xi^1_{IV}, \xi^2_{IV}\right)^T \end{array} \right]}_{4\times12} \mathbf{d}_r = \mathbf{0} \tag{2.48}$$

where each pair $\left(\xi^1_K, \xi^2_K\right)$ represents the natural coordinates of a specific integration point (for $K = I, \ldots, IV$). Doing so, $\mathbf{M}^u_{\xi^1\xi^3}\left(\xi^1_K, \xi^2_K\right)$ and $\mathbf{M}^u_{\xi^2\xi^3}\left(\xi^1_K, \xi^2_K\right)$ represent vectors (12 components each), referring to the very same integration point.

It is worth noting that $(\mathbf{M}_s^u)$ evaluation does not depend on the numerical integration over the thickness direction and, therefore, the $\left(\xi^3\right)$ orientation needs not to be included in the present analysis. This is quite useful in elastoplastic analyses with shell elements, where higher order numerical integration along thickness direction is often invoked in order to catch strong stress and strain gradients.

After these considerations, the analysis of the *degenerated* four-node (bilinear) shell element, characterized by a (linear) transverse shear strain field derivable from equations (2.25) and (2.26), provides a matrix $(\mathbf{M}_s^u)$ with the following characteristics:

$$\operatorname{rank}\left[\mathbf{M}_s^u\left(\boldsymbol{\xi}\right)\right] = 8 \quad \therefore \quad \operatorname{nullity}\left[\mathbf{M}_s^u\left(\boldsymbol{\xi}\right)\right] = 4 \tag{2.49}$$

As a direct consequence, the element can reproduce four fundamental (linearly independent) displacement patterns. For a case where a given displacement cannot be obtained as a linear combination of these four terms, transverse shear locking onset is verified. The displacement configurations forming a possible (admissible) basis of the null transverse shear strain subspace for the *degenerated* element $(\mathcal{I}_h^s\mid_d)$ can be schematically represented in Fig. 2.1.

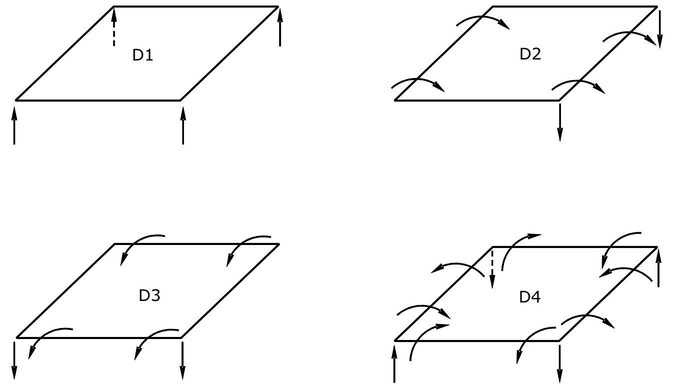

Figure 2.1: Basis elements for the null transverse shear strain subspace for *degenerated elements* (one-element mesh).

The arrows in the figure refer to *active* degrees-of-freedom. In detail, the displacement vector for the whole element (and following the representation in equation (2.45)) can be represented as follows

$$\begin{aligned}
&\mathsf{D1} \Rightarrow \mathbf{d}_r = \{1,0,0,1,0,0,1,0,0,1,0,0\}^{\mathrm{T}} \\
&\mathsf{D2} \Rightarrow \mathbf{d}_r = \{0,1,0,-1,1,0,-1,1,0,0,1,0\}^{\mathrm{T}} \\
&\mathsf{D3} \Rightarrow \mathbf{d}_r = \{-1,0,1,-1,0,1,0,0,1,0,0,1\}^{\mathrm{T}} \\
&\mathsf{D4} \Rightarrow \mathbf{d}_r = \{1,2,-2,-1,2,2,1,-2,2,-1,-2,-2\}^{\mathrm{T}}
\end{aligned} \tag{2.50}$$

An element based on this formulation is able, then, to reproduce these displacement patterns as well as any linear combinations between them.

2.3.3 Analysis of the *mixed interpolation* approach

The previous analysis is now applied to the four-node bilinear element following the *mixed interpolation* approach of Dvorkin and Bathe (1984). The concept behind the formulation is well-established in the finite element literature (Bathe and Dvorkin, 1985, 1986; Bathe, 1996; Bucalem and Bathe, 1997; Chapelle and Bathe, 1998; Bathe *et al.*, 2000; Chapelle and Bathe, 2000, 2003) being only summarized in the following. The procedure has roots in the earlier works of MacNeal (1982) and Hughes and Tezduyar (1981), being also sometimes classified as an *assumed natural strain* method, a term coined after the works of K. C. Park and co-workers (Park, 1986; Park and Stanley, 1986; Stanley *et al.*, 1986).

The *mixed interpolation of tensorial components* approach (*MITC*, for short) is a kind of *assumed strain method* in the sense that the original, displacement-based, transverse shear strain field of a given element is re-interpolated based on new sampling points, distinct from the Gaussian ones, and designed to satisfy the thin-plate/thin-shell conditions discussed in Section 2.3.1. In a general form, the interpolated transverse shear strain field is represented by the modified components

$$\begin{aligned}
E^{\mathrm{MITC}}_{\xi^1\xi^3}(\boldsymbol{\xi}) &= \sum_{p=1}^{2} N_p\left(\xi^1,\xi^2\right)\; E^{u}_{\xi^1\xi^3}\left(\xi^1_p,\xi^2_p,0\right) \\
E^{\mathrm{MITC}}_{\xi^2\xi^3}(\boldsymbol{\xi}) &= \sum_{q=1}^{2} N_q\left(\xi^1,\xi^2\right)\; E^{u}_{\xi^2\xi^3}\left(\xi^1_q,\xi^2_q,0\right)
\end{aligned} \tag{2.51}$$

In the latter, (p) and (q) indices represent the additional (*tying*, in the original work) integration points with natural coordinates $\left(\xi^1_p,\xi^2_p\right)$ and $\left(\xi^1_q,\xi^2_q\right)$, respectively, located on the reference surface $\left(\xi^3=0\right)$ and associated with the additional shape functions (N_p) and (N_q) (Bathe, 1996).

Analysis of equations (2.47) and (2.48) for this formulation, specifically for the case of the 4-node (bilinear) shell element (*MITC4* in Dvorkin and Bathe (1984)), reveals a matrix ($\mathbf{M}_s^m$) with the following properties:

$$\operatorname{rank}\left[\mathbf{M}_s^m\left(\boldsymbol{\xi}\right)\right] = 4 \quad \therefore \quad \operatorname{nullity}\left[\mathbf{M}_s^m\left(\boldsymbol{\xi}\right)\right] = 8 \tag{2.52}$$

The null transverse shear strain subspace ($\mathcal{I}_h^s \mid_m$) for the *mixed interpolated MITC4* element should, then, be represented by a basis including 8 linearly independent terms, being a possible candidate the one represented in Fig. 2.2.

Each element in the figure can be expressed by a set of reduced degrees-of-freedom vectors

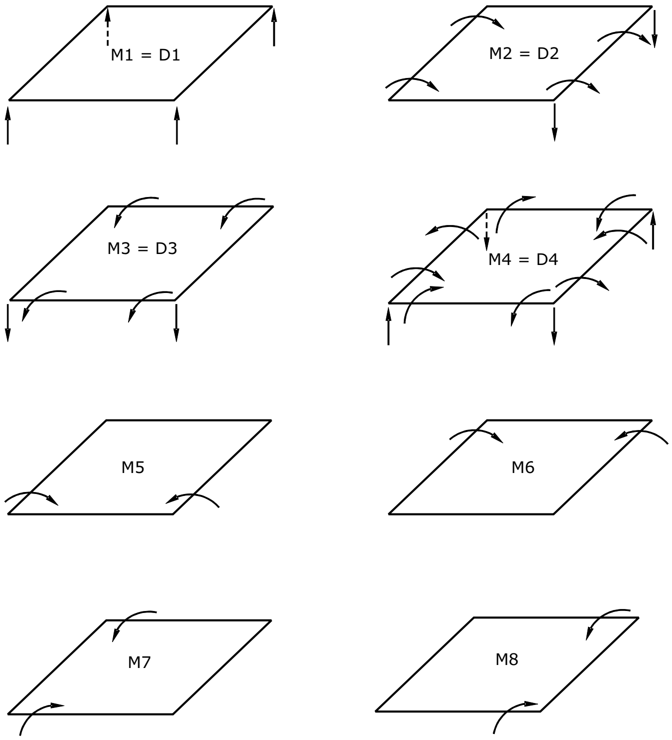

Figure 2.2: Basis elements for the null transverse shear strain subspace for the *mixed interpolated MITC4* shell element (one-element mesh).

in the form

$$\begin{aligned}
&\mathsf{M1} \Rightarrow \mathbf{d}_r = \{1,0,0,1,0,0,1,0,0,1,0,0\}^{\mathrm{T}}\\
&\mathsf{M2} \Rightarrow \mathbf{d}_r = \{0,1,0,-1,1,0,-1,1,0,0,1,0\}^{\mathrm{T}}\\
&\mathsf{M3} \Rightarrow \mathbf{d}_r = \{-1,0,1,-1,0,1,0,0,1,0,0,1\}^{\mathrm{T}}\\
&\mathsf{M4} \Rightarrow \mathbf{d}_r = \{1,2,-2,-1,2,2,1,-2,2,-1,-2,-2\}^{\mathrm{T}}\\
&\mathsf{M5} \Rightarrow \mathbf{d}_r = \{0,1,0,0,-1,0,0,0,0,0,0,0\}^{\mathrm{T}}\\
&\mathsf{M6} \Rightarrow \mathbf{d}_r = \{0,0,0,0,0,0,0,-1,0,0,1,0\}^{\mathrm{T}}\\
&\mathsf{M7} \Rightarrow \mathbf{d}_r = \{0,0,-1,0,0,0,0,0,0,0,0,1\}^{\mathrm{T}}\\
&\mathsf{M8} \Rightarrow \mathbf{d}_r = \{0,0,0,0,0,-1,0,0,1,0,0,0\}^{\mathrm{T}}
\end{aligned} \tag{2.53}$$

It can be noted that the first four terms of the *MITC4* shell element basis ($\mathsf{M1} \Rightarrow \mathsf{M4}$) are exactly those reproduced by the *degenerated* element subspace. The remaining four terms ($\mathsf{M5} \Rightarrow \mathsf{M8}$) do not belong to the latter null transverse shear strain subspace. Thus, any imposed displacement field, as long as being a linear combination of the ($\mathsf{M5} \Rightarrow \mathsf{M8}$) terms, will inevitably force the degenerated formulation to lock.

2.3.4 Analysis of the *selective reduced* technique

Starting with the degenerated element formulation, an additional analysis is performed over the *selective reduced integration* (*SRI*) procedure (Hughes *et al.*, 1978; Zienkiewicz *et al.*, 1979). For this purpose, a reduced Gaussian integration (one-point quadrature order) is adopted for the calculation of just the transverse shear strain terms.

The analysis of this formulation from the standpoint of equations (2.47) and (2.48), leads to a matrix ($\mathbf{M}_s^r$) characterized by

$$\operatorname{rank}\left[\mathbf{M}_s^r\left(\boldsymbol{\xi}\right)\right] = 2 \quad \therefore \quad \operatorname{nullity}\left[\mathbf{M}_s^r\left(\boldsymbol{\xi}\right)\right] = 10 \tag{2.54}$$

A possible basis, defining the null transverse shear strain subspace ($\mathcal{I}_h^s\,|_r$) for the *SRI* bilinear shell element, is reproduced in Fig. 2.3. For these possible patterns, the reduced degrees-of-freedom vectors are given by

$$\begin{aligned}
\mathsf{S1} &\Rightarrow \mathbf{d}_r = \{1,0,0,0,0,0,1,0,0,0,0,0\}^{\mathrm{T}} \\
\mathsf{S2} &\Rightarrow \mathbf{d}_r = \{0,0,0,1,0,0,0,0,0,1,0,0\}^{\mathrm{T}} \\
\mathsf{S3} &\Rightarrow \mathbf{d}_r = \{-1,0,1,-1,0,1,0,0,1,0,0,1\}^{\mathrm{T}} \\
\mathsf{S4} &\Rightarrow \mathbf{d}_r = \{0,1,0,-1,1,0,-1,1,0,0,1,0\}^{\mathrm{T}} \\
\mathsf{S5} &\Rightarrow \mathbf{d}_r = \{0,1,0,0,-1,0,0,0,0,0,0,0\}^{\mathrm{T}} \\
\mathsf{S6} &\Rightarrow \mathbf{d}_r = \{0,0,0,0,0,0,0,-1,0,0,1,0\}^{\mathrm{T}} \\
\mathsf{S7} &\Rightarrow \mathbf{d}_r = \{0,0,-1,0,0,0,0,0,0,0,0,1\}^{\mathrm{T}} \\
\mathsf{S8} &\Rightarrow \mathbf{d}_r = \{0,0,0,0,0,-1,0,0,1,0,0,0\}^{\mathrm{T}} \\
\mathsf{S9} &\Rightarrow \mathbf{d}_r = \{0,1,0,0,1,0,0,-1,0,0,-1,0\}^{\mathrm{T}} \\
\mathsf{S10} &\Rightarrow \mathbf{d}_r = \{0,0,-1,0,0,1,0,0,1,0,0,-1\}^{\mathrm{T}}
\end{aligned} \tag{2.55}$$

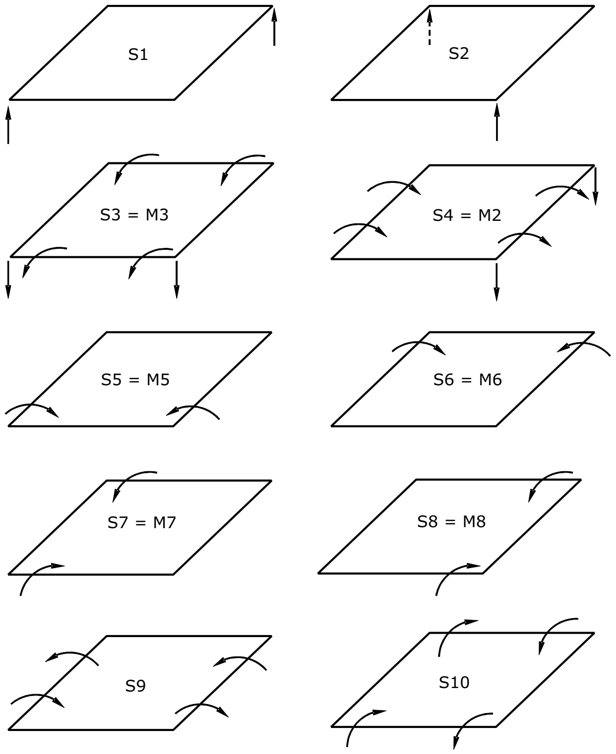

Figure 2.3: Basis elements for the null transverse shear strain subspace for the *selectively reduced* shell element (one-element mesh).

The subspace basis obtained with this formulation is composed of 10 terms. As can be seen in the figure, terms $(\mathsf{S3}) \rightarrow (\mathsf{S8})$ are included in the subspace basis of the *MITC4* shell element. Additionally, terms $(\mathsf{M1})$ and $(\mathsf{M4})$ of this last element can be obtained as a linear combination of the $(\mathsf{S}i)$ terms above in the form

$$\mathsf{M1} = \mathsf{S1} + \mathsf{S2} \tag{2.56}$$

and

$$\mathsf{M4} = \alpha_1\, \mathsf{S1} + \alpha_2\, \mathsf{S2} + \alpha_3\, \mathsf{S9} + \alpha_4\, \mathsf{S10} \quad \left(\alpha_1, \alpha_2, \alpha_3, \alpha_4, \alpha_1 \in \mathbb{R}^3\right) \tag{2.57}$$

From all the previous analysis, it can be verified that the subspace for the *SRI* formulation encompasses the previous ones (*degenerated* and *mixed interpolated*), once the statement

$$\mathcal{I}_h^s|_r \supset \quad \mathcal{I}_h^s|_m \supset \quad \mathcal{I}_h^s|_d \tag{2.58}$$

is verified.

In addition, from Fig. 2.3, it is interesting to note that some deformation patterns pertaining to the *selectively reduced* integration element are not included amongst the *MITC4* and *degenerated* element bases, and cannot be spanned by either of them. In case of imposing these displacement patterns, the mixed interpolation element will verify the occurrence of transverse shear locking phenomenon, performing *in the very same manner* as the degenerated element. Based on this conclusion, two sample example problems are proposed. Data values values adopted in the examples are merely indicative and, therefore, only a qualitative solution is sought, with no real physical meaning intended.

Example 1 Consider a single bilinear square element with sides measuring two units $(\mathsf{L} = 2)$, so that no distinction needs to be made between physical and isoparametric coordinates. The element possesses a thickness value of $(\mathsf{a} = 0.0002)$ and linear material properties given by a Young's modulus $\left(\mathsf{E} = 2.11 \times 10^{11}\right)$ and a Poisson coefficient $(\nu = 0.3)$. The element is restrained in such a way that only one type of rotations per node (rotation type $\left(\theta_k^1\right)$, following equation (2.45)) is allowed as shown in Fig. 2.4(a). In the figure the specific rotations activated amongst the total degrees of freedom are indicated. The arrows also correspond to applied unity moments.

Comparing the last figure with the patterns represented in Fig. 2.1, 2.2 and 2.3, it is possible to retain some conclusions. First of all the *degenerated* formulation can not, by itself, reproduce the imposed deformation from any linear combination of the basis terms showed in Fig. 2.1. In using the *mixed* and *selective reduced* interpolations, this problem is not likely to happen, with the deformation pattern in Fig 2.4(a) being easily obtained from the following linear combinations

$$\text{example 1} \Longrightarrow \left\{ \begin{array}{c} \mathsf{M5} + \mathsf{M6} \\ \mathsf{S5} + \mathsf{S6} \end{array} \right\}. \tag{2.59}$$

of the terms already presented in equations (2.53) and (2.55).

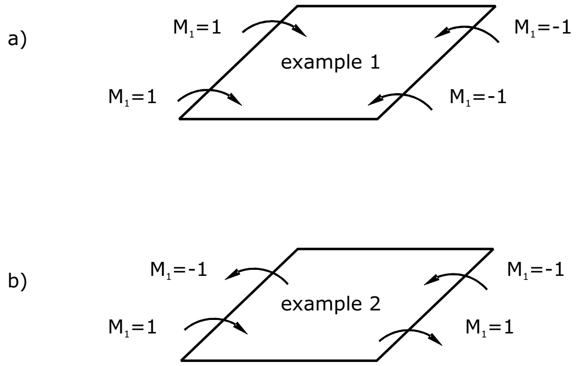

Figure 2.4: Allowed degrees-of-freedom for: a) Example 1 and b) Example 2. Arrows also indicate directions of the applied unity moments.

Following this idea, both *MITC4* and *SRI* shell elements might be supposed to reproduce the displacement field imposed, while the degenerated element would be expected to lock. In fact, for the application of unit moments along the rotational degrees of freedom (as depicted in the Fig. 2.4(a)), the numerically obtained rotations values are as following

$$\begin{aligned} &\textit{degenerated} \text{ formulation} \Longrightarrow \left|\theta_k^1\right| = 2.21801 \times 10^{-7} \\ &\textit{mixed interpolation} \text{ formulation} \Longrightarrow \left|\theta_k^1\right| = 6.46919 \\ &\textit{selective reduced} \text{ formulation} \Longrightarrow \left|\theta_k^1\right| = 6.46919 \end{aligned} \tag{2.60}$$

Qualitatively, the discrepancy is patent between the rotation values obtained for the *degenerated* and *MITC4/SRI* formulations. Elements based on the latters present the same rotational response to the imposed load and boundary conditions, as expected from the null transverse shear strain subspace analysis. On the meanwhile, the element based on the *degenerated* approach virtually gives no value for the rotation variable, which is in accordance to the points discussed so far.

Example 2 The same geometry, material and boundary conditions from the previous example are now applied in this test case. The only difference is the *orientation* of the applied unity-value moments, as represented in Fig. 2.4(b), enforcing a distinct rotation field.

From what is being discussed so far, the imposed analysed configuration would only be obtained from the *SRI* formulation (in fact, the resultant rotational field corresponds to the specific term S9, in Fig. 2.3). Once neither the *degenerated* nor the *mixed interpolated* elements can reproduce the present field, it is supposed that both elements would ultimately reveal a tendency to lock. In fact, this actually happens, as can be verified with the numerical results in the following

$$\begin{aligned}
&\textit{degenerated} \text{ formulation} \Longrightarrow \left|\theta_k^1\right| = 2.21801 \times 10^{-7}\\
&\textit{mixed interpolation} \text{ formulation} \Longrightarrow \left|\theta_k^1\right| = 2.21801 \times 10^{-7}\\
&\textit{selective reduced} \text{ formulation} \Longrightarrow \left|\theta_k^1\right| = 18.48340
\end{aligned} \tag{2.61}$$

The obtained values reveal a poor behaviour of the *mixed interpolation* approach, contrasting with the previous example, with both *MITC4* and the *degenerated* element leading to the very same numerical results. About the element based on the *SRI* formulation, as its null shear strain subspace accounts for the rotation pattern in Fig. 2.4(b), no transverse shear locking effects are verified.

2.4 Treatment of the transverse shear locking using the *EAS* method

Following previous works in 2D analysis (César de Sá and Natal Jorge, 1999; César de Sá *et al.*, 2001), the *enhanced assumed strain* (*EAS*) approach is employed in the following in order to increase the performance of the original *degenerated* formulation. Theoretical details about the method can be found in the pioneering works by J. C. Simo and co-workers (Simo and Rifai, 1990; Simo and Armero, 1992; Simo *et al.*, 1993).

From the analysis of these references (and also from posterior works in the field), it can be inferred that the specific problem of the transverse shear locking in thin-shell finite elements was never before successfully treated with the *EAS* method. This is quite interesting, once the method is known to prove effectively in dealing with other pathologies of displacement-based elements, such as locking in low-order 2D elements (Simo and Rifai, 1990; Simo and Armero, 1992), volumetric constraints in 3D elements (Simo *et al.*, 1993) and membrane locking in shell elements (Andelfinger and Ramm, 1993), just to name the initial works in the literature. Therefore, the study carried out in the present work, in the opinion of the author, would represent a step further into the knowledge of the transverse shear locking pathology in thin-shell finite element analysis.

The starting point in the present work was the choice of a suitable enhanced strain function to be added to the displacement-based strain field, in the form

$$\mathbf{E} = \mathbf{E}^u + \mathbf{E}^\alpha = \mathbf{M}^u(\boldsymbol{\xi}) \left\{ \begin{array}{c} \mathbf{d}_1 \\ \cdots \\ \mathbf{d}_k \end{array} \right\} + \mathbf{M}^\alpha(\boldsymbol{\xi}) \left\{ \begin{array}{c} \alpha_1 \\ \cdots \\ \alpha_l \end{array} \right\} \tag{2.62}$$

involving a number of (l) internal variables, defined at the element level and afterwards condensed out of the system of equations.

The approach in equation (2.62) is representative of the *linear* methodology initially introduced by Simo and Rifai (1990). Afterwards, for nonlinear geometric applications, those authors introduced a new methodology involving the additive enhancement of the displacement field gradient (or, in other words, the multiplicative enhancement of the deformation gradient) (Simo and Armero, 1992; Simo *et al.*, 1993). In the present work, however, the additive enhancement of the displacement-based strain field is kept and extended to nonlinear kinematics. This procedure has the advantage of introducing a more straightforward implementation and lower computational costs, at the same time with no loss in the quality of the final solution (Andelfinger and Ramm, 1993; Bischoff and Ramm, 1997; Klinkel and Wagner, 1997; Klinkel *et al.*, 1999; Vu-Quoc and Tan, 2003).

The main aspect of the formulation, at this point, relies entirely on the choice of the enhanced strain-displacement differential operator $(\mathbf{M}^\alpha)$ in equation (2.62). Following previous works in 2D analysis (César de Sá and Natal Jorge, 1999; César de Sá *et al.*, 2001), the enhanced functions that will act over the displacement-based transverse shear strain components involve the introduction of the two-dimensional *bubble-function* in the form

$$N_\alpha^2\left(\xi^1, \xi^2\right) = \left(1 - \xi^1\xi^1\right)\left(1 - \xi^2\xi^2\right) \tag{2.63}$$

This specific choice of functions is grounded on improved results obtained for distorted meshes in incompressibility conditions (César de Sá and Natal Jorge, 1999), and also in bending-dominated situations for two-dimensional problems (César de Sá *et al.*, 2001).

In order to exemplify the adopted methodology, component (S9) of the null shear strain subspace for the *SRI* formulation (as described in equation (2.55) and in Example 2) is once again analysed. However, instead of moments, unity value rotations are applied over the activated degrees of freedom (Figure 2.5).

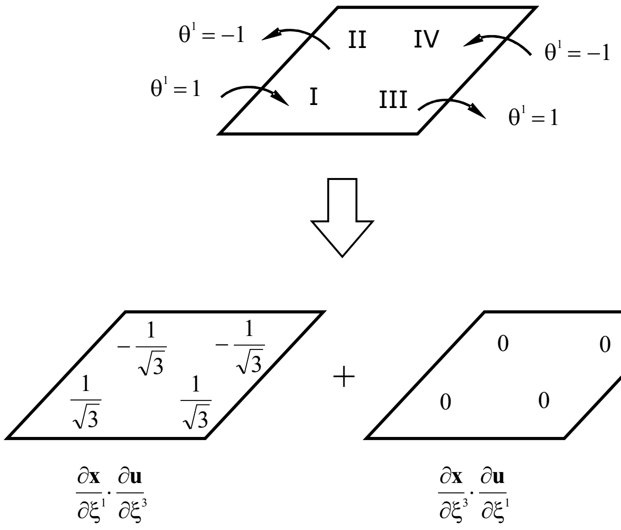

Figure 2.5: Shear strain $E^u_{\xi^1\xi^3}$ at Gauss points (I, II, III, IV) for the degenerated shell element

Focusing on the $\left(E^u_{\xi^1\xi^3}\right)$ transverse shear strain term, from equations (2.17)–(2.19) it can be stated that

$$2\,E^u_{\xi^1\xi^3} = \left(\frac{\partial \mathbf{x}}{\partial \xi^1} \cdot \frac{\partial \mathbf{u}}{\partial \xi^3}\right) + \left(\frac{\partial \mathbf{x}}{\partial \xi^3} \cdot \frac{\partial \mathbf{u}}{\partial \xi^1}\right) \tag{2.64}$$

taking only the linear part of the total strain and dropping the state indices. Adopting the same geometric and material configuration of Example 2, the displacement-based shear strain in equation (2.64) is obtained for each Gauss point for the *degenerated* element. From the subspace analysis described in the previous sections, it is clear that this element cannot reproduce the imposed displacement pattern.

The deformation values obtained can then be split over the contributions of each term in the right-hand side of equation (2.64), as schematically shown in Figure 2.5. As it can be seen, shear strain values are not null at Gauss points for this type of boundary-load configuration, as it would be desirable in order not to introduce shear locking effects into the formulation.

Aiming to force the *degenerated* element to obey the *Kirchhoff-Love* condition (equations (2.40a) and (2.40b)), an enhanced strain field (equation (2.62)) is then added to the Green-Lagrange displacement-based strain tensor, with the resulting total strain being defined, in the isoparametric space, as

$$E_{\xi^1\xi^3} = E^u_{\xi^1\xi^3} + E^\alpha_{\xi^1\xi^3} \tag{2.65}$$

Doing so, the total strain field component in equation (2.65) now aims to provide the missing term for expression (2.64), thus forcing the summation represented in Figure

2.5 to be zero. The same procedure can be extended to the analysis of the $\left(E_{\xi^2\xi^3}\right)$ strain component, including afterwards the (S10) term into the *degenerated* null transverse shear strain subspace $\left(\mathcal{I}_h^s\,|_d\right)$.

In the end, an optimized expression can be developed for the transverse *enhanced* shear strain field in the form

$$\left\{\begin{array}{c} E^{\alpha}_{\xi^1\xi^3} \\ E^{\alpha}_{\xi^2\xi^3} \end{array}\right\}_2 = \mathbf{M}^{\alpha}\left(\xi^1,\xi^2\right)\big|_2\,\boldsymbol{\alpha}|_2 = \left[\begin{array}{cc} \dfrac{\partial N_\alpha}{\partial \xi^2} & 0 \\ 0 & \dfrac{\partial N_\alpha}{\partial \xi^1} \end{array}\right]\left\{\begin{array}{c} \alpha_1 \\ \alpha_2 \end{array}\right\} \tag{2.66}$$

based on the $\left(\xi^1,\xi^2\right)$ partial derivatives of the bubble function (2.63) and introducing a two-component vector with internal (element-wise) variables $\left(\boldsymbol{\alpha}|_2\right)$.

The enhanced strain vector (2.66) can then be directly used in equation (2.62). The result is a strain field identical to the one coming from the *degenerated* formulation, but now including the so-far missing strain components (S9) and (S10), until now exclusive of the *selective reduced* approach.

2.4.1 The *S4E4* and *S4E4P7* shell elements

The four-node *degenerated* element, after the enhancement analysis performed in the previous section, presents an increased subspace dimension. However, an important part of deformation configurations is still missing when compared to *MITC4* and *SRI* formulations. These configurations refer to elements (S5), (S6), (S7) and (S8) of the subspace basis represented in Figure 2.3.

With the *enhanced assumed strain* method, and following the previous developments, it is possible to conceive a total shear strain field that simultaneously encompasses these four terms and also the two displacement patterns treated before. To accomplish this objective, a new enhanced shear strain field is proposed in the form

$$\left\{\begin{array}{c} E^{\alpha}_{\xi^1\xi^3} \\ E^{\alpha}_{\xi^2\xi^3} \end{array}\right\}_4 = \mathbf{M}^{\alpha}\left(\xi^1,\xi^2\right)\big|_4\,\boldsymbol{\alpha}|_4 = \left[\begin{array}{cccc} \dfrac{\partial N_\alpha}{\partial \xi^2} & 0 & \dfrac{\partial N_\alpha}{\partial \xi^1} & 0 \\ 0 & \dfrac{\partial N_\alpha}{\partial \xi^1} & 0 & \dfrac{\partial N_\alpha}{\partial \xi^2} \end{array}\right]\left\{\begin{array}{c} \alpha_1 \\ \alpha_2 \\ \alpha_3 \\ \alpha_4 \end{array}\right\} \tag{2.67}$$

As can be immediately noticed, the $\left(\mathbf{M}^{\alpha}\left(\xi^1,\xi^2\right)\big|_4\right)$ matrix comprises the matrix $\left(\mathbf{M}^{\alpha}\left(\xi^1,\xi^2\right)\big|_2\right)$ stated in equation (2.66). This four-variable enhancement, with the correspondent internal variables field $\left(\boldsymbol{\alpha}|_4\right)$, now allows for the reproduction of the 6 configurations previously missing – (S5), (S6), (S7) and (S8) – as well as the previously analysed (S9) and (S10) terms.

The explanation why this four-variable enhancement provides six additional displacement patterns for the basis of the null transverse shear strain subspace comes from the fact that the eight restrictions (equations (2.47) and (2.48)), imposing the null shear strain at the Gauss points, result now in only six linear independent equations. As the effective number of elemental degrees of freedom is 16 (12 from the reduced vector – equation (2.45) – plus 4 internal variables), the final number of displacement configurations turns out to be 10.

At this point, it is possible to introduce two new four-node bilinear shell elements, both of them based on the original degenerated formulation. The first element possesses an enhancement as presented in equation (2.67), acting only over the transverse shear strain field and involving 4 internal variables. In this sense, it is coined *S4E4*, due to the number of nodes and internal variables, with the (E) letter referring to shear strain enhancement only.

The second proposed element encompass not only the preceding shear strain enrichment but also an *in-plane enhancement* introduced by Andelfinger and Ramm (1993). This element is labelled *S4E4P7* in the following, where the previous notation was extending to accommodate the in-plane enhancement (P letter), including seven internal variables. Following the work of Andelfinger and Ramm (1993), the respective interpolation matrix for the in-plane enhancement is defined as

$$\mathbf{M}^{\beta}\left(\boldsymbol{\xi}\right) \equiv \mathbf{M}^{\beta}\left(\xi^1,\xi^2\right)\Big|_7 = \begin{bmatrix} \xi^1 & 0 & 0 & 0 & \xi^1\xi^2 & 0 & 0 \\ 0 & \xi^2 & 0 & 0 & 0 & \xi^1\xi^2 & 0 \\ 0 & 0 & \xi^1 & \xi^2 & 0 & 0 & \xi^1\xi^2 \end{bmatrix} \tag{2.68}$$

with the respective enhanced strain field given by

$$\left\{ \begin{array}{c} E^{\beta}_{\xi^1\xi^1} \\ E^{\beta}_{\xi^2\xi^2} \\ E^{\beta}_{\xi^1\xi^3} \end{array} \right\} = \mathbf{M}^{\beta}\left(\xi^1,\xi^2\right)\Big|_7 \left\{ \begin{array}{c} \beta_1 \\ \beta_2 \\ \beta_3 \\ \beta_4 \\ \beta_5 \\ \beta_6 \\ \beta_7 \end{array} \right\} \tag{2.69}$$

2.4.2 The *S4E6* and *S4E6P7* shell elements

The developed subspace analysis guided so far the choice of the enhanced terms to be included in the transverse shear strain field. As can be stated from the work of the author (César de Sá *et al.*, 2002), the obtained elements with four additional internal variables provided an improvement over the original degenerated element although, however, their performances were still far from "ideal" results, when thickness values involved tended to vanish. Examples involving those elements (*S4E4* and *S4E6P7*) were not included in the present work, being nevertheless presented in the paper of César de Sá *et al.* (2002).

On the other side, benefiting from the enhancement terms coming from the subspace analysis, a further improvement on the quality of the results can be obtained including in equation (2.67) the *cross derivatives of the bubble function* in order to $\left(\xi^1\right)$ and $\left(\xi^2\right)$. This extension over the enhanced polynomial functions leads then to a new interpolation matrix for the transverse shear strain terms on the form

$$\mathbf{M}^{\alpha}\left(\xi^1,\xi^2\right)\big|_6 = \begin{bmatrix} \dfrac{\partial N_\alpha}{\partial \xi^2} & 0 & \dfrac{\partial N_\alpha}{\partial \xi^1} & 0 & \dfrac{\partial N_\alpha}{\partial \xi^1}\dfrac{\partial N_\alpha}{\partial \xi^2} & 0 \\ 0 & \dfrac{\partial N_\alpha}{\partial \xi^1} & 0 & \dfrac{\partial N_\alpha}{\partial \xi^2} & 0 & \dfrac{\partial N_\alpha}{\partial \xi^1}\dfrac{\partial N_\alpha}{\partial \xi^2} \end{bmatrix} \tag{2.70}$$

The matrix $\left(\mathbf{M}^{\alpha}\left(\xi^1,\xi^2\right)\big|_6\right)$ can then be related, within the context of the present work, to an *optimal* choice for the enhanced interpolation for the transverse shear strain terms. In this case, the internal variable field is ultimately represented by a vector with six components.

Similarly to before, the elements obtained from this formulation are termed *S4E6* and *S4E6P7*, for cases including just a transverse shear or a transverse shear plus an in-plane enhancement, respectively. The in-plane enhancement follows again the one coming from equation (2.68).

2.4.3 A computational improvement: the *S4E6P5* shell element

At this point, a slightly distinct enhanced *in-plane* strain field can be introduced, just involving five (instead of seven) internal variables, and not interfering with the enhanced transverse shear strain field (6 variables) previously defined. This modification, leading to the *S4E6P5* shell element, involves no loss in accuracy for linear test cases when compared to the *S4E6P7* element and, involving less internal variables, provides a relative computational gain in terms of *CPU* time.

The improved in-plane enhanced strain-displacement matrix follows the work of Betsch *et al.* (1996), being given by

$$\mathbf{M}^{\beta}\left(\boldsymbol{\xi}\right) \equiv \mathbf{M}^{\beta}\left(\xi^1,\xi^2\right)\Big|_5 = \begin{bmatrix} \xi^1 & 0 & 0 & 0 & 0 \\ 0 & \xi^2 & 0 & 0 & 0 \\ 0 & 0 & \xi^1 & \xi^2 & \xi^1\xi^2 \end{bmatrix} \tag{2.71}$$

With results for linear problems completely equivalent to those given by the *S4E6P7* shell elements, the *S4E6P5* bilinear shell element turned out to be the *optimal* choice for applications in nonlinear problems, as can be inferred from the examples chapter in the end of the present work.

2.4.4 A distinct approach: the *MITC4–E2 enhanced + assumed strain* shell element

Changing the approach adopted herein, the *MITC4* bilinear shell element of Dvorkin and Bathe (1984) is now focused in the following.

As detailed in the analysis of the null transverse shear strain subspace described in Section 2.3.3, the chosen basis of the element has two missing components when compared to the one provided by the *SRI* formulation, namely the (`S9`) and (`S10`) terms of Figure 2.3. As detailed in the beginning of this section, these two components can be directly included into the deformation field, with the aid of the *EAS* method and using only two internal variables (equation (2.66)).

In this way, it is possible to improve the performance of the *MITC4* shell element, combining the *assumed strain method* with the *enhanced assumed strain* approach, just specifically affecting the transverse shear strain field. The shell finite element therefore obtained is termed *MITC4–E2* in this work, following the previous notation, and involves an improved transverse strain field in the general form

$$\left\{ \begin{array}{c} E_{\xi^1\xi^3} \\ E_{\xi^2\xi^3} \end{array} \right\} = \left\{ \begin{array}{c} E^{ANS}_{\xi^1\xi^3} \\ E^{ANS}_{\xi^2\xi^3} \end{array} \right\} + \left\{ \begin{array}{c} E^{\alpha}_{\xi^1\xi^3} \\ E^{\alpha}_{\xi^2\xi^3} \end{array} \right\}_2 \tag{2.72}$$

with the assumed natural strain terms being as in equations (2.51) and the interpolation matrix used in the enhanced strain field as defined in equation (2.66). As it would be expected, a new analysis of the Example 2 treated before, now with this improved element, provides the very same result as the *SRI* formulation.

2.5 Further reading

- **César de Sá JMA, Natal Jorge RM, Fontes Valente RA, Areias PMA** (2002) Development of shear locking-free shell elements using an enhanced assumed strain formulation. International Journal for Numerical Methods in Engineering 53: 1721–1750;

- **Fontes Valente RA, Natal Jorge RM, Cardoso RPR, César de Sá JMA, Grácio JJ** (2003) On the use of an enhanced *transverse* shear strain shell element for problems involving large rotations. Computational Mechanics 30: 286–296;

- **Fontes Valente RA, Natal Jorge RM, César de Sá JMA, Grácio JJ** (2004) Enhanced *transverse* shear strain shell formulation applied to large elasto-plastic deformation problems. International Journal for Numerical Methods in Engineering (submitted).

Chapter 3

Enhanced Solid-Shell Finite Elements

In this chapter, the concept of "solid-shell" is explored, as an alternative to degenerated shell elements. Starting from a trilinear, 8 node, three-dimensional element, improvements are carried out in order to overcome numerical pathologies such as the volumetric locking – appearing in incompressible or near incompressible problems – and the transverse shear strain locking – dominant in conventional formulations when thickness values tend to diminish. Based on a subspace analysis similar to the one carried out in Chapter 2, a reliable fully integrated solid-shell is then introduced, based on the Enhanced Strain Method and with a low number of internal variables when compared to formulations well-established in the literature.

3.1 State of the art

Finite element analysis of shell structures goes back in time until the onset of the so-called *degenerated approach* in works of Ahmad *et al.* (1970) and Zienkiewicz *et al.* (1979), as well as in early papers of Ramm (Ramm, 1977), and afterwards with Hughes and co-workers (Hughes and Liu, 1981; Hughes and Carnoy, 1983), among others. Following the exposed in the previous chapter, brick elements were soon found to be prone to the appearance of volumetric and transverse shear locking effects. The first one comes, for instance, from metal plasticity models, where plastic deformation is taken to be isochoric or, in other words, incompressible (Boër *et al.*, 1986). The second one comes from the analysis of thin shells, where the limit between "thick" and "thin" geometries is somewhat difficult to establish, with the occurrence of locking not only strictly relying on thickness/length ratios, as demonstrated by Chapelle, Bathe and co-workers (Chapelle and Bathe, 1998; Bathe *et al.*, 2000; Chapelle and Bathe, 2000; Bathe *et al.*, 2003; Chapelle and Bathe, 2003).

In order to circumvent these parasitic phenomena, selective reduced integration (or, equivalently, u/p formulation, mean-dilatation technique and *B-bar* methods) - for volumetric locking - and the "mixed interpolation of tensorial components"/assumed strain method - for transverse shear locking - had arisen as possible and successful techniques. Examples in the literature are, for instance, the works of Taylor *et al.* (1968); Key (1969); Argyris *et al.* (1974); Fried (1974); Nagtegaal *et al.* (1974); Malkus (1976); Hughes (1977); Malkus and Hughes (1978); Hughes (1980); Simo and Taylor (1982) and Simo *et al.* (1985), representing the grounds of the computational treatment of incompressibility, in elastic and elasto-plastic finite element cases. Papers of Hughes and Tezduyar (1981); MacNeal (1982); Dvorkin and Bathe (1984) and Bathe and Dvorkin (1986), on the other hand, showed the earlier contributions in dealing with transverse shear locking.

For the specific case of shell elements, original plane-stress assumptions were enough to avoid or postpone incompressibility issues in the nonlinear material range (Ramm, 1977; Hughes and Liu, 1981; Simo *et al.*, 1990a; Gruttmann *et al.*, 1992; Basar *et al.*, 1992), although at the expense of the inclusion of a rotation tensor into the formulation. As more generality was needed, higher order theories including thickness change via extensible director fields and "layerwise" approaches were developed, including (or not) rotational variables. Reference material in the field can be found in the works of (Simo *et al.*, 1990b; Braun *et al.*, 1994; Büchter *et al.*, 1994; Betsch and Stein, 1995; Dvorkin *et al.*, 1995; Sansour, 1995; Betsch *et al.*, 1996; Betsch and Stein, 1996; Basar and Ding, 1997; Bischoff and Ramm, 1997; Sorić *et al.*, 1997; Basar and Itskov, 1999; Betsch and Stein, 1999; Eberlein and Wriggers, 1999; Huettel and Matzenmiller, 1999; el-Abbasi and Meguid, 2000; Brank *et al.*, 2002) and Cardoso *et al.* (2002), although the list is far from being complete.

Despite the good results obtained by shell formulations in thick and thin shell problems, interest in trilinear (eight node) brick-type elements, resting solely on translation-type degrees-of-freedom, has been increasing over the last decade. A relative advantage gained with this three-dimensional formulation would then be the avoidance of a specific treatment for rotation variables. On the other side, for this kind of elements, locking pathologies must be appropriately treated while keeping its scope of application independent of thickness values. Such a hexahedral solid element should also naturally incorporate kinematical formulations typical of shell approaches with, at the same time, the automatic account for thickness variations.

According to Wriggers *et al.* (1996), reliable three-dimensional elements for shell-type applications with finite strains can be obtained using the Enhanced Assumed Strain (*EAS*) method of Simo and co-workers (Simo and Rifai, 1990; Simo and Armero, 1992; Simo *et al.*, 1993). Representative lines of research in this field are, for example, the intensive work of Schweizerhof and co-workers (Freischlager and Schweizerhof, 1996; Hauptmann and Schweizerhof, 1998; Hauptmann *et al.*, 2000; Doll *et al.*, 2000; Harnau and Schweizerhof, 2002); as well as Klinkel and Wagner (1997); Klinkel *et al.* (1999); Wagner *et al.* (2002) and Miehe (1998). Examples of recent papers on the field are the works of Vu-Quoc and Tan (2003) and Legay and Combescure (2003).

All these works have the common feature that enhanced assumed strain, assumed strain method and/or selective integration procedures have been combined in order to obtain a wide class of solid-shell elements with good performances. For typical shell problems, solid-shell elements can then represent an alternative with, as stated before, a simpler formulation when compared to shell elements, although more advantages can be specified. In metal forming simulations involving two-sided contact along the thickness direction (as in the presence of blank-holder) and in composites delamination problems (demanding an accurate evaluation of interlaminar shear and normal stresses), numerical simulations can be effectively carried out with this class of finite elements.

The grounds of the present work rely on the recent paper of Alves de Sousa *et al.* (2003a), where a new class of three-dimensional *EAS* elements for incompressible linear cases was introduced. Starting with a sound analysis of the deformation subspace granting the incompressibility condition ($\operatorname{div}\mathbf{u} = 0$), an enhanced strain field was then developed and introduced into the functional of the classical displacement-based solid element. It was then shown that the inclusion of 6 enhanced variables, acting on the volumetric components of the strain field, was sufficient to avoid the volumetric locking phenomenon. A first proposal for a new 3D element, characterized by a total of 18 internal variables has proved to be effective in solving general three-dimensional problems (*HCiS18 solid element*).

The adopted *EAS* approach avoids the direct use of classical selective reduced integration, consistent just for material models with decoupled isochoric and volumetric behavior. Another important feature was that the element has proved to be reliable in thin shell problems. However, for the specific case of shell structures, it is shown that the use of only

12 enhanced parameters (leading to more computational efficiency) was enough for the obtention of sound results (Alves de Sousa *et al.*, 2003a). Doing so, 6 enhanced variables are responsible for the elimination of transverse shear locking effects, without resorting to assumed strain methods and following the guidelines adopted for shell elements, as detailed in the previous chapter. The resulting solid-shell finite element, then coined *HCiS12 solid-shell element*, is then extended and applied in large deformation elasto-plastic shell problems in this work.

The distinguishing characteristic of the present formulation can be summarized by the fact that only the Enhanced Assumed Strain method is used to simultaneously treat volumetric and transverse shear locking in classical thin-shell problems. This point contrast with the generalized use of the assumed natural strain approach (for the transverse shear locking) and/or the selective reduced integration technique (for near-incompressibility constraints) in well-established solid-shell formulations in the literature. As cited before, linear benchmarks are provided in reference (Alves de Sousa *et al.*, 2003a), while the extension of the methodology to account for nonlinear geometric as well as elasto-plastic problems is carried out in the present work.

Besides leading to an unified and "neat" formulation for the solid-shell element as a whole, the present formulation relies upon an enhanced strain field based on the derivatives of a three-dimensional "bubble-function". This specific choice of functions is grounded on improved results obtained for distorted meshes in incompressibility conditions, and also in bending-dominated situations for two-dimensional problems (César de Sá and Natal Jorge, 1999; César de Sá *et al.*, 2001).

This chapter is organized as follows. In Section 3.2, kinematic aspects of the displacement-based formulation for solid-shell finite elements are described in a concise way. Section 3.3 details the procedures involved in the subspace analysis for volumetric locking, in order to provide a comparative study between fully and reduced integrated formulations for brick-type elements. The number of necessary enhanced (element-wise) internal variables is introduced, in order to provide a fully integrated solid-shell finite element able to solve either volumetric and transverse shear locking. In Section 3.4, these concepts are applied in the formulation of the *HCiS12* and *HCiS18* solid-shell elements, with an overview of the algorithmic aspects related to the finite element implementation, focusing on the specific form of the enhanced strain-displacement matrices implemented. Nonlinear benchmarks involving the *HCiS12* solid-shell element are finally presented in Chapter 5, while the nonlinear aspects of the implementation are described in Chapter 4.

3.2 Kinematics of solid-shell displacement-based elements

Contrary to shell elements, where rotation variables about a director vector are defined at each node, solid-shell elements are based upon the presence of physical nodes at the top and bottom of a (virtual) reference surface. Each node is defined by its position vector referred to the initial (undeformed or converged) configuration and the final (deformed or iterative) configuration. For the initial configuration, any point inside a given 8-node (hexahedral) element can be defined by its position vector, after being projected onto the upper and lower surfaces in the form (Hauptmann and Schweizerhof, 1998; Hauptmann *et al.*, 2000; Harnau and Schweizerhof, 2002; Remmers *et al.*, 2003; Vu-Quoc and Tan, 2003)

$$ {}^{n}\mathbf{x}\left(\xi\right) = {}^{n}\mathbf{x}\left(\xi^1,\xi^2,\xi^3\right) = \frac{1}{2}\left[\left(1+\xi^3\right){}^{n}\mathbf{x}_t\left(\xi^1,\xi^2\right) \ + \ \left(1-\xi^3\right){}^{n}\mathbf{x}_b\left(\xi^1,\xi^2\right)\right] \tag{3.1} $$

The subscripts (t) and (b) denote the projections of the variable onto the top and bottom surface, respectively. Implicit in eq. (3.1) is the degenerated-shell assumption that the normals to the element mid-surface remain straight but not necessarily normal during the deformation, therefore resulting the distinguish concepts of "normal" and "director" vectors (the latter referring solely to the vector pointing from the lower to the upper surfaces of the element).

The formulation is equivalent to a shell approach

$$ \begin{aligned} {}^{n}\mathbf{x}\left(\xi\right) &= \frac{1}{2}\left[{}^{n}\mathbf{x}_t\left(\xi^1,\xi^2\right) + {}^{n}\mathbf{x}_b\left(\xi^1,\xi^2\right)\right] + \frac{1}{2}\xi^3\left[{}^{n}\mathbf{x}_t\left(\xi^1,\xi^2\right) - {}^{n}\mathbf{x}_b\left(\xi^1,\xi^2\right)\right] \\ &= {}^{n}\mathbf{x}_m\left(\xi^1,\xi^2\right) + \frac{1}{2}\xi^3 a\left(\xi^1,\xi^2\right){}^{n}\mathbf{v}^3\left(\xi^1,\xi^2\right) \end{aligned} \tag{3.2} $$

including a director vector ${}^{n}\mathbf{v}^3$ at the projected position of the point onto the element mid-surface (${}^{n}\mathbf{x}_m$) and the thickness $a\left(\xi^1,\xi^2\right)$. Equivalent expressions can be obtained for the deformed configuration.

Equations (3.1) and (3.2) involve an *a priori* definition of the thickness orientation of the finite element. This starting point restricts the formulation to those class of problems usually solved by shell elements, although the number of nodes as well as degrees-of-freedom involved are still those coming from a three-dimensional approach. This fact characterize the "solid-shell" designation.

The displacement field can be give, as usual, by

$$ {}^{n+1}_{n}\mathbf{u}\left(\boldsymbol{\xi}\right) = {}^{n+1}\mathbf{x}\left(\boldsymbol{\xi}\right) - {}^{n}\mathbf{x}\left(\boldsymbol{\xi}\right) \tag{3.3} $$

Convected basis vector in the initial and deformed configurations can be defined, as carried out with the shell elements, in the form

$$ {}^{n+1}\mathbf{g}_l\left(\boldsymbol{\xi}\right) = \frac{\partial\, {}^{n+1}\mathbf{x}\left(\boldsymbol{\xi}\right)}{\partial \xi^l} \tag{3.4a} $$

$${}^{n}\mathbf{g}_l\left(\boldsymbol{\xi}\right) = \frac{\partial\,{}^{n}\mathbf{x}\left(\boldsymbol{\xi}\right)}{\partial \xi^l} \tag{3.4b}$$

This gives the grounds to the definition of the incremental deformation gradient between configurations (n) and $(n+1)$

$${}^{n+1}_{\ \ n}\mathbf{F}\left(\boldsymbol{\xi}\right) = \frac{\partial\,{}^{n+1}\mathbf{x}}{\partial\,{}^{n}\mathbf{x}} = {}^{n+1}\mathbf{g}_k \otimes {}^{n}\mathbf{g}^k \tag{3.5}$$

and, consequently, the displacement-based Green-Lagrange strain tensor

$${}^{n+1}_{\ \ n}\mathbf{E}^u = \frac{1}{2}\left({}^{n+1}_{\ \ n}\mathbf{F}^{\mathrm{T}}\ {}^{n+1}_{\ \ n}\mathbf{F} - \mathbf{I}_2\right) = E^u_{\xi^j\xi^l}\ {}^{n}\mathbf{g}^j \otimes {}^{n}\mathbf{g}^l \tag{3.6a}$$

$${}^{n+1}_{\ \ n}E^u_{\xi^j\xi^l} = \frac{1}{2}\left(\underbrace{{}^{n}\mathbf{g}_j \cdot \frac{\partial\,{}^{n+1}_{\ \ n}\mathbf{u}}{\partial\,\xi^l} + \frac{\partial\,{}^{n+1}_{\ \ n}\mathbf{u}}{\partial\,\xi^j} \cdot {}^{n}\mathbf{g}_l}_{\text{linear part}} + \underbrace{\frac{\partial\,{}^{n+1}_{\ \ n}\mathbf{u}}{\partial\,\xi^j} \cdot \frac{\partial\,{}^{n+1}_{\ \ n}\mathbf{u}}{\partial\,\xi^l}}_{\text{non-linear part}}\right) \tag{3.6b}$$

Also from the shell finite elements analysis of Chapter 2, comes the definition of the local frame in each Gauss point over a solid-shell element. Once the thickness direction is specified in the latter, it is straightforward to employ the set of equations (2.28) in order to obtain an initial local frame on the element. With deformation, this local frame is affected with the rigid-body part of the total deformation – see equation (2.29). The stress and strain tensors are then related to this frame leading to a corotational approach, identical to the one adopted for the shell elements in Chapter 2. The transformation procedures, from the convective frame to the local system, are the same as already specified for the shell elements, particular in what refers to the transformation of the convective-based Green-Lagrange strain tensor – equation (2.35). Finally, the non-linear part of the strain-displacement matrix (coming from the second member of the right-hand side of eq. (3.6)) in the local frame is analogous to the one presented in equation (2.36). Details on the displacement-based formulation for three-dimensional elements can be found, for instance, in the work of Bathe (1996).

3.3 Subspace analysis for volumetric locking

The incompressibility problem can be analysed, in a general sense, as a constrained minimization of a given functional (César de Sá and Natal Jorge, 1999), similar to what have been carried out for the transverse shear locking phenomena in Chapter 2.

In basic terms, the goal is to find, in a linear space of admissible solutions ($\mathcal{U}_h$), a specific finite element-based displacement solution ($\mathbf{u}_h$) (subset of the continuous displacement field – $\mathbf{u}$), such that it minimizes the total energy of the system granting, at the same time, the incompressibility constraint. This (approximated) finite element solution will then be located in the subspace of the incompressible deformations ($\mathcal{I}_h^v$) being, by definition, contained in the space of all the solutions. These statements can be posed in the mathematical form

$$\mathcal{I}_h^v = \{\mathbf{u}_h \in \mathcal{U}_h : \mathrm{div}\,(\mathbf{u}_h) = 0\} \tag{3.7}$$

which is analogous to the primary constraint adopted for the transverse shear locking treatment (see eq. (2.42), Chapter 2). Implicit in this equation is that both the linear space ($\mathcal{U}_h$) and its respective subspace ($\mathcal{I}_h^v$), once being generated by the finite element method, are approximations of their continuum counterparts ($\mathcal{U}_h \approx \mathcal{U}$ and $\mathcal{I}_h^v \approx \mathcal{I}$).

A two field finite element solution might be expressed for linear elasticity (César de Sá and Natal Jorge, 1999), in the form

$$\begin{bmatrix} \mathbf{K}_{uu}^{lg} & \mathbf{Q}^v \\ -\mathbf{Q}^v & \mathbf{0} \end{bmatrix} \begin{bmatrix} \mathbf{u}_h \\ \mathbf{p}_h \end{bmatrix} = \begin{bmatrix} \mathbf{F}^e \\ \mathbf{0} \end{bmatrix} \tag{3.8}$$

for a vector of external forces ($\mathbf{F}^e$), vectorial hydrostatic pressure field ($\mathbf{p}_h$) and the displacement-based linear stiffness matrix $\left(\mathbf{K}_{uu}^{lg}\right)$. Directly from the equation, comes the incompressibility constraint in its discrete form as

$$\mathbf{Q}^v \mathbf{u}^h = \mathbf{0} \equiv \mathbf{Q}^v\, \mathbf{N}(\boldsymbol{\xi})\mathbf{d}_e = \mathbf{0} \tag{3.9}$$

function of the element degrees-of-freedom vector ($\mathbf{d}_e$) and the three-dimensional shape functions ($\mathbf{N}\,(\boldsymbol{\xi})$). In the present work, the three-dimensional analysis relies on the tri-linear 8-node isoparametric finite element, with the degrees-of-freedom vector spanning a total of 24 components and shape functions as given in Bathe (1996).

As was dealt with in the transverse shear locking analysis of thin shells, in order to avoid the trivial solution $\left(\mathbf{u}^h = \mathbf{0}\right)$ in eq. (3.9), the displacement field $\left(\mathbf{u}^h\right)$ provided by the finite element method must belong to the null space of ($\mathbf{Q}^v$) and, consequently, to the subspace of the incompressible deformations ($\mathcal{I}_h^v$). Therefore, reproducible displacement patterns, avoiding volumetric locking, must be represent a linear combination of a given basis of the subspace ($\mathcal{I}_h^v$).

In this sense, volumetric locking phenomenon might occurs (for a combination of loading and boundary conditions) when the expected displacement solution can not be reproduced by any linear combination of the elements of a given basis of ($\mathcal{I}_h^v$). As happened with the shell finite element analysis of the last chapter, different formulations will inevitably lead to distinct predictability characteristics, which in turn is directly related to the dimension of its incompressible subspace.

Following the work of Alves de Sousa *et al.* (2003a), in order to fully characterize the subspace ($\mathcal{I}_h^v$) for a three-dimensional isoparametric formulation, consider an eight node hexahedral element within a volumetric domain

$$\mathbb{V}_e \equiv \xi^1 \times \xi^2 \times \xi^3 = [-1,1] \times [-1,1] \times [-1,1] \tag{3.10}$$

in the natural coordinates set. In the following, the calculations involving the element are assumed to be carried out with a full numerical integration rule, i.e., with $2 \times 2 \times 2$ integration points along each convective axis. Considering small strains, the incompressibility condition expressed in eq. 3.7 can be explicitly defined as

$$\int\limits_{\mathbb{V}_e} \operatorname{div}(\mathbf{u}) \ \mathrm{d}\mathbb{V}_e = \int\limits_{\mathbb{V}_e} \left(\frac{\partial u^1}{\partial \xi^1} + \frac{\partial u^2}{\partial \xi^2} + \frac{\partial u^3}{\partial \xi^3} \right) \ \mathrm{d}\mathbb{V}_e = 0 \tag{3.11}$$

Imposing a finite element discretization, the incompressibility condition can be expressed at the element level with the inclusion of the isoparametric shape functions, in the form

$$\underbrace{\begin{bmatrix} \dfrac{\partial N_1}{\partial \xi^1} & \dfrac{\partial N_1}{\partial \xi^2} & \dfrac{\partial N_1}{\partial \xi^3} & (\ldots) & \dfrac{\partial N_8}{\partial \xi^1} & \dfrac{\partial N_8}{\partial \xi^2} & \dfrac{\partial N_8}{\partial \xi^3} \end{bmatrix}}_{\mathbf{Q}^v \, \mathbf{N}(\boldsymbol{\xi})} \mathbf{d}_e = 0 \tag{3.12}$$

Extension of this equation to account for each of the $2 \times 2 \times 2$ Gauss points in the element, allows for the explicit definition of the constraint operator

$$\mathbf{Q}^v \, \mathbf{N}(\boldsymbol{\xi}) = \mathbf{M}^u(\boldsymbol{\xi}) =$$

$$= \left[\begin{array}{cccccccccccccccccccccccc}
-a & -a & -a & a & -c & -c & c & c & -b & -c & a & -c & -c & -c & a & c & -b & c & b & b & b & -b & c & c \\
-a & -c & -c & a & -a & -a & c & a & -c & -c & c & -b & -c & -b & c & c & -c & a & b & c & c & -b & b & b \\
-c & -c & -b & c & -a & -c & a & a & -a & -a & c & -c & -b & -b & b & b & -c & c & c & c & a & -c & b & c \\
-c & -a & -c & c & -c & -b & a & c & -c & -a & a & -a & -b & -c & c & b & -b & b & c & b & c & -c & c & a \\
-c & -c & -a & c & -b & -c & b & b & -b & -b & c & -c & -a & -a & a & a & -c & c & c & c & b & -c & a & c \\
-c & -b & -c & c & -c & -a & b & c & -c & -b & b & -b & -a & -c & c & a & -a & a & c & a & c & -c & c & b \\
-b & -b & -b & b & -c & -c & c & c & -a & -c & b & -c & -c & -c & b & c & -a & c & a & a & a & -a & c & c \\
-b & -c & -c & b & -b & -b & c & b & -c & -c & c & -a & -c & -a & c & c & -c & b & a & c & c & -a & a & a
\end{array} \right] \tag{3.13}$$

where the constants presented in eq. (3.13) refer to the following terms

$$a = \frac{1}{8}(1+f)(1+f) \tag{3.14a}$$

$$b = \frac{1}{8}(1-f)(1-f) \tag{3.14b}$$

$$c = \frac{1}{8}(1+f)(1-f) \tag{3.14c}$$

$$\text{with } \ f = \frac{\sqrt{3}}{3} \tag{3.14d}$$

The matrix presented in eq. (3.13) possess a rank of 7. As, for a trilinear three-dimensional finite element, the total number of degrees-of-freedom is 24, the dimension of the subspace of admissible solutions ($\mathcal{U}_h$) has an upper-limit of 24. Therefore, the subspace of incompressible deformations will be characterized by a dimension of 17, i.e.,

$$\operatorname{rank}\left[\mathbf{Q}^v\,\mathbf{N}\left(\boldsymbol{\xi}\right)\right]=7 \quad \therefore \quad \operatorname{nullity}\left[\mathbf{Q}^v\,\mathbf{N}\left(\boldsymbol{\xi}\right)\right]=17 \tag{3.15}$$

If, for the same element's topology, a full reduced numerical integration rule, consisting of just one Gauss point $\left(\xi^1=\xi^2=\xi^3=0\right)$, imposition of eq. (3.12) will then lead to a subspace of dimension 23, still for a maximum dimension of 24 for the space of admissible solutions. For this case, the matrix on eq. (3.13) now appears in the form

$$\begin{aligned}\mathbf{Q}^v\,\mathbf{N}\left(\boldsymbol{\xi}\right)&=\\ &=\frac{1}{8}\Big[\begin{matrix}-1 & -1 & -1 & +1 & -1 & -1 & +1 & +1 & -1 & -1 & +1 & -1 & (\cdots)\end{matrix}\\ &\qquad \begin{matrix}(\cdots) & -1 & -1 & +1 & +1 & -1 & +1 & +1 & +1 & +1 & -1 & +1 & +1\end{matrix}\Big]\end{aligned} \tag{3.16}$$

and, consequently,

$$\operatorname{rank}\left[\mathbf{Q}^v\,\mathbf{N}\left(\boldsymbol{\xi}\right)\right]=1 \quad \therefore \quad \operatorname{nullity}\left[\mathbf{Q}^v\,\mathbf{N}\left(\boldsymbol{\xi}\right)\right]=23 \tag{3.17}$$

Comparing the elements of candidate bases for the subspace of the incompressible deformations, coming from complete and reduced approaches, it can be clearly inferred that the use of the reduced integration allows for the reproduction of more six incompressible displacement modes than with the complete integration.

Since any admissible displacement solution (respecting the incompressibility restrain) must be a linear combination of a given basis for $\mathcal{I}_h^v$, reduced techniques are automatically less prone to show volumetric locking problems when compared with the full numerical integration approach, for a given imposed displacement or boundary condition set (Alves de Sousa *et al.*, 2003a). A graphic illustration of possible linearly independent candidates for the subspace basis of the reduced formulation can be seen in Fig. 3.1 and 3.2.

The nodal displacement field associated with each element can be defined by the general degrees-of-freedom vector ($\mathbf{d}_r$)

$$\mathbf{d}_r=\left\{\begin{matrix} u^1_{k=1} & u^2_{k=1} & u^3_{k=1} & \ldots & u^1_{k=8} & u^2_{k=8} & u^3_{k=8}\end{matrix}\right\}^{\mathrm{T}} \tag{3.18}$$

in a way similar to the one introduced in eq. (2.45), on Chapter 2. It is worth noting that, contrasting to what happens with the transverse shear locking in shell elements, now all the 24 displacement-type degrees-of-freedom within an element contribute to the analysis and treatment of volumetric locking.

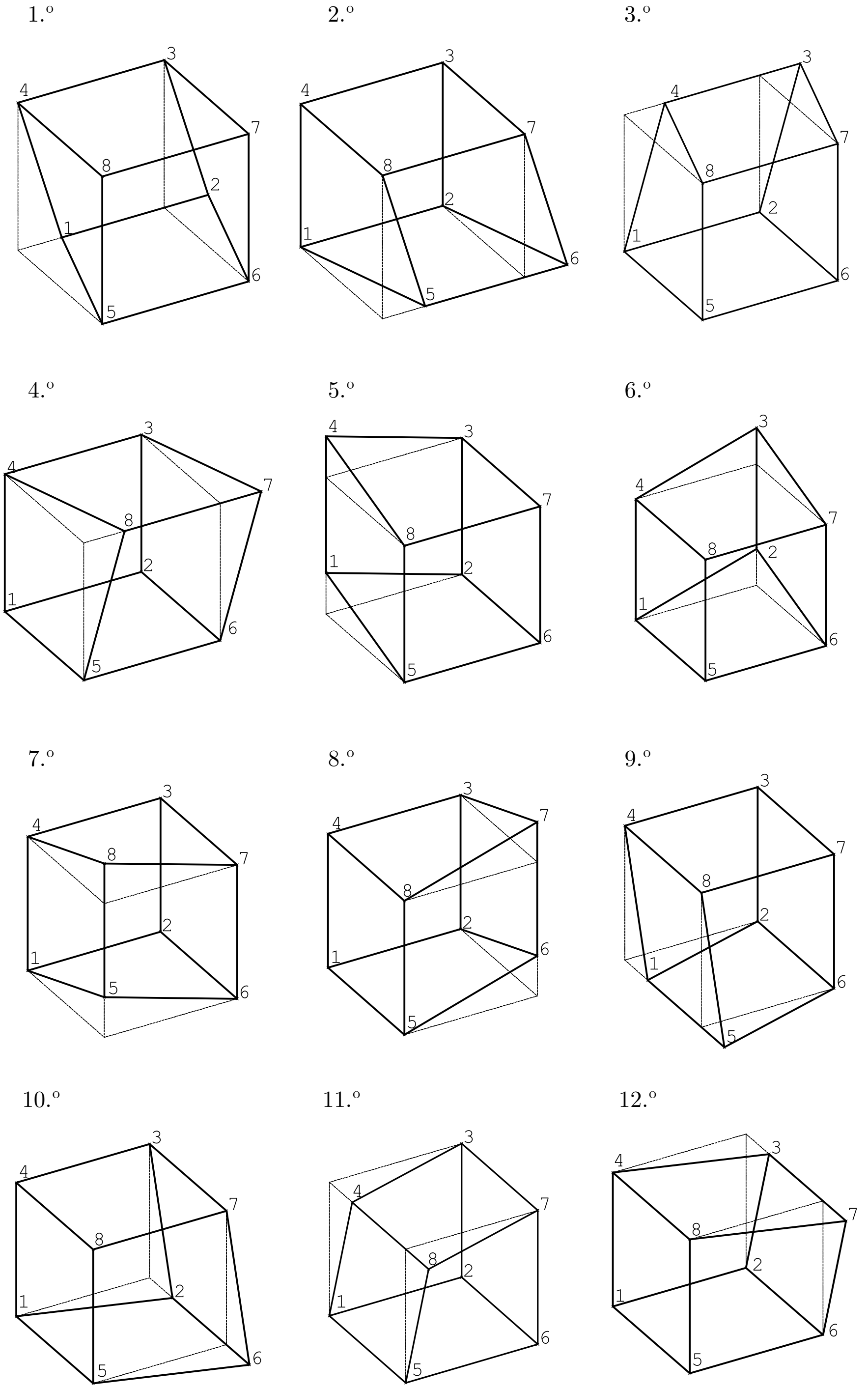

Figure 3.1: Set of possible linearly independent elements for the incompressible deformations subspace basis – edges' translation modes

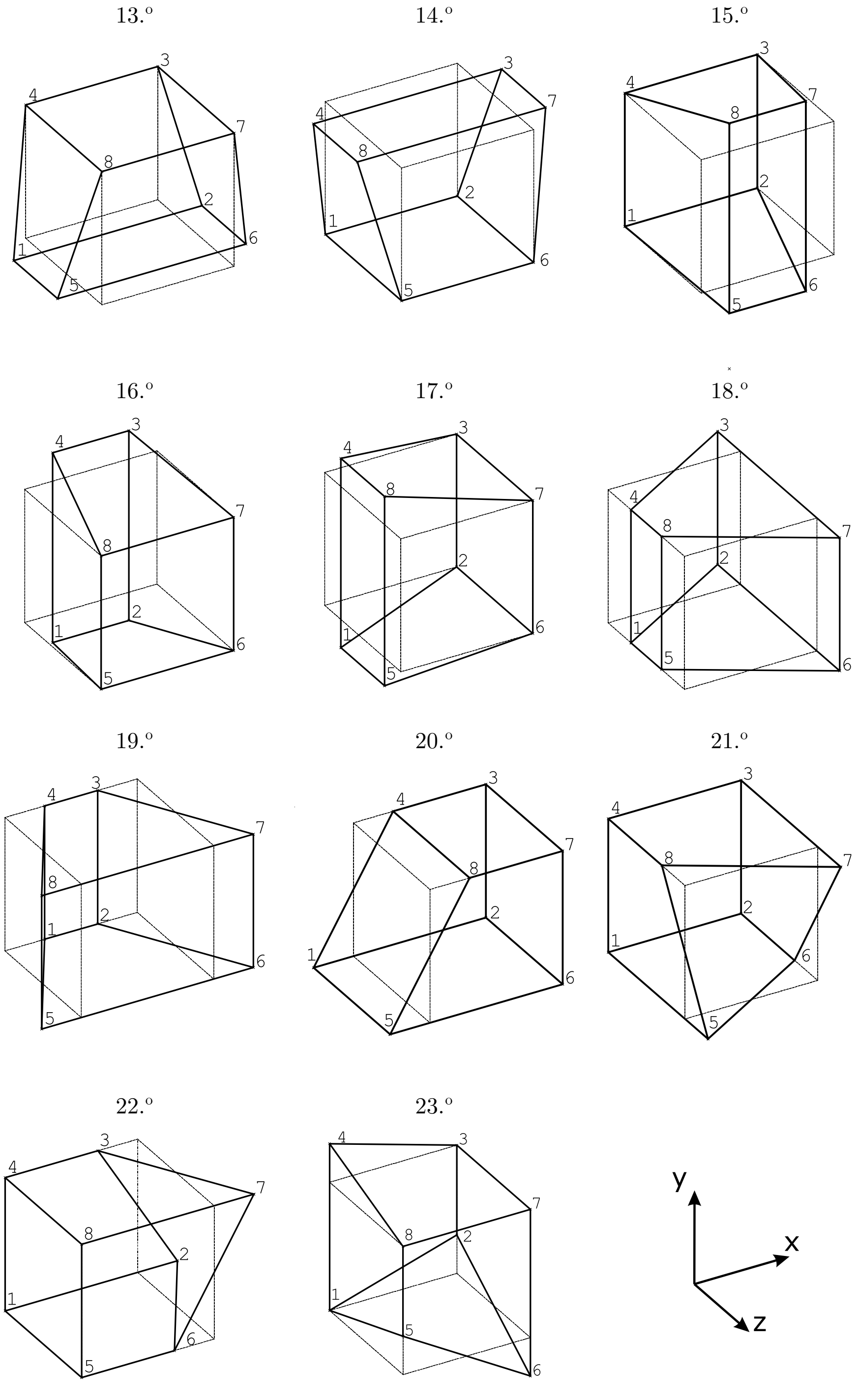

Figure 3.2: Set of possible linearly independent elements for the incompressible deformations subspace basis – expansion/contraction, hourglass and warping modes

Displacement vectors reproducing each of the patterns in Fig. 3.1 and 3.2 can be represented as follows

$$
\begin{aligned}
&\mathsf{V1} \Rightarrow \mathbf{d}_r = \{1,0,0,1,0,0,0,0,0,0,0,0,0,0,0,0,0,0,0,0,0,0,0,0\}^{\mathrm{T}}\\
&\mathsf{V2} \Rightarrow \mathbf{d}_r = \{0,0,0,0,0,0,0,0,0,0,0,0,1,0,0,1,0,0,0,0,0,0,0,0\}^{\mathrm{T}}\\
&\mathsf{V3} \Rightarrow \mathbf{d}_r = \{0,0,0,0,0,0,1,0,0,1,0,0,0,0,0,0,0,0,0,0,0,0,0,0\}^{\mathrm{T}}\\
&\mathsf{V4} \Rightarrow \mathbf{d}_r = \{0,0,0,0,0,0,0,0,0,0,0,0,0,0,0,0,0,0,1,0,0,1,0,0\}^{\mathrm{T}}\\
&\mathsf{V5} \Rightarrow \mathbf{d}_r = \{0,1,0,0,0,0,0,0,0,0,1,0,0,0,0,0,0,0,0,0,0,0,0,0\}^{\mathrm{T}}\\
&\mathsf{V6} \Rightarrow \mathbf{d}_r = \{0,0,0,0,1,0,0,1,0,0,0,0,0,0,0,0,0,0,0,0,0,0,0,0\}^{\mathrm{T}}\\
&\mathsf{V7} \Rightarrow \mathbf{d}_r = \{0,0,0,0,0,0,0,0,0,0,0,0,0,1,0,0,0,0,0,0,0,0,1,0\}^{\mathrm{T}}\\
&\mathsf{V8} \Rightarrow \mathbf{d}_r = \{0,0,0,0,0,0,0,0,0,0,0,0,0,0,0,0,1,0,0,1,0,0,0,0\}^{\mathrm{T}}\\
&\mathsf{V9} \Rightarrow \mathbf{d}_r = \{0,0,1,0,0,0,0,0,0,0,0,0,0,0,1,0,0,0,0,0,0,0,0,0\}^{\mathrm{T}}\\
&\mathsf{V10} \Rightarrow \mathbf{d}_r = \{0,0,0,0,0,1,0,0,0,0,0,0,0,0,0,0,0,1,0,0,0,0,0,0\}^{\mathrm{T}}\\
&\mathsf{V11} \Rightarrow \mathbf{d}_r = \{0,0,0,0,0,0,0,0,0,0,0,1,0,0,0,0,0,0,0,0,0,0,0,1\}^{\mathrm{T}}\\
&\mathsf{V12} \Rightarrow \mathbf{d}_r = \{0,0,0,0,0,0,0,0,1,0,0,0,0,0,0,0,0,0,0,0,1,0,0,0\}^{\mathrm{T}}\\
&\mathsf{V13} \Rightarrow \mathbf{d}_r = \{-1,0,1,1,0,1,0,0,0,0,0,0,-1,0,-1,1,0,-1,0,0,0,0,0,0\}^{\mathrm{T}}\\
&\mathsf{V14} \Rightarrow \mathbf{d}_r = \{0,0,0,0,0,0,1,0,1,-1,0,1,0,0,0,0,0,0,1,0,-1,-1,0,-1\}^{\mathrm{T}}\\
&\mathsf{V15} \Rightarrow \mathbf{d}_r = \{0,0,0,0,0,0,0,0,0,0,0,0,1,-1,0,-1,-1,0,-1,1,0,1,1,0\}^{\mathrm{T}}\\
&\mathsf{V16} \Rightarrow \mathbf{d}_r = \{1,-1,0,-1,-1,0,-1,1,0,1,1,0,0,0,0,0,0,0,0,0,0,0,0,0\}^{\mathrm{T}}\\
&\mathsf{V17} \Rightarrow \mathbf{d}_r = \{0,-1,1,0,0,0,0,0,0,0,1,1,0,-1,-1,0,0,0,0,0,0,0,1,-1\}^{\mathrm{T}}\\
&\mathsf{V18} \Rightarrow \mathbf{d}_r = \{0,0,1,0,0,-1,0,0,-1,0,0,1,0,0,-1,0,0,1,0,0,1,0,0,-1\}^{\mathrm{T}}\\
&\mathsf{V19} \Rightarrow \mathbf{d}_r = \{1,0,0,-1,0,0,-1,0,0,1,0,0,-1,0,0,1,0,0,1,0,0,-1,0,0\}^{\mathrm{T}}\\
&\mathsf{V20} \Rightarrow \mathbf{d}_r = \{-1,0,0,0,0,0,-1,0,0,0,0,0,-1,0,0,0,0,0,0,0,0,1,0,0\}^{\mathrm{T}}\\
&\mathsf{V21} \Rightarrow \mathbf{d}_r = \{0,0,0,0,0,0,0,0,0,0,0,0,0,0,1,0,0,-1,0,0,1,0,0,-1\}^{\mathrm{T}}\\
&\mathsf{V22} \Rightarrow \mathbf{d}_r = \{0,0,0,1,0,0,-1,0,0,0,0,0,0,0,0,-1,0,0,1,0,0,0,0,0\}^{\mathrm{T}}\\
&\mathsf{V23} \Rightarrow \mathbf{d}_r = \{0,0,0,0,1,0,0,0,0,0,1,0,0,1,0,0,-1,0,0,0,0,0,0,0\}^{\mathrm{T}}
\end{aligned}
\tag{3.19}
$$

Still from Fig. 3.1 and 3.2, it is possible to split the displacement modes into two main groups: a first one – containing modes 1-17 – which is reproducible by both the complete and selective reduced integration formulations; and a second group – containing the remaining 18-23 modes – which can be reproduced solely resorting to a reduced integration approach. In this sense, imposition of the latter patterns will lead to the onset of volumetric locking when a complete integration procedure is adopted.

From the point of view of the type of distortion introduced in each hexahedral element, the displacement modes can be further divided into four categories:

- simple edge translations along the OX, OY or OZ axes (modes 1-12);
- expansion or contraction of a given element's face (modes 13-17);

- ”hourglass” modes (Belytschko and Bindeman, 1993);
- ”warping” modes (Belytschko and Bindeman, 1993).

In the following sections – and based on the described subspace analysis and characterization – enhanced strain-based procedures, tailored for the overcoming of volumetric (and subsequently transverse shear) locking in solid and solid-shell elements are presented and described in detail.

3.4 Volumetric and transverse shear locking treatment

3.4.1 Basic formulation

From the exposed before, total reduced integration as well as selective reduced integration have proved to be efficient approaches on attenuating the volumetric locking phenomenon. The performed subspace analysis was useful in providing an extra insight into the limitations of complete integration techniques in incompressible or nearly-incompressible situations.

On the opposite, for bending-dominated situations, results coming from reduced formulations are known to not be completely reliable. Moreover, selective reduced approaches are limited to the analysis of material models where, implicitly, stress tensor fields could be split into volumetric and deviatoric components.

Allowing for the inclusion of specific strain modes into, for instance, a displacement-based formulation, Enhanced Assumed Strain procedures are able to (at least theoretically) be designed for precise applications or, in other words, to directly treat a set of undesirable pathologies within the original formulation. In this sense, the main goal of this section is to provide the major guidelines for an EAS-based formulation, applied directly over a (conventional) displacement-based approach for three-dimensional finite elements. The resulting advantages of this procedure are twofold: firstly, the treatment of the volumetric locking arising in incompressible (or nearly-incompressible) situations and coming from material properties or from elasto-plastic isochoric material models. Secondly, the numerical treatment of the transverse shear locking arising from the use of hexahedral elements in thin-shell structures modelling. This last point directly leads to the definition of a new solid-shell element with a low number of internal variables per element, when compared with the major solid-shell elements in the literature.

Starting with the volumetric locking pathology, attention is focused on the displacement-based, full integrated ($2 \times 2 \times 2$ Gauss points) eight-node three dimensional finite element. From the subspace analysis of the previous section, the goal is to enable the formulation to automatically cover the 23 incompressible displacement modes coming from a selectively reduced approach. As for the transverse shear locking in thin shells of Chapter 2, the crucial point is the introduction of an enhanced strain field, based on element-wise internal variables, and added to the displacement-based strain tensor. In this sense, eq. (2.62), Chapter 2 is recalled

$$\mathbf{E} = \mathbf{E}^u + \mathbf{E}^\gamma = \mathbf{M}^u(\boldsymbol{\xi}) \left\{ \begin{array}{c} \mathbf{d}_1 \\ \cdots \\ \mathbf{d}_k \end{array} \right\} + \mathbf{M}^\gamma(\boldsymbol{\xi}) \left\{ \begin{array}{c} \gamma_1 \\ \cdots \\ \gamma_l \end{array} \right\} \tag{3.20}$$

but now referred to a new set of internal variables ($\boldsymbol{\gamma}$), which must provide the extra deformation modes 18-23 in Fig. 3.2. Once again, the formalism of eq. (3.20) follows the general guidelines of Simo and Rifai (1990) for linear problems. The extension of this procedure, for the specific cases of the elements treated in the present work, will be detailed in the next chapter.

The core aspect of the enhanced strain field is the particular form of the ($\mathbf{M}^\gamma$) operator in eq. (3.20). For the present solid enhanced element, the starting point is the inclusion of nine additional variables for the enhanced strain field, each one related to a single component of the spatial derivatives of the displacement field (Alves de Sousa *et al.*, 2003a). The derivatives involve the three-dimensional counterpart of the bubble-function presented in eq. (2.63), that is

$$N_\gamma^3\left(\xi^1, \xi^2, \xi^3\right) = \left(1 - \xi^1\xi^1\right)\left(1 - \xi^2\xi^2\right)\left(1 - \xi^3\xi^3\right) \tag{3.21}$$

A first differential enhanced strain-displacement matrix can then be achieved in the form

$$\mathbf{M}^\gamma(\boldsymbol{\xi})|_9 = \begin{bmatrix} \frac{\partial N_\gamma^3}{\partial \xi^1} & 0 & 0 & 0 & 0 & 0 & 0 & 0 & 0 \\ 0 & \frac{\partial N_\gamma^3}{\partial \xi^2} & 0 & 0 & 0 & 0 & 0 & 0 & 0 \\ 0 & 0 & \frac{\partial N_\gamma^3}{\partial \xi^3} & 0 & 0 & 0 & 0 & 0 & 0 \\ 0 & 0 & 0 & \frac{\partial N_\gamma^3}{\partial \xi^1} & \frac{\partial N_\gamma^3}{\partial \xi^2} & 0 & 0 & 0 & 0 \\ 0 & 0 & 0 & 0 & 0 & \frac{\partial N_\gamma^3}{\partial \xi^1} & \frac{\partial N_\gamma^3}{\partial \xi^3} & 0 & 0 \\ 0 & 0 & 0 & 0 & 0 & 0 & 0 & \frac{\partial N_\gamma^3}{\partial \xi^2} & \frac{\partial N_\gamma^3}{\partial \xi^3} \end{bmatrix} \tag{3.22}$$

Accounting for this matrix, equation (3.12) can be rewritten in an extended form as

$$\left[\begin{array}{cc} \mathbf{M}^u\left(\xi^1, \xi^2, \xi^3\right) & \mathbf{M}^\gamma\left(\xi^1, \xi^2, \xi^3\right)\big|_9 \end{array}\right]\mathbf{d}_e = 0 \tag{3.23}$$

In a similar way as considered in building the preliminary matrix ($\mathbf{M}^u(\boldsymbol{\xi})$) in eq. (3.13), for a complete 3D integration rule eq. (3.23) turns out to be in the form

$$\left[\begin{array}{cccccccccc} & d & d & d & 0 & 0 & 0 & 0 & 0 & 0 \\ & -d & d & d & 0 & 0 & 0 & 0 & 0 & 0 \\ & -d & -d & d & 0 & 0 & 0 & 0 & 0 & 0 \\ & d & -d & d & 0 & 0 & 0 & 0 & 0 & 0 \\ \mathbf{M}^u(\boldsymbol{\xi}) & d & d & -d & 0 & 0 & 0 & 0 & 0 & 0 \\ & -d & d & -d & 0 & 0 & 0 & 0 & 0 & 0 \\ & -d & -d & -d & 0 & 0 & 0 & 0 & 0 & 0 \\ & d & -d & -d & 0 & 0 & 0 & 0 & 0 & 0 \end{array}\right] \mathbf{d}_e = \mathbf{0} \tag{3.24}$$

where

$$d = f\left(1 - f^2\right)^2 \tag{3.25}$$

with, as referred before,

$$f = \frac{\sqrt{3}}{3}$$

The subspace of incompressible deformations for this mixed proposal will be then characterized by

$$\operatorname{rank}\left[\begin{array}{cc} \mathbf{M}^u\left(\xi^1, \xi^2, \xi^3\right) & \mathbf{M}^\gamma\left(\xi^1, \xi^2, \xi^3\right)\big|_9 \end{array}\right] = 7 \tag{3.26}$$

with, consequently,

$$\operatorname{nullity}\left[\begin{array}{cc} \mathbf{M}^u\left(\xi^1, \xi^2, \xi^3\right) & \mathbf{M}^\gamma\left(\xi^1, \xi^2, \xi^3\right)\big|_9 \end{array}\right] = 26 \tag{3.27}$$

From the exposed so far, equation (3.24) points to a possible basis for the subspace of incompressible deformations, the latter now with a total dimension of 20. This value comes from considering an overall number of degrees-of-freedom per element $(24 + 9)$, less the number of linearly dependent columns in the final differential matrix (7, from eq. (3.26)) and the number of null displacement modes, represented by the null columns in eq. (3.24). It is worth noting that the last six neglected modes respect the incompressibility constraint – trivial solution of null displacements – although involving non-zero values for the enhanced field. The possible 20 modes are represented by the first 20 elements in Figures 3.1 and 3.2. Still, 3 additional modes are missing, when compared to those obtained by a reduced formulation.

In order to provide the inclusion of these modes into the subspace basis, three more internal variables are proposed. The latter come from the second derivatives of the bubble-function (3.21), and are arranged in a new enhanced strain-displacement operator in the form

$$\mathbf{M}^{\gamma}\left(\boldsymbol{\xi}\right)|_{12} = \left[\begin{array}{cccc} & \dfrac{\partial^2 N_{\gamma}^3}{\partial\xi^1\partial\xi^2} & \dfrac{\partial^2 N_{\gamma}^3}{\partial\xi^1\partial\xi^3} & \dfrac{\partial^2 N_{\gamma}^3}{\partial\xi^2\partial\xi^3} \\ & \dfrac{\partial^2 N_{\gamma}^3}{\partial\xi^1\partial\xi^2} & \dfrac{\partial^2 N_{\gamma}^3}{\partial\xi^1\partial\xi^3} & \dfrac{\partial^2 N_{\gamma}^3}{\partial\xi^2\partial\xi^3} \\ \mathbf{M}^{\gamma}\left(\xi\right)|_{9} & \dfrac{\partial^2 N_{\gamma}^3}{\partial\xi^1\partial\xi^2} & \dfrac{\partial^2 N_{\gamma}^3}{\partial\xi^1\partial\xi^3} & \dfrac{\partial^2 N_{\gamma}^3}{\partial\xi^2\partial\xi^3} \\ & 0 & 0 & 0 \\ & 0 & 0 & 0 \\ & 0 & 0 & 0 \end{array}\right] \tag{3.28}$$

These new three terms ensure the incompressibility constraint, as previously stated by Simo *et al.* (1993), Korelc and Wriggers (1996) and de Borst and Groen (1999). The equivalent of eq. (3.24), but now considering $\left(\mathbf{M}^{\gamma}\left(\xi\right)|_{12}\right)$, would be given by

$$\left[\begin{array}{ccccccccccccc} & d & d & d & 0 & 0 & 0 & 0 & 0 & 0 & e & e & e \\ & -d & d & d & 0 & 0 & 0 & 0 & 0 & 0 & -e & e & -e \\ & -d & -d & d & 0 & 0 & 0 & 0 & 0 & 0 & e & -e & -e \\ & d & -d & d & 0 & 0 & 0 & 0 & 0 & 0 & -e & -e & e \\ [\text{eq.}8] & d & d & -d & 0 & 0 & 0 & 0 & 0 & 0 & e & -e & -e \\ & -d & d & -d & 0 & 0 & 0 & 0 & 0 & 0 & -e & -e & e \\ & -d & -d & -d & 0 & 0 & 0 & 0 & 0 & 0 & e & e & e \\ & d & -d & -d & 0 & 0 & 0 & 0 & 0 & 0 & -e & e & -e \end{array}\right] \mathbf{d}_e = \mathbf{0} \tag{3.29}$$

once again considering

$$d = f\left(1 - f^2\right)^2 \quad \text{and} \quad f = \frac{\sqrt{3}}{3}$$

and now introducing

$$e = f^2 + 1 \tag{3.30}$$

As the rank is kept the same (see eq. (3.26)), the increase in the overall degrees-of-freedom vector (physical and enhanced ones) leads to a subspace of incompressible deformations with a final dimension of 23 (coming from 24+12-7-6), after neglecting the null displacement modes in eq. (3.29). Therefore, the total number of linearly independent (and non-null) displacement modes pertaining to the reduced formulation is finally achieved.

3.4.2 The ***HCiS18*** solid element

Once the theoretical requirements for a volumetric locking-free 3D element were achieved, attention is focused on the elimination of transverse shear locking in thin shell applications. In fact, the formulations detailed in the last Section showed to be prone to the onset of transverse shear locking in problems originally treated by plate or shell elements, when low values of thickness are considered (Alves de Sousa *et al.*, 2002).

Dealing just with the shear components of the enhanced strain field (in order to preserve the volumetric locking-free patterns discussed before), 6 new internal variables are added to the enhanced strain field, resulting in a new interpolation matrix coming from an extension of the one presented in eq. (3.28), in the form

$$\mathbf{M}^{\gamma}\left(\boldsymbol{\xi}\right)\big|_{18} = \left[\begin{array}{ccccccc} & 0 & 0 & 0 & 0 & 0 & 0 \\ & 0 & 0 & 0 & 0 & 0 & 0 \\ & 0 & 0 & 0 & 0 & 0 & 0 \\ \mathbf{M}^{\gamma}\left(\xi\right)\big|_{12} & \dfrac{\partial^2 N_{\gamma}^3}{\partial\xi^1\partial\xi^3} & \dfrac{\partial^2 N_{\gamma}^3}{\partial\xi^2\partial\xi^3} & 0 & 0 & 0 & 0 \\ & 0 & 0 & \dfrac{\partial^2 N_{\gamma}^3}{\partial\xi^1\partial\xi^2} & \dfrac{\partial^2 N_{\gamma}^3}{\partial\xi^2\partial\xi^3} & 0 & 0 \\ & 0 & 0 & 0 & 0 & \dfrac{\partial^2 N_{\gamma}^3}{\partial\xi^1\partial\xi^2} & \dfrac{\partial^2 N_{\gamma}^3}{\partial\xi^1\partial\xi^3} \end{array}\right] \tag{3.31}$$

This proposal is, to some extent, based on the approach previously suggested by Andelfinger and Ramm (1993). Nevertheless, two major differences must be pointed out. First, the functions involved in both formulations are not the same. Second, and most important, the present enhanced strain element, thereafter called *HCiS18*, needs a total of 18 variables, compared to the 21 of Andelfinger and Ramm (1993). This difference may prove of importance, since each additional internal variable added represents an overspend in CPU time. The *HCiS18* three-dimensional element proved to be reliable in problems usually leading to the appearance of volumetric and transverse shear locking, with either regular and distorted mesh topologies (Alves de Sousa *et al.*, 2002, 2003a,b; Alves de Sousa, 2003c).

3.4.3 The ***HCiS12*** solid-shell element

A distinct approach, although benefiting from the previous analysis, can lead to an element suitable for the modelling of thin geometries, typically treated with shell elements. In this case, however, the three-dimensional kinematic relations are kept unchanged, as the element topology, thus generating the concept of ”solid-shell” element.

The adopted methodology has its starting point in the split of the matrix $(\mathbf{M}^{\gamma}(\boldsymbol{\xi})|_{18})$ on eq. (3.31) into two separate matrices (Alves de Sousa *et al.*, 2003a). The first one, named $(\mathbf{M}^{\gamma}(\boldsymbol{\xi})|_{vl})$, encompasses the enhanced deformation modes directly related to the volumetric part of the total enhanced strain tensor (thus also directly related to volumetric locking), being defined as

$$\mathbf{M}^{\gamma}(\boldsymbol{\xi})|_{vl} = \begin{bmatrix} \dfrac{\partial N_{\gamma}^{3}}{\partial \xi^{1}} & 0 & 0 & \dfrac{\partial^{2} N_{\gamma}^{3}}{\partial \xi^{1} \partial \xi^{2}} & \dfrac{\partial^{2} N_{\gamma}^{3}}{\partial \xi^{1} \partial \xi^{3}} & \dfrac{\partial^{2} N_{\gamma}^{3}}{\partial \xi^{2} \partial \xi^{3}} \\ 0 & \dfrac{\partial N_{\gamma}^{3}}{\partial \xi^{2}} & 0 & \dfrac{\partial^{2} N_{\gamma}^{3}}{\partial \xi^{1} \partial \xi^{2}} & \dfrac{\partial^{2} N_{\gamma}^{3}}{\partial \xi^{1} \partial \xi^{3}} & \dfrac{\partial^{2} N_{\gamma}^{3}}{\partial \xi^{2} \partial \xi^{3}} \\ 0 & 0 & \dfrac{\partial N_{\gamma}^{3}}{\partial \xi^{3}} & \dfrac{\partial^{2} N_{\gamma}^{3}}{\partial \xi^{1} \partial \xi^{2}} & \dfrac{\partial^{2} N_{\gamma}^{3}}{\partial \xi^{1} \partial \xi^{3}} & \dfrac{\partial^{2} N_{\gamma}^{3}}{\partial \xi^{2} \partial \xi^{3}} \\ 0 & 0 & 0 & 0 & 0 & 0 \\ 0 & 0 & 0 & 0 & 0 & 0 \\ 0 & 0 & 0 & 0 & 0 & 0 \end{bmatrix} \tag{3.32}$$

where the subscript (vl) points to the *volumetric locking* analysis. The direct additive application of the enhanced differential operator (3.32) on the displacement-based original strain tensor is satisfactory in order to enlarge the incompressible deformations subspace to a dimension of 23. For this case a three-dimensional finite element, less susceptible to be affected by locking, can be obtained. In fact, from the comparison between equations (3.32) and (3.28), imposition of the incompressibility constraint (3.12) in each of the 8 Gauss points over an element will provide a matrix similar to the one presented in the equality (3.29), but now without the six null columns in the latter. Therefore, in this case the incompressible deformations subspace can be characterized by

$$\operatorname{rank}\left[\ \mathbf{M}^{u}\left(\xi^{1},\xi^{2},\xi^{3}\right) \quad \mathbf{M}^{\gamma}\left(\xi^{1},\xi^{2},\xi^{3}\right)\big|_{9}\ \right] = 7 \tag{3.33}$$

and, consequently,

$$\operatorname{nullity}\left[\ \mathbf{M}^{u}\left(\xi^{1},\xi^{2},\xi^{3}\right) \quad \mathbf{M}^{\gamma}\left(\xi^{1},\xi^{2},\xi^{3}\right)\big|_{9}\ \right] = 23 \tag{3.34}$$

As a consequence, the number of linearly independent components in the subspace basis will equal those coming from reduced formulations.

The remaining part of $(\mathbf{M}^{\gamma}(\boldsymbol{\xi})|_{18})$ is finally represented by the $(\mathbf{M}^{\gamma}(\boldsymbol{\xi})|_{tsl})$ matrix in the form

$$\mathbf{M}^{\gamma}\left(\boldsymbol{\xi}\right)\big|_{tsl} =$$

$$= \begin{bmatrix} 0 & 0 & 0 & 0 & 0 & 0 & 0 & 0 & 0 & 0 & 0 & 0 \\ 0 & 0 & 0 & 0 & 0 & 0 & 0 & 0 & 0 & 0 & 0 & 0 \\ 0 & 0 & 0 & 0 & 0 & 0 & 0 & 0 & 0 & 0 & 0 & 0 \\ \frac{\partial N_{\gamma}^{3}}{\partial \xi^{1}} & \frac{\partial N_{\gamma}^{3}}{\partial \xi^{2}} & 0 & 0 & 0 & 0 & \frac{\partial^{2} N_{\gamma}^{3}}{\partial \xi^{1} \partial \xi^{3}} & \frac{\partial^{2} N_{\gamma}^{3}}{\partial \xi^{2} \partial \xi^{3}} & 0 & 0 & 0 & 0 \\ 0 & 0 & \frac{\partial N_{\gamma}^{3}}{\partial \xi^{1}} & \frac{\partial N_{\gamma}^{3}}{\partial \xi^{3}} & 0 & 0 & 0 & 0 & \frac{\partial^{2} N_{\gamma}^{3}}{\partial \xi^{1} \partial \xi^{2}} & \frac{\partial^{2} N_{\gamma}^{3}}{\partial \xi^{2} \partial \xi^{3}} & 0 & 0 \\ 0 & 0 & 0 & 0 & \frac{\partial N_{\gamma}^{3}}{\partial \xi^{2}} & \frac{\partial N_{\gamma}^{3}}{\partial \xi^{3}} & 0 & 0 & 0 & 0 & \frac{\partial^{2} N_{\gamma}^{3}}{\partial \xi^{1} \partial \xi^{2}} & \frac{\partial^{2} N_{\gamma}^{3}}{\partial \xi^{1} \partial \xi^{3}} \end{bmatrix} \tag{3.35}$$

where, analogously to eq. (3.32), the subscript (tsl) points to the *transverse shear locking* analysis. The major difference between the previous analyzed *HCiS18* solid element and the presently introduced *HCiS12* solid-shell one is related to the specific aspect of the matrix $\mathbf{M}^{\gamma}\left(\boldsymbol{\xi}\right)\big|_{tsl}$.

Benefiting from the exposed in Chapter 2, and departing from the *HCiS18* formulation, the enhanced concepts used in shell elements *S4E6P5* and *S4E6P7* will be directly applied here. Doing so, the 6 enhanced variables therein included in the displacement-based strain field (equation (2.70), Chapter 2) will be retained now, replacing the 12 internal variables involved in eq. (3.35). Transverse strain energy terms can, then, also be taken for granted to vanish with the three-dimensional element, for thickness values tending to diminish. The enhanced strain field is, as carried out until this point, additively included in the displacement-based formulation, now considering the modified differential matrix

$$\mathbf{M}^{\gamma}\left(\boldsymbol{\xi}\right)\big|_{tsl}^{*} = \begin{bmatrix} 0 & 0 & 0 & 0 & 0 & 0 \\ 0 & 0 & 0 & 0 & 0 & 0 \\ 0 & 0 & 0 & 0 & 0 & 0 \\ 0 & 0 & 0 & 0 & 0 & 0 \\ \frac{\partial N_{\alpha}^{2}}{\partial \xi^{2}} & 0 & \frac{\partial N_{\alpha}^{2}}{\partial \xi^{1}} & 0 & \frac{\partial^{2} N_{\alpha}^{2}}{\partial \xi^{1} \partial \xi^{2}} & 0 \\ 0 & \frac{\partial N_{\alpha}^{2}}{\partial \xi^{1}} & 0 & \frac{\partial N_{\alpha}^{2}}{\partial \xi^{2}} & 0 & \frac{\partial^{2} N_{\alpha}^{2}}{\partial \xi^{1} \partial \xi^{2}} \end{bmatrix} \tag{3.36}$$

for the two-dimensional bubble-functions already referred

$$N_{\alpha}^{2}\left(\xi^{1}, \xi^{2}\right) = \left(1 - \xi^{1}\xi^{1}\right)\left(1 - \xi^{2}\xi^{2}\right)$$

The final enhanced strain differential operator is, therefore, a combination of the previous matrices, that is

$$\mathbf{M}^{\gamma}\left(\boldsymbol{\xi}\right)\big|_{12} = \left[\begin{array}{cc} \mathbf{M}^{\gamma}\left(\boldsymbol{\xi}\right)\big|_{vl} & \mathbf{M}^{\gamma}\left(\boldsymbol{\xi}\right)\big|_{tsl}^{*} \end{array}\right] \tag{3.37}$$

The main advantage of the *HCiS12* solid-shell element, when compared with the *HCiS18* solid element, is its lower number of variables. Compared with other elements in the literature, the use of a total of just 12 internal parameters for each element is still an improvement. Another point of interest remains in that only the enhanced assumed strain method is employed for both the treatment of volumetric and transverse shear locking in an unified way. The most referred solid-shell elements in the literature – Freischlager and Schweizerhof (1996); Hauptmann and Schweizerhof (1998); Hauptmann *et al.* (2000); Doll *et al.* (2000); Harnau and Schweizerhof (2002); Klinkel and Wagner (1997); Klinkel *et al.* (1999); Wagner *et al.* (2002) and Miehe (1998) – employs combinations of distinct approaches, such as reduced integration (for volumetric locking) and the assumed natural strain method (for the transverse shear locking). The *HCiS18* solid element, on the other side, does not need to have a preferred convective direction for thickness dimension, an argument that is valid in the case of the *HCiS12* solid-shell element. This can be clear seen from the aspect of the derivatives involved in eq. (3.36), where the $\left(\xi^3\right)$ is not taken into account. Nevertheless, it is worth remembering that this requirement is not such a strong imposition, once the range of applicability of element *HCiS12* is, by definition, related to the analysis of shell structures or problems classically treated with shell elements. Other solid-shell elements in the literature, in addition, also need an *a-priori* definition of the thickness direction if, for instance, the assumed natural strain procedure of Dvorkin and Bathe (1984) is employed.

For *linear* test cases using the *HCiS12* solid-shell element, as well as examples involving the *HCiS18* solid element, the reader is suggested to see the work of Alves de Sousa *et al.* (2003a) and the references herein. Implementation details regarding the treatment of *nonlinearities* are given in Chapter 4, with nonlinear benchmarks involving the *HCiS12* solid-shell element being discussed in Chapter 5. The implemented nonlinear concepts, as applied to the solid-shell formulation (as well as to the before mentioned *EAS* shell element), will be presented in the next chapter.

3.5 Further reading

- **Alves de Sousa RJ, Natal Jorge RM, Fontes Valente RA, César de Sá JMA** (2003) A new volumetric and shear locking-free 3D enhanced strain element. Engineering Computations 20: 896–925;

- **Fontes Valente RA, Alves de Sousa RJ, Natal Jorge RM** (2004) An enhanced strain 3D element for large deformation elastoplastic thin-shell applications. Computational Mechanics 34: 38–52.

Chapter 4

Topics in Nonlinear Formulations

This chapter is devoted to the algorithmic guidelines followed in the numerical implementation within the in-house finite element program used in the present work. Starting with the specific nonlinear continuum mechanics topics employed, the theoretical frame behind the co-rotational approach is described. After that, the extension of the Enhanced Assumed Strain method to account for nonlinearities is treated in detail, with the main advantages of the adopted approach being highlighted. Computational plasticity aspects are described, along with the main steps in the corresponding implementation for the previously treated shell and solid-shell elements. Finally, the main characteristics of the arc-length path-following technique are described in detail, in the way they were implemented.

4.1 Nonlinear continuum mechanics

In this section, the author aims to introduce and describe the main aspects related to the nonlinear continuum mechanics fundamentals, as employed and implemented in this work. The choice of build up a section rather than an entire chapter in the field is two-fold. Firstly, there are a relatively high number of didactic books dealing with the subject, ranging from concise to advanced treatments, either adopting a theoretical or applied approaches. Secondly, in providing a summary description of this topic, the author would more easily highlight the points that have been indeed accounted for in the development of the thesis.

Nevertheless, and among the references studied, it is worth noting the works of Truesdell and Noll (1965), Marsden and Hughes (1994),Khan and Huang (1995), Chadwick (1999), Novozhilov (1999), Basar and Weicher (2000), Belytschko *et al.* (2000), Doghri (2000), Doyle (2001), Fung and Tong (2001), Gambin (2001), Haupt (2002) and Dhondt (2004), just to name those published in monograph forms.

As described in Chapters 2 and 3, the kinematics aspects behind the formulation of *S4E6P5* shell and *HCiS12* solid-shell finite elements include the evaluation of the displacement-based Green-Lagrange strain tensor, in the convective frame, from the basic equations in tensorial and components forms

$${}^{n+1}_{\;\;n}\mathbf{E}^u = \frac{1}{2}\left({}^{n+1}_{\;\;n}\mathbf{F}^{\mathrm{T}}\;{}^{n+1}_{\;\;n}\mathbf{F} - \mathbf{I}_2\right) = E^u_{\xi^j\xi^l}\;{}^{n}\mathbf{g}^j \otimes {}^{n}\mathbf{g}^l$$

$${}^{n+1}_{\;\;n}E^u_{\xi^j\xi^l} = \frac{1}{2}\left(\underbrace{{}^{n}\mathbf{g}_j \cdot \frac{\partial\,{}^{n+1}_{\;\;n}\mathbf{u}}{\partial\,\xi^l} + \frac{\partial\,{}^{n+1}_{\;\;n}\mathbf{u}}{\partial\,\xi^j} \cdot {}^{n}\mathbf{g}_l}_{\text{linear part}} + \underbrace{\frac{\partial\,{}^{n+1}_{\;\;n}\mathbf{u}}{\partial\,\xi^j} \cdot \frac{\partial\,{}^{n+1}_{\;\;n}\mathbf{u}}{\partial\,\xi^l}}_{\text{non-linear part}}\right)$$

For the subsequent constitutive behavior simulation of the material, however, this strain tensor needs to be transformed (referred to) a *local frame*, defined in each Gauss point within an element, and following the rigid body rotation part of the overall deformation imposed between (load) states (n) and $(n+1)$. After that, the co-rotated (local) Green-Lagrange strain tensor $\left({}^{n+1}_{\;\;n}\bar{\mathbf{E}}^u\right)$ is then available. From the implementation point-of-view, this last tensor is obtained directly from the strain-displacement differential matrix, firstly evaluated in the convective frame and afterwards transformed to the local frame with the aid of the previously defined operator

$${}^{l}_{c}\mathbf{T} = \begin{bmatrix} T_{11}\,T_{11} & T_{12}\,T_{12} & T_{13}\,T_{13} & T_{11}\,T_{12} & T_{11}\,T_{13} & T_{12}\,T_{13} \\ T_{21}\,T_{21} & T_{22}\,T_{22} & T_{23}\,T_{23} & T_{21}\,T_{22} & T_{21}\,T_{23} & T_{22}\,T_{23} \\ 2\,T_{11}\,T_{21} & 2\,T_{12}\,T_{22} & 2\,T_{13}\,T_{23} & (T_{11}\,T_{22}) + (T_{21}\,T_{12}) & (T_{11}\,T_{23}) + (T_{21}\,T_{13}) & (T_{12}\,T_{23}) + (T_{22}\,T_{13}) \\ 2\,T_{11}\,T_{31} & 2\,T_{12}\,T_{32} & 2\,T_{13}\,T_{33} & (T_{11}\,T_{32}) + (T_{31}\,T_{12}) & (T_{11}\,T_{33}) + (T_{31}\,T_{13}) & (T_{12}\,T_{33}) + (T_{32}\,T_{13}) \\ 2\,T_{21}\,T_{31} & 2\,T_{22}\,T_{32} & 2\,T_{23}\,T_{33} & (T_{21}\,T_{32}) + (T_{31}\,T_{22}) & (T_{21}\,T_{33}) + (T_{31}\,T_{23}) & (T_{22}\,T_{33}) + (T_{32}\,T_{23}) \end{bmatrix}$$

with each component being calculated from expressions (2.31) and (2.32), already presented in Chapter 2.

As stated in that Chapter, the local frame is first built considering the distortion pattern of each element. This criterion is somewhat arbitrary, but it was the one that best "affects" each Gauss points with the distortion characteristics of a given finite element. After that, and with the beginning of the simulation, the local frame is subsequently updated based on the rotation tensor coming from the incremental deformation gradient

$${}^{n+1}_{\;\;n}\mathbf{F} = {}^{n+1}_{\;\;n}\mathbf{R}\;\;{}^{n+1}_{\;\;n}\mathbf{U}$$

The incremental character of the deformation gradient is the basis of an "updated Lagrangian" algorithmic implementation, where each converged state becomes the reference one for the following load increment. The current local frame at each increment (and iteration) during a deformation path is then simply given in the form

$$\begin{bmatrix} {}^{n+1}\mathbf{r}^1 & {}^{n+1}\mathbf{r}^2 & {}^{n+1}\mathbf{r}^3 \end{bmatrix} = {}^{n+1}_{\;\;n}\mathbf{R} \begin{bmatrix} {}^{n}\mathbf{r}^1 & {}^{n}\mathbf{r}^2 & {}^{n}\mathbf{r}^3 \end{bmatrix}$$

For a given increment between states (n) and $(n+1)$, and specifically for a given iteration (i), the "driving force" of the whole algorithm is the cumulative (degrees-of-freedom) displacement vector $\left({}^{i}_{n}\mathbf{d}\right)$, encompassing the displacement (and rotation, for shells) nodal variables within an element. It is worth remembering that, for the shell elements introduced in the present work, the rotation-like variables need a specific treatment in order to be described in an additive way (see equations (2.11)–(2.16) in Chapter 2).

The incremental rotation tensor $\left({}^{n+1}_{\;\;n}\mathbf{R}\right)$ is theoretically obtained from the so-called "polar decomposition theorem", mostly with the determination of the eigenvalues of the right Cauchy-Green tensor $\left(\mathbf{C} = \mathbf{F}^{\mathrm{T}}\mathbf{F} = \mathbf{U}^2\right)$. In practice, a set of numerical algorithms are provided in the literature. In some of them, and particularly for the case of shell elements – for instance, in the works of Yoon *et al.* (1999) and Cardoso *et al.* (2002) – a 2D simplified procedure is employed, based on Cayley-Hamilton theorem for linear algebra (Marsden and Hughes, 1994). However, as in the present work three-dimensional elements are introduced, a more general procedure was adopted for the computation of a true (three-dimensional based) rotation tensor. This is in conformity with the original proposal of Franca (1989), and is presented in Box 4.1 in the end of the Section (where indices were dropped out for simplifying purposes).

The main advantage of the adoption of a co-rotational local frame is the simplified treatment of nonlinearities in the following, either geometric (Section 4.2) or material (Section 4.3). About the latter, a complete description of the constitutive behavior of a given body can be obtained resorting to material stress and strain co-rotational tensors, continuously referred to the local frame and, consequently, following the deformation path from the beginning. Examples of such tensors are the second Piola-Kirchhoff stress tensor and the Green-Lagrange strain tensor, evaluated at the continuously rotated local reference system. This fact turns to be very useful, once the enhanced assumed strain procedure was entirely designed resorting to the material frame. Additionally, the use of material tensors avoids objectivity questions within the formulation. In fact, the primary choice of a reference system rotating with the continuum body grant the objectivity requirements, for an observer situated at the body and affected by the rotation (but not the stretch) part of the deformation.

In general terms, starting from the total deformation gradient for a given Gauss point ($\boldsymbol{\xi}$) at a given stage $(n+1)$, as a function of a previous (equilibrated) state (n) (Flanagan and Taylor, 1987)

$$^{n+1}\mathbf{F}\left(\boldsymbol{\xi}\right) = {}^{n}\mathbf{F}\left(\boldsymbol{\xi}\right)\ {}^{n+1}_{\quad n}\mathbf{F}\left(\boldsymbol{\xi}\right) \tag{4.2}$$

it is possible to define the velocity gradient between (n) and $(n+1)$ states (now dropping the Gauss point position vector) in the form

$$\mathbf{L} = \frac{\mathrm{d}\mathbf{F}}{\mathrm{d}t}\mathbf{F}^{-1} \tag{4.3}$$

where

$$\frac{d\mathbf{F}}{dt} = \mathbf{R}\frac{d\mathbf{U}}{dt} + \frac{d\mathbf{R}}{dt}\mathbf{U} \tag{4.4}$$

and

$$\mathbf{F}^{-1} = \left(\mathbf{R}\mathbf{U}\right)^{-1} = \mathbf{U}^{-1}\mathbf{R}^{-1} \tag{4.5}$$

Substitution of equations (4.4) and (4.5) into the expression for the velocity gradient tensor (4.3), leads to the important relation

$$\mathbf{L} = \underbrace{\frac{d\mathbf{R}}{dt}\mathbf{R}^{\mathrm{T}}}_{\boldsymbol{\Omega}} + \mathbf{R}\frac{d\mathbf{U}}{dt}\mathbf{U}^{-1}\mathbf{R}^{\mathrm{T}} \tag{4.6}$$

The rotation rate tensor ($\boldsymbol{\Omega}$) physically represents the rate of rigid-body rotation at a given material point (instantaneous spatial gradient or angular velocity) about a predefined axis (Dienes, 1979). Its importance is related to the definition of the Green-Naghdi-McInnis objective stress rate of the Cauchy stress ($\boldsymbol{\sigma}$) in the form (Marsden and Hughes, 1994; Doghri, 2000)

$$\overset{\mathrm{G}}{\boldsymbol{\sigma}} = \dot{\boldsymbol{\sigma}} - \boldsymbol{\Omega}\boldsymbol{\sigma} + \boldsymbol{\sigma}\boldsymbol{\Omega} \tag{4.7}$$

The velocity gradient can be alternatively decomposed into a symmetric ($\mathbf{D}$) and anti-symmetric ($\mathbf{W}$) parts

$$\mathbf{L} = \mathbf{D} + \mathbf{W} \tag{4.8}$$

representing the spatial rate of deformation and the spin rate tensors, respectively, and given by

$$\mathbf{D} = \frac{1}{2}\left(\mathbf{L} + \mathbf{L}^{\mathrm{T}}\right) = \mathbf{R}\left(\frac{d\mathbf{U}}{dt}\mathbf{U}^{-1}\right)_{s}\mathbf{R}^{T} \tag{4.9}$$

and

$$\mathbf{W} = \frac{1}{2}\left(\mathbf{L} - \mathbf{L}^{\mathrm{T}}\right) = \frac{d\mathbf{R}}{dt}\mathbf{R}^{-1} + \mathbf{R}\left(\frac{d\mathbf{U}}{dt}\mathbf{U}^{-1}\right)_{a}\mathbf{R}^{T} \tag{4.10}$$

where the subscripts (a) and (s) denote the anti-symmetric and symmetric part of the respective tensor, that is,

$$\left(\frac{d\mathbf{U}}{dt}\mathbf{U}^{-1}\right)_s = \frac{1}{2}\left(\frac{d\mathbf{U}}{dt}\mathbf{U}^{-1} + \mathbf{U}^{-1}\frac{d\mathbf{U}}{dt}\right) \tag{4.11a}$$

$$\left(\frac{d\mathbf{U}}{dt}\mathbf{U}^{-1}\right)_a = \frac{1}{2}\left(\frac{d\mathbf{U}}{dt}\mathbf{U}^{-1} - \mathbf{U}^{-1}\frac{d\mathbf{U}}{dt}\right) \tag{4.11b}$$

The spin rate tensor ($\mathbf{W}$) represents the rate of deformation of the principal axes of the spatial rate of deformation ($\mathbf{D}$). This tensor is used in the definition of the Jaumann stress rate of the Cauchy stress tensor in the form (Marsden and Hughes, 1994; Doghri, 2000)

$$\overset{\mathrm{J}}{\boldsymbol{\sigma}} = \dot{\boldsymbol{\sigma}} - \mathbf{W}\boldsymbol{\sigma} + \boldsymbol{\sigma}\mathbf{W} \tag{4.12}$$

which are formally identical to the Green-Naghdi-McInnis objective stress rate of equation (4.7). The only difference is the anti-symmetric term affecting the spin tensor ($\mathbf{W}$) in (4.10).

Once the rotation tensor from the polar decomposition of ($\mathbf{F}$) is entirely used for the update of the local reference frame, the principal material lines of ($\mathbf{U}$) and $\left(\frac{d\mathbf{U}}{dt}\right)$ are kept the same and, consequently, the tensor $\left(\frac{d\mathbf{U}}{dt}\mathbf{U}^{-1}\right)$ is equal to its symmetric part. In that case, equations (4.9) and (4.10) are simplified

$$\mathbf{D} = \mathbf{R}\frac{d\mathbf{U}}{dt}\mathbf{U}^{-1}\mathbf{R}^T \tag{4.13}$$

$$\mathbf{W} = \frac{d\mathbf{R}}{dt}\mathbf{R}^{-1} \tag{4.14}$$

At this point, the tensors ($\boldsymbol{\Omega}$) and ($\mathbf{W}$) are identical, with the principal axes of ($\mathbf{D}$) being coincident to those of ($\mathbf{U}$).

The symmetric part of the second term in the right-hand side in equation (4.6) points to the rotated (or rotation neutralized) deformation rate tensor

$$\bar{\mathbf{d}} = \frac{1}{2}\left(\dot{\mathbf{U}}\mathbf{U}^{-1} + \mathbf{U}^{-1}\dot{\mathbf{U}}\right) \tag{4.15}$$

which defines an instantaneous strain rate in the local (follower) reference frame. From the orthogonality character of the rotation tensor ($\mathbf{R}$) it is possible to define the rotated deformation rate as the pull-back of the spatial rate of deformation ($\mathbf{D}$) in (4.9) as

$$\bar{\mathbf{d}} = \mathbf{R}^{\mathrm{T}}\mathbf{D}\mathbf{R} \tag{4.16}$$

Once the spatial rate of deformation tensor is work-conjugated to the spatial Cauchy stress tensor, it is possible to define a rotation neutralized (rotated) spatial stress tensor, related, therefore, to the local co-rotational frame, and expressed as

$$\bar{\boldsymbol{\sigma}} = \mathbf{R}^{\mathrm{T}}\boldsymbol{\sigma}\mathbf{R} \tag{4.17}$$

This rotated stress tensor is, obviously, energy-conjugated to the rotated deformation rate $\left(\bar{\mathbf{d}}\right)$ which, following equation (4.15), is of pure stretch character.

The next steps are based on the classical work of Hughes (1984), also treated in detail by Doghri (2000). Following these references, any objective stress rate tensor can be rewritten simply by means of a time derivative of its corresponding rotated stress tensor. Therefore, within the framework of the relative rotation tensor $\left({}^{n+1}_{\;\;n}\mathbf{R}\right)$, it is possible to link the objective Green-Naghdi-McInnis stress rate $\left(\overset{\mathrm{G}}{\boldsymbol{\sigma}}\right)$ to the time derivative of the previous rotated Cauchy stress tensor $(\bar{\boldsymbol{\sigma}})$ in the form

$$\frac{d\bar{\boldsymbol{\sigma}}}{dt} = \left({}^{n+1}_{\;\;n}\mathbf{R}\right)^{\mathrm{T}} \overset{\mathrm{G}}{\boldsymbol{\sigma}} \left({}^{n+1}_{\;\;n}\mathbf{R}\right) \quad \text{or, equivalently,} \tag{4.18a}$$

$$\overset{\mathrm{G}}{\boldsymbol{\sigma}} = \left({}^{n+1}_{\;\;n}\mathbf{R}\right) \frac{\mathrm{d}\bar{\boldsymbol{\sigma}}}{\mathrm{d}t} \left({}^{n+1}_{\;\;n}\mathbf{R}\right)^{\mathrm{T}} \tag{4.18b}$$

Since $\left(\overset{\mathrm{G}}{\boldsymbol{\sigma}}\right)$ is an objective stress rate, the following equalities are valid

$$\overset{\mathrm{G}}{\boldsymbol{\sigma}} = \mathbf{c} : \mathbf{D} \quad \Longrightarrow \quad \frac{\mathrm{d}\bar{\boldsymbol{\sigma}}}{\mathrm{d}t} = \bar{\mathbf{c}} : \bar{\mathbf{d}} \tag{4.19}$$

for the spatial and rotated 4^{th} order constitutive tensors $(\mathbf{c})$ and $(\bar{\mathbf{c}})$, respectively.

Starting from the rotated Cauchy stress tensor, a constitutive update between (n) and $(n+1)$ configurations can be performed in the form

$${}^{n+1}\bar{\boldsymbol{\sigma}} = {}^{n}\bar{\boldsymbol{\sigma}} + \Delta t \frac{d\bar{\boldsymbol{\sigma}}}{dt} \tag{4.20}$$

This equation will be the basic one for the update of stress in the following. Retaining the hypothesis that elastic strains developed during deformation remains small when compared to the plastic counterparts (as is common in ductile metal plasticity, with an elastic modulus orders of magnitude greater than the plastic yield stress value), it follows that

$$\mathbf{F}^{e} \approx \mathbf{I}_2 \tag{4.21}$$

and, consequently,

$$\mathbf{L} = \dot{\mathbf{F}}^{e}\mathbf{F}^{-e} + \mathbf{F}^{e}\dot{\mathbf{F}}^{p}\mathbf{F}^{-p}\mathbf{F}^{-e} = \mathbf{L}^{e} + \mathbf{F}^{e}\mathbf{L}^{p}\mathbf{F}^{-e} \approx \mathbf{L}^{e} + \mathbf{L}^{p} \tag{4.22}$$

where the superscripts (e) and (p) point to the elastic and plastic parts of deformation, respectively. Doing so, the symmetric part of $(\mathbf{L})$ can be then written in the form

$$\mathbf{D} \approx \mathbf{D}^{e} + \mathbf{D}^{p} \tag{4.23}$$

Substitution in (4.16) leads to

$$\bar{\mathbf{d}} = \mathbf{R}^{\mathrm{T}} \left(\mathbf{D}^{e} + \mathbf{D}^{p}\right) \mathbf{R} = \bar{\mathbf{d}}^{e} + \bar{\mathbf{d}}^{p} \tag{4.24}$$

As this strain rate has an instantaneous definition, its computational treatment requires an integration over the time step between configurations (n) and $(n+1)$ (Yoon *et al.*, 1999)

$$ {}^{n+1}_{n}\bar{\mathbf{e}} = \int_{t_n}^{t_{n+1}} \bar{\mathbf{d}}\,\mathrm{d}t \equiv {}^{n+\frac{1}{2}}_{n}\bar{\mathbf{d}}\,\Delta t \tag{4.25} $$

The mid-point configuration $\left(n+\frac{1}{2}\right)$ is introduced in order to ensure an unconditionally stable and second-order accurate transition from the continuum to the discrete algorithmic formulation (Key and Krieg, 1982; Pinsky *et al.*, 1983; Hughes, 1984; Ortiz and Popov, 1985). With the spatial incremental tensor in (4.25), the algorithmic counterpart of the state equation (4.20) is simply an extension of the linear framework, in the form

$$ {}^{n+1}\bar{\boldsymbol{\sigma}} = {}^{n}\bar{\boldsymbol{\sigma}} + {}^{n+1}_{n}\bar{\boldsymbol{\sigma}} \equiv {}^{n}\bar{\boldsymbol{\sigma}} + \bar{\mathbf{c}}\left({}^{n+1}_{n}\bar{\mathbf{e}} - {}^{n+1}_{n}\bar{\mathbf{e}}^{p}\right) \tag{4.26} $$

The last detail in the implementation of the constitutive equations is the transformation of the incremental spatial tensors to incremental material tensors. For small strains $\left({}^{n+1}_{n}\mathbf{U} \approx \mathbf{I}_2\right)$ and following the previously defined *rotated* local axes, the incremental *rotated* (co-rotational) Cauchy stress tensor turns to be equivalent to the incremental *rotated* 2^{nd} Piola-Kirchhoff stress tensor (Belytschko *et al.*, 2000; Doghri, 2000), and it is possible to rewrite equation (4.26) in the form (Masud *et al.*, 2000; Masud and Tham, 2000)

$$ {}^{n+1}\bar{\boldsymbol{\sigma}} = {}^{n}\bar{\boldsymbol{\sigma}} + {}^{n+1}_{n}\bar{\boldsymbol{\sigma}} = {}^{n}\bar{\boldsymbol{\sigma}} + {}^{n+1}_{n}\bar{\mathbf{S}} \tag{4.27} $$

In consequence, the increment on the material stress tensor $\left({}^{n+1}_{n}\bar{\mathbf{S}}\right)$ referred to the (rotated) local frame (and thus affected by the rigid-body rotation part of the deformation) can be directly summed up to the converged spatial-based Cauchy stress tensor $({}^{n}\bar{\boldsymbol{\sigma}})$, in a way identical to the one used for small strain theories (Doghri, 2000). The algorithmic treatment of equation (4.27) will be detailed in Section 4.3.

Remark: This equivalence of the second Piola-Kirchhoff and the Cauchy stress tensors for small strains can be further illustrated in considering both tensors related to conventional (out of the body) frames, as appears in classical approaches of continuum mechanics (Doghri, 2000). By definition, the relation between these material and spatial tensors is given by

$$ \begin{aligned} \mathbf{S} &= \det(\mathbf{F})\,\mathbf{F}^{-1}\boldsymbol{\sigma}\mathbf{F}^{-\mathrm{T}} \\ &= \det(\mathbf{F})\,(\mathbf{R}\mathbf{U})^{-1}\,\boldsymbol{\sigma}\,(\mathbf{R}\mathbf{U})^{-\mathrm{T}} \end{aligned} \tag{4.28} $$

For small strains, the following simplifications are carried out

$$ \mathbf{U} \approx \mathbf{I}_2 \Longrightarrow \mathbf{F} \approx \mathbf{R} \;\text{ and }\; \det(\mathbf{F}) \approx 1 \tag{4.29} $$

and equation (4.28) can be stated as

$$\mathbf{S} = \mathbf{R}^{-1}\boldsymbol{\sigma}\mathbf{R}^{-\mathrm{T}} = \mathbf{R}^{\mathrm{T}}\boldsymbol{\sigma}\mathbf{R} \tag{4.30}$$

which is a pull-back of the Cauchy stress tensor – just involving the rigid-body rotation part of the deformation – from the spatial (current) onto the material (converged) fixed frames. Physically, the second Piola-Kirchhoff stress tensor acts as if ”frozen” into a co-ordinate system rotating with the body. This behavior is represented by equation (4.27).

Box 4.1. Algorithm for the Polar Decomposition
(some indices were dropped out for simplifying purposes)

```
i. Determine the right Cauchy-Green deformation tensor
    $\mathbf{C} = \mathbf{F}^{\mathrm{T}}\mathbf{F}$
ii. Compute the invariants of $\mathbf{C}$
    $I_C = \mathrm{tr}\ \mathbf{C}$
    $II_C = \frac{1}{2}\left[I_C^2 - \mathrm{tr}\left(\mathbf{C}^2\right)\right]$
    $III_C = \det \mathbf{C}$
iii. Compute the additional variable
    $k = I_C^2 - 3II_C$
iv. Check the lower bound for $k$
    IF $\left(k \leq 10^{-5}\right)$ THEN
        $\Upsilon = \left(\frac{I_C}{3}\right)^{\frac{1}{2}}$
        $\mathbf{U} = \Upsilon \mathbf{I}_2$
        $\mathbf{U}^{-1} = \Upsilon^{-1}\mathbf{I}_2$
        EXIT
    ELSE
v. Directly calculate the largest eigenvalue $\Upsilon$
        $l = I_C^3 - \frac{9}{2}I_C II_C + \frac{27}{2}III_C$
        $\phi = \cos^{-1}\left(\frac{l}{k^{\frac{3}{2}}}\right)$
        $\Upsilon^2 = \frac{1}{3}\left[I_C + 2k^{\frac{1}{2}}\cos\left(\frac{\phi}{3}\right)\right]$
vi. Compute the invariants of $\mathbf{U}$
        $III_U = \left(III_C\right)^{\frac{1}{2}}$
        $I_U = \Upsilon + \left(-\Upsilon^2 + I_C + \frac{2III_U}{\Upsilon}\right)^{\frac{1}{2}}$
        $II_U = \frac{I_U^2 - I_C}{2}$
vii. Calculate $\mathbf{U}$ and $\mathbf{U}^{-1}$
        $\mathbf{U} = \left(\frac{1}{I_U II_U - III_U}\right)\left[I_U III_U \mathbf{I}_2 + \left(I_U^2 - II_U\right)\mathbf{C} - \mathbf{C}^2\right]$
        $\mathbf{U}^{-1} = \left(\frac{1}{III_U}\right)\left(II_U \mathbf{I}_2 - I_U \mathbf{U} + \mathbf{C}\right)$
    ENDIF
viii. Finalize
    $\mathbf{R} = \mathbf{F}\mathbf{U}^{-1}$
END
```

4.2 Nonlinear implementation of the *EAS* method

4.2.1 General aspects

The core point of this work relies on the Enhanced Assumed Strain method, in its linear version as originally presented by Simo and Rifai (1990). The main goal in adopting this kind of mixed formulation is, for the present work, the efficient elimination of the transverse shear as well as volumetric locking pathologies in shell and solid-shell finite elements. For the shell elements, enhanced terms are judiciously chosen and directly included into the displacement-based convective strain field, in order to enlarge the subspace of null (transverse shear strain) energy modes and, consequently, retain the Kirchhoff–Koiter conditions in situations where a pure displacement-based formulation (theoretically grounded on the Reissner-Mindlin hypotheses) would fail. For solid-shell elements, additionally, enhanced strain modes are included into the formulation in order to automatically account for the incompressibility conditions. These topics were already covered in Chapters 2 and 3. In this Section, nonlinear algorithmic aspects related to the Enhanced Assumed Strain method are covered, in order to provide an overview of the procedures implemented by the author.

In the present work, and although dealing with nonlinearities, the original frame of additive enhancement over the displacement-based convective Green-Lagrange strain tensor is kept, in a way successfully employed at first by Ramm and co-workers (Andelfinger and Ramm (1993) – linear cases – and Bischoff and Ramm (1997) – nonlinear cases), after that by Klinkel and Wagner (1997) and Klinkel *et al.* (1999) and, more recently, consolidated by Vu-Quoc and Tan (2003). As showed in these references, this approach is indeed computationally simpler (and leading to virtually the same results) than the one originally advocated by Simo and Armero (1992) and subsequently used, for example, by Simo *et al.* (1993) and Miehe (1998).

In general terms, and as in the linear analysis, the starting point relies in the Hu-Washizu-de Veubeke 3-field functional for static cases (Bischoff and Ramm, 1997)

$$\Pi^{HWV}\left(\mathbf{u},\mathbf{E},\mathbf{S}\right) = \int_{\mathbb{V}} W_s\left(\mathbf{E}\right)\,\mathrm{d}\mathbb{V} + \int_{\mathbb{V}} \mathbf{S} : \left[\frac{1}{2}\left(\mathbf{F}^{\mathrm{T}}\,\mathbf{F} - \mathbf{I}_2\right) - \mathbf{E}\right]\,\mathrm{d}\mathbb{V} - \Pi^{ext} \tag{4.31a}$$

$$\Pi^{ext} = \int_{\mathbb{V}} \mathbf{u}\cdot\hat{\mathbf{b}}\,\rho\mathrm{d}\mathbb{V} + \int_{\mathbb{S}} \mathbf{u}\cdot\hat{\mathbf{t}}\,\mathrm{d}\mathbb{S} \tag{4.31b}$$

where the displacement ($\mathbf{u}$), the Green-Lagrange strain tensor ($\mathbf{E}$) and the – energy conjugated counterpart – $2nd$ Piola-Kirchhoff stress tensor ($\mathbf{S}$) are independent variables. Equations (4.31a) and (4.31b) involve the displacement-driven strain energy (W_s), the traction and volume force vectors ($\mathbf{t}$) and ($\rho\mathbf{b}$), respectively, altogether with their corresponding prescribed fields ($\hat{\mathbf{t}}$) and ($\hat{\mathbf{b}}$), over control area $\mathbb{S}$ and volume $\mathbb{V}$. It is also worth noting that all variables are referred to the reference configuration (either initial or converged), while the boundary conditions for the displacement field were omitted in equation (4.31).

As described in Chapters 2 and 3, the total strain field coming from the Enhanced Assumed Strain method is then assumed to be composed of a compatible (displacement-based) and an element-wise part, in the form (Simo and Rifai, 1990)

$$\mathbf{E} = \mathbf{E}^u + \mathbf{E}^\alpha \tag{4.32}$$

where the left indexes relating to the (current) configuration were omitted for the sake of simplicity, while the right indexes report to the characteristic of the strain field (note that the α index now has a more general character, encompassing the enhancements already presented for the transverse shear *and* the volumetric lockings in the previous chapters).

Substitution of equation (4.32) into (4.31a), together with (4.31b), and the imposition of an orthogonality condition between the stress field and the enhanced strain field (Simo and Rifai, 1990; Simo and Armero, 1992; Simo *et al.*, 1993) in the form

$$\int\limits_{\mathbb{V}} \mathbf{S} : \mathbf{E}^\alpha \, \mathrm{d}\mathbb{V} = 0 \tag{4.33}$$

reduces the number of independent variables in the original functional to just two. The weak form of this modified (enhanced) functional is obtained with the Gateaux or directional derivative, leading to the total variation (Vu-Quoc and Tan, 2003)

$$\delta\Pi\left(\mathbf{u}, \mathbf{E}^\alpha\right) = \delta\Pi^{int} - \delta\Pi^{ext} \tag{4.34a}$$

$$\delta\Pi^{int} = \int\limits_{\mathbb{V}} \left(\delta\mathbf{E}^u + \delta\mathbf{E}^\alpha\right) : \frac{\partial W_s\left(\mathbf{E}^u + \mathbf{E}^\alpha\right)}{\partial\left(\mathbf{E}^u + \mathbf{E}^\alpha\right)} \, \mathrm{d}\mathbb{V} \tag{4.34b}$$

$$\delta\Pi^{ext} = \int\limits_{\mathbb{V}} \delta\mathbf{u} \cdot \hat{\mathbf{b}} \, \rho \, \mathrm{d}\mathbb{V} + \int\limits_{\mathbb{S}} \delta\mathbf{u} \cdot \hat{\mathbf{t}} \, \mathrm{d}\mathbb{S} \tag{4.34c}$$

The weak form can now be expanded via a truncated Taylor series about the solution (fixed point) at the nth state $\left(\mathbf{u}|_n, \mathbf{E}^\alpha|_n\right)$ (Bischoff and Ramm, 1997)

$$\delta\Pi\left(\mathbf{u}|_{n+1}, \mathbf{E}^\alpha|_{n+1}\right) \approx \delta\Pi\left(\mathbf{u}|_n, \mathbf{E}^\alpha|_n\right) + \mathcal{D}\left[\delta\Pi\right]\left(\mathbf{u}|_n, \mathbf{E}^\alpha|_n\right) \cdot \left(\Delta\mathbf{u}, \Delta\mathbf{E}^\alpha\right) \tag{4.35}$$

where, in the present context, the (Δ) operator points to a finite variation between (n) and ($n+1$) states.

The finite element interpolation for the enhanced strain field is described next, along with the explicit expression for the $\mathcal{D}\left[\delta\Pi\right]$ operator and the main advantages of including the additive approach as in (4.32).

4.2.2 Linearized discrete weak form

After the description of the interpolation functions and variables for both the displacement-based and enhanced strain fields for shell and solid-shell elements (Chapters 2 and 3, respectively), the second member of the right-hand side of the linearized weak form (4.35) can be rewritten (dropping the state and elemental indices) in the form

$$\mathcal{D}\left[\delta\Pi\right](\mathbf{d},\boldsymbol{\alpha})\cdot(\Delta\mathbf{d},\Delta\boldsymbol{\alpha}) = \frac{\partial\left(\delta\Pi^{int}-\delta\Pi^{ext}\right)}{\partial(\mathbf{d},\boldsymbol{\alpha})}\cdot(\Delta\mathbf{d},\Delta\boldsymbol{\alpha}) \tag{4.36}$$

as described, for instance, in the works of Bischoff and Ramm (1997); Klinkel and Wagner (1997); Klinkel *et al.* (1999) and Vu-Quoc and Tan (2003). Including the corresponding displacement and enhanced based interpolation, the variations in (4.36) take the form

$$\delta\Pi^{int}(\mathbf{d},\boldsymbol{\alpha}) = \delta\mathbf{d}^{\mathrm{T}}\int\limits_{\mathbb{V}}\left(\bar{\mathbf{M}}^{u}\right)^{\mathrm{T}}\bar{\mathbf{S}}\,\mathrm{d}\mathbb{V} + \delta\boldsymbol{\alpha}^{\mathrm{T}}\int\limits_{\mathbb{V}}\left(\bar{\mathbf{M}}^{\alpha}\right)^{\mathrm{T}}\bar{\mathbf{S}}\,\mathrm{d}\mathbb{V} \tag{4.37a}$$

$$\delta\Pi^{ext}(\mathbf{d}) = \delta\mathbf{d}^{\mathrm{T}}\int\limits_{\mathbb{V}}\mathbf{N}^{\mathrm{T}}\hat{\mathbf{b}}\,\rho\,\mathrm{d}\mathbb{V} + \delta\mathbf{d}^{\mathrm{T}}\int\limits_{\mathbb{S}}\mathbf{N}^{\mathrm{T}}\hat{\mathbf{t}}\,\mathrm{d}\mathbb{S} \tag{4.37b}$$

where the $\left(\bar{\mathbf{M}}^{\alpha}\right)$ matrix refer to the enhanced strain tensor in the *local frame* while, in the same way, $\left(\bar{\mathbf{S}}\right)$ points to the 2^{nd} Piola-Kirchhoff stress tensor also related to the local orthogonal frame.

Focusing on the variation of the internal part (4.37a) of the whole potential, it is possible to state that

$$\begin{aligned}\mathcal{D}\left[\delta\Pi^{int}\right]\cdot(\Delta\mathbf{d},\Delta\boldsymbol{\alpha}) =& \frac{\partial\left(\delta\Pi^{int}\right)}{\partial\mathbf{d}}\cdot\Delta\mathbf{d} + \frac{\partial\left(\delta\Pi^{int}\right)}{\partial\boldsymbol{\alpha}}\cdot\Delta\boldsymbol{\alpha}\\ =& \,\delta\mathbf{d}^{\mathrm{T}}\left[\left(\mathbf{K}_{uu}^{lg}+\mathbf{K}_{uu}^{nlg}\right)\Delta\mathbf{d}+\mathbf{K}_{u\alpha}\Delta\boldsymbol{\alpha}\right] \;+\\ &+\;\delta\boldsymbol{\alpha}^{\mathrm{T}}\left[\mathbf{K}_{\alpha u}\Delta\mathbf{d}+\mathbf{K}_{\alpha\alpha}\Delta\boldsymbol{\alpha}\right]\\ &(\forall\,\delta\mathbf{d}\,,\forall\,\delta\boldsymbol{\alpha})\end{aligned} \tag{4.38}$$

Linear and nonlinear geometric (initial stress) stiffness matrices ($\mathbf{K}_{uu}^{lg}$ and $\mathbf{K}_{uu}^{nlg}$, respectively) are defined as in a fully displacement-based formulation (Bathe, 1996), coming from the expressions defined in Chapters 2 and introduced in Chapter 3.

The main result of the inclusion of the enhanced parameters into the variational formulation is the appearance of the coupling stiffness matrices ($\mathbf{K}_{\alpha u},\mathbf{K}_{u\alpha}$), as well as the introduction of the fully-enhanced stiffness operator ($\mathbf{K}_{\alpha\alpha}$), all of them possessing the same structure as in the linear formulation of Simo and Rifai (1990).

In fact, the adopted additive approach (4.32) leads to a straightforward algorithmic extension from the linear case, with no inclusion of nonlinear geometric stiffness matrices associated with the enhanced variables, as happens in formulations based on the multiplicative enhancement of the deformation gradient, as in the works of Simo and Armero (1992) and Miehe (1998), among others. The final result (Bischoff and Ramm, 1997; Klinkel and Wagner, 1997; Klinkel *et al.*, 1999; Vu-Quoc and Tan, 2003) is then an equivalent system of equations, on matrix form, presented as

$$\begin{bmatrix} \left(\mathbf{K}_{uu}^{lg} + \mathbf{K}_{uu}^{nlg}\right) & \mathbf{K}_{u\alpha} \\ \mathbf{K}_{\alpha u} & \mathbf{K}_{\alpha\alpha} \end{bmatrix} \begin{Bmatrix} \Delta\mathbf{d} \\ \Delta\boldsymbol{\alpha} \end{Bmatrix} = \begin{Bmatrix} \int\limits_{\mathbb{V}} \mathbf{N}^{\mathrm{T}} \bar{\mathbf{b}}\, \rho \, \mathrm{d}\mathbb{V} + \int\limits_{\mathbb{S}} \mathbf{N}^{\mathrm{T}} \bar{\mathbf{t}} \, \mathrm{d}\mathbb{S} - \int\limits_{\mathbb{V}} \left(\bar{\mathbf{M}}^{u}\right)^{\mathrm{T}} \bar{\mathbf{S}} \, \mathrm{d}\mathbb{V} \\ -\int\limits_{\mathbb{V}} \left(\bar{\mathbf{M}}^{\alpha}\right)^{\mathrm{T}} \bar{\mathbf{S}} \, \mathbf{d}\mathbb{V} \end{Bmatrix} \tag{4.39}$$

The internal force vectors related to displacement and enhanced fields, ($\int\limits_{\mathbb{V}} \left(\bar{\mathbf{M}}^{u}\right)^{\mathrm{T}} \bar{\mathbf{S}} \, \mathrm{d}\mathbb{V}$, $\int\limits_{\mathbb{V}} \left(\bar{\mathbf{M}}^{\alpha}\right)^{\mathrm{T}} \bar{\mathbf{S}} \, \mathrm{d}\mathbb{V}$,) come from the discrete form of equation (4.34b). Also, no coupling between the two enhanced strain field appears in the equivalent expression (4.39), and the two fields can be treated altogether in the implementation.

As was seen in Chapters 2 and 3, the enhanced strain interpolation matrices $\left(\mathbf{M}^{\alpha}, \mathbf{M}^{\beta}, \mathbf{M}^{\gamma}\right)$, defined in the convective frame, pass the primary design condition originally imposed by Simo and Rifai (1990)

$$\int_{\square} \mathbf{M}^{\alpha}(\xi^1, \xi^2) \, \mathrm{d}\xi^1 \mathrm{d}\xi^2 = \mathbf{0}; \ \int_{\square} \mathbf{M}^{\beta}(\xi^1, \xi^2) \, \mathrm{d}\xi^1 \mathrm{d}\xi^2 = \mathbf{0}; \ \int_{\square} \mathbf{M}^{\gamma}(\xi^1, \xi^2, \xi^3) \, \mathrm{d}\xi^1 \mathrm{d}\xi^2 \mathrm{d}\xi^3 = \mathbf{0} \tag{4.40}$$

for the presented shell (α and β enhancement type) and solid-shell elements (γ enhancement type), respectively. Before their use in the overall system of equations (4.39), the enhanced matrices need, however, to be transformed onto the local reference frame. This is accomplished in the way proposed by Simo and Rifai (1990) (and subsequently in Simo and Armero (1992) and Simo *et al.* (1993)), evaluating the already defined transformation matrix $\left({}^{l}_{c}\mathbf{T}\right)$ both in the element's center $\left(\xi^1 = \xi^2 = \xi^3 = 0\right)$ and in the analyzed Gauss point itself $\left(\xi^1, \xi^2, \xi^3\right)$. The enhanced strain-displacement matrix in the local frame can be then stated in the form

$$\bar{\mathbf{M}}^{\alpha}(\xi^1, \xi^2, \xi^3) = \frac{\det {}^{l}_{c}\mathbf{T}_{\mathbf{0}}}{\det {}^{l}_{c}\mathbf{T}_{\boldsymbol{\xi}}} \, {}^{l}_{c}\mathbf{T}_{\mathbf{0}} \, \mathbf{M}^{\alpha}(\xi^1, \xi^2) \tag{4.41a}$$

$$\bar{\mathbf{M}}^{\beta}(\xi^1, \xi^2, \xi^3) = \frac{\det {}^{l}_{c}\mathbf{T}_{\mathbf{0}}}{\det {}^{l}_{c}\mathbf{T}_{\boldsymbol{\xi}}} \, {}^{l}_{c}\mathbf{T}_{\mathbf{0}} \, \mathbf{M}^{\beta}(\xi^1, \xi^2) \tag{4.41b}$$

$$\bar{\mathbf{M}}^{\gamma}(\xi^1, \xi^2, \xi^3) = \frac{\det {}^{l}_{c}\mathbf{T}_{\mathbf{0}}}{\det {}^{l}_{c}\mathbf{T}_{\boldsymbol{\xi}}} \, {}^{l}_{c}\mathbf{T}_{\mathbf{0}} \, \mathbf{M}^{\gamma}(\xi^1, \xi^2, \xi^3) \tag{4.41c}$$

where

$${}^{l}_{c}\mathbf{T}_{\mathbf{0}} = {}^{l}_{c}\mathbf{T}(0,0,0) \ \text{and} \ {}^{l}_{c}\mathbf{T}_{\boldsymbol{\xi}} = {}^{l}_{c}\mathbf{T}\left(\xi^1, \xi^2, \xi^3\right) \tag{4.42}$$

This transformation is supposed to grant the satisfaction of the patch-test over a single element, for a general-purpose distorted configurations.

4.3 Constitutive update algorithms

In this section, it is explicitly defined the return algorithm implemented for the elasto-plasticity constitutive behavior simulation. An isotropic model of von Mises with isotropic hardening was initially taken into account. This choice of characteristics for the constitutive model is motivated by its spread use in the elasto-plastic evaluation of new finite elements.

The numerical implementation of constitutive models for the proposed shell elements is straightforward, benefiting from the imposition of a plane-stress behavior, a common assumption in the analysis of thin-shell structures. The algorithm details of implementation follow the classical works of Ramm and Matzenmiller (1988) and Brank *et al.* (1997), the starting point of the predictor-corrector procedure of return mapping is equation (4.27), and the overall procedure is described in Boxes 3.2 and 3.3 in the end of this Section.

The simplicity of this algorithm comes from the imposition of the plane-stress condition directly into the formulation, turning the first and second derivative of the yield (loading) function $\left({}^{n+1}Y\right)$, related to the stress field, a simple task. In fact, implicit in the steps on Boxes 3.2 and (mainly) 3.3, it is defined that

$$\frac{\partial\left({}^{n+1}Y\right)}{\partial\bar{\boldsymbol{\sigma}}} = \mathbf{P}\bar{\sigma} \tag{4.43}$$

and

$$\frac{\partial^2\left({}^{n+1}Y\right)}{\partial\bar{\boldsymbol{\sigma}}^2} = \mathbf{P} \tag{4.44}$$

where the $(\mathbf{P})$ matrix components are constants in the form

$$\mathbf{P} = \begin{bmatrix} {}^2\!/\!_3 & & & & \textit{symm.} \\ -{}^1\!/\!_3 & {}^2\!/\!_3 & & & \\ 0 & 0 & 2 & & \\ 0 & 0 & 0 & 2 & \\ 0 & 0 & 0 & 0 & 2 \end{bmatrix} \tag{4.45}$$

Additionally, in Box 3.2, the calculation of the trial (supposed elastic) stress increment is performed on the intermediate point $\left(n+\frac{1}{2}\right)$ between the converged state (n) and the current step $(n+1)$, at a given iteration. To do so, the total incremental-iterative displacement and internal variables field (accumulated from the converged state) is considered. For the particular case of the presented shell elements, this implies the obtaining of the equivalent (additive-type) total rotation degrees-of-freedom within the analyzed step, in a way referred to in Chapter 2. The use of the approximated strain increments at the mid-step is in conformity with the conclusions of Hughes (1984), who established that the constitutive (discrete) analysis over point $\left(n+\frac{1}{2}\right)$ represents a second-order approximation to the exact integration of the instantaneous rate of strain, between states (n) and $(n+1)$.

For the three-dimensional constitutive implementation suitable for the *HCiS12* solid-shell element, the adopted procedures followed those described in the *FEAP* finite element program theory manual (Taylor, 2003). The general aspects are close to those described for the plane-stress based algorithm for the shell elements in Boxes 3.2 and 3.3.

Nevertheless, main differences remain in the first and second derivatives of the yield function, relative to the local (rotated) Cauchy stress tensor (counterpart of equations (4.43) and (4.44) for the plane-stress hypothesis). The starting point is the (local) deviatoric stress field components, defined in the form (Alves de Sousa, 2003c)

$$\bar{s}_{ij} = \bar{\sigma}_{ij} - \frac{1}{3}\,\bar{\sigma}_{ij}\,\delta_{ij} \tag{4.46}$$

for the Kronecker-delta operator

$$\begin{aligned} \delta_{ij} &= 1 \text{ , if } i = j \\ &= 0 \text{ , if } i \neq j \end{aligned} \tag{4.47}$$

The second invariant of the deviatoric stress field can be stated as

$$J_2 = \frac{1}{2}\bar{s}_{ij}\,\bar{s}_{ji} \tag{4.48}$$

From the definition of the invariants, the scalar (J_2) is kept unchanged irrespective of the reference frame for the stress field. The algorithm is then complete with the calculation of the first and second derivatives of the yield function, simply defined as

$$\frac{\partial\left({}^{n+1}Y\right)}{\partial\bar{\boldsymbol{\sigma}}} = \frac{1}{2\sqrt{J_2}}\left\{\begin{array}{cccccc} \bar{s}_{11} & \bar{s}_{22} & \bar{s}_{33} & \bar{s}_{12} & \bar{s}_{13} & \bar{s}_{23} \end{array}\right\}^{\mathrm{T}} \tag{4.49}$$

and

$$\frac{\partial^2\left({}^{n+1}Y\right)}{\partial\bar{\boldsymbol{\sigma}}^2} =$$

$$= \frac{\sqrt{3}}{2\sqrt{J_2}}\begin{bmatrix} \frac{2}{3}-\frac{\bar{s}_{11}\bar{s}_{11}}{2J_2} & -\frac{1}{3}-\frac{\bar{s}_{11}\bar{s}_{22}}{2J_2} & -\frac{1}{3}-\frac{\bar{s}_{11}\bar{s}_{33}}{2J_2} & -\frac{\bar{s}_{11}\bar{s}_{12}}{J_2} & -\frac{\bar{s}_{11}\bar{s}_{13}}{J_2} & -\frac{\bar{s}_{11}\bar{s}_{23}}{J_2} \\ & \frac{2}{3}-\frac{\bar{s}_{22}\bar{s}_{22}}{2J_2} & -\frac{1}{3}-\frac{\bar{s}_{22}\bar{s}_{33}}{2J_2} & -\frac{\bar{s}_{22}\bar{s}_{12}}{J_2} & -\frac{\bar{s}_{22}\bar{s}_{13}}{J_2} & -\frac{\bar{s}_{22}\bar{s}_{23}}{J_2} \\ & & \frac{2}{3}-\frac{\bar{s}_{33}\bar{s}_{33}}{2J_2} & -\frac{\bar{s}_{33}\bar{s}_{12}}{J_2} & -\frac{\bar{s}_{33}\bar{s}_{13}}{J_2} & -\frac{\bar{s}_{33}\bar{s}_{23}}{J_2} \\ & & & 2-\frac{2\bar{s}_{12}\bar{s}_{12}}{J_2} & -\frac{2\bar{s}_{12}\bar{s}_{13}}{J_2} & -\frac{2\bar{s}_{12}\bar{s}_{23}}{J_2} \\ & \text{symmetric} & & & 2-\frac{2\bar{s}_{13}\bar{s}_{13}}{J_2} & -\frac{2\bar{s}_{13}\bar{s}_{23}}{J_2} \\ & & & & & 2-\frac{2\bar{s}_{23}\bar{s}_{23}}{J_2} \end{bmatrix} \tag{4.50}$$

respectively.

For the specific case of the shell elements proposed in the present work, the thickness update is performed enforcing the plane-stress condition over each Gauss point. Therefore, thickness values relative to the interpolation points within an element are obtained and afterwards extrapolated to each node pertaining to the mentioned element. The process is carried out as follows (Yoon *et al.*, 1999). After calculation of the updated stress field at the material cycle described, updated thickness strain values are obtained from the elastic (isotropic) material properties along with the equilibrated (at the material level) plastic strain field components in the form

$$\bar{E}_{\xi^3\xi^3} = -\frac{\nu}{E}\left({}^{n+1}\bar{\sigma}_{\xi^1\xi^1} + {}^{n+1}\bar{\sigma}_{\xi^2\xi^2}\right) - \left({}^{n+1}\bar{E}^p_{\xi^1\xi^1} + {}^{n+1}\bar{E}^p_{\xi^2\xi^2}\right) \tag{4.51}$$

and the updated thickness value at this point is given by

$$^{n+1}a\left(\xi^1,\xi^2,\xi^3\right) = \exp\left(\vartheta\right) {}^{n}a\left(\xi^1,\xi^2,\xi^3\right) \tag{4.52}$$

where $\left({}^{n+1}a\right)$ and $\left({}^{n}a\right)$ are the current (updated) and converged values of the thickiness at Gauss point $\left(\xi^1,\xi^2,\xi^3\right)$. The factor (ϑ) corresponds to the integral (summation) of the normal out-of-plane strain component, along the thickness direction $\left(\xi^3\right)$, in the form

$$\vartheta \equiv \vartheta\left(\xi^1,\xi^2\right) = \int\limits_{\xi^3} \bar{E}_{\xi^3\xi^3}\left(\xi^1,\xi^2,\xi^3\right) \mathrm{d}\xi^3 \tag{4.53}$$

Box 4.2. Return-Mapping Algorithm for the von Mises Plasticity Model (1)

i. Trial (elastic) incremental material stress tensor in the local frame

$${}^{n+1}_{\;n}\bar{\mathbf{S}} = \bar{\mathbf{C}}\left(\underbrace{{}^{n+1}\bar{\mathbf{E}}^{u} + {}^{n+1}\bar{\mathbf{E}}^{\alpha}}_{{}^{n+1}\bar{\mathbf{E}}} - {}^{n}\bar{\mathbf{E}}^{p}\right) \equiv {}^{n+1}_{\;n}\bar{\mathbf{S}}^{\,trial}$$

Remark: The strain fields are derived from the mid-point configuration-based strain-displacement matrices

$${}^{n+\frac{1}{2}}_{\;n}\bar{\mathbf{M}}^{u}\,;\; {}^{n+\frac{1}{2}}_{\;n}\bar{\mathbf{M}}^{\alpha}$$

ii. Trial (elastic) incremental Cauchy stress tensor in the local frame

$${}^{n+1}_{\;n}\bar{\boldsymbol{\sigma}}^{\,trial} \equiv {}^{n+1}_{\;n}\bar{\mathbf{S}}^{\,trial}$$

iii. Update of the (co-rotational) Cauchy stress tensor

$${}^{n+1}\bar{\boldsymbol{\sigma}}^{\,trial} = {}^{n}\bar{\boldsymbol{\sigma}} + {}^{n+1}_{\;n}\bar{\boldsymbol{\sigma}}^{\,trial}$$

iv. Evaluation of the yield function

$${}^{n+1}Y^{\,trial} = \frac{1}{2}\left({}^{n+1}\bar{\boldsymbol{\sigma}}^{\,trial}\right)^{\mathrm{T}} \mathbf{P} \left({}^{n+1}\bar{\boldsymbol{\sigma}}^{\,trial}\right) - \frac{1}{3}\left(\sigma_y\left({}^{n+1}\epsilon^{p}\right)\right)^2$$

based on the effective plastic strain value

$${}^{n+1}\epsilon^{p} = {}^{n}\epsilon^{p}$$

and on the correspondent strain-induced isotropic hardening law

$$\sigma_y\left({}^{n+1}\epsilon^{p}\right) = \sigma_{y0} + \mathsf{H}_{\mathsf{iso}}\,{}^{n+1}\epsilon^{p}$$

v. Check for plasticity onset

```
IF $\left({}^{n+1}Y^{\,trial} \leq 0\right)$ THEN
    ${}^{n+1}\bar{\boldsymbol{\sigma}} = {}^{n+1}\bar{\boldsymbol{\sigma}}^{\,trial}$
    EXIT
ELSEIF $\left({}^{n+1}Y^{\,trial} > 0\right)$ THEN
    GOTO Box 4.3
ENDIF
```

Box 4.3. Return-Mapping Algorithm for the von Mises Plasticity Model (2)

i. Determination of the plastic multiplier (λ) through the closed cycle on (k)

initialize variables: $\left(k = 0;\ \lambda_k = 0;\ \lambda_{k+1} = 1;\ \mathrm{TOLER} = 10^{-7}\right)$

$$\text{DO WHILE}\ \left(\frac{\lambda_{k+1}-\lambda_k}{\lambda_{k+1}}\right) > \ \text{TOLER}$$

starting with the yield condition as a function of (λ_k)

$${}^{n+1}Y\left(\lambda_k\right) = \ldots$$

for a corrected effective plastic strain in the form

$${}^{n+1}\epsilon^p = {}^{n}\epsilon^p + \lambda_k\left(\sqrt{\tfrac{2}{3}\left({}^{n+1}\bar{\boldsymbol{\sigma}}^{\mathrm{T}}\,\mathbf{P}\,{}^{n+1}\bar{\boldsymbol{\sigma}}\right)}\right)$$

evaluate the derivative

$$\frac{d\,{}^{n+1}Y}{d\lambda_k} = \left(1-\left(\frac{2}{3}\right)^{1.5}\sigma_y\left({}^{n+1}\epsilon^p\right)\frac{d\sigma_y\left({}^{n+1}\epsilon^p\right)}{d\,{}^{n+1}\epsilon^p}\frac{\lambda_k}{\sqrt{\bar{\boldsymbol{\sigma}}^{\mathrm{T}}\,\mathbf{P}\,\bar{\boldsymbol{\sigma}}}}\right)\frac{d\left(\frac{1}{2}\bar{\boldsymbol{\sigma}}^{\mathrm{T}}\,\mathbf{P}\,\bar{\boldsymbol{\sigma}}\right)}{d\lambda_k} \ -$$

$$-\ \left(\frac{2}{3}\right)^{1.5}\sigma_y\left({}^{n+1}\epsilon^p\right)\frac{d\sigma_y}{d\,{}^{n+1}\epsilon^p}\sqrt{\bar{\boldsymbol{\sigma}}^{\mathrm{T}}\,\mathbf{P}\,\bar{\boldsymbol{\sigma}}}$$

now it is possible to perform the plastic multiplier update

$$\lambda_{k+1} = \lambda_k - \frac{{}^{n+1}Y\left(\lambda_k\right)}{\left(\frac{d\,{}^{n+1}Y(\lambda_k)}{d\lambda_k}\right)};\ \lambda = \lambda_{k+1}$$

update the iteration counter ($k = k+1$)

ENDDO

ii. Evaluate the algorithmic tangent modulus

$$\bar{\mathbf{C}}^a = \left(\bar{\mathbf{C}}^{-1} + \lambda\mathbf{P}\right)^{-1}$$

iii. Definition of the updated (plastic) Cauchy stress tensor in the local frame

$${}^{n+1}\bar{\boldsymbol{\sigma}} = \bar{\mathbf{C}}^a\left({}^{n+1}\bar{\mathbf{E}}^u + {}^{n+1}\bar{\mathbf{E}}^\alpha - {}^{n}\bar{\mathbf{E}}^p\right)$$

iv. Update the Green-Lagrange plastic strain tensor

$${}^{n+1}\bar{\mathbf{E}}^p = {}^{n}\bar{\mathbf{E}}^p + \lambda\mathbf{P}\,{}^{n+1}\bar{\boldsymbol{\sigma}}$$

v. Update the effective plastic strain

$${}^{n+1}\epsilon^p = {}^{n}\epsilon^p + \lambda\left(\sqrt{\tfrac{2}{3}\left({}^{n+1}\bar{\boldsymbol{\sigma}}^{\mathrm{T}}\,\mathbf{P}\,{}^{n+1}\bar{\boldsymbol{\sigma}}\right)}\right)$$

vi. Evaluate the consistent elasto-plastic constitutive operator

$$\bar{\mathbf{C}}^p = \bar{\mathbf{C}}^a - \frac{\left(\bar{\mathbf{C}}^a\mathbf{P}\,{}^{n+1}\bar{\boldsymbol{\sigma}}\right)\left({}^{n+1}\bar{\boldsymbol{\sigma}}^{\mathrm{T}}\mathbf{P}\bar{\mathbf{C}}^a\right)}{A + \left({}^{n+1}\bar{\boldsymbol{\sigma}}^{\mathrm{T}}\mathbf{P}\bar{\mathbf{C}}^a\mathbf{P}\,{}^{n+1}\bar{\boldsymbol{\sigma}}\right)}$$

where

$$A = \frac{4}{9}\left[\frac{\sigma_y\left({}^{n+1}\epsilon^p\right)^2\,\frac{d\sigma_y\left({}^{n+1}\epsilon^p\right)}{d\,{}^{n+1}\epsilon^p}}{1-\frac{2}{3}\lambda\frac{d\sigma_y\left({}^{n+1}\epsilon^p\right)}{d\,{}^{n+1}\epsilon^p}}\right]$$

4.4 The arc-length path-following technique

4.4.1 General aspects

In dealing with the analysis of shell structures, the possible occurrence of structural instabilities must be accounted for. On the viewpoint of the numerical simulation process, this is equivalent to the tracing of load-displacement paths for problems with possible zero or negative tangent stiffness matrices. In summary, the use of particular path-following techniques would be desirable for situations where a conventional Newton-Raphson incremental-iterative technique, simply based on load-level control, fail.

The first (and simpler approach) to force the incremental-iterative algorithm to pass limit points (corresponding to maximum and minimum load bounds) was the switch to a displacement control advance technique (Sabir and Lock, 1972; Batoz and Dhatt, 1979). Although efficient in reproducing load-deflection curves with the presence of "snap-through" zones, this path-following approach fails in situations where "snap-back" behaviour appears (Crisfield, 1997, volume 1).

A general algorithm, suitable for handling the two before-referred situations, would be the so-called "arc-length" continuation method, presented in commercial finite element programs and also implemented by the author within the present work. Loosely speaking, the method "extend" the displacement-based equilibrium equation (driver of the conventional Newton-Raphson approach), in order to account for the linear distance between two successive points in the load-deflection nonlinear path. This linear distance is taken as the radius of a cylinder, out of the plane defined by the load-deflection curve (and with the center in the known configuration), intersecting the load-deflection plane in the desired (next iteration or increment) point [1].

The roots of the arc-length method appeared in the early developments of the Riks algorithm (Wempner, 1971; Riks, 1972, 1979). Its current formalism came thereafter with the works of Crisfield (1981, 1983), and after that with the contributions of Powell and Simons (1981), Ramm (1981, 1982), Bathe and Dvorkin (1983), Watson and Holzer (1983), Simo *et al.* (1984), Gierlinski and Graves-Smith (1985), César de Sá (1986), Schweizerhof and Wriggers (1986), Forde and Sttemer (1987), Belleni and Chulya (1987), Clarke and Hancock (1990) and more recently by the works of Barbosa (1992), Huang and Atluri (1995), Vila *et al.* (1995), Feng *et al.* (1996), Feng *et al.* (1997), Hellweg and Crisfield (1998), Widjaja (1998), Szyszkowski and Husband (1999) and de Souza Neto and Feng (1999), providing developments on prediction and convergence capabilities over the original

---

[1] Implicit on this statement is the implementation, in the present work, of the "cylindrical version" of the arc-length method, as devised in the works of Crisfield, within the frame of proportional loading.

version.

A survey of the method can also be found in the book of Crisfield (1997, volume 1) and in the work of Riks (1992). In the following, the main relevant points for implementation are highlighted.

For a load increment (state) $(n+1)$, at equilibrium iteration $(i+1)$, the nodal displacement vector $\left({}^{n+1}\mathbf{d}^{i+1}\right)$ coming from the Newton-Raphson method can be given as

$$ {}^{n+1}\mathbf{d}^{i+1} = {}^{n}\mathbf{d} + {}^{n+1}_{\;\;n}\mathbf{d}^{i+1} \tag{4.54} $$

thus involving the known converged displacement vector at state (n) – $({}^{n}\mathbf{d})$ – along with the iterative variation on the latter, from the first to the last iteration within the increment, in the form

$$ {}^{n+1}_{\;\;n}\mathbf{d}^{i+1} = {}^{n+1}_{\;\;n}\mathbf{d}^{i} + \delta\mathbf{d} \tag{4.55} $$

where $(\delta\mathbf{d})$ is the iterative displacement vector, solution of the linearized residual equation

$$ \mathbf{K}\left({}^{n+1}\mathbf{d}^{i}\right)\delta\mathbf{d} = -\mathbf{r}\left({}^{n+1}\mathbf{d}^{i}, {}^{n}\rho + {}^{n+1}_{\;\;n}\rho\right) \tag{4.56} $$

with the residual vector $(\mathbf{r})$ being subjected to the nonlinear constraint

$$ \mathbf{r}\left({}^{n+1}\mathbf{d}^{i}, {}^{n}\rho + {}^{n+1}_{\;\;n}\rho\right) = \mathbf{F}^{i}\left({}^{n+1}\mathbf{d}^{i}\right) - \left({}^{n}\rho + {}^{n+1}_{\;\;n}\rho\right)\mathbf{F}^{e} = \mathbf{0} \tag{4.57} $$

involving the equilibrium between the internal force vector $\left(\mathbf{F}^{i}\right)$ and the external force vector $(\mathbf{F}^{e})$, affected by the load factor $\left({}^{n}\rho + {}^{n+1}_{\;\;n}\rho\right)$, which is fully attained after the convergence in $(n+1)$ configuration. In the equations before, it is implicit the influence of the enhanced assumed strain internal variables either in the overall stiffness matrix $(\mathbf{K})$ or in the internal force vector $\left(\mathbf{F}^{i}\right)$, as shown in the system of equations (4.39). Therefore, the representation of the internal force vector as function of the displacement field alone in (4.57) points to the condensed form of the equilibrium equations, which retain the formal structure of those coming from a single-field (displacement-based) functional. Nevertheless, this simplified representation is useful since the implementation of the arc-length path-following procedure relies in the displacement-load vectorial space.

For a fixed referential external load vector $(\mathbf{F}^{e})$, if the load level parameter $\left({}^{n}\rho + {}^{n+1}_{\;\;n}\rho\right)$ is considered fixed (and known) in advance, one comes to a conventional load control advance procedure in the Newton-Raphson algorithm. The arc-length method, however, treats this increment (better to say, its iterative variation $(\delta\rho)$) as a primary variable of the nonlinear problem, being the value of $\left({}^{n+1}_{\;\;n}\rho\right)$ unknown at the beginning of the increment.

Once a new variable is introduced in the system, a new constraint equation is needed. Considering again a given iteration (i) in the load-displacement path, focusing on the iterative displacement vector $\left({}^{n+1}_{\;\;n}\mathbf{d}^i\right)$ and the corresponding iterative load factor $\left({}^{n+1}_{\;\;n}\rho^i\right)$, it is possible to define the linear distance from the converged state (n) up to (i), in the load-displacement space, as (Crisfield, 1981, 1983)

$$l^2 = \left({}^{n+1}_{\;\;n}\mathbf{d}^i\right)^{\mathrm{T}}\, {}^{n+1}_{\;\;n}\mathbf{d}^i + \psi^2 \left({}^{n+1}_{\;\;n}\rho^i\right)^2 \left(\mathbf{F}^e\right)^{\mathrm{T}} \mathbf{F}^e \tag{4.58}$$

This extra constraint to the residual one (4.57) thus limit the length of the incremental solution which, in turn, is an approximation to the incremental arc length. For a fixed (desired) length value, the load parameter iterative variation can then be calculated. The weighting parameter $\left(\psi^2\right)$ scales the contribution of either the incremental displacements and loads (de Souza Neto and Feng, 1999; Crisfield, 1997). In this sense, equation (4.58) is general and is characteristic of the *spherical* version of the arc-length method. For the more widely used *cylindrical* arc-length method (adopted in the present work), the weighting parameter is just set to zero and the constraint equation turns out to be simply given by

$$\left({}^{n+1}_{\;\;n}\mathbf{d}^i\right)^{\mathrm{T}}\, {}^{n+1}_{\;\;n}\mathbf{d}^i = l^2 \quad \therefore \quad \left({}^{n+1}_{\;\;n}\mathbf{d}^i\right)^{\mathrm{T}}\, {}^{n+1}_{\;\;n}\mathbf{d}^i - l^2 = 0 \tag{4.59}$$

Having specifying the required length (l), it is possible to linearize the residual constraint (4.57) altogether with the length constraint (4.59) via a truncated Taylor series, leading to a linearized system of equations (for the cylindrical version of the arc-length method) in the form

$$\begin{bmatrix} \mathbf{K}\left({}^{n+1}\mathbf{d}^i\right) & -\mathbf{F}^e \\ 2\left({}^{n+1}_{\;\;n}\mathbf{d}^i\right)^{\mathrm{T}} & 0 \end{bmatrix} \begin{Bmatrix} \delta\mathbf{d} \\ \delta\rho \end{Bmatrix} = -\begin{Bmatrix} \mathbf{r}\left({}^{n+1}\mathbf{d}^i, {}^{n}\rho + {}^{n+1}_{\;\;n}\rho^i\right) \\ \left({}^{n+1}_{\;\;n}\mathbf{d}^i\right)^{\mathrm{T}}\, {}^{n+1}_{\;\;n}\mathbf{d}^i - l^2 \end{Bmatrix} \tag{4.60}$$

for the iterative displacement and load factor variations $(\delta\mathbf{d},\, \delta\rho)$, respectively.

In practice, and once the "equivalent" stiffness matrix in (4.60) is neither symmetric nor banded, it is more convenient to adopt a non-consistent scheme (de Souza Neto and Feng, 1999), where the original augmented system of equations to be solved at each iteration is replaced by the decoupled equations

$$\begin{bmatrix} \mathbf{K}\left({}^{n+1}\mathbf{d}^i\right) & -\mathbf{F}^e \end{bmatrix} \begin{Bmatrix} \delta\mathbf{d} \\ \delta\rho \end{Bmatrix} = -\mathbf{r}\left({}^{n+1}\mathbf{d}^i, {}^{n}\rho + {}^{n+1}_{\;\;n}\rho^i\right) \tag{4.61}$$

along with the direct enforcement of restriction (4.59) for iteration $(i+1)$ (Batoz and Dhatt, 1979)

$$\left({}^{n+1}_{\;\;n}\mathbf{d}^{i+1}\right)^{\mathrm{T}}\, {}^{n+1}_{\;\;n}\mathbf{d}^{i+1} = l^2 \tag{4.62}$$

Equation (4.61) is equivalent to the introduction of a load factor perturbation $(\delta\rho)$ into the residual constraint (4.57), which then turns to be the unbalanced vector $\left\{\mathbf{r}\left({}^{n+1}\mathbf{d}^i, {}^{n}\rho + {}^{n+1}_{\;\;n}\rho + \delta\rho\right)\right\}$.

Directly from equation (4.61), the iterative displacement vector ($\delta\mathbf{d}$) can be split into two parts, in the form (de Souza Neto and Feng, 1999)

$$\delta\mathbf{d} = \delta\mathbf{d}^* + \delta\rho\,\delta\bar{\mathbf{d}} \tag{4.63}$$

where the iterative vector ($\delta\mathbf{d}^*$) comes directly from the Newton-Raphson procedure for the load controlled path-following method

$$\delta\mathbf{d}^* = -\mathbf{K}^{-1}\mathbf{r} \tag{4.64}$$

and $\left(\delta\bar{\mathbf{d}}\right)$ is the tangential solution for the reference (external) load

$$\delta\bar{\mathbf{d}} = \mathbf{K}^{-1}\mathbf{F}^e \tag{4.65}$$

Substituting equation (4.63) into (4.55), together with the constraint (4.62), will lead to the scalar quadratic equation

$$a\delta\rho^2 + b\delta\rho + c = 0 \tag{4.66}$$

where the real coefficients are given as

$$a = \delta\bar{\mathbf{d}}^{\mathrm{T}}\,\delta\bar{\mathbf{d}} \tag{4.67a}$$

$$b = 2\left({}^{n+1}_{\;\;n}\mathbf{d}^i + \delta\bar{\mathbf{d}}^*\right)^{\mathrm{T}}\delta\bar{\mathbf{d}} \tag{4.67b}$$

$$c = \left({}^{n+1}_{\;\;n}\mathbf{d}^i + \delta\bar{\mathbf{d}}^*\right)^{\mathrm{T}}\left({}^{n+1}_{\;\;n}\mathbf{d}^i + \delta\bar{\mathbf{d}}^*\right) - l^2 \tag{4.67c}$$

Solving of equation (4.66) will give, at best, two possible real roots that can be used in the iterative update of the load level, and one of them must be chosen (as shown in the next section). After that decision point, the load level can be finally obtained for iteration $(i+1)$ as

$${}^{n+1}_{\;\;n}\rho^{i+1} = {}^{n+1}_{\;\;n}\rho^i + \delta\rho \tag{4.68}$$

as well as the corresponding nodal displacement vector (4.55)

$${}^{n+1}_{\;\;n}\mathbf{d}^{i+1} = {}^{n+1}_{\;\;n}\mathbf{d}^i + \delta\mathbf{d}$$

and the constraint condition applied to the residual force vector is evaluated

$$\mathbf{r}\left({}^n\mathbf{d} + {}^{n+1}_{\;\;n}\mathbf{d}^i + \delta\mathbf{d}\,,\, {}^n\rho + {}^{n+1}_{\;\;n}\rho^i + \delta\rho\right) = \mathbf{0} \tag{4.69}$$

The whole calculations are repeated and iterations are carried out until equation (4.69) is satisfied.

4.4.2 Implementation details

Load level and arc-length for the first increment, first iteration

In the predictor phase of the first increment of the analysis, the initial value of the load level, to be imposed over the reference external load vector, can be simply given in the form

$$\delta\rho = + \frac{l}{\sqrt{\delta\bar{\bar{\mathbf{d}}}^{\mathrm{T}}\,\delta\bar{\bar{\mathbf{d}}}}} \tag{4.70}$$

as a function of an arc-length value, given by the user, and valid for the first increment $\left(l \equiv {}_{0}^{1}l\right)$. This expression can be further used for the predictor phase of any new increment, where the (+) sign on the right-hand side of equation (4.70) is replaced by a (±) choice (as detailed in the following).

Nevertheless, for this equation to be valid, it is necessary to specify the initial arc length value. This parameter is characteristic of each particular problem, not being, therefore, known in advance by the user. In order to overcome this question, in the present work it is assumed that the analysis starts as a load-controlled advancing procedure, being the incremental load a specific fraction of the total one. Doing so, the initial guess of the arc-length value is simply obtained from equation (4.70) in the form

$${}_{0}^{1}l = \delta\rho\sqrt{\delta\bar{\bar{\mathbf{d}}}^{\mathrm{T}}\,\delta\bar{\bar{\mathbf{d}}}} \tag{4.71}$$

where it is implicit the assumption of $(0 < \delta\rho \leq 1.0)$. Within this imposed initial load increment, the arc-length obtained in (4.71) is kept constant, and the iterative process is conducted. If convergence is not attained, the load level imposed is simply reduced to a half. On the other side, if convergence is attained, the arc-length value is updated for the next increment, depending on the comparison between the number of desired iterations on the increment (given by the user) and the actual number of iterations just performed by the algorithm, following the relation (Ramm, 1981, 1982), (Crisfield, 1997, volume 1)

$${}_{n}^{n+1}l = \sqrt{\frac{N_{opt}}{N_{act}}}\ \left({}_{n-1}^{n}l\right) \tag{4.72}$$

where $\left({}_{n-1}^{n}l\right)$ and $\left({}_{n}^{n+1}l\right)$ are the previously used and predicted (next) arc-length values, respectively. This criterion of adjustment of the arc-length is nevertheless used in the whole numerical simulation.

Upper and lower bounds for the arc-length values

In order to control the evolution of the numerical solution provided by the algorithm, it is useful to provide upper and lower bounds for the arc-length value, from one increment to the other. After the recalculation at the end of a given step – in the way suggested in equation (4.72), this value is compared with those bounds, in order not to allow severe drifts (and, consequently, losses in convergence) in subsequent steps. The maximum (l_{max}) and minimum (l_{min}) bounds specification is somewhat arbitrary and, to some extent, problem dependent. Nevertheless, in the present work the adopted solution is a function of the adopted arc-length in the first successfully converged increment, that is, $\left({}^{1}_{0}l\right)$ in equation (4.71), in the form

$$(l_{max}) = 3.0\ {}^{1}_{0}l \tag{4.73a}$$

$$(l_{min}) = 0.01\ {}^{1}_{0}l \tag{4.73b}$$

These limit values are those adopted in the examples covered in Chapter 5.

Sign and value of the load level prediction for a new increment

After the update of the arc-length value for a new increment, it is necessary to compute the corresponding increment in the load level. In this predictor state $(i = 0)$, and for a increment other than the first, equation (4.70) is correctly written in the form

$$\delta\rho = \pm \frac{l}{\sqrt{\delta\bar{\mathbf{d}}^{\mathrm{T}}\,\delta\bar{\mathbf{d}}}} \tag{4.74}$$

The problem that now arises is the proper choice of the sign to be used in equation (4.74), in order to define the path to be covered by the algorithm in the beginning of a new increment. Usual undertaken procedures are the evaluation of the sign of the current tangent stiffness determinant and the sign coming from the calculation of the incremental work. The common point between these two approaches is the fact that both methods rely on information of just the current equilibrium point (in the beginning of the increment). As pointed out by de Souza Neto and Feng (1999), the choice of the sign for $(\delta\rho)$ takes no account for the previous history of the solution path, which may lead to erroneous choices in the presence of bifurcations and snap-back zones.

The criterion chosen in the present work, based on previous investigations of Feng *et al.* (1996) and de Souza Neto and Feng (1999), takes the "recent" history of the near points along the equilibrium path, involving the previous converged incremental displacement $\left({}^{\ n}_{n-1}\mathbf{d}\right)$ and its predictor (current) iterative variation $\left(\delta\bar{\mathbf{d}}\right)$, in the form

$$\operatorname{sign}(\delta\rho) = \operatorname{sign}\left({}^{\ n}_{n-1}\mathbf{d}\,\delta\bar{\mathbf{d}}\right) \tag{4.75}$$

Remark 1: At this point, a question arises as if the inclusion of just one previous state in the determination of the sign for equation (4.74) would be sufficient for the correct reproduction of complex load-displacement paths. Going back a specific number of converged states, along with the collection of information about load and displacement incremental variations would, theoretically, provide a deeper insight into the main characteristics of the path evolution. This idea is on the core of the predictor-corrector approach of Kim and Kim (2001), who employed information, for a predictor iteration of a given increment, about the 3 previous converged increments. In this reference, this whole set of data was treated in an unified way within the framework of neural networks. Within the present work, on the other hand, a similar but simplified procedure was implemented, in order to provide a higher convergence rate. However, the results (or their rate of convergence) did not change drastically when compared to the standard implementation of the arc-length procedure.

Remark 2: Abaqus finite element program (ABAQUS, 2002a) proposes a small difference in the implementation. For a new increment (other than the first) the last iterated stiffness matrix is used in the evaluation of the iterative displacement vectors (4.64) and (4.65). The key idea is to keep a previously stiffness matrix, in the general case affected by material nonlinearities, other than a fully elastic-based one (implicit in those equations). Likewise what was described in Remark 1 before, for the examples studied in the present work, this modification did not turned itself of great importance, with the overall results not changing when compared to the conventional procedure described before. It is worth noting, nevertheless, that the stiffness matrix described accounts for nonlinear geometric effects automatically, once the local reference frame is updated at each converged (equilibrium) point.

Choosing the appropriate root for $(\delta\rho)$

In solving the quadratic equation (4.66), two real roots are obtainable in the general case $(\delta\rho_1\ ,\ \delta\rho_2)$. The choice relies (César de Sá, 1986; de Souza Neto and Feng, 1999) in the specific value of the iterative change $(\delta\rho)$ that would yield the minimum angle between the two successive displacement vectors $\left({}^{n+1}_{\ \ n}\mathbf{d}^{i}\right)$ and $\left({}^{n+1}_{\ \ n}\mathbf{d}^{i+1}\right)$ (maximum internal product), that is

$$\delta\rho = \arg\left\{ \max_{\delta\bar{\rho}\ \mid\ a\delta\bar{\rho}^2+b\delta\bar{\rho}+c=0} \left[\left({}^{n+1}_{\ \ n}\mathbf{d}^{i}\right)^{\mathrm{T}} \left({}^{n+1}_{\ \ n}\mathbf{d}^{i} + \delta\mathbf{d}^{*} + \delta\bar{\rho}\delta\bar{\mathbf{d}}\right) \right] \right\} \tag{4.76}$$

As mentioned before, there are cases where no real roots are obtained. In this case, instead of aborting the analysis, the algorithm simply retrocedes to the last converged configuration, scaling down the value of the arc-length for the current increment with the corresponding recalculation of the incremental load level.

Chapter 5

Numerical Examples

In this chapter benchmark cases are presented in order to evaluate the performance of the shell and solid-shell formulations implemented. Intrinsically, the adopted (and implemented) nonlinear material and geometric procedures are also tested. Solutions taken from the literature are used for comparison purposes, and a complete characterization of the overall procedures introduced in this work is then achieved.

5.1 Enhanced shell elements - Linear elastic problems

Although most of the time involving simple geometries, loading and boundary conditions, the following linear problems give a deep insight into the convergence behaviour of the proposed shell elements' formulations. The evolution of the solution quality starting from coarse meshes into refined ones is compared to well-established approaches. Two conclusions that must prevail after these tests: the improvement obtained with elements *S4E6P5*, *S4E6P7* and *MITC4–E2* when compared to the original degenerated and assumed natural strain formulations, respectively; and the very same response achieved by elements *S4E6P5* and *S4E6P7*, turning the use of 5 internal variables for membrane locking treatment the optimum choice.

5.1.1 Effect of mesh distortion

Out-of-plane loads

In order to evaluate the effect of mesh distortion, the analysis of a thin square, simply supported plate under uniform pressure (Bathe and Dvorkin, 1985) is carried out. Two different types of distortion patterns are adopted, according to Fig. 5.1. The nodal positions in the figure were based on the indications of Saleeb and Chang (1987), who also advanced a Poisson's ratio of $\nu = 0.3$ for this problem. Young modulus and pressure load values are not referred in those works, but once the reference solution comes from the Kirchhoff theory, this is not a problem. Also no values are advanced for the geometric relations, except that the length to thickness ratio of the plate must be equal to $\mathsf{L}/\mathsf{a} = 1000$. Due to symmetry, only a quarter of the plate is represented.

The normalized out-of-plane displacements $(w_{fem}/w_{analytical})$ at point C obtained with the proposed finite elements are compared with the values of the assumed natural strain bilinear shell element (Dvorkin and Bathe, 1984), as given in the work of Saleeb and Chang (1987). Results obtained with the original bilinear degenerated shell element relying on the approach of Ahmad *et al.* (1970) are also presented, all of them being summarized in Table 5.1. In the latter it is noticeable the good results of elements *S4E6P5*, *S4E6P7* and *MITC4–E2* for both mesh topologies I and II, while the original degenerated formulation completely locks. In mesh II, a fixed distortion parameter Δ is employed, being defined as $\Delta = \mathsf{L}/10$.

A distinct comparison analysis can be carried out with the transverse shear strain enhancement proposed by Simo and Rifai (1990), in the way implemented by Sansour and Bocko (1998), and applied over the mesh II in Fig. 5.1 for varying distortion parameters Δ. Material and geometric parameters are now different from the previous ones: Young modulus $\mathsf{E} = 1.0 \times 10^7$, Poisson ratio $\nu = 0.3$, length $\mathsf{L} = 100$ and thickness $\mathsf{a} = 0.1$. The plate is now considered clamped and a concentrated load is applied directly at point C, while its correspondent vertical displacement is monitored.

Normalized results obtained by elements *S4E6P5*, *S4E6P7* and *MITC4–E2* for different values of the distortion parameter Δ, are compared to those coming from the work of Sansour and Bocko (1998), using the formulation of Simo and Rifai (1990), as stated before. They are presented in Table 5.2, and show a pattern of mesh sensitivity for all formulations. Nevertheless, the element based on the enhancement proposed by Simo and Rifai (1990) reveals the poorest performance. Elements *S4E6P5* and *S4E6P7* also present a decrease in the quality of results. The best performance is however obtained with the *MITC4–E2* element, reproducing almost the same results over the analysed range of distortion. The assumed natural strain formulation of Dvorkin and Bathe (1984) leads to the same results as the latter formulation.

In-plane loads

A cantilever beam, modelled by two elements as shown in Fig. 5.2, is loaded by a pair of concentrated forces, inducing a resultant moment on the structure. The idea of this test is to compare the response of a given element formulation when submitted to increasing levels of in-plane mesh distortion. Material, geometry, boundary and loading parameters are according to Fig. 5.2, based on the works of Simo and Rifai (1990), Andelfinger and Ramm (1993) and Slavković *et al.* (1994). Similar analysis including different boundary conditions can be found in the papers of Lautersztajn-S and Samuelsson (2000) and César de Sá *et al.* (2001). Andelfinger and Ramm (1993) use different parameters (keeping the same boundary conditions), and their results were re-normalized to be included in this work. The distortion level is reflected by the geometrical parameter δ, as represented in the figure before, while the goal is the monitoring of the vertical displacement (i.e., along OY) of point C.

For comparison purposes, a plane strain formulation including 5 enhanced parameters, as introduced by Simo and Rifai (1990), the membrane enhanced element (7 parameters) of Andelfinger and Ramm (1993) and the 4-node (membrane) enhanced shell element of Slavković *et al.* (1994) (both including the interpolation scheme of Dvorkin and Bathe (1984)) are considered. In the first of the references before, results from the classical assumed stress approach of Pian and Sumihara (1985) and the well-known modified incompatible modes element of Taylor *et al.* (1976) are presented, being also reproduced here for comparisons. Shell elements $S4$, $S4R$ and $S4R5$ from $ABAQUS$ commercial code (ABAQUS, 2002a) and the mixed interpolated element of Dvorkin and Bathe (1984) itself (as implemented by the author) are also considered.

In Fig. 5.3 it is shown the evolution of the numerical solution provided by the above formulations. It is worth noting the crucial role of a correct membrane (in-plane) enhancement on the overall response. Dvorkin and Bathe (1984) and *MITC4–E2* formulations present the worst behaviors, even for the undistorted mesh, and mainly due to the absence of those strain improvement. Nevertheless, focusing in the use of 7 internal variables in the in-plane strain field, and comparing the results obtained using the formulation of Andelfinger and Ramm (1993) with those provided by the *S4E6P7* shell element, it is noticeable the better performance of the last approach. This difference can be explained by the transformation matrices employed in the present work, mapping the convective frame into the local (elemental) system, which are of different character than those employed by

Simo and Rifai (1990) and Andelfinger and Ramm (1993). This also can help to justify the different results provided by Simo and Rifai (1990) and *S4E6P5* formulations, both involving 5 internal variables acting over the membrane strain field, where it is noticeable the superior quality of the later formulation (*S4E6P7* formulation, involving 7 parameters does not greatly influence the final result). It is interesting to note that for the maximum distortion level ($\delta = 5$) the reference solution is attained with *S4E6P5* and *S4E6P7* shell elements.

Also of interest is the inability of shell bilinear finite elements (with full or selective/reduced numerical integration rules) from *ABAQUS* commercial code to reproduce acceptable numerical results, as can be seen in Table 5.3, even for the undistorted mesh. For the sake of completeness, Fig. 5.4 shows the monitoring of the vertical displacement of the point D in Fig. 5.2, for the *S4E6P5*, *S4E6P7* and *MITC4–E2* shell formulations presented.

5.1.2 Transverse shear locking test with warped elements over a cylindrical surface

Usually, shell finite elements fail when mesh configurations involve out-of-plane distortion patterns. An interesting example where this aspect can be explored involves a coarse mesh over a cylindrical surface. In this case, even for a regular (mapped) mesh, warped elements appear. If the mesh is then further distorted over the surface, the problem turns out to be even more difficult.

Following these lines, Andelfinger and Ramm (1993) proposed the analysis of an infinitely long curved panel, defined by a quarter of a cylinder (Fig. 5.5), clamped on one end and free on the other. A constant momentum is applied on the latter, so that the problem can be considered as a ”pure bending” one. Geometric properties of the structure refer to a radius $\mathsf{R} = 10.0$, demonstrative length $\mathsf{L} = 10$ and varying values of the thickness (a). Elastic material properties are given by the Young’s modulus $\mathsf{E} = 10^3$ along with the Poisson’s ratio $\nu = 0.3$. In this problem, and as have been pointed out by Andelfinger and Ramm (1993), only transverse shear locking is involved, which turns out this test case useful on the evaluation of the enhanced strain procedures proposed for shell elements. In this sense, and in order to test the transverse shear locking of the finite elements involved, the thickness of the cylinder is successively reduced by a factor of 10, leading to a value of displacement (component u^1 in the figure) increased each time by a factor of 10^3.

Following the steps of Andelfinger and Ramm (1993), starting with an initial thickness value of $\mathsf{a} = 10.0$ ($\mathsf{a}/\mathsf{R} = 1.0$) and focusing on the regular 3×3 mesh in Fig. 5.5, as thickness values decrease, the evolution of displacement is correctly reproduced by both the formulation of Dvorkin and Bathe (1984) and by the present transverse shear strain enhanced approach (included in the *S4E6P5* and *S4E6P7* shell elements).

However, if the mesh is distorted – forcing even further the elements to be more warped – shell elements based on the approach of Dvorkin and Bathe (1984) show severe shear locking. In this case, the evolution of displacements shows an increase of a factor of 10, in opposition to the expected factor of 10^3, as first noticed by Andelfinger and Ramm (1993). The distorted mesh adopted in the present work follow this reference, corresponding to the second mesh on Fig. 5.5. In detail, the level of distortion can be assessed by the projected mesh view presented in Fig. 5.6.

A transverse shear locking treatment using the enhanced assumed transverse shear strain proposed in this work provides, on the other hand, results that are more stable than those coming from the *mixed interpolation of the tensorial components* formulation. This can be seen in the analysis of the graph presented in Fig. 5.7. In the figure, it is shown the ratio between a displacement solution coming from the distorted mesh $\left(u^1_{dist}\right)$ when compared to its counterpart obtained with regular elements $\left(u^1_{reg}\right)$. Also in the graph, values for element *MITC4* are shown as previously presented by Andelfinger and Ramm (1993).

It is clear that elements relying on the formulation proposed by Dvorkin and Bathe (1984) (*MITC4* and *MITC4-E2*, in the present case) rapidly have showed an increase in stiffness (locking) as thickness values tend to zero in this example. On the other hand, the enhanced assumed strain procedure, grounding shell elements *S4E6P5* and *S4E6P7*, proved to be less sensitive to thickness variations (although still showing some differences from the solution provided by the regular 3 × 3 mesh).

Finally, and for completeness purposes, results coming from the *selective reduced formulation*, as implemented by Andelfinger and Ramm (1993) on bilinear shell elements, are also shown in Fig. 5.7. The evolution of results are similar to those of elements *S4E6P5* and *S4E6P7*, but showing less sensitivity to thickness reduction. Additionally, and in accordance to what was verified by Andelfinger and Ramm (1993), transverse shear locking onset is dependent on the boundary conditions. Once the symmetry conditions are removed, leading to a curved shell with three free edges, deterioration of results for the distorted mesh is not verified.

5.1.3 Plate bending I

A square plate with clamped edges is subjected to a concentrated load F, applied at its center (Andelfinger and Ramm, 1993). Following this reference, and benefiting from symmetry, one quadrant of the structure is modelled with two coarse meshes: with 2 × 2 and 4×4 elements, following a mapped pattern. The center point's out-of-plane deflection obtained with the present formulation is analysed and compared with the results coming from the works of Dvorkin and Bathe (1984) and Andelfinger and Ramm (1993).

The plate is characterized by the following geometric parameters: length $\mathsf{L} = 100$ and thickness $\mathsf{a} = 1$. Elastic material parameters involve the Young's modulus $\mathsf{E} = 10^4$ consistent unities and a Poisson's ratio of $\nu = 0.3$. In order to have a unity-valued out-of-plane (w) deflection at the center of the plate, the concentrated load is taken equal to $\mathsf{P} = 16.367$, according to the relation $w = 0.061\frac{\mathsf{PL}^2}{\mathsf{Ea}^3}$, based on the Kirchhoff theory. The results are listed in Table 5.4 and again comparisons are carried out related to the original degenerated approach of Ahmad *et al.* (1970), the assumed natural strain method of Dvorkin and Bathe (1984) and the enhanced strain field as proposed by Andelfinger and Ramm (1993).

For both meshes, the results obtained with elements *S4E6P5*, *S4E6P7* and *MITC4-E2* are quite acceptable when compared with the reference solutions referenced before.

5.1.4 Plate bending II

In this example, the previous clamped square plate is again taken into account for monitoring of the central point deflection, but now allowing a higher length to thickness ratio. The convergence of the finite element solution is investigated as the mesh is refined.

This test case, proposed by Kui *et al.* (1985), was then analysed with a value of 10^4 for the length to thickness ratio (L/a), in order to emphasize any tendency toward transverse shear locking appearance. Following the latter reference, the plate is subjected to an uniformly distributed load with, due to symmetry, only a quarter of the structure being analysed.

The obtained out-of-plane displacement (w) is normalized using the expression

$$w_{norm} = \frac{w\mathsf{D}}{\mathsf{PL}^4} \tag{5.1}$$

involving the external pressure P, the complete side length L and the flexural rigidity of the plate D. The latter is function of the thickness a of the plate, the Young's modulus $\left(\mathsf{E} = 3.0 \times 10^6\right)$ and the Poisson's ratio ($\nu = 0.3$), in the form (Ugural, 1981)

$$\mathsf{D} = \frac{\mathsf{Ea}^3}{12\,(1-\nu^2)} \tag{5.2}$$

The results are presented in Table 5.5. Not surprisingly, the degenerated formulation of Ahmad *et al.* (1970) shows a strong level of shear locking. On the other side, elements

S4E6P5, *S4E6P7* and *MITC4–E2* lead to the same result as those obtained using the formulations of Dvorkin and Bathe (1984) and Kui *et al.* (1985).

5.1.5 Cook's membrane problem

As introduced by Simo *et al.* (1989b), a trapezoidal plate clamped on one end and subjected to a distributed in-plane bending load, as shown in Fig. 5.8, is analysed. Other references dealing with this problem in the linear range are, for instance, the works of Ibrahimbegović *et al.* (1990) (plane stress elements), Slavković *et al.* (1994) (shell elements) and Kasper and Taylor (2000) (plane strain elements), among others.

In this example, in-plane shear deformations are predominant, which represents a test for the membrane enhancement employed in the present work. Besides that, the robustness of a given finite element formulation is tested against the skewed mesh topology employed, as shown in Fig. 5.8 for a representative 8 × 8 elements model.

The geometry, material, boundary and load conditions are also represented in Fig. 5.8. The idea is to correctly evaluate the vertical (in the direction of the applied force F) displacement of the free end mid-point. The reference solution was taken as 23.91 (Simo *et al.*, 1989a), and the corresponding results obtained with *S4E6P5*, *S4E6P7* and *MITC4–E2* shell elements are represented in Fig. 5.9, for a increasingly refinement level. Results obtained with the mixed-interpolated (Dvorkin and Bathe, 1984) bilinear shell element, as published by Slavković *et al.* (1994), are also reproduced. As stated before, the inclusion of a in-plane shear strain field into the formulation greatly improves the convergence ratio obtained, when compared with elements only prepared to transverse shear strain locking. Once again, there is small difference in the choice between 5 or 7 internal variables for the membrane enhanced strain field, only visible for the coarser meshes.

5.1.6 Morley's 30° skew plate

Another classical problem for the testing of distortion influence and transverse shear locking is the skew, simply supported plate originally introduced by Morley (1963), who provided an analytical series solution to the boundary value problem.

The idea is once more to evaluate the performance of the proposed elements when used in coarse and distorted meshes. The distortion level is defined by the 30° angle in Fig. 5.10, where a representative mesh of 4 × 4 elements over the entire plate is shown. About the kind of mapping used in the adopted meshes, it follows the indications of Simo *et al.* (1989b), who considered the topology in Fig. 5.10 "a demanding configuration due to the rhombic shape of the elements and the lack of mesh refinement at the singularity points" (the obtuse vertices).

Still about the geometric parameters, a characteristic length to thickness ratio $\mathsf{L}/\mathsf{a} = 100$ is employed ($\mathsf{L} = 100$ and $\mathsf{a} = 1$). Additionally, material properties refer to a Young's modulus of $\mathsf{E} = 10^5$ and Poisson's ratio $\nu = 0.3$. The loading conditions are represented by a uniformly distributed pressure of $\mathsf{P} = 1$. These parameters agree with those advanced by Andelfinger and Ramm (1993) (Fig. 5.10).

The results obtained with the *S4E6P5*, *S4E6P7* and *MITC4–E2* formulations are compared with those by Andelfinger and Ramm (1993), using an enhancement of the in-plane strain field. These authors also tested the assumed natural strain formulation of Dvorkin and Bathe (1984), and the corresponding results are reproduced here. Additionally, an enhanced plate element proposed by Simo and Rifai (1990) is also used as reference, as implemented by Yunhua and Eriksson (1999). For the sake of completeness, results coming from the original degenerated approach are also taken into account. A set of meshes is considered, comprising 4 × 4, 8 × 8, 16 × 16 and 32 × 32 shell elements. All results are shown in Table 5.6 and graphically in Fig. 5.11. The value of 4.640 for the out-of-plane displacement of point C in Fig. 5.10 is taken according to Andelfinger and Ramm (1993), and is adopted here as the reference solution.

It is worth noting the improvement over the solution coming from the assumed natural strain formulation, when combined with the enhanced strain approach. This can be seen with the results of element *MITC4–E2*. Nevertheless, the results of *S4E6P5* and *S4E6P7* elements are coincident and equal to those from *MITC4–E2*. Andelfinger and Ramm (1993) concluded that their enhancement over the in-plane strain field was crucial for a better performance of the assumed natural strain formulation of Dvorkin and Bathe (1984). However, for the present case, the proposed transverse shear strain enhancement has revealed enough for the overall results. In fact, and as can be seen from the author's work in César de Sá *et al.* (2002), no influence exclusively coming from the in-plane enhancement was verified, with the respective internal variables playing no role in the analysis. Another useful conclusion can be traced when comparing the present formulations with the performance of $S4R5$ shell element of *ABAQUS* commercial code (ABAQUS, 2002b) for the coarser meshes. Keeping the same aspect ratio as before, $S4R5$ presents a displacement error of 7.7% (4 × 4 elements) and 7.9% (8 × 8 elements), when compared to the respective reference solution. The *S4E6P5*, *S4E6P7* and *MITC4–E2* formulations are characterized by deviations of −2.8% and −4.4%, respectively, for the same mesh topologies. For more refined meshes, the results in all cases are closer to the reference solutions. Still analyzing the same coarse meshes, a couple of error level comparisons can also be carried out in relation to the results of Simo *et al.* (1989b). These authors obtain values of −3.9% and −4.3% for errors in displacement values with the cited meshes, employing stress resultant based shell elements with the assumed natural strain method.

5.1.7 Shearing analysis of a twisted beam

This problem deals with the analysis of a clamped beam that is twisted by 90º, subjected to loading patterns inducing bending and warping over the finite elements. A first version of the problem was introduced by MacNeal and Harder (1985), who provided a reference solution for a thick beam. Simo *et al.* (1989b) adopted a "more demanding version of the same problem", involving then a thin twisted shell, which became a classical problem in shell elements evaluation (Parisch, 1991; Batoz and Dhatt, 1992). This version is analysed in this work, and a schematically representation of the modelled structure is represented in Fig. 5.12, along with geometric, material and boundary data. Mesh topologies consisting of 1 × 6, 2 × 12, 4 × 24 and 8 × 48 shell elements (*width direction* × *length direction*) are employed (Simo *et al.*, 1989b). About the loading conditions, two cases of end loading are considered:

(a) Unit shear load along the width direction;

(b) Unit shear load along the thickness direction.

For each of these load patterns, values for the beam end deflection (on the load direction) come from the work of Simo *et al.* (1989b). They are used here for comparison purposes and are given by: 1.390 for the in-plane loading (load case (a)), and 0.3431 for the out-of-plane loading (load case (b)). The results obtained with *S4E6P5*, *S4E6P7* and *MITC4–E2* shell elements are the same, all of them being in accordance to those presented by Simo *et al.* (1989b), as can be stated from Tables 5.7 and 5.8 (showing the normalized results). It is interesting to note that even for the coarser mesh of 1 × 6 elements, the proposed formulations lead to the reference result.

5.1.8 Circular plate subjected to a combination of loads and boundary conditions

This is another interesting problem to evaluate the influence of mesh distortion upon the proposed shell elements behavior. The main goal is to evaluate the evolution of the displacement field of points over a circular plate subjected to concentrated and uniformly distributed loads, with strong (clamped) or soft (simply supported) boundary conditions. Between the authors that treated this test case are Simo and Rifai (1990), Belytschko and Leviathan (1994), Liu *et al.* (2000) and Piltner and Joseph (2001), to name but a small sample.

Starting with the guidelines of Belytschko and Leviathan (1994), a circular plate with radius $\mathsf{R} = 10.0$, uniform thickness $\mathsf{a} = 0.1$ ($\mathsf{R}/\mathsf{a} = 100$), Young's modulus $\mathsf{E} = 3.0 \times 10^6$ and Poisson's ratio $\nu = 0.3$ is considered. In this first configuration, the plate is assumed to be clamped on the circumferential edge and subjected to a point load on its center. Due to symmetry conditions, only a quarter of the plate is considered and meshed with distorted elements, as can be seen in Fig. 5.13. In their work, Belytschko and Leviathan (1994) only analysed the mesh containing 48 elements, although employing elements less distorted than those presented here. For this specific mesh, the deflection of the nodes along one edge are monitored and compared to analytical results coming from the Kirchhoff and Reissner-Mindlin theories. As the plate thickness tends to vanish, the two theories converge to the same analytical results, and the behaviour of *S4E6P5*, *S4E6P7* and *MITC4-E2* elements is represented in Fig. 5.14. It is patent the very good behavior of the proposed elements. For the sake of completeness, a convergence analysis with successive mesh refinements (Fig. 5.13) is presented in Table 5.9, with the results being normalized to the solution for deflections $w = 0.7242$. It is evident the good quality of the results for the whole mesh range.

Another type of configuration dealing with a circular plate with the same mesh configurations as in Fig. 5.13 was introduced by Simo and Rifai (1990), being further analysed by Liu *et al.* (2000) and Piltner and Joseph (2001). Now, the plate has a radius value of $\mathsf{R} = 5.0$, with thickness $\mathsf{a} = 0.1$ ($\mathsf{R}/\mathsf{a} = 50$), Young's modulus $\mathsf{E} = 10.92$ and Poisson's ratio $\nu = 0.3$. However, the greater differences are on the boundary and loading conditions. The plate is now considered as simply-supported on its limiting edges (out-of-plane displacement restriction), being subjected to a uniformly distributed pressure $\mathsf{P} = 1$. Again, the central node out-of-plane deflection is monitored, and a reference value of 3.9831×10^4 is advanced (Simo and Rifai, 1990) for normalization purposes. Besides the comparison of the results obtained with the present elements with those proposed by Simo and Rifai (1990) and Piltner and Joseph (2001), values coming from the work of Hughes and Tezduyar (1981) are also included, due to their overall good quality. The results from that comparison are presented in Table 5.10. It is clear the robust performance of the elements proposed, even for the coarser mesh of 3 elements.

5.1.9 Scordelis-Lo roof problem

In this classical example a shallow cylindrical shell is supported by rigid diaphragms and is subjected to its self-weight, leading to a membrane-dominated problem. Earlier references to treat this test case are, firstly, the original work of Scordelis and Lo (1964), and later on with the contributions of Ashwell (1976); Belytschko *et al.* (1985); MacNeal and Harder

(1985); Saleeb *et al.* (1987); Simo *et al.* (1989b); Andelfinger and Ramm (1993); Belytschko and Leviathan (1994); Sze *et al.* (1997); Liu *et al.* (2000), among others, and also in the books of Batoz and Dhatt (1992); Bernadou (1996).

The physical basis of the problem is an arched roof (as an aircraft hanger) supported only at its curved edges in a way that the curved shape is kept unmodified. These boundary conditions reflect themselves as $u = w = \phi_y = 0$ in Figure 5.15, where ϕ_y represents the rotation related to the global axis OY. The geometry is such that the center point of the roof (apex point) moves upward under the self-weight (directed downwards) load.

For this problem the vertical displacement at the midpoint of the free edge (point A in Figure 5.15) is monitored, and a reference numerical solution of $w = 0.3024$ is taken into account, as documented by Belytschko *et al.* (1985) and (Simo *et al.*, 1989a), who reported directly to the solution obtained by Scordelis and Lo (1964). Due to symmetry, only one quarter of the structure is considered, as shown in the mapped area of the figure, where the geometric and material properties are also outlined. For the sake of comparisons, displacement values obtained with the assumed natural strain formulation (Dvorkin and Bathe, 1984) and coming from the conjunction of this approach and the enhanced assumed strain formulation (Andelfinger and Ramm, 1993) are considered. Values obtained using the degenerated formulation (Ahmad *et al.*, 1970) are also taken into account. Mesh topologies consisting of 4×4, 6×6 and 8×8 elements were chosen, and the corresponding (normalized) results are presented in Table 5.11 and graphically in Figure 5.16.

From the table and figure cited, it is evident the better performance of elements *S4E6P5* and *S4E6P7* which, even for the coarser mesh, lead virtually to the reference result. Comparing the *S4E6P7* element with the one coming from the formulation of Andelfinger and Ramm (1993), it is patent the improvement obtained with the shear enhancement proposed in this work when compared to the assumed natural strain method (adopted in the last reference), once the in-plane enhancement is the same for both approaches. Element *MITC4–E2*, additionally, provides very similar results than those coming from the assumed natural strain approach (as implemented by Andelfinger and Ramm (1993)).

5.1.10 Pinched cylinder problem

This example (ABAQUS, 2002b) deals with the analysis of a finite length circular cylinder, bounded by rigid diaphragms in its ends (as in the example before). The cylinder is subjected to a pair of concentrated forces, as shown schematically in Fig. 5.17, altogether with a sample mesh over one eight of the whole structure. This classical test is used to evaluate the behavior of shell formulations when reproducing inextensional bending modes and complex membrane states. Following Belytschko *et al.* (1985), this example is one among three that constitute "an obstacle course for shell elements" (the remaining two examples are the Scordelis-Lo roof case treated before and the pinched hemispherical shell, analysed in the following).

In Fig. 5.17 geometric, material and load data are given in consistent unities. The thickness of the cylinder is 1/100 of its radius, and the displacement of point A in the figure along OZ direction is monitored. A reference value $w = 1.825 \times 10^{-5}$ is adopted for comparison and normalization purposes, coming from the work of Lindberg *et al.* (1969) and based on a series solution provided by Flügge (1973).

The results obtained with *S4E6P5*, *S4E6P7* and *MITC4–E2* formulations are compared to those obtained with the assumed natural strain approach (Bucalem and Bathe, 1993, 1997), the selective reduced integration (Belytschko *et al.*, 1985) and with the original degenerated approach. Mapped meshes with 4×4, 10×10 and 20×20 shell elements are employed, and the convergence behavior for each studied formulation is shown in Fig. 5.18. The convergence rate for all formulations are quite the same, with the in-plane and out-of-plane proposed enhancement being effective in the elimination of locking effects.

5.1.11 Hemispherical shell problem

This test case deals with a free hemispherical shell which is subjected to point loads of opposite signs. Since the problem geometry, loads and boundary conditions are symmetric, only a quarter of the structure needs to be modelled by finite elements. The geometric, material and boundary details are schematically presented in Fig. 5.19 , following works of Simo *et al.* (1989b) and Bucalem and Bathe (1993). The symmetry boundary conditions imposed on the mesh surface are sufficient to keep the problem well-conditioned, with no need to extra restraints (although the introduction of extra constrained nodes is common in the literature, as in Parisch (1991)).

This problem performs a challenging test of an element's ability to represent inextensional modes, exhibiting almost no membrane strains. When treated with coarse meshes, the resulting skewed elements lead to fewer degrees of freedom when compared with a regular mesh. In these cases, the element's ability to handle rigid body rotations about their normal vectors is checked, with large sections of the structure rotating almost as rigid bodies.

An analytical answer of 0.0924 (MacNeal and Harder, 1985) is used for the normalization of results and the values obtained with the stress resultant-based shell element of Simo *et al.* (1989a,b) are also represented. Also considered are the results obtained with the assumed natural strain bilinear shell element of Dvorkin and Bathe (1984).

A convergence study is represented in Fig. 5.20, for successively refined meshes. For the coarser mesh of 4 elements per side of the mesh surface, it is noticeable the improvement obtained with the *S4E6P5* and *S4E6P7* formulations, when compared to the assumed natural strain formulation. It is also worth noting that the inclusion of just two enhanced variables and keeping the assumed natural strain approach (*MITC4–E2* formulation) leads to a relatively small improvement on the results for the coarser mesh. In this sense, the transverse shear locking formulation entirely based on enhanced variables is clearly more efficient. When compared to the formulation of Simo *et al.* (1989a,b) (and also to the works of Belytschko and Leviathan (1994), Groenwold and Slander (1995), Cardoso *et al.* (2002), Cardoso (2002) and Choi and Lee (2003)), the greater difference rely on the coarser mesh, although the results tend to converge to superior values as the mesh is refined. The original degenerated element, on the other hand, presents a strong locking for all meshes employed.

5.1.12 Raasch's hook problem

According to Kemp *et al.* (1998), this test is useful in the evaluation of a given element's ability to properly reproduce coupling among bending, extension and twisting deformation patterns. The geometry corresponds to a curved strip rigidly clamped at one end and subjected to a unit load distributed along the width of the free end. Figure 5.21 shows the top view of the hook, modelled by two circular segments connected at the tangent point. Geometric, material, boundary and loading conditions are according to the work of Knight (1997). A reference solution of 5.027, for the displacement in the load direction of the free edge, is employed (Knight, 1997; Kemp *et al.*, 1998; Massin and al Mikdad, 2002). Mesh topologies consisting of 1×9, 3×18, 5×36, 10×72 and 20×144 shell elements are analysed, as shown in Fig. 5.22. The performance of the proposed *S4E6P5*, *S4E6P7* and *MITC4–E2* elements is compared to those obtained with the assumed natural strain formulation of Dvorkin and Bathe (1984) (as implemented by the author). In addition, results coming from the work of Kemp *et al.* (1998) and from the commercial code *ABAQUS* (ABAQUS, 2002b), using *S4R* and *S4* shell elements are taken into account. Kemp *et al.* (1998) proposes an enhancement of the displacement field using a total number of 23 internal variables to improve the four-node shell element.

The results for the above formulations are presented in Fig. 5.23. The convergence rate of shell elements *S4E6P5*, *S4E6P7* and *MITC4–E2* are quite good, with almost the reference result (deviation of 0.7%) already with the coarse mesh of 5×36 elements. The bilinear shell element employing the mixed interpolation procedure of Dvorkin and Bathe (1984) shows a very low convergence rate in this example, while *ABAQUS S4R* shell element presents very poor results for the coarser mesh. In relation to the formulation of Kemp *et al.* (1998), only with 23 internal variables the convergence is acceptable. Elements using 17 and 20 enhanced parameters, as shown in that reference, lead to unacceptable results, with a lower convergence rates as the number of additional variables decreases. In this sense, elements *S4E6P5* and *S4E6P7*, entirely based in respectively 11 and 13 enhanced parameters represent a noticeable evolution. In addition, it is also worth noting the improvement obtained with *MITC4–E2* shell element, with the inclusion of just 2 enhanced parameters into the formulation.

5.1.13 Bending dominated test I - Partly clamped hyperbolic paraboloid

In analyzing the asymptotic behavior of shell elements as thickness values tend to zero, it is possible to define problems as being *membrane* or *bending* dominated. When this distinction is not clear the asymptotic deformation character is said to pertain to an *intermediate* state (Pitkäranta *et al.*, 1995).

Following the analysis of Malinen and Pitkäranta (2000), bending-dominated problems are known to be hard tests for standard finite element formulations, which sometimes provide a poor approximation for inextensional displacements, with the consequent onset of deficient numerical results.

A particularly interesting bending-dominated test case was introduced in the work of Chapelle and Bathe (1998) (further developed by Bathe *et al.* (2000) and Chapelle and Bathe (2003), with a predominant finite elements and mathematical insights, respectively). The problem consists of a hyperbolic paraboloid shell structure, loaded by self weight and clamped along one side, as schematically represented in Fig. 5.24. The geometric, material and load data are those coming from Bathe *et al.* (2000), and only one-half of the structure needs to be modelled with finite elements. Directions OX, OY and OZ correspond to a global coordinate set, the first two generating a projection plane with bounds $[-0.5; +0.5]$. The out-of-plane coordinate of each point in the paraboloid is then obtained using the relation $Z = X^2 - Y^2$. The self-weight load adopted can be represented in vectorial form as $\{0; 0; -8000\}$ acting, then, along the OZ global direction.

Bathe *et al.* (2000) proposes the monitoring of point A in Fig. 5.24 (coordinates $X = 0.5$ and $Y = 0$), with the analysis of the strain energy error obtained with a finite element discretization, when compared with a reference value. Once for this problem there is no analytical solution for displacements (and, consequently, strain energy) Bathe *et al.* (2000) adopted a converged value obtained with a refined mesh of 16-node shell elements as the reference value. In the present work, the energy resulting from this solution is also adopted for comparison purposes. The behavior of *S4E6P5*, *S4E6P7* and *MITC4–E2* formulations is compared to the one coming from the bilinear assumed natural strain shell element of Dvorkin and Bathe (1984), as reproduced in Bathe *et al.* (2000).

About the finite element meshes, sequences of $(N \times N/2)$ elements, where N represents the subdivisions along the X-axis, were adopted ($N = 4, 8, 16, 32, 64$). For instance, in Fig. 5.24 a representative mesh of 16×8 elements is shown. Following the proposal of Bathe *et al.* (2000), thickness-length (a/L) relations of 1/100, 1/1000 and 1/10000 are considered. Graphically, the strain energy error of the finite element solution in comparison to the reference value is represented by the scalar value

$$E_{error} = \frac{E - E_h}{E} = 1 - \frac{E_h}{E} \tag{5.3}$$

with E_h being the strain energy resulting from the finite element approximation while E refers to the reference value.

The performance of the *S4E6P5*, *S4E6P7* and *MITC4–E2* formulations can be stated from the analysis of Fig. 5.25, 5.26 and 5.27 where, as stated before, the results of Bathe *et al.* (2000) using the assumed natural strain formulation are also included for comparison.

Elements *S4E6P5*, *S4E6P7* and *MITC4–E2* show similar results for the whole range of thickness to length ratios. For coarser meshes, these elements reveals an excess of flexibility when compared to the results from Bathe *et al.* (2000). As the meshes are refined, however, the results rapidly approach the reference solution. One conclusion not shown in the graphs, but demonstrated with the author's work in César de Sá *et al.* (2002), is the importance of the use of 6 enhanced variables in the transverse strain field. For a/L values of 1000 and 10000, the bilinear shell element with just 4 transverse shear enhanced variables presents a strong transverse shear locking pattern, with the consequent deterioration of results.

5.1.14 Bending dominated test II - Free cylindrical shell

In this example, a cylindrical shell of uniform thickness a, length $2 \times \mathsf{L}$ and radius R is loaded by an axially-constant pressure distribution. The pressure varies with the angular distance from the apex (see Fig. 1 in Bathe *et al.* (2000)) following the function

$$p(\varphi) = P_0 \cos(2\varphi) \tag{5.4}$$

where the amplitude factor P_0 is scaled according to thickness values as

$$P_0 = p_0 \mathsf{a}^3 \tag{5.5}$$

being p_0 a constant independent of a.

The cylinder possesses free ends with no kinematical constraints, being self-supported by the load pattern. The geometry, material and load data are the ones provided by the study of Bathe *et al.* (2000). This problem has been extensively described by the group of Juhani Pitkäranta, with the publication of an analytical locking insight for various shell models early in 1995 (Pitkäranta *et al.*, 1995). The reference solutions for the test case are the ones published in the paper of Malinen and Pitkäranta (2000).

In this simulation, 1/8 of the structure were modelled by uniform mesh patterns of $N \times 2N$ elements, being N $(N = 4, 8, 16, 32)$ the number of elements along the axial direction. As for the previous example, thickness to length ratios a/L of 1/100, 1/1000 and 1/10000 were employed, and a strain energy analysis was carried out, as in the last example, with the results being presented in Fig. 5.28, 5.29 and 5.30.

In this example all the proposed elements performed in a very similar way. For the thickness-length ratio of 1/100 the assumed natural strain formulation revealed is clearly superior, as for the most refined mesh (32 × 64 elements) the *S4E6P5*, *S4E6P7* and *MITC4–E2* elements keep an strain energy deviation of 1.0%. However, as thickness values decrease, all formulations tend to converge to the same performance.

5.1.15 Membrane dominated test I - Clamped cylindrical shell

The geometry and loading for this example are the same as for the previous one, but now the cylinder presents clamped ends. This modification leads to a membrane dominated problem, where pure bending is inhibited but still conducting to a well-posed problem (Pitkäranta *et al.*, 1995; Chapelle and Bathe, 1998; Bathe *et al.*, 2000; Chapelle and Bathe, 2000).

Although the load pattern remains the same, it is scaled in a way consistent of the membrane characteristic of the asymptotic behaviour. Doing so, eq. 5.5 is replaced by

$$P_0 = p_0 \mathsf{a} \tag{5.6}$$

that is, the load amplitude now being a linear function of thickness values.

Using the same mesh configuration as for the free cylinder problem before, the strain energy is evaluated for every element formulation, along with the thickness-length ratios described before. Reference solutions come from Pitkäranta *et al.* (1995) and Malinen and Pitkäranta (2000), and results from the assumed natural strain formulations (Bathe *et al.*, 2000) are again used for comparison purposes. The overall results are reproduced in Fig. 5.31, 5.32 and 5.33.

As thickness values tends to zero, the strain energy error implicit in all formulations increases. Nevertheless, *S4E6P5*, *S4E6P7* and *MITC4–E2* formulations present similar results as those shown by Bathe *et al.* (2000) for the bilinear mixed interpolated shell element. Anyhow, for the coarser mesh ($N = 4$) the latter provides slightly better performances, although the mesh refinement tends to make differences between the elements to vanish.

5.1.16 Membrane dominated test II - Clamped hemispherical cap

This benchmark, proposed by Chapelle and Bathe (1998), represents a hemisphere of radius R and uniform thickness a, fully clamped and subjected to an axisymmetric pressure distribution on its outer surface (directed inward, as in Fig. 11 in the previous reference). The imposed load is the same as the cylinder considered before, with the amplitude being scaled linearly with the thickness.

For the numerical simulation, the pertained data values are those from Bathe *et al.* (2000), including the adopted mesh parameters (such as the number of divisions in each of the directions of the structure). As usual with spherical type structures, a demonstrative 1/4 partition of the shell is divided into 3 macro-surfaces (mesh-areas), each of one being modelled in a mapped way (in a similar fashion as in the hemispherical shell of Fig. 5.19). The results from the mixed interpolated bilinear shell element in Bathe *et al.* (2000) are reproduced for comparison, with the range of thickness to radius adopted being the same as in the previous examples ($\mathsf{a}/\mathsf{R} = 1/100, 1/1000, 1/10000$).

Similar to what happened with the hemispherical test of Section 5.1.11, this problem is well-suited for assessing distortion sensitivity levels on low-order, bilinear finite elements, once the surface able to be reproduced by the finite elements is only a crude representation of the real one. Not having an analytical solution, references values coming from Bathe *et al.* (2000) have employed $1D$ highly refined meshes with axisymmetric elements. Doing so, benchmark values are attained for the displacement of the cap apex and, consequently, the strain energy used in this work. The results obtained with the present *S4E6P5*, *S4E6P7* and *MITC4-E2* formulations can be assessed in Fig. 5.34, 5.35 and 5.36, for the representative value of elements N along the latitude direction.

From the obtained results, it is clear a low convergence pattern of the solution for all the formulations (including the values from the assumed natural strain approach) although *S4E6P5* and *S4E6P7* formulations still show the best results.

5.2 Enhanced shell elements - Non-linear problems

After the preliminary linear tests, this section aims to evaluate the *S4E6P5* shell element performance, within the non-linear framework implemented, when compared to other shell formulations in the literature. This particular choice of finite element is related to the equivalent results, in the majority of the problems, obtained with *S4E6P5* and *S4E6P7* formulations (being, additionally, superior to element *MITC4–E2*, as seen in some of the problems before). It is then shown that the proposed 6-parameter enhanced transverse shear strain procedure, in conjunction with the 5 membrane internal variables, leads to equivalent results than those provided by well-established procedures such as the mixed interpolation of tensorial components and the reduced integration scheme for shell structures.

In the following examples, relative convergence tolerances for forces and displacements were set to 1.0×10^{-5}. Both convergence indicators were treated simultaneously in each analysis. Some problems involved the use of the "cylindrical" standard arc-length method of Crisfield (Crisfield, 1981, 1983, 1997). The first examples relate to nonlinear geometric problems, being followed by a set of large deformations elasto-plastic numerical examples. On the linear material examples, two points along the thickness direction are adopted.

5.2.1 Roll-up of a cantilever beam

In this classical nonlinear geometric benchmark, an initially flat clamped beam on one end is subjected to a (gradually increasing) bending moment on the free end. Starting in the paper of Simo *et al.* (1990a) until the more recent works of Zhu and Zacharia (1996); Betsch *et al.* (1998); Cardoso (2002); Massin and al Mikdad (2002), to name but a few, this example has been treated by a variety of authors.

Resorting to the original problem (Simo *et al.*, 1990a), the length of the beam is $\mathsf{L} = 10$, with width $\mathsf{w} = 1$ and thickness $\mathsf{a} = 0.1$. Material properties involved are the elasticity modulus $\mathsf{E} = 1.2 \times 10^7$ and Poisson coefficient $\nu = 0.0$. For a specific imposed moment value of $\left(\mathsf{M}_0 = \dfrac{2\pi \mathsf{EI}}{\mathsf{L}}\right)$, the cantilever free tip performs a complete turn, while the beam collapses into a perfect cylinder (in the equation before, I represents the second-order moment of the beam cross-section, in relation to the bending moment direction).

Different mesh configurations are employed by different authors. Nevertheless, in the present case the choice of Simo *et al.* (1990a) is adopted. This consists of a mesh with 25×1 shell elements, along the longitudinal and width directions, respectively. For both *S4E6P5* and *S4E6P7* formulations, the application of the analytical moment stated before leads to the correct final deformation, as can be seen in Fig. 5.37, where successive deflection stages are also shown. The final configuration is achieved without the appearance of singularities in the rotation matrix involving the rotational degrees-of-freedom, a mathematical deficiency that appears in the work of Massin and al Mikdad (2002).

5.2.2 Torsion of a flat plate strip

This well-known test case (see, for example, Simo *et al.* (1990a), Cardoso *et al.* (2002), Cardoso (2002), among others) involves large rotations and displacements, illustrating the robustness of the proposed element for this kind of situations. As represented in Fig. 5.38, a torsional moment is imposed to the midside node on the free edge of a clamped flat plate strip, in order to impose a final total rotation of 180° [1]. The geometric parameters involved are the length $\mathsf{L} = 1.0$, width $\mathsf{w} = 0.25$ and thickness $\mathsf{a} = 0.1$. Material properties relate to Young modulus $\mathsf{E} = 12.0 \times 10^6$ and Poisson coefficient $\nu = 0.3$[2]. The final configuration is attained in five equally spaced load-steps, with the corresponding displacement stages, without magnification, being represented in Fig. 5.39. For comparison purposes, Simo *et al.* (1990a) provides the best reported result in the literature, reaching the final configuration after 3 load steps.

5.2.3 Nonlinear geometric analysis of a twisted beam

Motivated by the linear analysis of the twisted beam presented in Section 5.1.7, a geometrically nonlinear simulation of the structure shown in Fig. 5.12 is now performed with the *S4E6P5* shell formulation, employing the coarse 2×12 mesh. To enforce the most demanding situation, both in-plane and out-of-plane loadings are applied simultaneously. All the geometric, material and boundary conditions are kept the same, but the load level is now defined as $\mathsf{F} = 250 \times \lambda$, with λ ranging from 0.0 to 1.0. This load level (and, additionally, the coarse mesh employed) is enough to induce large displacement and rotations to the elements involved. The results for the in-plane and out-of-plane displacements components are presented altogether in Fig. 5.40, and are identical to those provided with *S4E6P7* shell element. The maximum load factor is attained in 48 steps, and the final deformed beam configuration is shown in Fig. 5.41. It is worth noting that Sansour and Kollmann (2000) also analysed a nonlinear geometric version of the twisted beam, but with different geometry and mesh topology (2×24 bilinear shell elements), and only accounting for the in-plane load component (as in case (a) in Section 5.1.7).

---

[1] As far as the knowledge of the author, no specific value of the external moment is defined in the literature for this particular example and set of properties. Therefore, the value $\mathsf{M} = 1100.0$ was adopted in this work, corresponding to the moment that causes a 180° rotation in a plate strip simulated in *ABAQUS* program, with an equal mesh of *S4* shell elements. The total rotation in *ABAQUS* takes 10 increments to be completely performed.

[2] Similar analysis with distinct properties were carried out, for instance, in Parisch (1995) and Zhu and Zacharia (1996).

5.2.4 Cantilever ring plate

Motivated by the classic work of Basar *et al.* (1992), a ring plate subjected to a vertical line load on one end and clamped on the other (Fig. 5.42) is considered. According to Basar *et al.* (1992), this test can be considered "the most sensitive" in the evaluation of finite rotation models, involving large rigid body rotations and displacements. Other works dealing with this example are, for instance, Büchter and Ramm (1992); Wriggers and Gruttmann (1993); Brank *et al.* (1995); Sansour and Bocko (1998); Li (2000); Li and Zhan (2000); Sansour and Kollmann (2000). With respect to geometric parameters, internal radius is $\mathsf{R_i} = 6$ while external radius is $\mathsf{R_e} = 10$. Thickness is set constant over the plate and equal to $\mathsf{a} = 0.03$. The applied distributed line load has a nominal value of $\mathsf{F_{tot}} = 100.0 \times \lambda$ per unit length, where λ is a load factor. Regarding material parameters, the Young modulus considered is set to $\mathsf{E} = 2.1 \times 10^{10}$ with a Poisson ratio of $\nu = 0.0$.

In the present numerical simulation two meshes were considered: a coarse mesh configuration, with 2×16 elements, and a refined mesh with 6×40 *S4E6P5* shell elements (radial × circumferential direction). For each mesh, the obtained displacements (along OZ) of points A and B (Fig. 5.42) are compared with those obtained by Simo and Rifai (as reproduced in Basar *et al.* (1992)), for a maximum load factor of 2.0. According to the last work, this limited load factor is enough for comparisons purposes, corresponding to the load zone with more drastic shape variations. The results for each point are presented in Fig. 5.43. It is clear the good behavior of *S4E6P5* element, even for the less refined mesh. It is worth noting that the solution, for each mesh, is attained within 12 steps, and without resorting to an arc-length control procedure (as adopted in Brank *et al.* (1995)). The results are also comparable to those obtained with reduced integration procedures (Cardoso, 2002).

Going further with the maximum applied load, for a total load level of $\lambda = 20$ the final configuration for both meshes, as represented in Fig. 5.44, can be obtained. At these configurations, displacements for point B are 21.655 and 23.889, for the 2×16 and 6×40 meshes, respectively (over 2 times the external radius value in each case). It is interesting to note that even with the coarser mesh adopted, this final load level can be achieved.

5.2.5 Snap-through and snap-back analysis

In this case the large rotation response of a pinched cylindrical shell is analyzed. The shell, schematically represented in Fig. 5.45, is subjected to a concentrated load on point A. In the figure, $\mathsf{L_1} = 508.0$, $\mathsf{L_2} = 507.15$ and $\mathsf{R} = 2540.0$. Thickness value considered is $\mathsf{a} = 6.35$. Material parameters are $\mathsf{E} = 3102.75$ and $\nu = 0.3$. The maximum load level attained is $\mathsf{F_{tot}} = 1000.0$. Due to the symmetry of the problem, only one quarter of the structure is modelled with a mesh of 5×5 *S4E6P5* shell elements.

In addition to model the structure with a regular mesh, a perturbation in selected elements (gray area in Fig. 5.45) is introduced. For this case, a particular node (C in the figure) is set movable, leading to four distorted configurations each of one including a different "collapsed" quadrilateral element, also shown in the figure. To the knowledge of the author, this kind of strong distortion (and the correspondent influence in the results) was never before treated in the literature.

The straight edges of the structure are hinged while the curved edges are taken free. This kind of boundary conditions induces an unstable behavior clearly represented in the graphic of Fig. 5.46, where displacements of points A and B (along OZ) are represented for the regular mesh. These are compared with results presented by Horrigmoe and Bergan (1978), and the good agreement between the two solutions is noticeable. The presented solution made use of the "cylindrical" arc-length procedure, being the results also in agreement with those presented by Crisfield (1981).

For the case of the distorted meshes, the results are presented in Figures 5.47 and 5.48 for points A and B, respectively. When compared with the results from the regular mesh the deviations are evident (mainly due to the fact that a low number of elements is employed in the whole mesh). Nevertheless, for the present case, it is noticeable the strong influence of the distortion level, even when restricted to a narrow area.

5.2.6 Pinched hemispherical shell with non-linear geometric behavior

This problem is an extension of a benchmark problem for linear analysis (MacNeal and Harder, 1985), and was firstly extended to the non-linear range in the work of Simo *et al.* (1990a). After that, a number of authors have extensively treated the problem, such as Sansour and Bufler (1992); Parisch (1995); Bischoff and Ramm (1997); Betsch *et al.* (1998); Sansour and Bocko (1998); el-Abbasi and Meguid (2000); Li and Zhan (2000); Sansour and Kollmann (2000); Wang and Thierauf (2001), just to name a few of them dealing with shell formulations. In most of these references, the original results from Simo *et al.* (1990a) are quoted, and therefore they are adopted here as the reference for comparison.

In this test case (similar to the one presented in Section 5.1.11), a hemispherical shell with an 18° hole at the top is subjected to two inward and two outward forces 90° apart. Due to symmetry, only one-quarter of the structure is analyzed, and a schematic mesh of 8×8 shell elements is represented in Fig. 5.49. A refined mesh consisting of 16×16 elements is also taken into account.

Material and geometric properties considered are: $\mathsf{E} = 6.825\times10^7$, $\nu = 0.3$, radius $\mathsf{R} = 10$ and thickness $\mathsf{a} = 0.04$. The load factor is taken to increase from $\lambda = 0.0$ until the final value $\lambda = 100.0$. Although a higher maximum load level might be used, the present choice provides the better range for comparison with other formulations.

The obtained results are in agreement with those provided by Simo *et al.* (1990a) (employing the mixed interpolation of transverse shear strains and the refined mesh of 16×16 elements to achieve the converged solution), and are presented in Fig. 5.50. With the latter mesh, *S4E6P5* shell element shows a very close behavior to the reference one, with some improvements when compared to the 8×8 mesh. Here, the additional membrane enhanced variables of formulation *S4E6P7* provides better results starting from the coarser mesh. Anyway, from the figure, it is noticeable the excellent performance both elements. Although not included in the graphic, the results obtained with *S4E6P5* shell element and those provided by Simo *et al.* (1990a), both with the coarse mesh of 8×8 elements, are equivalent.

For the sake of completeness, deformed configurations for both the 8×8 and 16×16 meshes for the maximum load factor $\lambda = 100.0$ are presented in Fig. 5.51. Also in the figure, the final configuration for a load factor $\lambda = 200.0$ and a mesh with 16×16 shell elements is shown.

5.2.7 Pinching of a clamped cylinder

This test problem accounts for a cylindrical shell, fully clamped at one end and subjected to a pair of concentrated loads at the other (free) end. The two load acts in opposite directions, and a sketch of the problem is given in Fig. 5.52.

One-quarter of the structure is analyzed with a mapped mesh of 16×16 elements, following the works of Brank *et al.* (1995) and Ibrahimbegović *et al.* (2001). Additionally, mapped coarser meshes of 8×8, 10×10 and 12×12 *S4E6P5* shell elements are also accounted for. The elastic material properties are $\mathsf{E} = 2.0685\times10^7$ and $\nu = 0.3$. The length of the cylinder is $\mathsf{L} = 3.048$, with radius of $\mathsf{R} = 1.016$ and thickness $\mathsf{a} = 0.03$. The nominal load in Fig. 5.52 is $\mathsf{F}_{\mathsf{tot}} = 1600\times\lambda$, where the load factor employed is supposed to vary between $\lambda = 0.0$ to $\lambda = 1.0$. The main goal in this numerical test is the monitoring of the displacement (on the load direction) of point A in Fig. 5.52.

The present results, obtained with the enhanced transverse shear strain method, are compared with the results of Brank *et al.* (1995), using a 16×16 mesh. In the latter reference, a four-node degenerated, stress resultant based, shell element with mixed interpolation of transverse shear strain was employed. Also results coming from the *S4E6P7* shell element, and reported in Fontes Valente *et al.* (2003) are included. The reason is that in the latter case, good results were obtained with coarser meshes of 12×12 and 14×14. Below these values, numerical instabilities arise, following the patterns reported for the first time by Crisfield and Peng (1996) in this specific example. From the analysis of Fig. 5.53, 5.54 and 5.55, it is clear that, for these meshes, *S4E6P5* shell element retain those numerical instabilities, with the reproduction of the reference solution for the 16×16 mesh (see Fig. 5.56). In this case, therefore, it is interesting to note the influence of the lack of the 2 internal membrane enhanced variables when compared to *S4E6P7* shell formulation. For that most refined mesh, the results coming from the two elements coincide, and an evolution of deformed patterns is presented in Fig. 5.57. All tested meshes, anyway, reproduce displacement levels that go beyond the highest physically possible displacement of the loaded points (which is the radius of the cylinder), being attained with the "cylindrical" arc-length procedure.

5.2.8 Stretching of a cylinder with free ends

In this geometrically nonlinear example, the cylindrical shell shown in Fig. 5.58 is subjected to a pair of concentrated forces, inducing large displacements and rotations to the finite elements. This example involves a combination of membrane and bending deformation modes, and have been analyzed in a number of publications, including Sansour and Bufler (1992); Peng and Crisfield (1992); Jiang and Chernuka (1994a); Brank *et al.* (1995); Sansour and Bocko (1998); Sansour and Kollmann (2000); Masud *et al.* (2000); Ibrahimbegović *et al.* (2001), to name but a few, using with shell and solid elements.

The total length of the shell is $\mathsf{L} = 10.35$, with a radius $\mathsf{R} = 4.953$ and thickness $\mathsf{a} = 0.094$. Material properties are: Young modulus $\mathsf{E} = 10.5\times10^6$, and Poisson ratio $\nu = 0.3125$. No boundary conditions are applied to the free ends of the shell, being the applied load pair responsible for the equilibrium of the cylinder.

Making use of the symmetry conditions, one eighth of the structure is modelled with two distinct topologies: 12×8 elements (Jiang and Chernuka, 1994a) and 16×8 elements (Masud *et al.*, 2000) (number of elements along the periphery and along the semi-length, respectively) with regular meshes. Additionally, a distorted mesh as presented in Fig. 5.58 is analyzed. For this case, 12×8 shell elements are used, the smaller one located next to the point where the concentrated load is applied. In each direction (periphery and semi-length) the last element (away from the load point) is characterized by a length 10 times greater than the smaller one.

The total load in the figure increases until a maximum value of $\mathsf{F}_{\mathsf{tot}} = 40000\times\lambda$. For the arc-length parameters specified before, the problem can be solved with the *S4E6P5* shell element in a total of 29 steps (in order to catch accurately the abrupt path changes in the displacement evolution). This evolution for points A and B is traced and compared with the corresponding one obtained by (Jiang and Chernuka, 1994a) and also (Masud *et al.*, 2000), with the results being plotted in Fig. 5.59 (for point A) and Fig. 5.60 (for point B). The final configuration, for the load factor $\lambda = 1.0$, with the 12×8 distorted and 16×8 regular meshes, is shown in Fig. 5.61.

From both graphs, some conclusions can be attained. Ranging from the coarse to the most refined (regular) mesh, the solution tends to equal the one obtained by Jiang and Chernuka (1994a), departing from that of Masud *et al.* (2000). The reason might be the fact that the latter authors employed a 3D formulation (with reduced integration procedure for transverse shear locking), in opposition to Jiang and Chernuka (1994a), who (as in the present work) adopted a shell formulation (although employing mixed interpolation of transverse shear components). For the distorted mesh case, the evolution of displacements remains close to those coming from the regular patterns, not showing excessive deviations.

Still from Fig. 5.59 and 5.60, it is clear that the simulation response of the cylinder can be divided into two main phases: a first one dominated by the bending strain energy and characterized by large displacements and rotations; and a second one associated with a stiffer response coming from membrane strain energy terms. The transition between the two behaviors presents a localized and abrupt buckling, noticeable mainly over point B. It is also worth noting that the present solutions for *S4E6P5* shell formulation is also in agreement with results provided by Sansour and Bufler (1992) (in their so-called "hybrid strain" formulation), Peng and Crisfield (1992), Brank *et al.* (1995) and Ibrahimbegović *et al.* (2001), although in these cases no localized buckling was tracked (being, however, reproduced in the recent work of Sansour and Kollmann (2000), employing an enhanced formulation). For the sake of completeness, the maximum physically acceptable load factor (for which the displacement of point B in Fig. 5.58 equals the radius value) corresponds to $\lambda = 1.74$, and the overall presented results are equivalent to those using the *S4E6P7* formulation (Fontes Valente *et al.*, 2003).

5.2.9 Elasto-plastic bending of a clamped beam

In this very simple example a cantilever beam with elasto-plastic behavior is analysed. The length to thickness ratio is $\mathsf{L}/\mathsf{a} = 100$, corresponding to the test case previously analysed by Dvorkin *et al.* (1995) and subsequently by Eberlein and Wriggers (1999), among others.

The geometry of the beam is characterized by the length $\mathsf{L} = 10$, thickness $\mathsf{a} = 0.1$ and width $\mathsf{w} = 1.0$. The beam is clamped on one end, being subjected to concentrated loads on the (opposite) free edge (Fig. 5.62). Material properties refer to a Young modulus $\mathsf{E} = 1.2 \times 10^7$, Poisson coefficient $\nu = 0.3$, initial yield stress $\sigma_{y0} = 2.4 \times 10^4$ and isotropic hardening coefficient $\mathsf{H}_{\mathsf{iso}} = 1.2 \times 10^5$, (for a linear hardening law of the type $\sigma_y(\epsilon^p) = \sigma_{y0} + \mathsf{H}_{\mathsf{iso}}\epsilon^p$). Following Dvorkin *et al.* (1995), the adopted mesh consists of 20 equally-spaced *S4E6P5* shell elements along the longitudinal direction of the beam. This is also in accordance with Eberlein and Wriggers (1999), for its so-called "5–parameter" formulation (with an inextensible director field and no drilling degrees-of-freedom).

With the main parameters defined, the displacement of the free end is monitored (as a function of the applied external load) and compared to those presented in the cited references (Dvorkin *et al.*, 1995; Eberlein and Wriggers, 1999). The resulting graph for the present simulation is presented in Fig. 5.63. The agreement between all the formulations is noticeable. For the sake of completeness, it is important to refer the quadrature rule for the numerical integration in the out-of-plane direction. In the work of Dvorkin *et al.* (1995), 4 Gauss points are considered along the thickness direction, while the use of 5 integration points is invoked by Eberlein and Wriggers (1999). About the present work, 5 Gauss points along thickness direction are considered.

5.2.10 Elasto-plastic stretching of a short cylinder with free edges

In this test case, the cylindrical shell of Section 5.2.8 is again analysed. As stated before, previous formulations tackling this example include, among others, the works of Peng and Crisfield (1992), Sansour and Bufler (1992), Jiang and Chernuka (1994a), Brank *et al.* (1995), Masud *et al.* (2000) and Ibrahimbegović *et al.* (2001). In all these cases, only geometric nonlinearities were considered, while the nonlinear material analysis have previously been considered by Masud and Tham (2000). Data and results from this last work will be treated as the reference for comparisons in the following.

The initial configuration corresponds to the cylindrical geometry already presented in Section 5.2.8 (see Fig. 5.58), involving a total length of $\mathsf{L} = 10.35$, radius of $\mathsf{R} = 4.953$ and a constant thickness value $\mathsf{a} = 0.094$. Material properties are: Young modulus $\mathsf{E} = 10.5{\times}10^6$, and Poisson's ratio $\nu = 0.3125$. As said before, no boundary conditions are applied to the free ends of the shell, with the load pair being responsible for the equilibrium of the cylinder. Plastic parameters are the initial yield stress $\sigma_{y0} = 1.05 \times 10^5$, and a linear isotropic hardening coefficient of $\mathsf{H}_{\mathsf{iso}} = 10.5 \times 10^5$. Mesh topology differs from that of Section 5.2.8, following now the proposal of Masud and Tham (2000), that is: 16×8 *S4E6P5* enhanced shell elements (now restricted to the regular mesh). The numbers once more relate to elements along the periphery and the semi-length directions, respectively.

The external load level for this elasto-plastic example corresponds to $\mathsf{F}_{\mathsf{tot}} = 40000 \times \lambda$, where λ ranges from 0.0 until 1.0. Results for the deflection of points A and B in Fig. 5.58, as a function of the λ parameter, are given altogether in Fig. 5.64. In the work of Masud and Tham (2000), a mesh of $16 \times 8 \times 2$ three-dimensional elements with reduced integration was employed.

This example is characterized by two well-defined deformation zones: an initial part which is bending-dominated; and the final part, with deformations mainly coming from membrane effects. In the initial region, characterized by large rotations and displacements, the *S4E6P5* formulation is almost coincident with the reference one. After the buckling point, visible in the graph of Fig. 5.64, the proposed shell formulation tends to present a softer response when compared to the continuum-like (3D) elements presented by Masud and Tham (2000). Contrasting with the constant load increments procedure of these authors, in the present example the "cylindrical" arc-length control procedure was used, with implementation following the general guidelines of Crisfield (Crisfield, 1981, 1983), and including the refinements introduced by de Souza Neto and Feng (1999). The overall deformation path is completed in 29 load (arc-controlled) steps, in opposition to the 140 employed by Masud and Tham (2000).

5.2.11 Channel-section beam with plasticity

A channel-section (U-shaped) beam, clamped at one end and subjected to a concentrated force at its free end, is now analysed. The geometry is according to Fig. 5.65, where values for length, width, height and thickness of the beam follow those originally proposed by Chroscielewski *et al.* (1992). Well-known works following with the treatment of this problem within shell formulations are, for instance, (Ibrahimbegović and Frey, 1994; Betsch *et al.*, 1996; Eberlein and Wriggers, 1999; Li and Zhan, 2000). All of these formulations employ drilling degrees-of-freedom. Particularly in the case of Betsch *et al.* (1996), the folded zones of the plate are modelled with rigid intersections accounting for 3 rotational degrees-of-freedom. Also for these formulations, only non-linear geometric analyses were performed, exception being the work of Eberlein and Wriggers (1999), where for the first time elasto-plasticity were accounted for. Therefor, data parameters and results coming from Eberlein and Wriggers (1999) will be taken as the reference ones, for the present work.

In this sense, an initial yield stress $\sigma_{y0} = 5.0 \times 10^3$ and isotropic hardening coefficient $\mathsf{H}_{\mathsf{iso}} = 0.0$ (perfect plasticity) were adopted. The director update procedure invoked in the present work – along with the inextensibility condition – are similar to the procedures adopted in the so-called "5/6–parameter" formulation of Eberlein and Wriggers (1999) (pages 247-248). The main difference remains in that *S4E6P5* shell element does not include drilling rotations in its formulation, treating in the same way smooth and folded thin plates or shells. According to the conclusions of Eberlein and Wriggers (1999), such a formulation would "completely fail in the present example". However, the behavior of the proposed enhanced strain element is quite acceptable (mainly in the combined elasto-plastic non-linear geometric case), as can be clearly seen in Fig. 5.66, where the displacement of the loaded node (in the direction of F in Fig. 5.65) is shown graphically, both for only geometric (*nlgeom*) and geometric plus material (*nlgeom+ep*) non-linearities. In reference Eberlein and Wriggers (1999), a mesh consisting of 24×72 shell elements was considered, while in the present work 24×36 *S4E6P5* elements were adopted (further mesh refinements have given the same results). About the number of load steps in each analysis, the non-linear geometric path was achieved in 56 increments, compared to 90 for the full geometric and material non-linear behavior. In both cases, the "cylindrical" arc-length control procedure was employed. It is also worth mention that just two Gauss points along thickness direction were adopted (contrasting with the formulation of Eberlein and Wriggers (1999), employing five Gauss points along thickness direction).

As advanced by Eberlein and Wriggers (1999), equivalent plastic strain peaks occur near the clamped end of the structure, and start in the early stages of loading. With the increase of deformation, however, residual plastic zones along the longitudinal direction of the beam appear, as can be seen in Fig. 5.67, where the deformed configuration for an absolute displacement of 1.471 (of the loaded node point) is represented.

5.2.12 Elasto-plastic analysis of a simply-supported plate

In this example, a simply-supported square plate is subjected to a set of pressure loads, as shown schematically in Fig. 5.68. This example has been treated in a number of references, including shell and solid-shell formulations and adopting a number of mesh topologies – see, for instance, (Büchter *et al.*, 1994; Miehe, 1998; Eberlein and Wriggers, 1999; Betsch and Stein, 1999; Hauptmann *et al.*, 2000; Doll *et al.*, 2000; Harnau and Schweizerhof, 2002). About Fig. 5.68, and following the previous references, the total length of the plate is $2\mathsf{L} = 508$, with thickness $\mathsf{a} = 2.54$ consistent unities. Only one quarter of the plate needs to be analysed, due to symmetry. Material behavior is described by a Young's modulus $\mathsf{E} = 6.9 \times 10^4$, Poisson's ratio $\nu = 0.3$, initial yield stress $\sigma_{y0} = 248$ and isotropic hardening coefficient $\mathsf{H}_{\mathsf{iso}} = 0.0$ (for a linear hardening law of the type $\sigma_y(\epsilon^p) = \sigma_{y0} + \mathsf{H}_{\mathsf{iso}}\epsilon^p$). For each simulation just 2 Gauss points along thickness direction are employed, once for a higher interpolation order the same results were obtained. For comparison, Eberlein and Wriggers (1999) adopt five Gauss points along thickness direction, while Doll *et al.* (2000) and Harnau and Schweizerhof (2002) invoke 6 integration points. About boundary and loading conditions, displacements along the OZ direction are restrained on the outer edges, while a deformation dependent pressure load $\mathsf{p} = \mathsf{f} \times \mathsf{p}_0$ is applied on one side of the shell, for a nominal load level of $\mathsf{p}_0 = 10^{-2}$.

In the present work, 4 mesh topologies were adopted to attest the convergence behavior of the proposed enhanced strain formulation: a first coarser mesh consisting of equally-spaced 15 × 15 $S4E6P5$ shell elements (as represented in Fig. 5.68); a second mesh with the same number of elements but refined towards the outer corners (as adopted by Eberlein and Wriggers (1999)); a third mesh consisting of 24 × 24 regularly spaced elements (following Betsch and Stein (1999)) and a last, extremely refined, mesh with 1375 elements, as recently suggested by Cardoso *et al.* (2002). The last 3 meshes are schematically represented in Fig. 5.69.

Figure 5.70 shows the load-deflection curve, for a maximum load factor ($\mathsf{f} = 60.0$), with the corresponding out-of-plane deflection of the central point of the plate (point C in Fig. 5.69). Results are compared to those provided by Eberlein and Wriggers (1999) and Betsch and Stein (1999). Within the analysed meshes, all of them converge to the solution presented by Betsch and Stein (1999). The only exception is the regular mesh with 15×15 shell elements, and just for the range of displacement between 30 to 65 consistent unities, where the present solution approach the one by Eberlein and Wriggers (1999). However, the overall behavior obtained with $S4E6P5$ shell element is quite good.

More insight into this problem can be obtained with the analysis of the deformed configuration ($\mathsf{f} = 60.0$) for each mesh, as represented in Figures 5.71, 5.72, 5.73 and 5.74. The deformed structures assume a "pillow-like" configuration, with the elements in the corner zones being subjected to a high level of out-of-plane distortions (naturally more visible with the regular mesh of 15×15 elements). From the plots of the equivalent plastic strain levels, it is noticeable the onset of their maximum values in the corner zones of the plates. The number of load increments necessary to reach the load factor ($\mathsf{f} = 60.0$) are: 44 for the 15 × 15 regular mesh; 47 for the 15 × 15 refined mesh; 54 for the 24 × 24 mesh and, finally, 56 for the 1375 shell element's mesh. Also from the figures, it is possible to assess some level of mesh dependency of the equivalent plastic strain numerical values, an interesting aspect which is not addressed in the previous references.

A deeper insight of the structural behavior can be further retained with the increase of the load factor applied to the pressure loads. In Fig. 5.75, six deformation stages of the plate (viewed from the top) are represented, for the refined mesh of 1375 elements. The first one (Fig. 5.75, (*a*)) represents the deformed plate for a load factor ($\mathsf{f} = 285.4$). At this stage, the out-of-plane displacement verified for point C (Fig. 5.69) is equal to 121.4 consistent unities. More relevant than this is the fact that, at this load factor, it can be verified the onset of wrinkles at the mid-side of each plate's edge. With a further increase of the load factor, this phenomenon is even more noticeable, as represented in the sequence on Fig. 5.75(*b*) (load factor $\mathsf{f} = 386.8$), Fig. 5.75(*c*) (load factor $\mathsf{f} = 479.9$) and Fig. 5.75(*d*) (load factor $\mathsf{f} = 557.6$), corresponding to central point displacements of 131.6, 140.5 and 149.0, respectively. Above this load level, and with an even higher load factor, the plate is only able to accommodate more deformation if adopting a spherical shape. The corner zones of the plate (still those with higher levels of plastic strains) tend, therefore, to assume a rounded shape (losing their sharp aspect still visible on Fig. 5.75(a), (b) and (c)). The spread of plastic areas is noticeable, starting in configuration (b), with the plate, for the final two steps (Fig. 5.75(e) and (f)), virtually covered by plastic zones as a whole. Displacement of the central point for the last two configurations is equal to 157.0 and 164.5, for load factors of ($\mathsf{f} = 600.7$) and ($\mathsf{f} = 635.5$), respectively. Dimetric projections of configurations at load levels (a), (c) and (f) are reproduced in Fig. 5.76, where the final rounded shape of the plate can be further observed.

5.2.13 Pinched cylinder including elasto-plasticity

This last example deals with a cylindrical shell, subjected to a pair of concentrated loads and bounded by rigid diaphragms on its extremities. It is a common benchmark in shell and solid-shell elements technology, and have been treated by a number of authors (firstly by Simo and Kennedy (1992) and after that, for instance, with Wriggers *et al.* (1996); Brank *et al.* (1997); Sorić *et al.* (1997); Miehe (1998); Eberlein and Wriggers (1999); Sansour and Kollmann (2000)). In the present work, the problem will be considered in the same way as stated in the last references, particularly following Miehe (1998) and Eberlein and Wriggers (1999).

The initial geometry of the shell is as illustrated in Fig. 5.77, where the mesh area is just one eight of the cylinder, due to symmetry reasons. Geometrical data refer to the whole length of the cylinder $\mathsf{L} = 600$, the radius $\mathsf{R} = 300$ and thickness $\mathsf{a} = 3$. The rigid diaphragm boundary condition acts in a way that only displacements along the OY direction are allowed in the cylinder free-ends. Material properties are the elasticity modulus $\mathsf{E} = 3000.0$, Poisson's coefficient $\nu = 0.3$, initial yield stress $\sigma_{y0} = 24.3$ and isotropic hardening coefficient $\mathsf{H}_{\mathsf{iso}} = 300.0$, for the same linear hardening law used in the previous examples.

After Miehe (1998) and Eberlein and Wriggers (1999), a mesh consisting of 32×32 $S4E6P5$ shell elements is employed. In the present work, however, the previously referred incremental load controlled procedure, based on the Newton-Raphson method with the "cylindrical" arc-length control, is used (in contrast to the works cited before, which employed displacement controlled advance methods to ensure stable convergence).

In Fig. 5.78 the displacement of the loaded node is monitored and plotted against the total load level F in Fig. 5.77. For the same mesh, and as said before, the results coming from the presented elasto-plastic formulation applied to the $S4E6P5$ enhanced strain shell element are compared to the solid-shell formulation proposed by Miehe (1998) and to the "5–parameter" shell formulation of Eberlein and Wriggers (1999). The results are almost coincident in the major displacement range, with the present element being slightly more flexible for displacements greater than 175 consistent unities (being in accordance with results obtained by Wriggers *et al.* (1996) for a 3D formulation – not shown in the figure). Even dealing with a load control procedure, convergence is easily achieved, with the whole displacement path being covered in 108 (automatically incremented) load steps. For the sake of completeness, evolution of the equivalent plastic strain, in successive deformation states, is shown in Fig. 5.79.

5.3 Enhanced solid-shell elements - Non-linear problems

In this section, the performance of the *HCiS12* enhanced solid-shell element is evaluated in the non-linear range. An extensive treatment of linear problems has been previously carried out by Alves de Sousa *et al.* (2003a), for a set of classical benchmarks in shell finite element analysis, not being covered in the present work.

5.3.1 Thick-wall sphere problem with geometric nonlinearity

Enhanced strain methods are known to provide non-stable response in the nonlinear range for large homogeneous compressive strain states. This pathology has been identified by a number of authors, with a sound analysis being carried out initially by Wriggers and Reese (1996) and, subsequently, in references (Korelc and Wriggers, 1996; Reese *et al.*, 1999; Reese and Wriggers, 2000; Reese, 2002, 2003), to name but a few. The common point in all these works is the focusing on plane-strain and full three-dimensional problems.

As the formulation for the present case, on the other side, is devoted to simulation of typical shell problems, the analysis of a (free) thick-wall sphere subjected to an internal pressure field was chosen in order to attest the level of occurrence of numerical instabilities in compression loading cases.

The problem is accounted for following the guidelines of Kasper and Taylor (2000), who considered a geometrically linear, nearly incompressible, problem. In the present work, material, boundary conditions and geometric data are kept the same (elastic modulus $\mathsf{E} = 250$, inner radius $\mathsf{R_i} = 7.5$, external radius $\mathsf{R_e} = 10.0$ and a varying Poisson's ratio ν). However, a nonlinear geometric behavior is now also taken into account, altogether with a higher pressure load (internal pressure $\mathsf{p} = 2.0$). Mesh topology also follows the one presented in reference (Kasper and Taylor, 2000), being reproduced in Fig. 5.80, where a symmetric (undeformed) one-eight of the total volume is depicted.

The evolution of the radial displacements with the Poisson's ratio, for nodes located at both the internal and external radius, is shown in Table 5.12. Apart from the variation of the results as incompressibility condition is progressively achieved, it is worth reporting that, for values of $\nu \geq 0.49999999$, convergence is completely lost and hourglass patterns appears (even for the relatively low displacement values involved).

5.3.2 Elastic large deflections (membrane) bending problem

This example relates to the analysis of a clamped beam which is loaded by a transverse force $\mathsf{F} = 1000$ on its free edge (see, for instance, references (Simo *et al.*, 1990a,b)). The resultant in-plane bending deformation is reproduced using a mesh of 10 solid-shell elements, in both regular and distorted patterns (Betsch *et al.*, 1996; Miehe, 1998). The elastic properties refer to a bulk modulus of $\kappa = 83.33{\times}10^5$ and a Lame's parameter of $\mu = 38.46\times10^5$, whilst the geometry is characterized by the relationship height/width/length of $\mathsf{h/w/l} = 0.1/0.1/1.0$ consistent units.

In order to infer the effect of mesh distortion in the nonlinear geometric range, three meshes are considered as represented in Fig. 5.81. The first two meshes are defined following the previous references, the skewed pattern of the second mesh obtained, in the present work, with the translation of nodes (0.05 unit) along the beam axis. A third mesh is taken into account (coming from the 90$^{\text{o}}$ rotation of the second one) in order to evaluate a *real* tridimensional mesh distortion level. The load-deflection curves for the displacement of nodes A and B is presented in Fig. 5.82 and compared to the solution presented by Simo, Fox and Rifai (Simo *et al.*, 1990a,b). For the shown meshes the results are almost the same, being in good agreement with those presented in the last references. It is worth noting that results with *HCiS12* solid-shell element also correspond to those obtained by Miehe (Miehe, 1998) (with a solid-shell enhanced+assumed strain formulation) and by Betsch *et al.* (Betsch *et al.*, 1996) (using a bilinear shell formulation incorporating extensibility of the director field and also enhanced strains).

5.3.3 Elastic large deflections (out-of-plane) bending problem

Consider now an elastic cantilever beam with length $\mathsf{L} = 10$ and rectangular section with constant width $\mathsf{w} = 1$, clamped in one end and subjected to (out-of-plane) point loads on the opposite (free) end. This example has been treated by a number of authors, either with extensible-director shell or solid-shell formulations, such as in (Simo *et al.*, 1990b), (Büchter *et al.*, 1994), (Parisch, 1995), (Miehe, 1998) and (el-Abbasi and Meguid, 2000), among others.

Following the last two references, the thickness of the beam is taken as $\mathsf{a} = 0.1$, and the material properties are defined as $\mathsf{E} = 10^7$ and $\nu = 0.3$. The external load considered has a constant value of $\mathsf{F} = 40 \times \lambda$, where for the present case λ is a geometrical factor, function of the thickness, and defined as ($\lambda = 10^3 \times \mathsf{a}^3$). In the present work three mapped meshes were considered, with 10, 16 and 20 *HCiS12* elements along the length direction.

For the small deformation theory, a solution of 16.0 consistent unities for the tip displacement can be advanced (el-Abbasi and Meguid, 2000), according to linear beam theory. In this case, *HCiS12* element gives results of 15.820 (10 elements' mesh), 15.880 (16 elements' mesh) and 15.890 (20 elements' mesh).

In case of large rotations and displacements, the same load level as before is now applied in 10 equal steps, as proposed by el-Abbasi and Meguid (2000). Following this reference, solutions are compared to a theoretical one, coming from the work of Frisch-Fay (1962). The analysis of the present results for the three meshes and the theoretical one is presented in Fig. 5.83. For the three meshes, it is noticeable the performance of the proposed element, with solutions in good agreement with the reference one. Still referring to the work of el-Abbasi and Meguid (2000), no Poisson's locking appears with *HCiS12* element in this test case.

Focusing on the 16×1×1 mesh, and based on the proposal of Hauptmann *et al.* (2000), a set of numerical analysis with different Poisson's ratio is carried out. The load level is the same as before, being likewise applied in 10 equal steps. The results presented in Fig. 5.84 clearly show a virtually insensitivity of the load-deflection curve for the various Poisson's coefficients presented.

5.3.4 Nonlinear geometric pinching of a clamped cylinder

In this test problem an elastic cylindrical shell, fully clamped at one end, is subjected to a pair of concentrated loads at its free end. Following references dealing with shell elements, such as Stander *et al.* (1989); Brank *et al.* (1995); Ibrahimbegović *et al.* (2001); Fontes Valente *et al.* (2003) and, more recently, Sze *et al.* (2004), a regular mesh of 16×16 elements is employed (Fig. 5.85). An additional mesh topology with 20×20 solid-shell elements over the mid-surface of the cylinder is also considered. In both cases, only 1 element along the radial direction is employed. For the sake of comparison, Sze *et al.* (2004) analyses the performance of Abaqus shell element *S4R* (ABAQUS, 2002a), obtaining reliable results with mesh topologies consisting of 32×32 and 40×40 elements.

Elastic constitutive parameters are Young modulus $\mathsf{E} = 2.0685 \times 10^7$ and Poisson coefficient $\nu = 0.3$. The length of the cylinder is $\mathsf{L} = 3.048$, with mean radius of $\mathsf{R} = 1.016$ and thickness $\mathsf{a} = 0.03$. Nominal load in Fig. 5.85 is $\mathsf{F}_{\mathsf{tot}} = 1600 \times \lambda$, where the load factor employed is supposed to vary between $\lambda = 0.0$ to $\lambda = 1.0$. Due to symmetry, only 1/4 of the structure needs to be meshed.

The results obtained with *HCiS12* element for the deflection of the point under the concentrated load is represented in Fig. 5.86, and compared to those of Brank *et al.* (1995). The value of the cylinder radius is highlighted in the picture, establishing the physical limit of the deformation. From the last picture it is clear that the refined mesh of $20 \times 20 \times 1$ is necessary in order the results can be in good agreement with those from the reference. However, the overall predictive capability of the presented solid-shell formulation in an example traditionally analyzed with shell elements is worth noting. In Fig. 5.87 successive deformed equilibrium configurations at different load stages are shown for the coarser mesh over one half of the cylinder, until a value of displacement near its radius.

5.3.5 Unstable behavior of a shallow roof structure

In this classical shell example, the snap-through and snap-back load-displacement path of a cylindrical shell is analyzed (see references Horrigmoe and Bergan (1978); Crisfield (1981); Surana (1983); Oliver and Oñate (1984); Sansour and Bufler (1992); Cho *et al.* (1998); Eriksson and Pacoste (2002); Massin and al Mikdad (2002); Fontes Valente *et al.* (2003); Sze *et al.* (2004), to name but a few) . The structure, schematically represented in Fig. 5.88 (not on scale), is mapped with 5×5 *HCiS12* elements over one-quarter of its mid-surface, along with 2 elements in the thickness direction. The imposition of these two elements is related to the proper reproduction of the hinged support over the straight edges. About the input data for this problem, linear dimensions are $\mathsf{L}_1 = 508.0$ and $\mathsf{L}_2 = 507.15$, with a nominal radius $\mathsf{R} = 2540.0$ and thickness value of $\mathsf{a} = 6.35$. Material parameters are $\mathsf{E} = 3102.75$ and $\nu = 0.3$. The maximum load level attained is equal to $\mathsf{F}_{\mathsf{tot}} = 1000$.

The displacement along OZ direction for points A and B is reproduced in Fig. 5.89, plotted against the reference load level and compared to the solution advanced by Horrigmoe and Bergan (1978), coming from a shell formulation. It is noticeable the agreement between both solutions, with the proposed approach spanning the whole nonlinear range in a total of 39 arc-length controlled steps.

A deeper insight into the performance of the *HCiS12* solid-shell element can be obtained by comparisons with the results coming from the hexahedral finite element proposed in the work of Areias *et al.* (2003a) (detailed in Areias *et al.* (2003b)). The latter formulation is also based on the *EAS* method, but now relying on the use of 18 internal variables per element, being *similar* to the *HCiS18* solid element on Chapter 3 (references Alves de Sousa *et al.* (2003a,b); Alves de Sousa (2003c)), in the sense that derivatives of a bubble-function are employed in the enhanced strain-displacement matrix.

Back to the example in analysis, in the work of Areias *et al.* (2003a) a slightly more refined mesh, consisting of 6×6×2 elements, is adopted. The corresponding displacement-load path is presented in Fig. 5.90, where it is visible the close correspondence between the results coming from Areias *et al.* (2003a) and those obtained with the solid-shell element *HCiS12*, no matter the lower number of internal variables of the latter formulation.

5.3.6 Geometric- and material- nonlinear analysis of a pinched hemispherical shell

The well-known nonlinear geometric hemispherical shell test case, introduced by Simo *et al.* (1990a), is now considered with the inclusion of elastoplastic effects. This combined nonlinear behavior has been previously investigated by Masud and Tham (2000), based on a class of reduced integrated solid elements (Liu *et al.*, 1998; Masud *et al.*, 2000).

According to reference (Masud and Tham, 2000), geometric and elastic parameters, as well as restraint conditions, are kept the same as in the work of Simo *et al.* (1990a), while a new set of plastic properties in coherent unities (initial yield stress $\sigma_{y0} = 6.825 \times 10^5$; isotropic linear hardening factor $\mathsf{H}_{\mathsf{iso}} = 6.825 \times 10^6$) are now introduced.

In (Masud and Tham, 2000), a maximum load level of $\mathsf{F} = 400.0$ is proposed (in opposition to the value of 200.0 in (Simo *et al.*, 1990a)), along with mapped meshes of 16×16×2 and 18×18×2 elements. For the sake of comparison, the results using the last topology are included in this work.

In the present simulation, a coarser mesh of 16×16×1 *HCiS12* solid-shell elements was adopted. The results obtained for the displacement along the OX and OY directions (traction and compression external loads, respectively) are represented in Fig. 5.91. It is noticeable the good correspondence between the present and reference results, even with the lower number of elements in the earlier case. It is also worth noting that the complete deformation path is obtained in 20 steps, 5 times less than the number of increments adopted by Masud and Tham (2000). The deformed configuration for the maximum load level is shown in Fig. 5.92.

5.3.7 Elastic and elastoplastic stretching of a short cylinder with free ends

A cylindrical shell is submitted to a pair of concentrated forces, inducing large displacements and rotations to the elements. A schematic representation is presented in Fig. 5.93 where, due to symmetry reasons, only one octant of the hole shell is showed. Previous publications dealing with this example include, among others, the works of Peng and Crisfield (1992), Sansour and Bufler (1992), Jiang and Chernuka (1994a), Brank *et al.* (1995), Masud *et al.* (2000), Ibrahimbegović *et al.* (2001) and Fontes Valente *et al.* (2003). In all of these cases, only geometric nonlinearities were taken into account, whereas a nonlinear material analysis has previously been considered in the work of Masud and Tham (2000).

The starting point relies on an initially cylindrical geometry characterized by a length of $\mathsf{L} = 10.35$, radius of $\mathsf{R} = 4.953$ and a constant thickness value $\mathsf{a} = 0.094$. Material properties are: Young modulus $\mathsf{E} = 10.5{\times}10^6$, and Poisson's ratio $\nu = 0.3125$. No boundary conditions are applied to the free ends of the shell, being the load pair responsible for the equilibrium of the cylinder. Plastic parameters are the initial yield stress $\sigma_{y0} = 1.05{\times}10^5$, and a linear isotropic hardening coefficient of $\mathsf{H}_{\mathsf{iso}} = 10.5 \times 10^5$, as adopted in reference (Masud and Tham, 2000).

Mesh topologies are analogous to those employed in (Fontes Valente *et al.*, 2003), that is: $12 \times 8 \times 1$ *HCiS12* elements, regular and distorted, and also $16 \times 8 \times 1$ elements (regular only). The numbers relate to elements along the periphery, the semi-length and radial directions, respectively. In Fig. 5.93, the distorted pattern with $12{\times}8{\times}1$ elements is schematically represented. The main goal is to evaluate the effects of mesh distortions in the final solution of the proposed solid-shell element. For this distorted mesh, the element most far away from the load point is 10 times larger than the smaller one.

The maximum load level, both for the elastic and elasto-plastic cases, is $\mathsf{F}_{\mathsf{tot}} = 40000{\times}\lambda$, where λ ranges from 0.0 until 1.0. Results for the deflection of points A and B, as a function of the λ parameter, are given respectively in Fig. 5.94 and 5.95 (for the purely nonlinear geometric case) and in Fig. 5.96 and 5.97 (for the elasto-plastic nonlinear geometric case). For the present *HCiS12* element, all curves were obtained with the arc-length procedure, as stated before, in a total of 26 automatic load steps.

In both the elastic and elasto-plastic cases, the present solution tends to follow the one obtained in (Masud *et al.*, 2000) and (Masud and Tham, 2000), but with less elements. For the coarser meshes, in the elastic case, there is a deviation of results when compared to the earlier reference. It is also interesting to note, for this example, the increase in displacements when distorted elements are employed, in opposition to what happened with the enhanced shell elements (see Figures 5.59 and 5.60). For the refined mesh employed, the results are acceptable either in the elastic and elasto-plastic regimens, still keeping a lower number of increments to achieve the full deformation path.

Once again it would be interesting to compare the results obtained with the *HCiS12* solid-shell element with those coming from the work of Areias *et al.* (2003a). In the latter, only the elastic nonlinear geometric configuration was analyzed, with the aid of a *regular* mesh consisting of $16 \times 8 \times 2$ elements, each one with 18 element-wise *EAS* variables. Results for points A and B are shown in Fig. 5.98 and 5.99, respectively, for the load range of interest, following the proposal of Masud *et al.* (2000) and Masud and Tham (2000), and the references herein. It can be seen that the *HCiS12* element results are comparable to those presented by the solid-shell element from Areias *et al.* (2003a), even (for that case) involving less elements in the mesh and less internal variables in each element.

5.3.8 Elasto-plastic analysis of a simply supported plate with pressure loads

In this test case the inflation of a square plate is analyzed. This example has been treated before in a number of references, including Miehe (1998); Betsch and Stein (1999); Eberlein and Wriggers (1999); Doll *et al.* (2000); Hauptmann *et al.* (2000) and Harnau and Schweizerhof (2002). Along these references, a variety of mesh topologies is employed, while in references (Doll *et al.*, 2000; Harnau and Schweizerhof, 2002) a higher number of Gauss points (6) is employed for the integration in thickness direction.

The geometric properties for this test are defined by the relations length/width/thickness of 508/508/2.54 consistent unities (Betsch and Stein, 1999). The plate is submitted to an uniformly distributed load of $\mathsf{p} = 60\,\mathsf{p}_0$, where $\mathsf{p}_0 = 10^{-2}$. Material properties are given as $\mathsf{E} = 6.9 \times 10^4$, with a perfectly plastic law characterized by an initial yield stress of $\sigma_{y0} = 248$ ($\mathsf{H}_{\mathsf{iso}} = 0$). Boundary conditions only restrain the displacements in the direction normal to the plate, being applied to just the lower nodes of the mesh (defined over one quarter of the plate). Do to this fact, it is valid the occurrence of a sort of "edge-rotations" and, as the pressure value increases, the plate assumes a "pillow-type" deformation mode, changing from a bending dominated deformation (in the beginning) to a membrane dominated one.

From the meshes available for comparison, a 15×15×1 topology, refined in the corners (inspired by Eberlein and Wriggers (1999)) and a second one with 24 × 24 × 1 mapped elements (following Betsch and Stein (1999)) are adopted. The so-called "6-parameter" formulation on reference (Eberlein and Wriggers, 1999) is the one chosen for comparison purposes. For both meshes, the maximum load level is attained in 45 load steps, and the resulting out-of-plane displacement curves are shown in Fig. 5.100, where the central node of the plate was monitored. It can be seen that the present results are in agreement with both reference solutions, although the predictive capability of few *HCiS12* elements approaches the values obtained with the refined mesh, even with a two-point integration rule across thickness direction. The deformed configurations for the full load and both meshes are represented in Fig. 5.101.

As carried out in some of the previous examples, some conclusions can be taken from the comparison of results coming from the present *HCiS12* solid-shell element and the one from the work of Areias *et al.* (2003a), accounting for more internal variables. In the latter reference, a mapped mesh consisting of 24×24× 1 elements is considered, with the corresponding results been shown in Fig. 5.102. In the figure, results coming from the work of Eberlein and Wriggers (1999) are kept for reference. It is interesting to note that the formulation presented by Areias *et al.* (2003a), still with more internal variables per element, provided results (for this example) stiffer than the ones obtained with the *HCiS12* solid-shell element. In fact, the load-displacement curve coming from the last reference (with the refined mesh of 24×24× 1) is comparable to the one obtained with 15×15× 1 *HCiS12* elements. Nevertheless, it is worth remembering that, from Fig. 5.100, results obtained with the *HCiS12* element are in accordance to those referred to by Betsch and Stein (1999), using a shell formulation.

As carried out with the shell version of this example (Section 5.2.12), the increase of the pressure level over the plate tend to induce the appearance of wrinkles, shown in its onset on Fig. 5.103. This phenomenon was also related by Areias *et al.* (2003a), although with a deformed configuration presenting just one wrinkle at each mid-side of the inflated plate, whereas in the present case two wrinkles are formed, in the same pattern as happened within the presented shell formulation (see example at Section 5.2.12).

5.3.9 Elasto-plastic nonlinear geometric response of a pinched cylinder

This example deals with the elastoplastic deformation of a thin-walled cylinder, submitted to a pair of concentrated forces. It is a classical test to analyze the behavior of finite element in problems involving localized plasticity and strong shape modifications. Earlier works dealing with this problem includes the contributions of Simo and Kennedy (1992), Wriggers *et al.* (1996), Hauptmann and Schweizerhof (1998), Miehe (1998), Eberlein and Wriggers (1999) and Wagner *et al.* (2002), among others.

For the present case, comparisons will be carried out with the results presented in references (Wriggers *et al.*, 1996) and (Miehe, 1998). Following these guidelines, the cylinder geometry is characterized by a relation radius/thickness/length of 300/3/300 consistent unities, respectively. The boundary conditions are such that the circular shape of the cylinder's end is preserved although free deformation in longitudinal direction is allowed. Once each element has upper and lower nodes, a "hard support", in the sense of Wagner *et al.* (2002), is considered. A von Mises yield criterion is assumed, with yield stress $\sigma_{y0} = 24.3$ and a linear isotropic hardening parameter $\mathsf{H}_{\mathsf{iso}} = 300$. Elastic parameters are $\kappa = 2500$ and $\mu = 1154$ (Miehe, 1998). Two discretization models were accounted for: a coarse mesh of 16×16×1 elements (Wriggers *et al.*, 1996; Wagner *et al.*, 2002) and a finer one with 32×32×1 elements (Wriggers *et al.*, 1996; Miehe, 1998; Eberlein and Wriggers, 1999), applied over one eighth of the cylinder, benefiting from symmetric geometry. The simulation is performed in a load-controlled way and the whole path is covered, with the arc-length method, in 65 steps for both meshes. The obtained results for the displacement value in the external load direction (against this same load) are presented in Fig. 5.104. For both meshes, a good agreement between the present and reference results is obtained. For the refined mesh, the *HCiS12* element agrees quite well with the results presented in the work of Miehe (1998). It is also worth noting that the apparent "snap-through" behavior noticeable in the 16×16×1 mesh almost disappear with the adoption of the 32×32×1 mesh, reproducing a mesh-dependent behavior already pointed out by Hauptmann and Schweizerhof (1998).

In a way similar to the example before, comparisons are carried out between the present *HCiS12* solid-shell element and the solid element introduced by Areias *et al.* (2003a), both grounded on the *EAS* approach. For completeness, results coming from the shell formulation proposed by Eberlein and Wriggers (1999) are also taken into account, being presented in Fig. 5.105. In a way similar to the last example, the 18-internal variable based element from Areias *et al.* (2003a) seems to behave in a way stiffer than both the *HCiS12* solid-shell and the shell formulation of Eberlein and Wriggers (1999), namely in the final stages of deformation. A remarkable point in the element coming from Areias *et al.* (2003a), for the present example, is the lack of instabilities in the load-deflection path for the coarse mesh presented by those authors (16×16×1 solid elements). Nevertheless, this numerical effect do disappear with mesh refinement, as can be clearly seen by the behaviour of the *HCiS12* solid-shell element and from the work of Eberlein and Wriggers (1999), for more refined meshes.

Finally, in Fig. 5.106 a sequence of deformed configurations for the adopted meshes is presented, starting from the undeformed point and ranging until the physically acceptable displacement value of 300 consistent unities (equal to the cylinder radius).

5.4 Industrial applications

5.4.1 Hydro-bulge forming of a circular plate including anisotropy

This example is a well-known and useful test to determine stress vs. strain curves as well as forming limit diagrams for a given material, being also adopted on the validation of anisotropic models. In this case, and although the geometric, loading and boundary conditions could induce symmetric strain contours with deformation, anisotropic properties of the 2008-T4 Aluminum alloy analyzed will inevitably lead to differences from purely isotropic plasticity models. For the latter case, approximate analytical solutions are available (Marciniak *et al.*, 2002). The chosen anisotropic constitutive model follows the criterion proposed by Barlat *et al.* (1991) for aluminum alloys, while implementation details are according the works of Parente (2003) and Parente *et al.* (2004).

The bulge forming starts with a circular plate with an initial radius $\mathsf{R} = 81$ mm and initial thickness $\mathsf{a} = 1.24$ mm. Isotropic material properties refer to Young modulus $\mathsf{E} = 69$ GPa, Poisson coefficient $\nu = 0.33$, isotropic hardening factor $\mathsf{H}_{\mathsf{iso}} = 0.0$, initial yield stress value of $\sigma_{y0} = 185.0$ MPa, saturation yield stress value of $\sigma_{y\infty} = 408.0$ MPa and exponential hardening factor $n = 6.14$. All these terms are interrelated in the evolution law for the yield stress level, as a function of the equivalent plastic strain value, in the form

$$\sigma_y = \sigma_{y0} + \mathsf{H}_{\mathsf{iso}}\,\epsilon^p + \left(\sigma_{y\infty} - \sigma_{y0}\right)\left(1 - \mathrm{e}^{-n\epsilon^p}\right) \tag{5.7}$$

Anisotropic parameters, in turn, are given as the values for the constant parameters to be used in the criterion proposed by Barlat *et al.* (1991), being numerically equal to $\mathsf{C}_1 = 1.223$, $\mathsf{C}_2 = 1.014$, $\mathsf{C}_3 = 0.986$, $\mathsf{C}_4 = 1.0$, $\mathsf{C}_5 = 1.0$, $\mathsf{C}_6 = 1.0$ and $\mathsf{m} = 11.0$, for the present example (Yoon, 1996; Cardoso, 2002).

The adopted finite element mesh consists of 392 elements, following the mesh distribution represented in Figure 5.107, where one-fourth of the plate is represented due to symmetry reasons. The same mesh was used either for shell or solid-shell elements, both adopting the same distribution over the circular plate. For the *S4E6P5* shell element, 5 Gauss points over the thickness direction were adopted, whilst for the *HCiS12* solid-shell element, that direction was discretized with one single element, corresponding to the use of 2 integration points. The finite element model is a simplified one, when compared to other authors (Yoon, 1996; Cardoso, 2002), since no contact between the blank-holder and the plate (blank) was taken into account. Instead, the borders of the plate are considered clamped, and the hydrostatic pressure load is represented by an uniform pressure load over the plate surface, with nominal value of $\mathsf{p}_0 = 4$ MPa.

Starting with the imposition of an isotropic von Mises material model, it is possible to establish a set of comparisons between the present shell and solid-shell formulations against results coming from shell and three-dimensional elements of Abaqus finite-element commercial code (shell elements *S4*, *S4R*, *S4R5* and 3D elements *C3D8* and *C3D8i*). Shell elements in Abaqus code have employed 5 Gauss points through-thickness direction, in accordance to what was done with the present shell element. In the same manner, the plate thickness was discretized by one three-dimensional element in the Abaqus model, corresponding to 2 Gauss points in that direction. The analysis of the out-of-plane apex point displacement evolution, with increasingly pressure levels, led to the graphs represented in Figures 5.108 and 5.109, for the shell and three-dimensional finite elements, respectively.

It is interesting to note that with the present shell and solid-shell formulations, both elements are able to avoid locking effects for the set of boundary, geometry and loading conditions. Additionally, for the present example, the methodology behind the enhanced shell and solid-shell elements has not revealed sensitivity to the mesh distortion (namely on the apex zone), which is frequently a strong pitfall for enhanced-based finite elements in the literature. The results obtained with the present finite elements are close to those obtained with Abaqus commercial code. Nevertheless, deviations appear between the simulation results with the *S4E6P5* and *HCiS12* finite elements and the experimental ones.

In order to assess the importance of the constitutive law on the quality of the solution, results with the *S4E6P5* shell element and the anisotropic criterion Yld'91 (Barlat *et al.*, 1991) are also considered. Experimental results (including anisotropic effects) give a final pole displacement of approximately 23 millimeters (Yoon, 1996). For the shell enhanced assumed strain element, results now including the anisotropic criterion of Barlat *et al.* (1991) are reproduced in Figure 5.110 and compared to the experimental data. At the final pressure level, the enhanced assumed strain shell formulation led to a pole displacement of 23.6 millimeters, which is in good agreement with the experimental solution, and considerably higher than the analogous result considering an isotropic yield criterion.

For the sake of completeness, equivalent plastic strain contours are presented for specimens with rolling directions at 0° and 45° relative to a reference direction OX. On algorithm terms, the local axis $\left(\mathbf{r}^1\right)$ of each Gauss point (Chapters 2 and 3) is initially taken along these directions, at the start of the numerical process. Subsequent deformation will drive the evolution of the local triad, as described in the chapters before. For a rolling direction of 0° with OX, the contour plots of the equivalent plastic strains are reproduced in Figure 5.111, for the maximum pressure level. For a rolling direction of 45° relative to the reference direction, contour plots of the equivalent plastic strain now change, as can be seen in Figure 5.112. From the last figure, it is visible the lack of concentricity of the contour curves, as well as the influence of measurements along distinct rolling directions, as expected when considering anisotropic constitutive evolution laws.

5.4.2 Forming of the S-Rail industrial component (*Numisheet'96*)

This (now classical) benchmark was proposed within the scope of the NUMISHEET (1996) International Conference, as the test *B2*, thereafter being known simply as the *S-Rail* problem. It consists in the forming, by deep-drawing, of an initial plane metal blank into a final component with a S-shaped three-dimensional geometry.

From the whole problem set posed at the Conference, only the forming of the aluminum alloy (Al 6111-T4) sheet will be simulated in this work. From the two blank-holding force levels proposed, the value of 10 KN was the one chosen. This combination of material and blank-holding force leads to interesting characteristics of the deformed final part, as will be seen in the following.

Simulation of contact and friction conditions were carried out by means of the implementation of the *HCiS12* enhanced assumed strain solid-shell element into Abaqus commercial code (*user defined* finite element capabilities). This allows for the full use of the contact search and stiffness contribution calculation directly from the commercial package.

Geometry definitions for the blank, die, punch and blank-holder are provided in the NUMISHEET (1996) proceedings. All the tools are considered rigid in the simulation. The initial thickness of the blank is $\mathsf{a} = 1.0$ mm, and the elastic material constants are the Young modulus $\mathsf{E} = 69$ GPa and the Poisson coefficient $\nu = 0.3$. Following indications posed on the last reference, the averaged value for the friction coefficient to be used in the simulation is equal to $\mu = 0.1$.

About the hardening constitutive law for this specific problem, the simulation was carried out following the indications of Stephen J. Makosey and Kwansoo Chung – at that time at ALCOA (Aluminum Company of America) – who belonged to the simulation group SB2.21 (NUMISHEET (1996), page 670 in the proceedings). The reason for this choice remains in the fact that those authors provide the complete set of parameters for the full characterization of the hardening law. In this sense, the yield behavior is assumed to be independent of the rate of deformation, with a hardening law following a Voce's function in the form

$$\sigma_y = \mathsf{A} - \mathsf{B}\,\mathrm{e}^{(-\mathsf{C}\epsilon^p)} \tag{5.8}$$

The set of constants in the equation was defined through ALCOA testing experiments, and happens to be $\mathsf{A} = 368$ MPa, $\mathsf{B} = 207$ MPa and $\mathsf{C} = 9.74$. The mesh employed in the simulation consists of 6000 solid-shell elements, with a total of 21160 nodes, and is in conformity with the mesh used by Areias *et al.* (2003b) who, on turn, adopts solid-shell elements with a higher number of internal variables (18) than in the present case.

Schematic views of the tools, the mesh and the deformed structure, as modelled in Abaqus commercial code, are presented in Figures 5.113, 5.114 and 5.115, respectively. In Figure 5.116, it is possible to assess the evolution of the punch height with the punch force, during the deformation process. From the set of 6 curves coming from experimental analysis, as published in the proceedings of the NUMISHEET (1996) Conference (page 637), only the upper and lower curves were reproduced and shown in the present work (references EB2.03 and EB2.01, respectively). From the graph in Figure 5.116, it is possible to infer that the results provided by the *HCiS12* solid-shell element, as implemented in

Abaqus, are within the range of results obtained experimentally.

The present results are also compared with results coming from other finite element (implicit) codes, and published in the proceedings of the NUMISHEET (1996) Conference (page 742). The corresponding graph can be seen in Figure 5.117. In the latter, all the 6 curves presented in the conference proceedings were now reproduced, for the sake of completeness. All results have distinct patterns, although it is valid to say that the curve obtained with the *HCiS12* solid-shell element follow the evolution trend of the majority of authors.

Finally, Figures 5.118, 5.119 and 5.120 provide detailed views of the formed final part. For the material and blank-holder force adopted in the simulation, wrinkles onset is visible at the end of the forming process. The wrinkling zone is more noticeable in the detailed pictures on Figures 5.119 and 5.120, and its presence in the real formed part was actually verified by experimental means.

5.5 Tables

	normalized deflection ($w_{fem}/w_{analytical}$)	
formulation	Mesh I	Mesh II
Ahmad *et al.* (1970)	0.000	0.000
Bathe and Dvorkin (1985)	1.010	0.930
S4E6P5	0.997	0.984
S4E6P7	0.997	0.984
MITC4-E2	1.007	0.927

Table 5.1: Plates with distorted meshes - Results for point C for simply-supported edges and uniform pressure loads. Mesh II uses $\Delta = \mathsf{L}/10$

	normalized deflection ($w_{fem}/w_{analytical}$)		
distortion value (Δ)	Sansour and Bocko (1998)	**S4E6P5**, **S4E6P7**	**MITC4-E2**
0.0	0.8310	0.8694	0.8694
2.5	0.0344	0.8267	0.8650
5.0	0.0085	0.7739	0.8533
7.5	0.0036	0.7174	0.8352
10.0	0.0020	0.6632	0.8114
12.5		0.6161	0.7792

Table 5.2: Influence of distortion level Δ on mesh II - Results for point C for clamped edges and concentrated load

	deflection value		
distortion parameter (δ)	S4	S4R	S4R5
0	84.69	907.1	7356.0
1	57.69	838.1	3536.0
2	30.31	666.3	1302.0
3	24.46	471.4	578.1
4	14.74	303.7	304.8
5	7.325	154.6	189.3

Table 5.3: Cantilever beam with distorted mesh - Results for *ABAQUS* bilinear shell elements

formulation	absolute deflection	
	2 × 2 elements	4 × 4 elements
Ahmad *et al.* (1970)	0.0082	0.0347
Dvorkin and Bathe (1984)	0.8683	0.9690
Andelfinger and Ramm (1993)	0.8885	0.9762
S4E6P5	0.8694	1.0150
S4E6P7	0.8694	1.0150
MITC4-E2	0.8694	1.0020
analytical solution	1.0000	

Table 5.4: Clamped plate - Central point deflection for the concentrated load case

formulation	normalized deflection		
	2 × 2 elements	4 × 4 elements	5 × 5 elements
Ahmad *et al.* (1970)	0.000	0.000	0.000
Kui *et al.* (1985)	1.211	1.250	1.256
Dvorkin and Bathe (1984)	1.211	1.251	1.256
S4E6P5	1.211	1.251	1.256
S4E6P7	1.211	1.251	1.256
MITC4-E2	1.211	1.251	1.256
analytical solution		1.270	

Table 5.5: Clamped plate - Central point normalized deflection ($\times 10^{-3}$) for the distributed load case

Mesh	Dvorkin and Bathe (1984)	Andelfinger and Ramm (1993)	Yunhua and Eriksson (1999)
4×4	3.9182	4.2122	3.9305
8×8	3.8991	4.2239	3.9841
16×16	4.1875	4.3738	4.2727
32×32	4.4098	4.4827	4.4668

Mesh	Ahmad *et al.* (1970)	Ref. Solution
4×4	0.1151	4.6400
8×8	0.3841	4.6400
16×16	0.9882	4.6400
32×32	1.9110	4.6400

Mesh	**S4E6P5**	**S4E6P7**	**MITC4-E2**
4×4	4.5090	4.5090	4.5090
8×8	4.4380	4.4380	4.4380
16×16	4.4820	4.4820	4.4820
32×32	4.5610	4.5610	4.5610

Table 5.6: Morley's skew plate - Out-of-plane deflection of point C for different meshes and formulations

	normalized deflection $w_{fem}/w_{ref.}$	
mesh size	Simo *et al.* (1989b)	**S4E6P5, S4E6P7, MITC4-E2**
1×6	0.9914	1.0000
2×12	0.9978	0.9986
4×24	0.9993	0.9978
8×48	1.0000	1.0000

Table 5.7: Twisted beam - Normalized results for load case (a) in Fig. 5.12

	normalized deflection $w_{fem}/w_{ref.}$	
mesh size	Simo *et al.* (1989b)	**S4E6P5, S4E6P7, MITC4-E2**
1×6	0.9505	1.0000
2×12	0.9860	0.9863
4×24	0.9971	0.9962
8×48	1.0000	1.0000

Table 5.8: Twisted beam - Normalized results for load case (b) in Fig. 5.12

	S4E6P5, S4E6P7, MITC4-E2	
number of elements	absolute value	normalized values
3	0.8390	1.1585
12	0.7327	1.0117
48	0.7258	1.0002
192	0.7255	1.0001
768	0.7243	1.0000

Table 5.9: Circular plate with clamped edges and concentrated loads - Convergence of results for central point deflection with the mesh refinement presented in Fig. 5.13

	normalized result $w_{fem}/w_{ref.}$	
nb. elements	Hughes and Tezduyar (1981)	Simo and Rifai (1990)
3	not available	not available
12	0.9809	0.9281
48	0.9954	0.9827
192	0.9989	0.9958
768	0.9998	0.9990
nb. elements	Piltner and Joseph (2001)	**S4E6P5, S4E6P7, MITC4-E2**
3	not available	0.8605
12	0.9366	0.9448
48	0.9819	0.9861
192	0.9954	0.9969
768	0.9788	0.9996

Table 5.10: Circular plate with simply-supported edges and pressure loads - Convergence of results for central point deflection with the mesh refinement presented in Fig. 5.13

	normalized result $(w_{fem}/w_{analytical})$		
formulation	5 nodes per side	7 nodes per side	9 nodes per side
Ahmad *et al.* (1970)	0.06806	0.10152	0.13439
Dvorkin and Bathe (1984)	0.93651	not available	0.97315
Andelfinger and Ramm (1993)	1.04068	not available	1.00625
S4E6P5	1.00099	1.01323	1.00165
S4E6P7	1.00099	1.01323	1.00165
MITC4-E2	0.90046	0.95800	0.96892

Table 5.11: Scordelis-Lo roof problem - Normalized result at point A on the free edge

	radial displacement $\left(\times 10^{-2}\right)$	
Poisson's ratio	$\mathsf{R_i} = 7.5$	$\mathsf{R_e} = 10.0$
$\nu = 0.3$	8.750	6.305
$\nu = 0.49$	8.049	4.589
$\nu = 0.499$	8.014	4.509
$\nu = 0.4999$	8.000	4.510
$\nu = 0.49999$	8.000	4.540
$\nu = 0.499999$	8.000	4.583
$\nu = 0.4999999$	7.989	4.598

Table 5.12: Nonlinear geometric thick-wall sphere - Evolution of radial displacements for an internal pressure level $\mathsf{p} = 2.0$

5.6 Figures

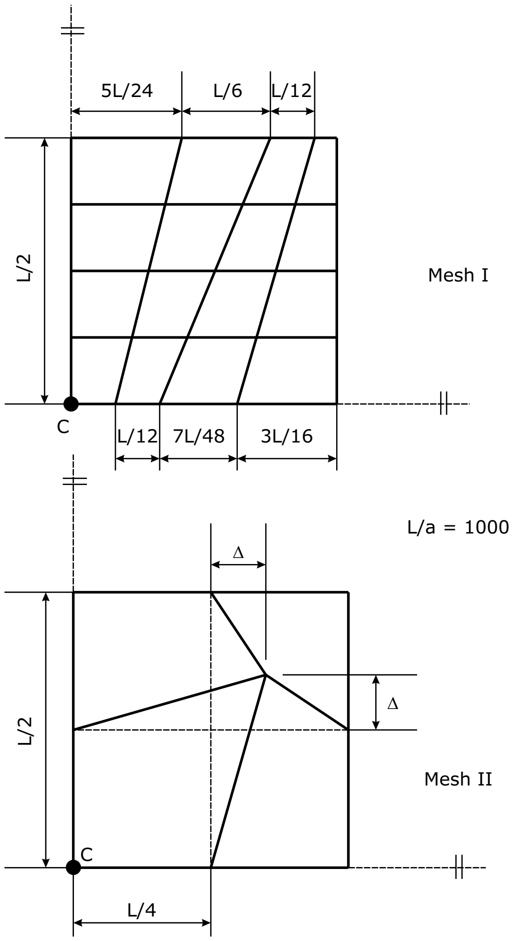

Figure 5.1: Distorted meshes for thin plate problems

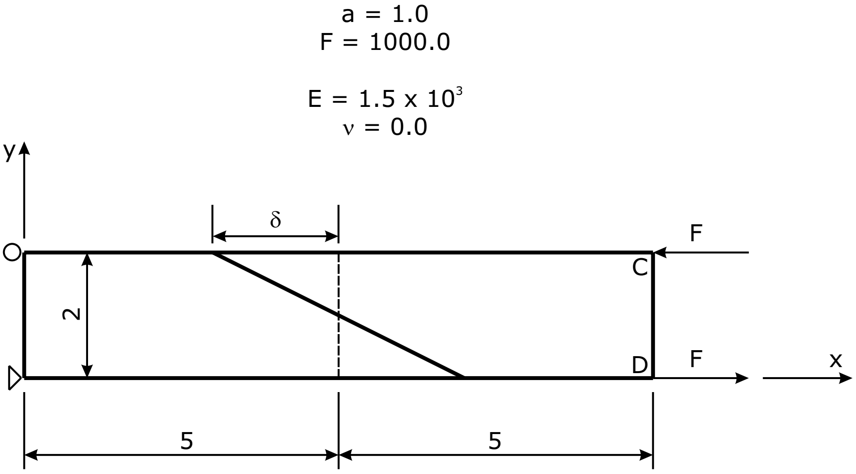

Figure 5.2: Cantilever beam with distorted mesh - Model definition

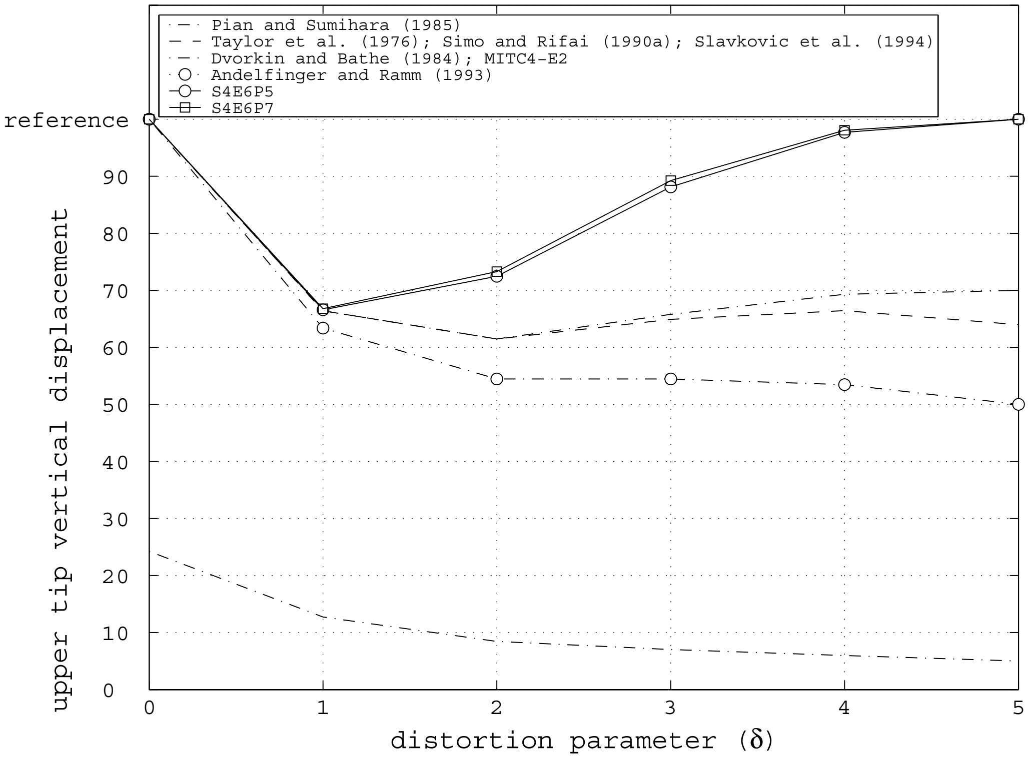

Figure 5.3: Cantilever beam with distorted mesh - Sensitivity to mesh distortion when monitoring point C in Fig. 5.2

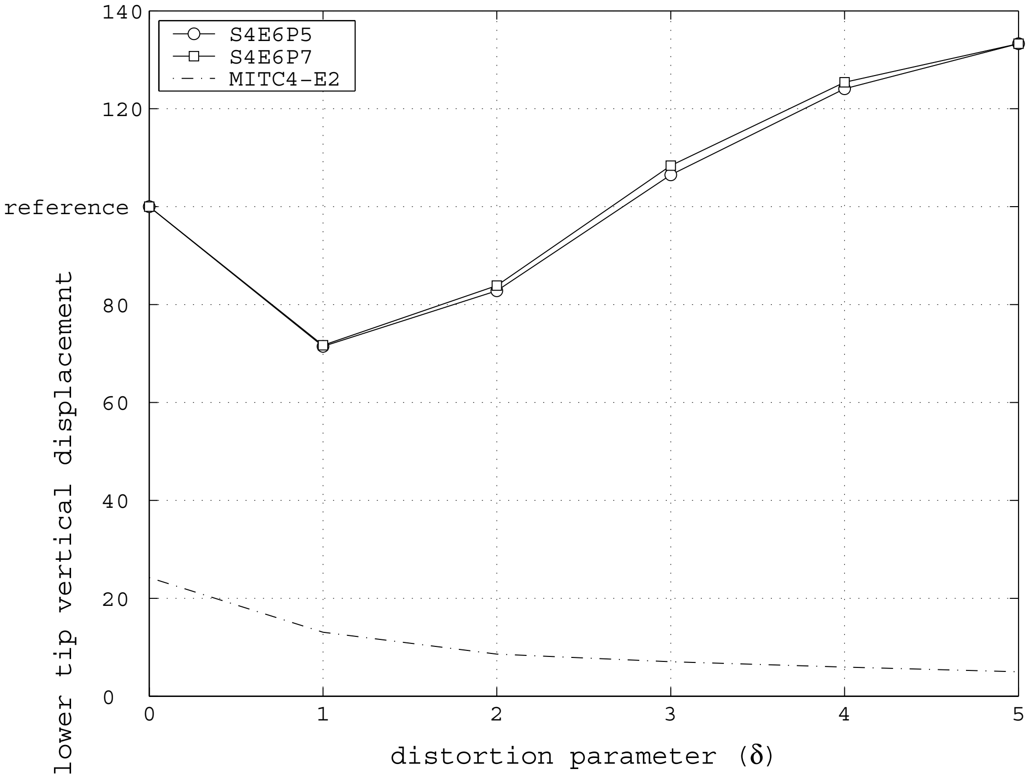

Figure 5.4: Cantilever beam with distorted mesh - Sensitivity to mesh distortion when monitoring point D in Fig. 5.2

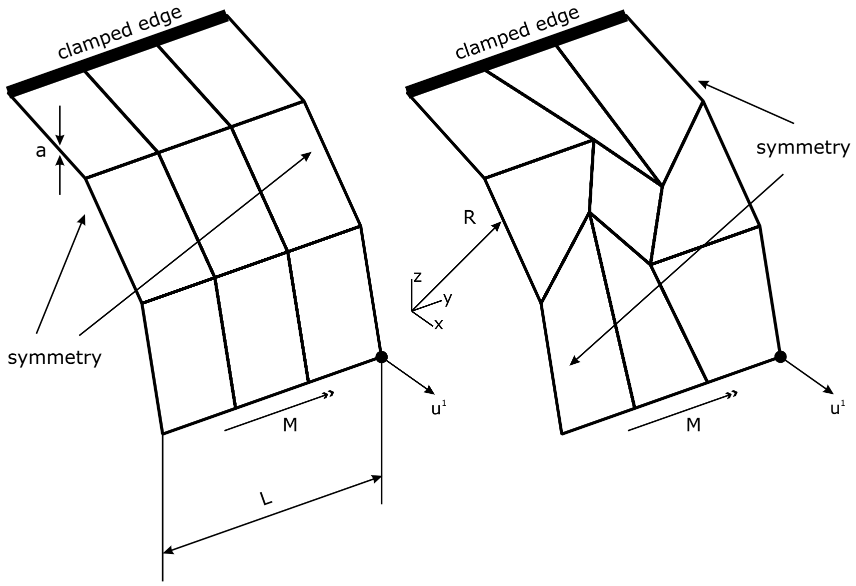

Figure 5.5: Clamped infinitely long curved panel - Regular and distorted coarse meshes

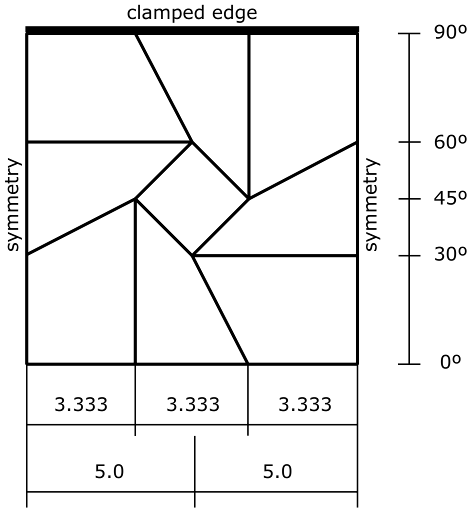

Figure 5.6: Clamped infinitely long curved panel - Detail on nodes positioning for the distorted mesh

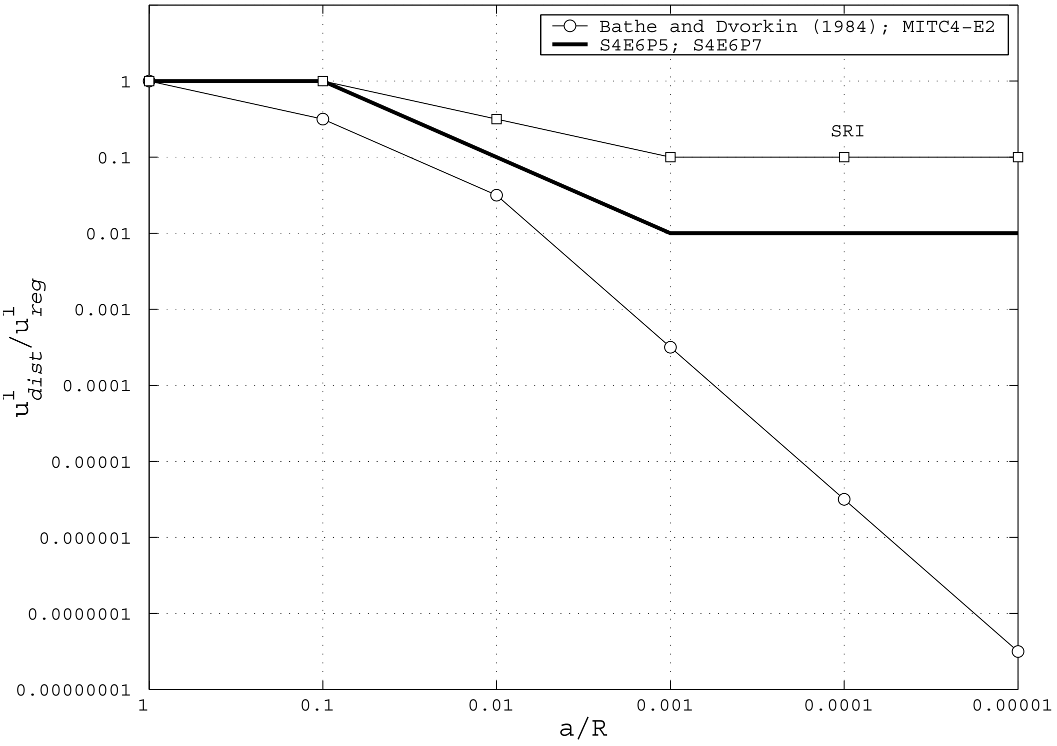

Figure 5.7: Clamped infinitely long curved panel - Comparative results

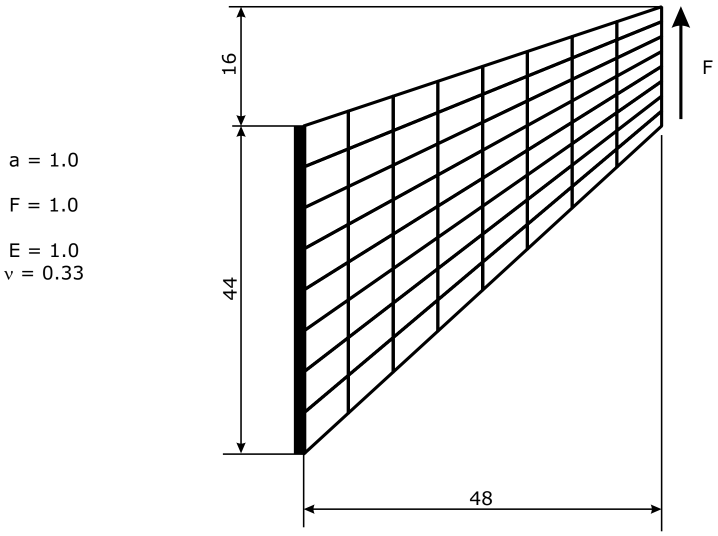

Figure 5.8: Cook's membrane problem - Geometry, material and boundary conditions

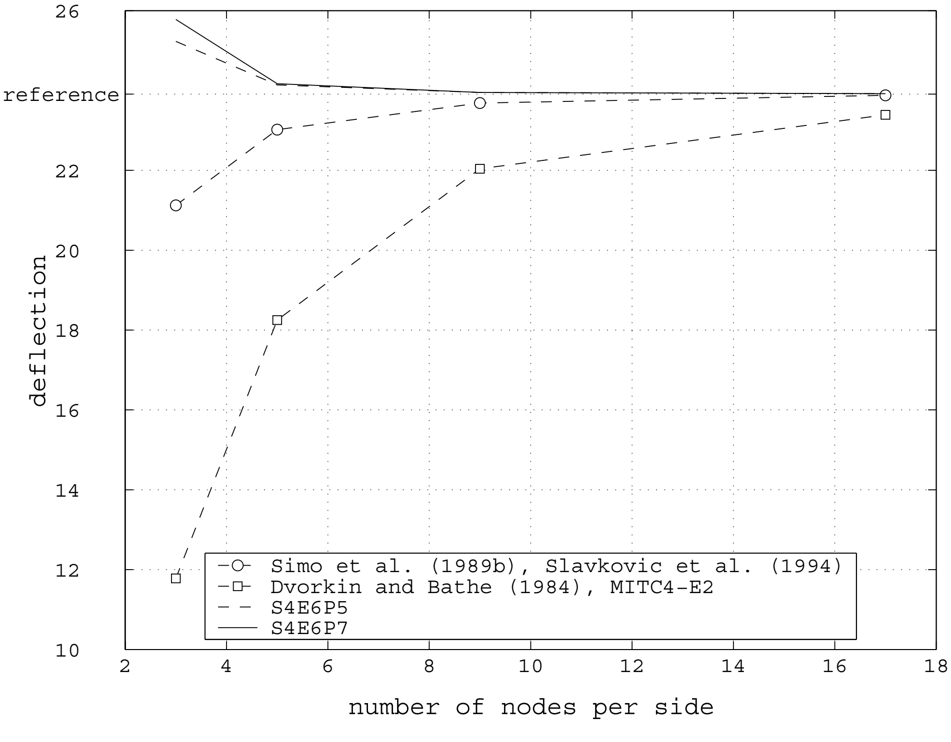

Figure 5.9: Cook's membrane problem - Convergence behavior

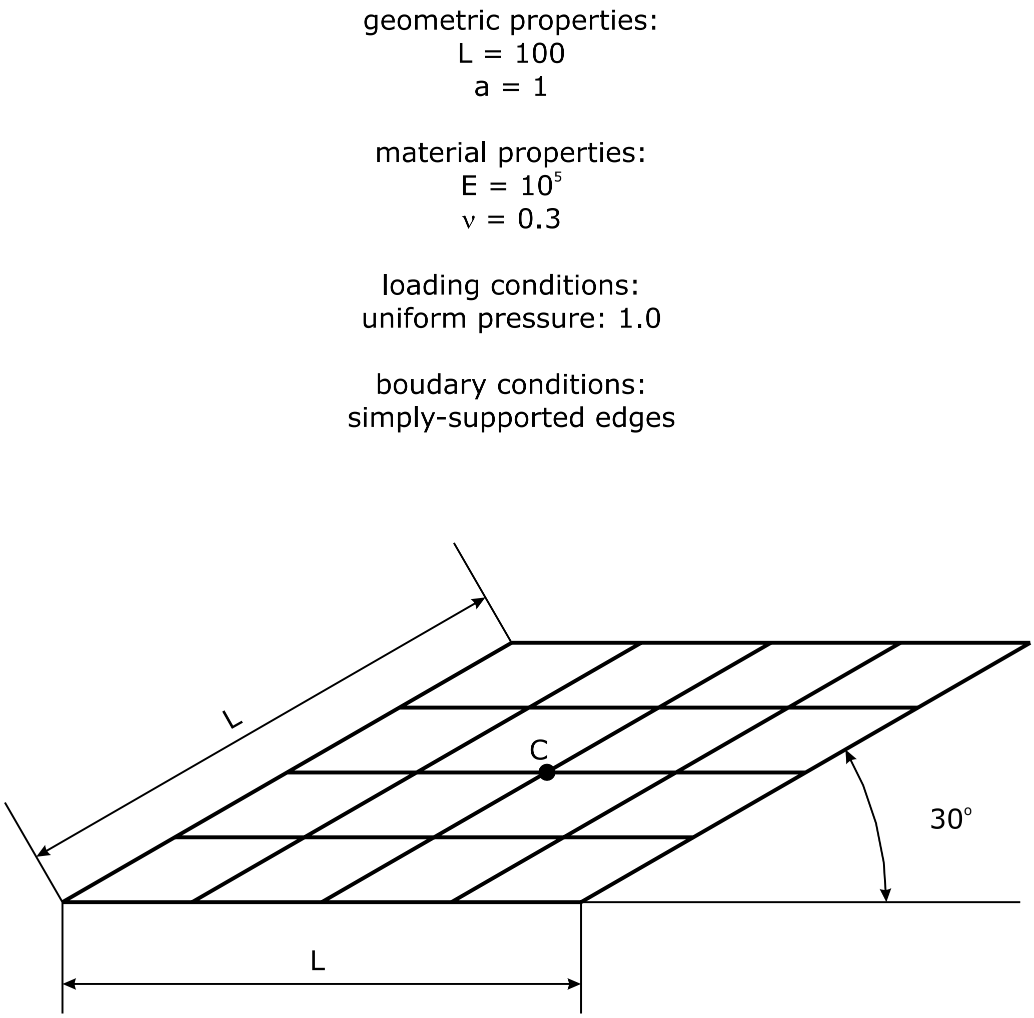

Figure 5.10: Morley's skew plate - Problem definition

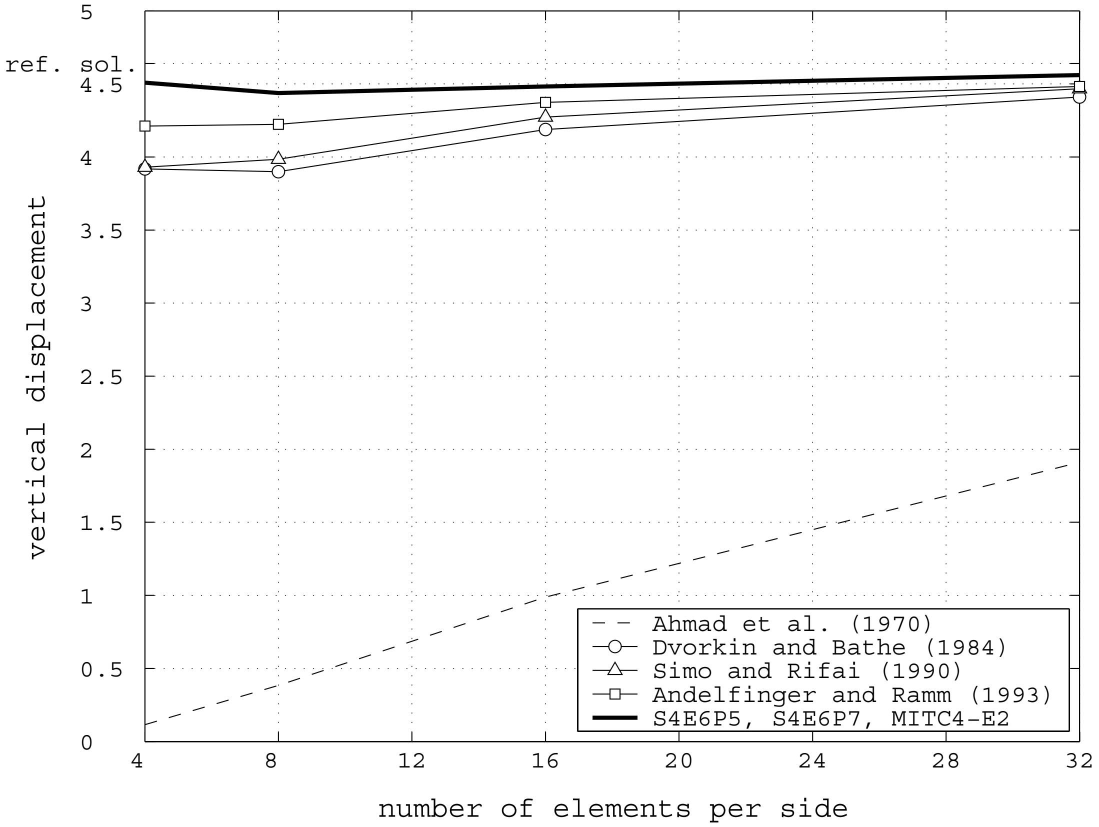

Figure 5.11: Morley's skew plate - Convergence verification with mesh refinement

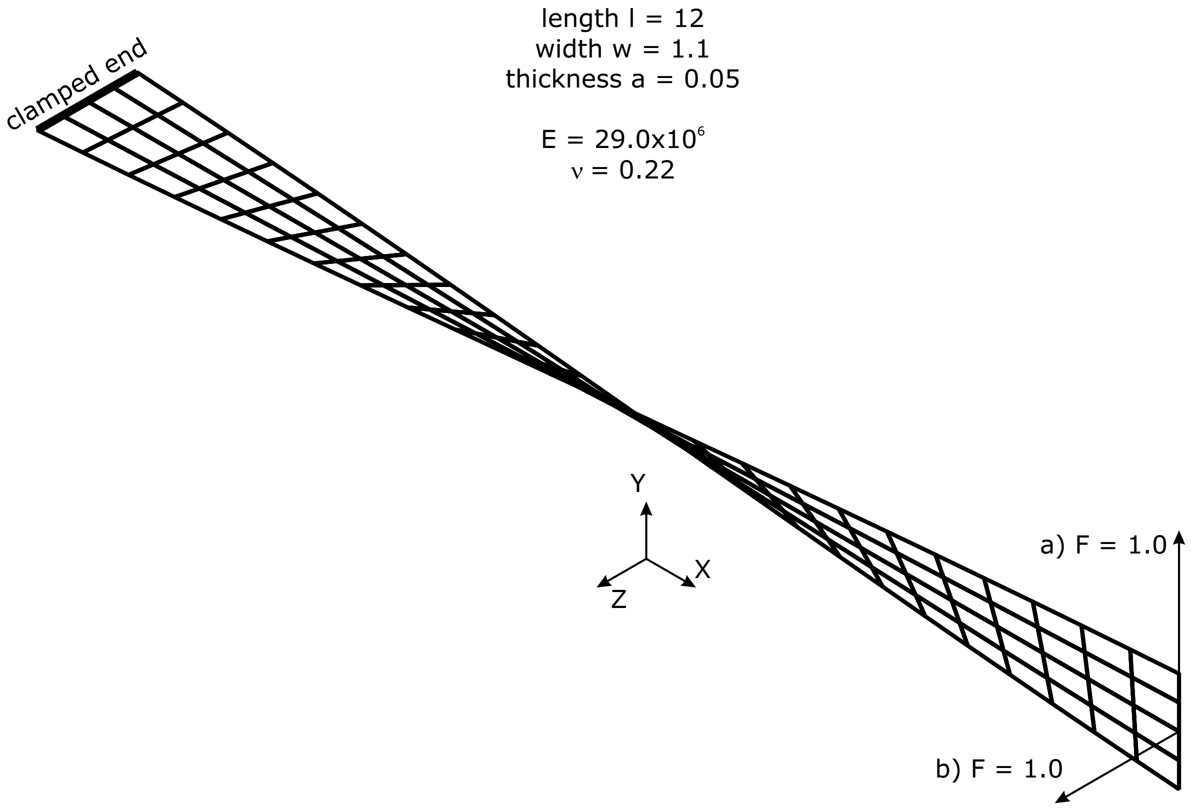

Figure 5.12: Twisted beam model with the representation of the two cases of shear loading: (a) in the width direction, (b) in the thickness direction

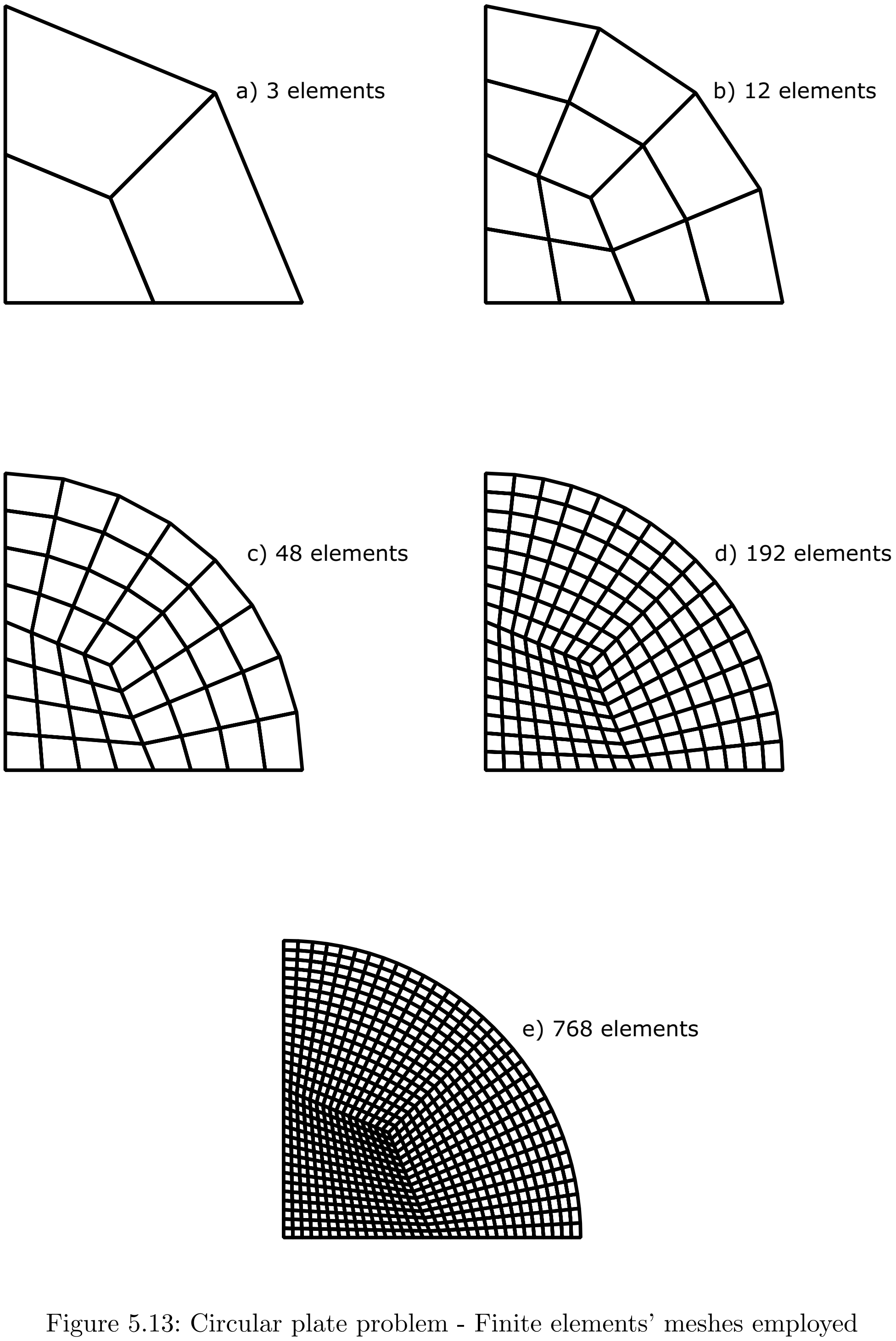

Figure 5.13: Circular plate problem - Finite elements' meshes employed

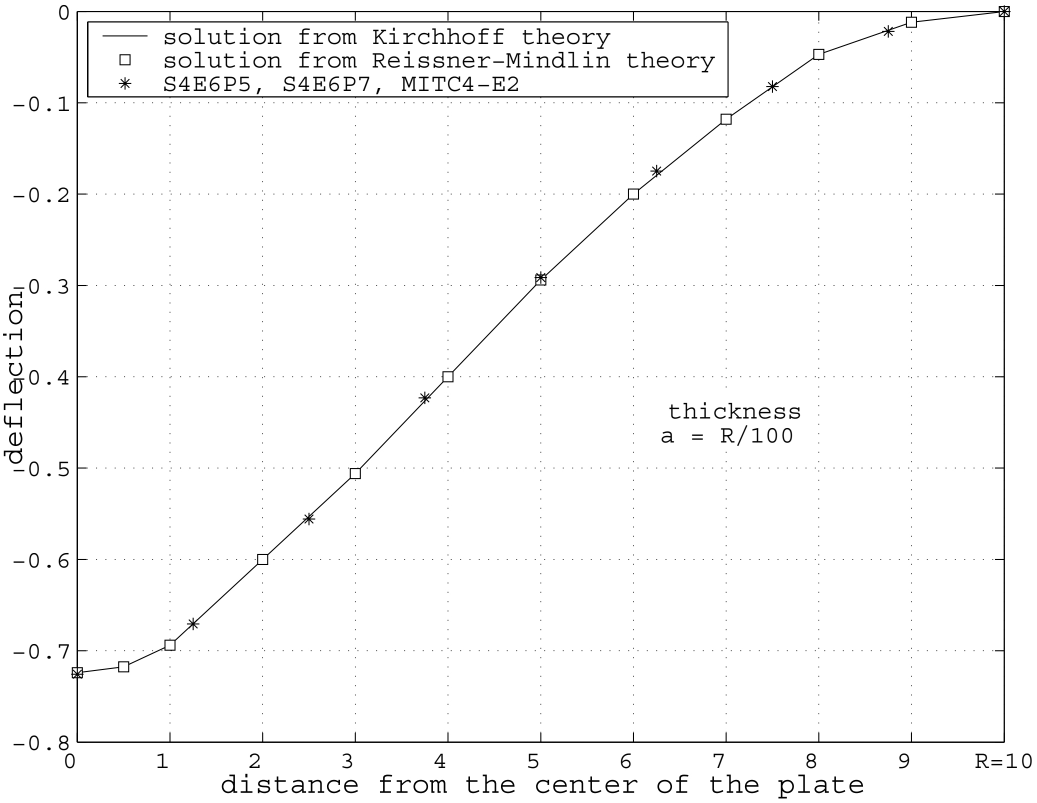

Figure 5.14: Circular plate problem - Deflection along a plate edge for clamped boundary conditions and concentrated load (mesh with 48 elements, as represented in Fig. 5.13)

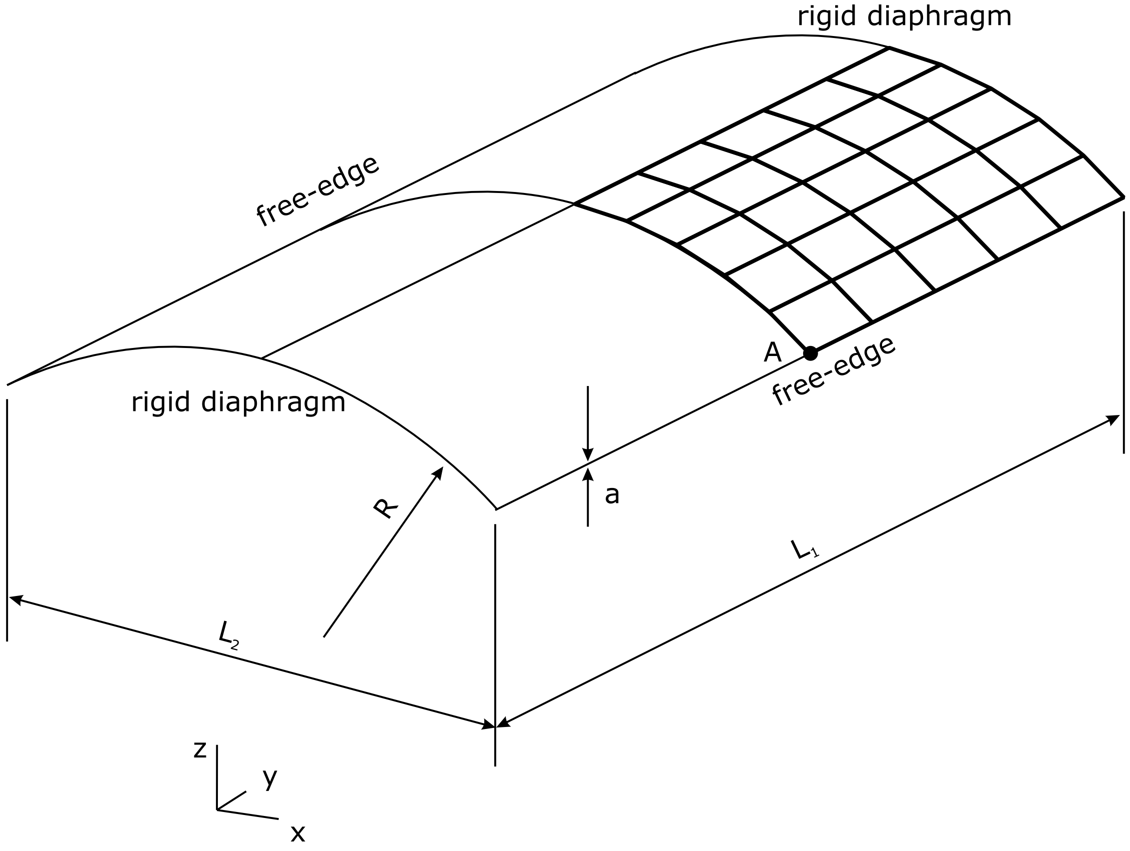

geometric properties:
$L_1 = 50.0$
$L_2 = 32.14$
$R = 25.0$
$a = 0.25$

material properties:
$E = 4.32 \times 10^8$
$\nu = 0.0$

Figure 5.15: Scordelis-Lo roof - Problem definition

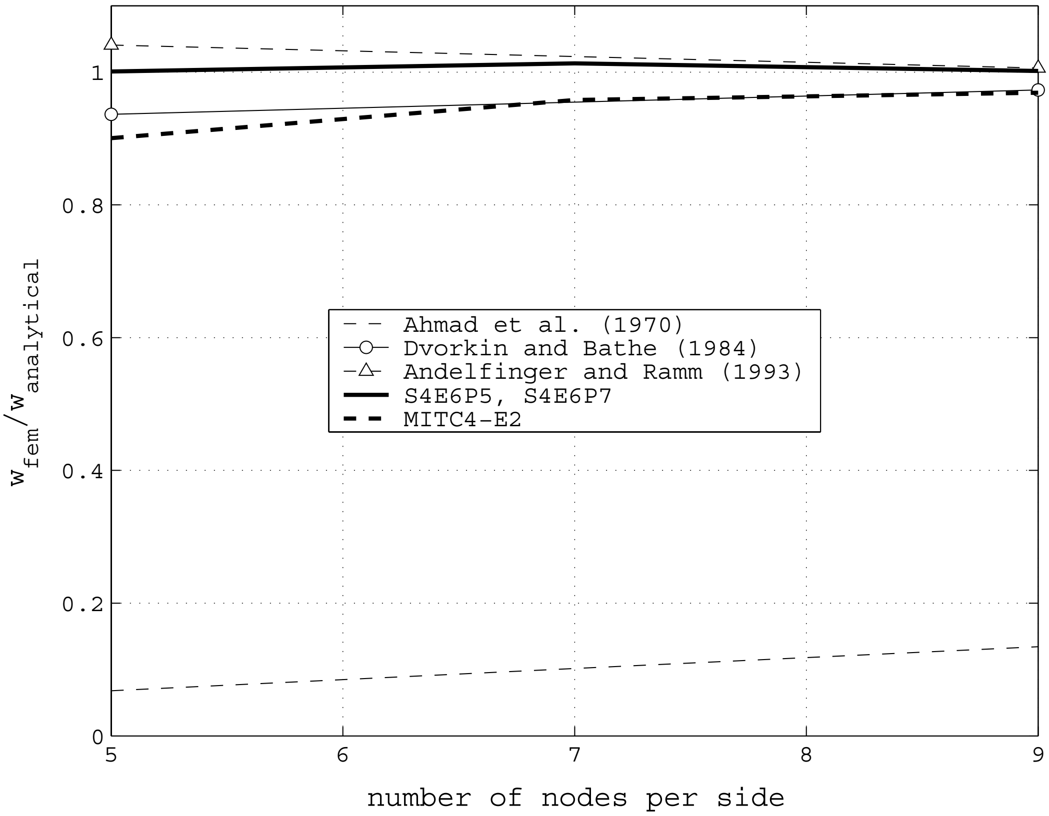

Figure 5.16: Scordelis-Lo roof - Convergence results

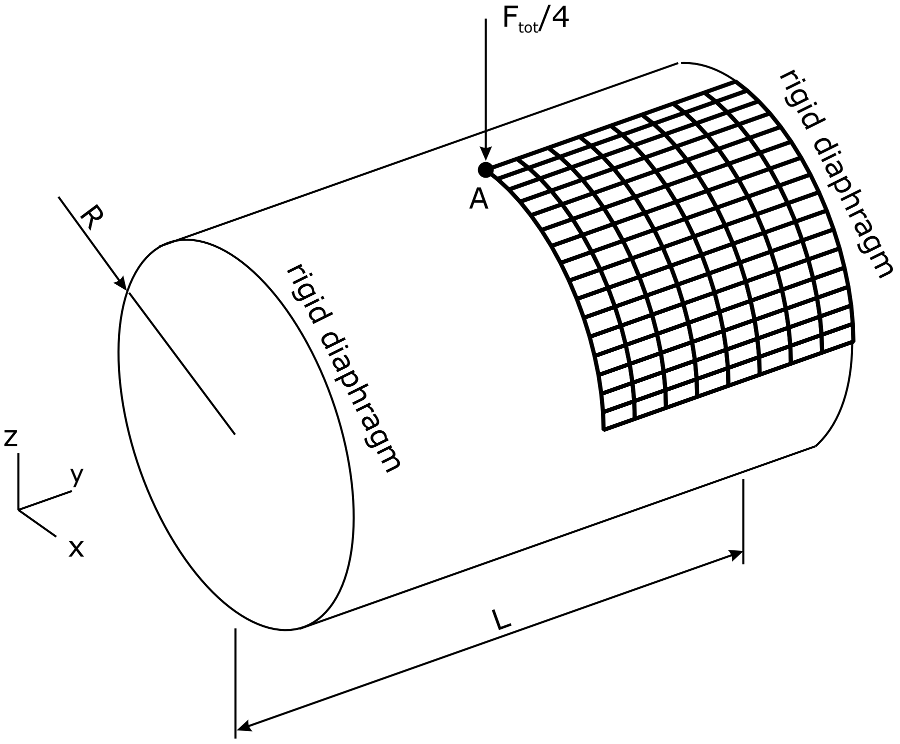

geometric properties:
$L = 600.0$
$R = 300.0$
$a = 3.0$

material properties:
$E = 3.0 \times 10^6$
$\nu = 0.3$

total load:
$F_{tot} = 1.0$

Figure 5.17: Pinched cylinder - Model with numerical data and mesh area

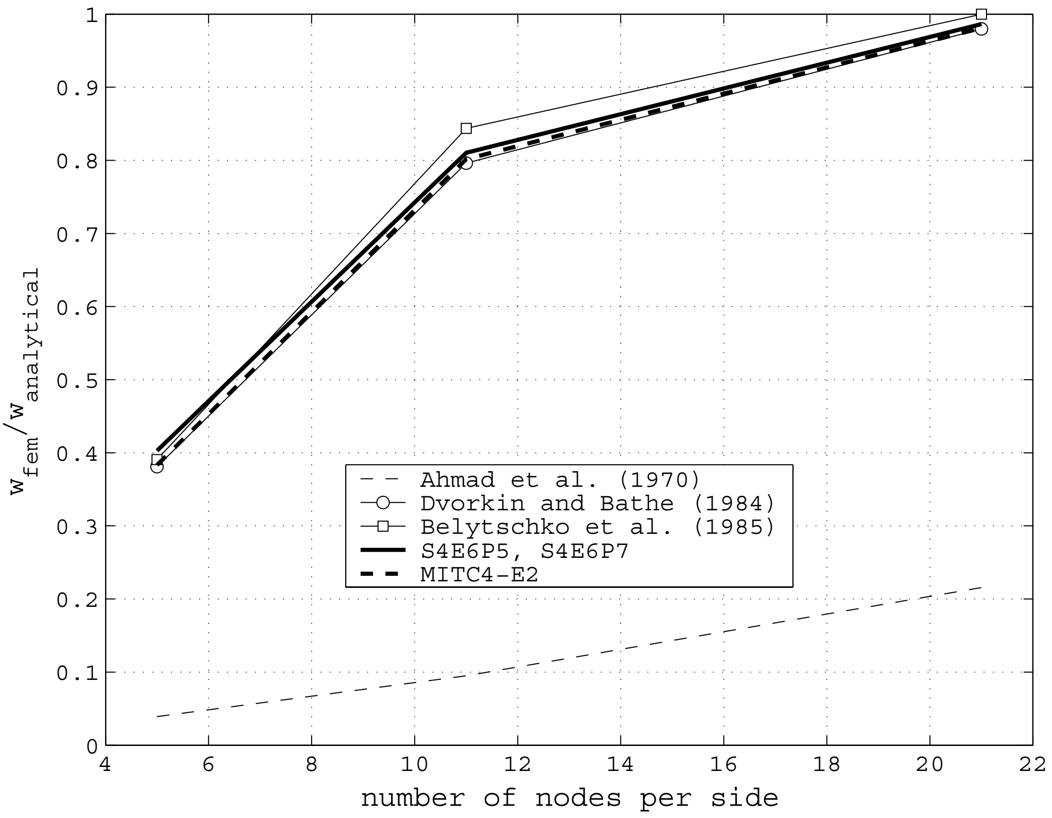

Figure 5.18: Pinched cylinder - Convergence behavior in terms of normalized displacements

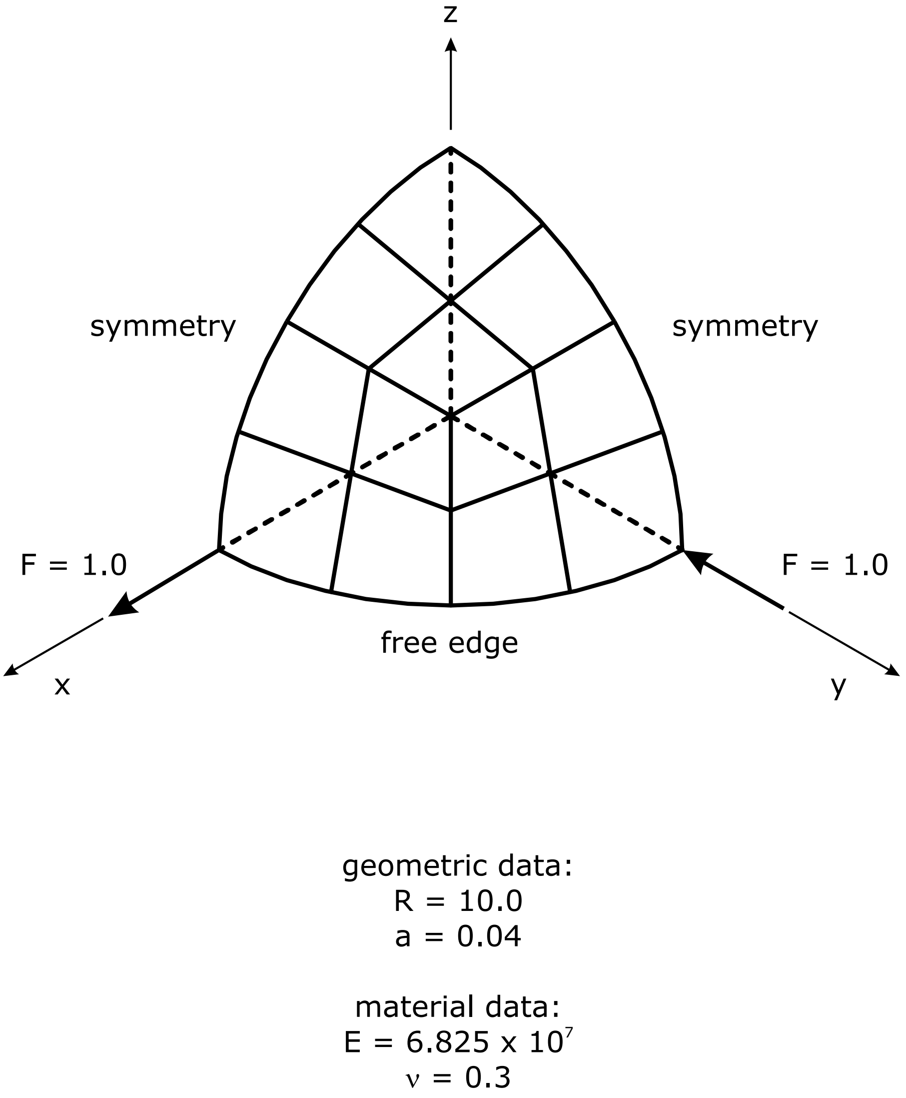

Figure 5.19: Hemispherical shell - Schematic representation of the mesh area

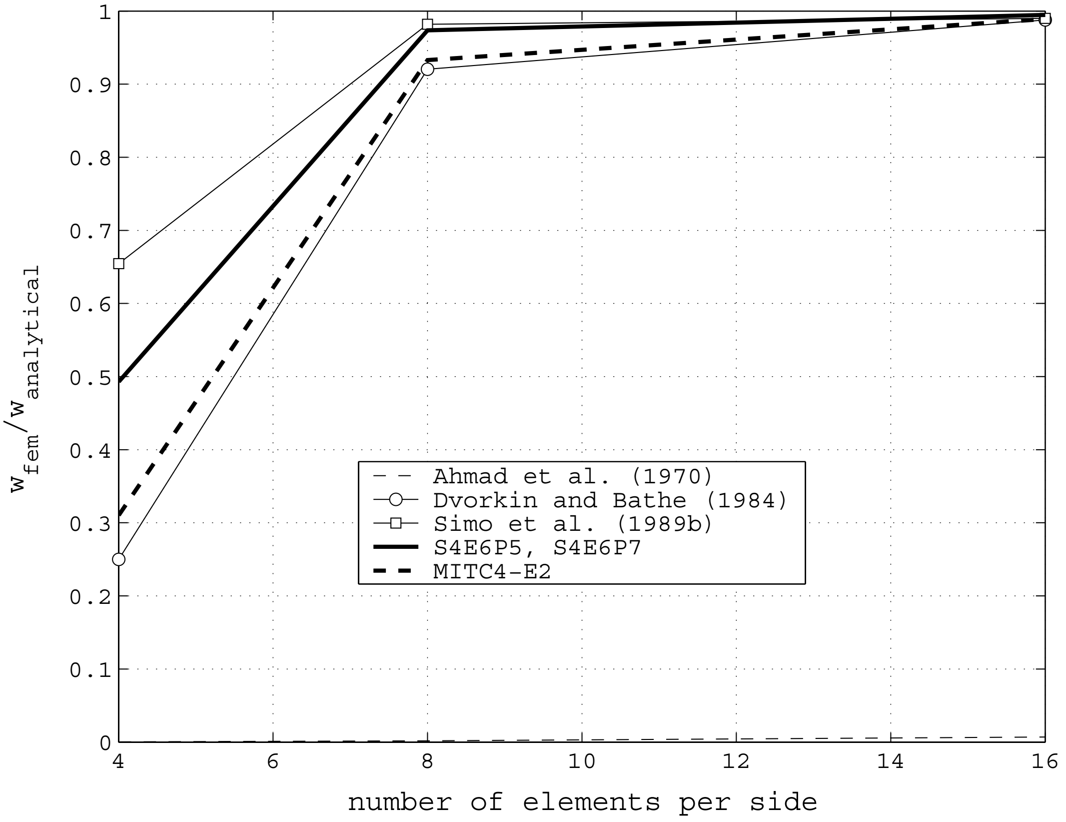

Figure 5.20: Hemispherical shell - Normalized displacement in load direction

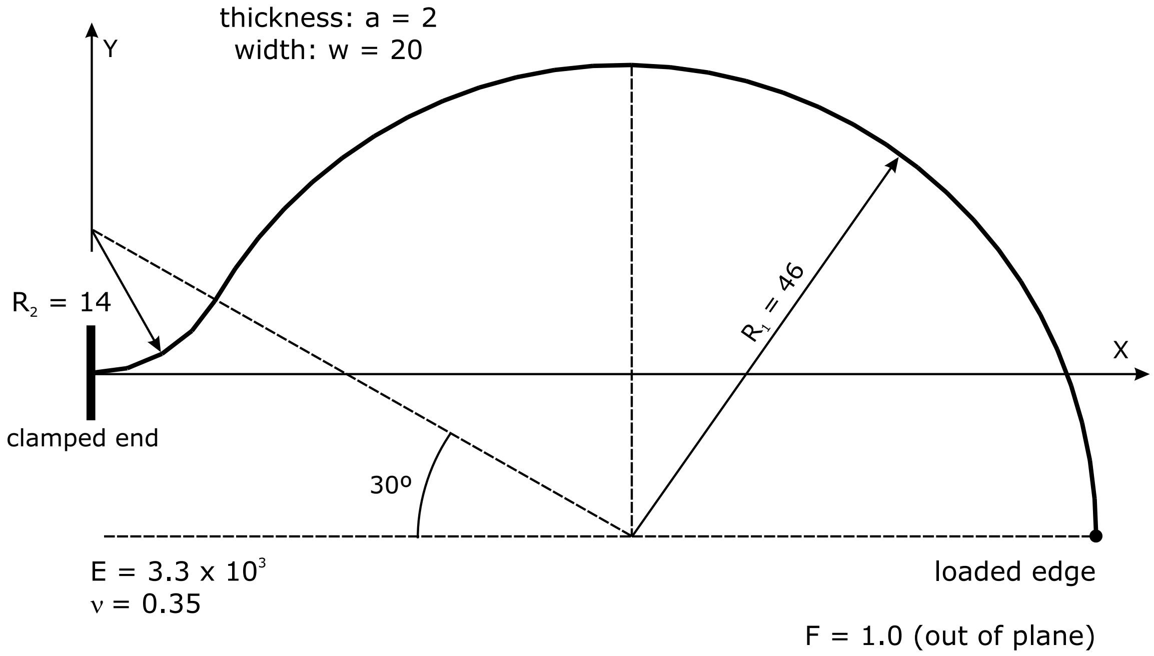

Figure 5.21: Raasch's hook problem - Geometry, material, loading and boundary conditions

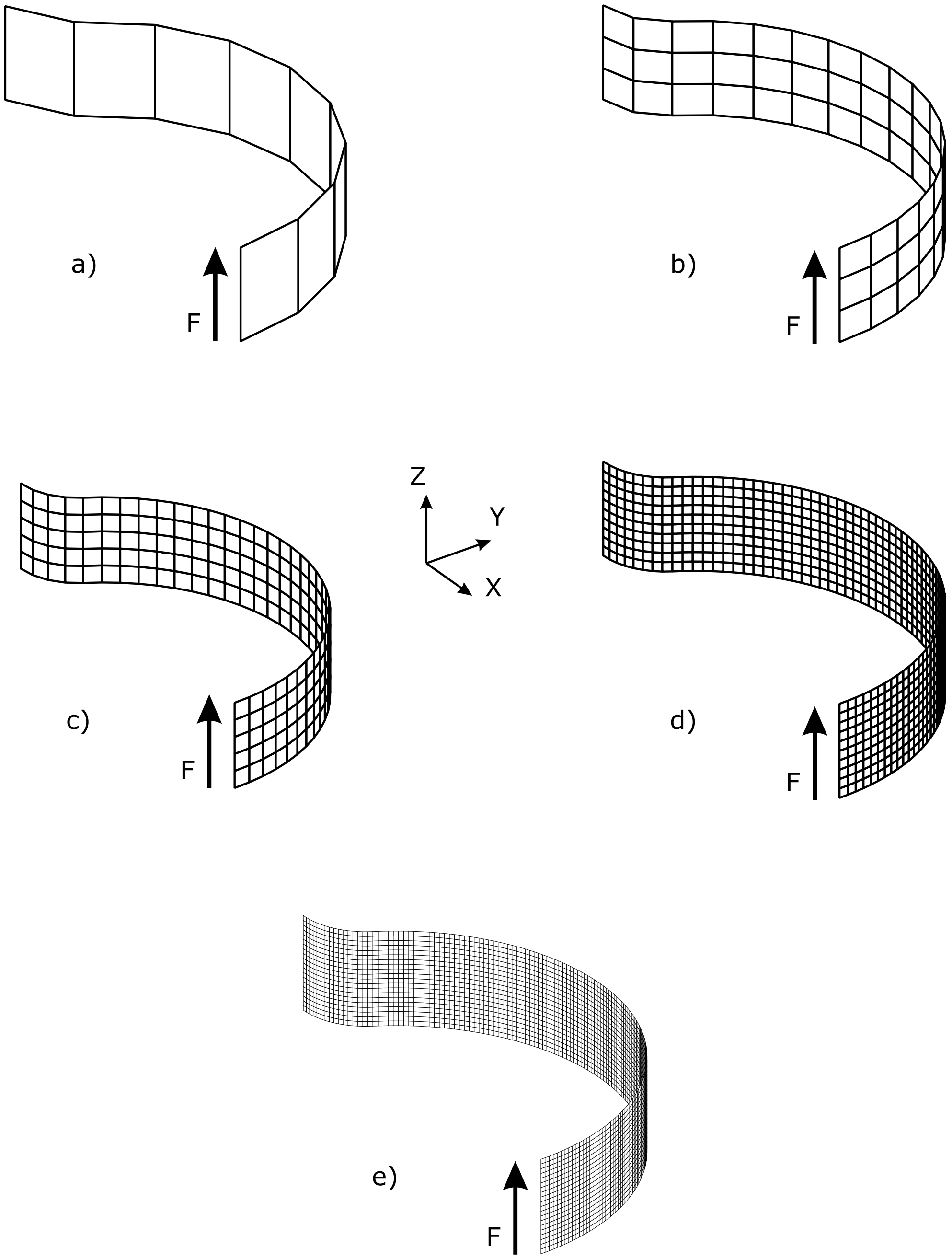

Figure 5.22: Raasch's hook problem - Mesh configurations employed a) 1×9 elements; b) 3×18 elements; c) 5×36 elements; d) 10×72 elements; e) 20×144 elements

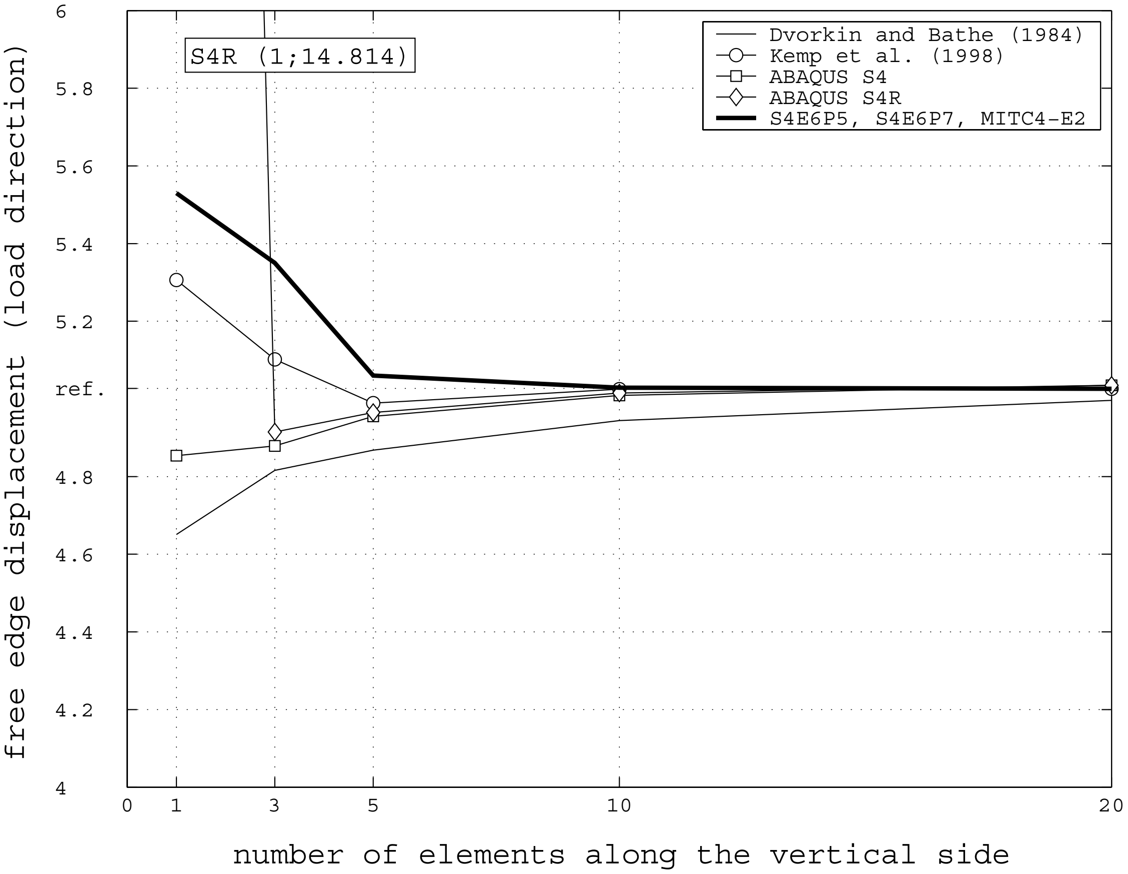

Figure 5.23: Raasch's hook problem - Results

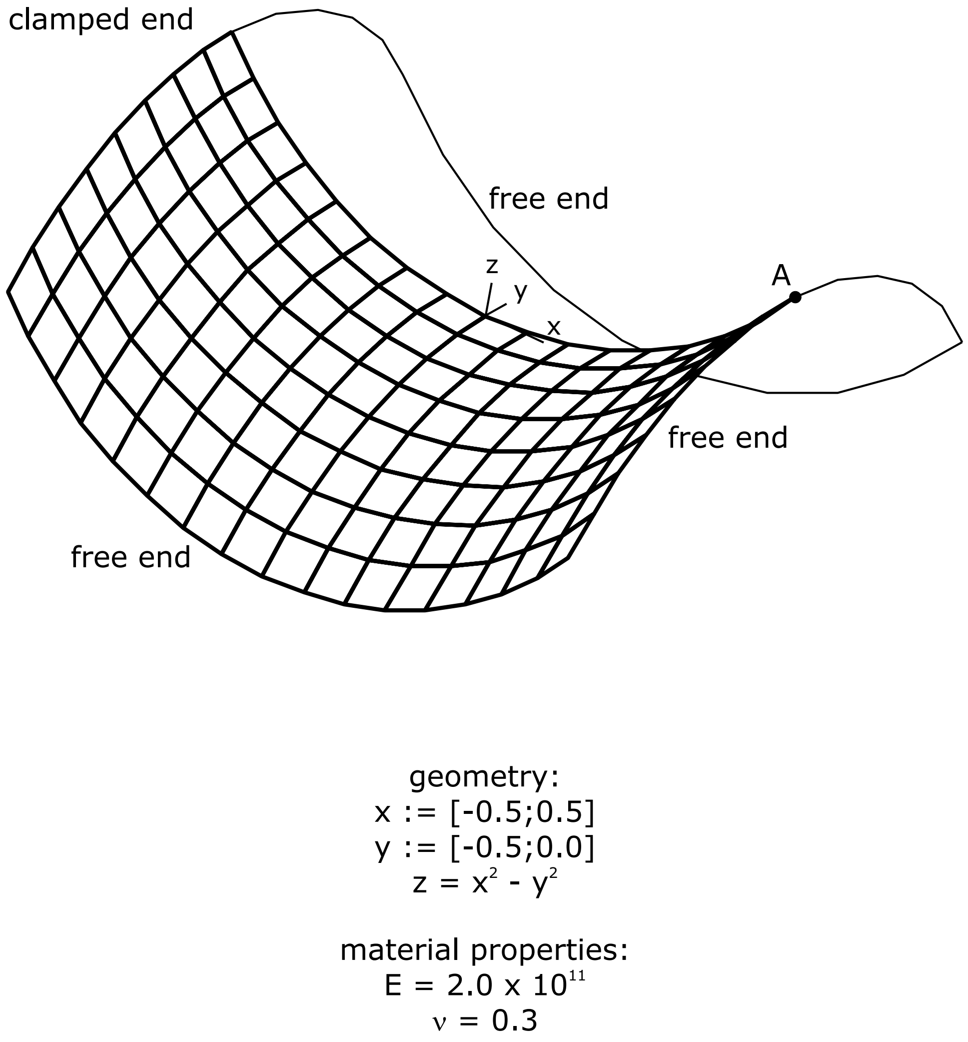

Figure 5.24: Partly clamped hyperbolic paraboloid - One half of the structure meshed with 16×8 four-node elements

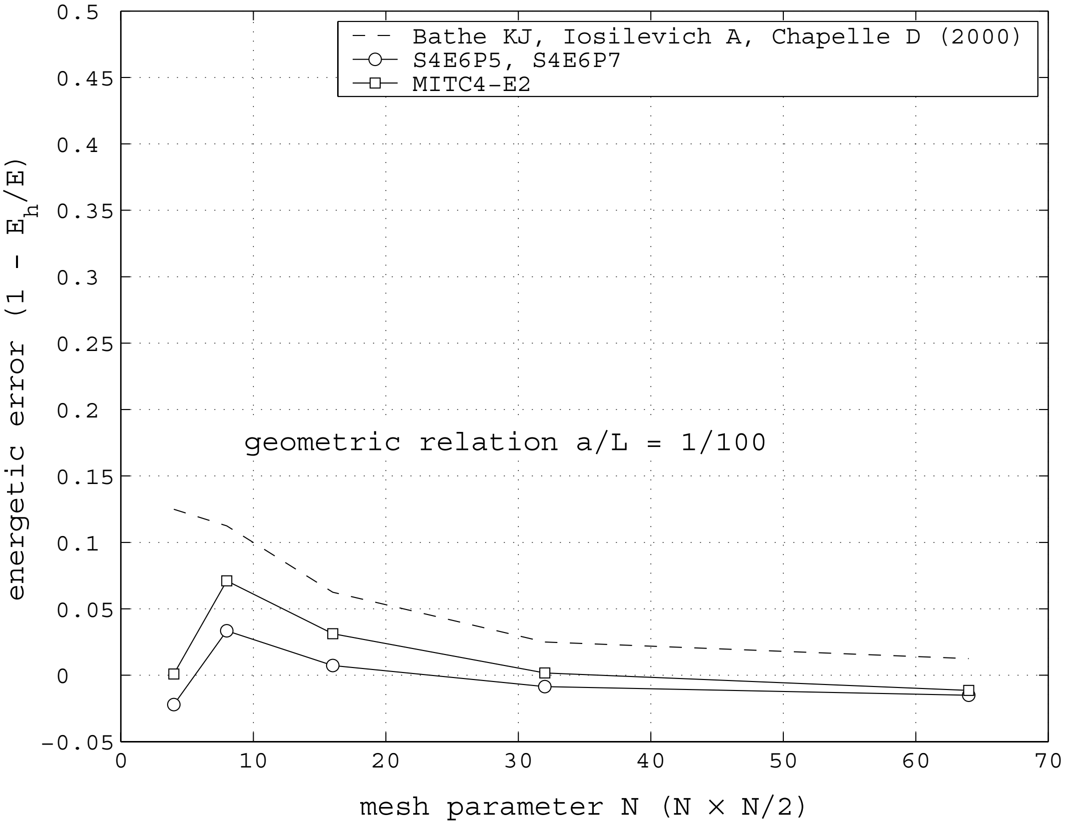

Figure 5.25: Partly clamped hyperbolic paraboloid - Convergence in stain energy for a/L = 1/100

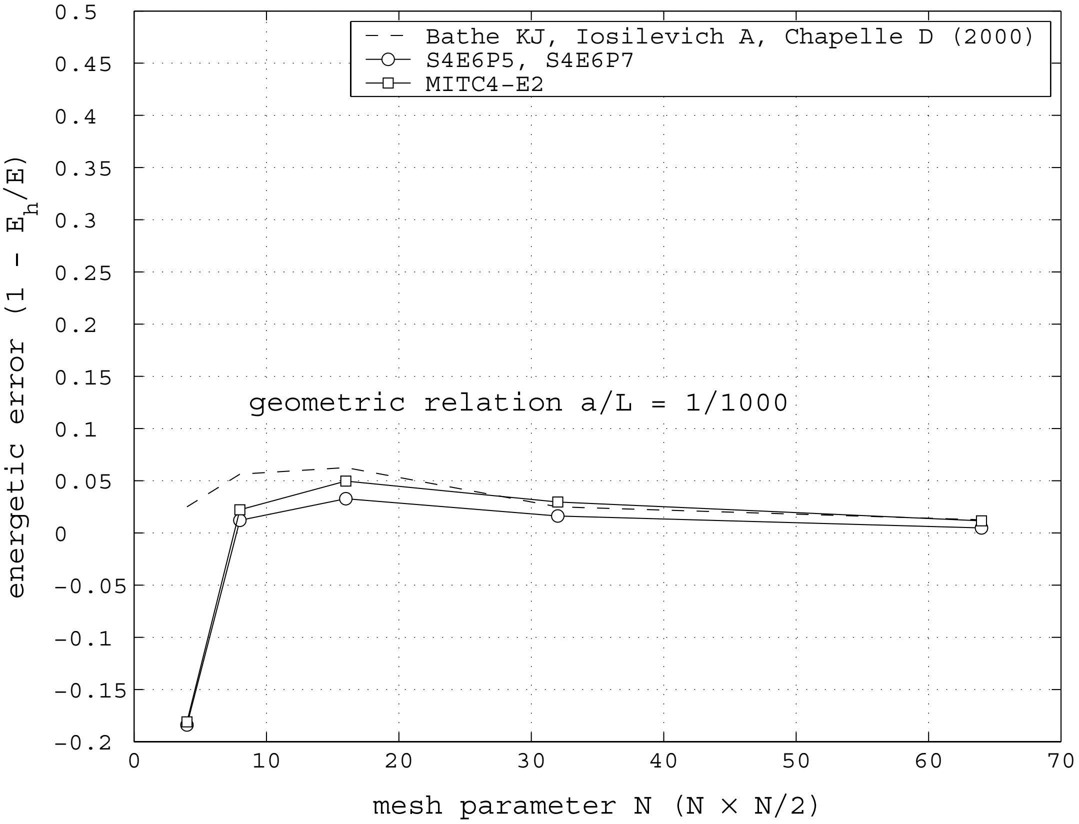

Figure 5.26: Partly clamped hyperbolic paraboloid - Convergence in stain energy for $\mathsf{a}/\mathsf{L} = 1/1000$

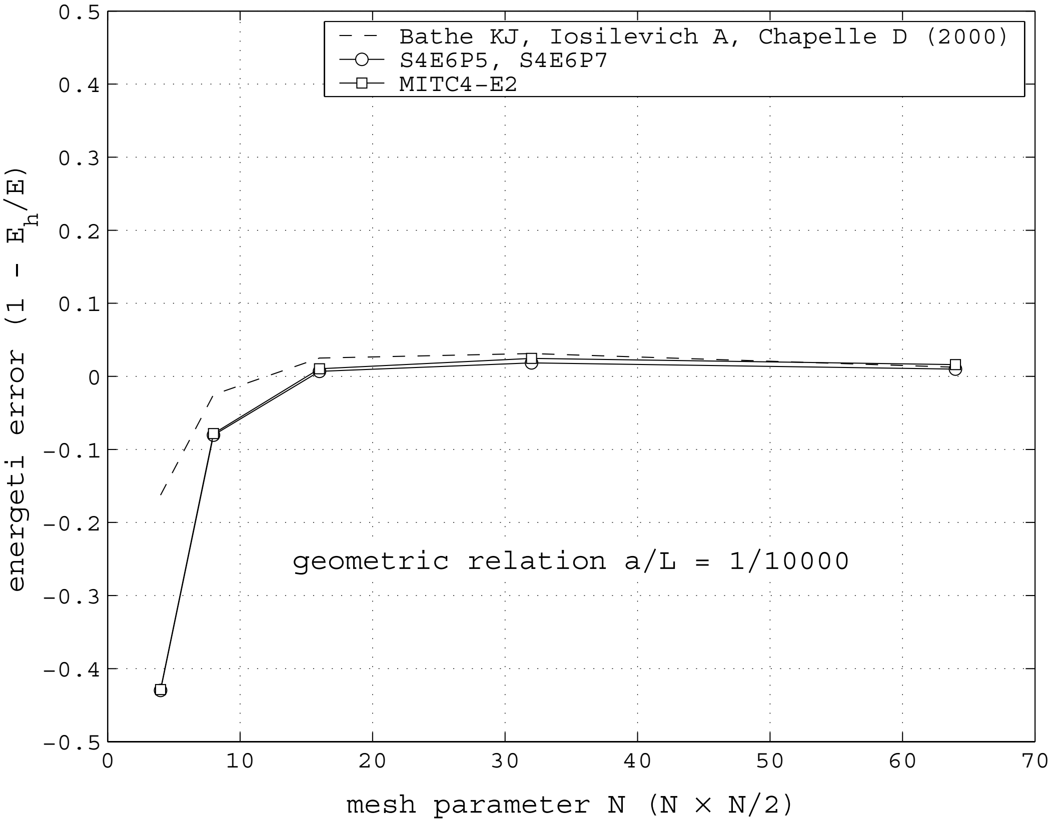

Figure 5.27: Partly clamped hyperbolic paraboloid - Convergence in stain energy for $\mathsf{a/L} = 1/10000$

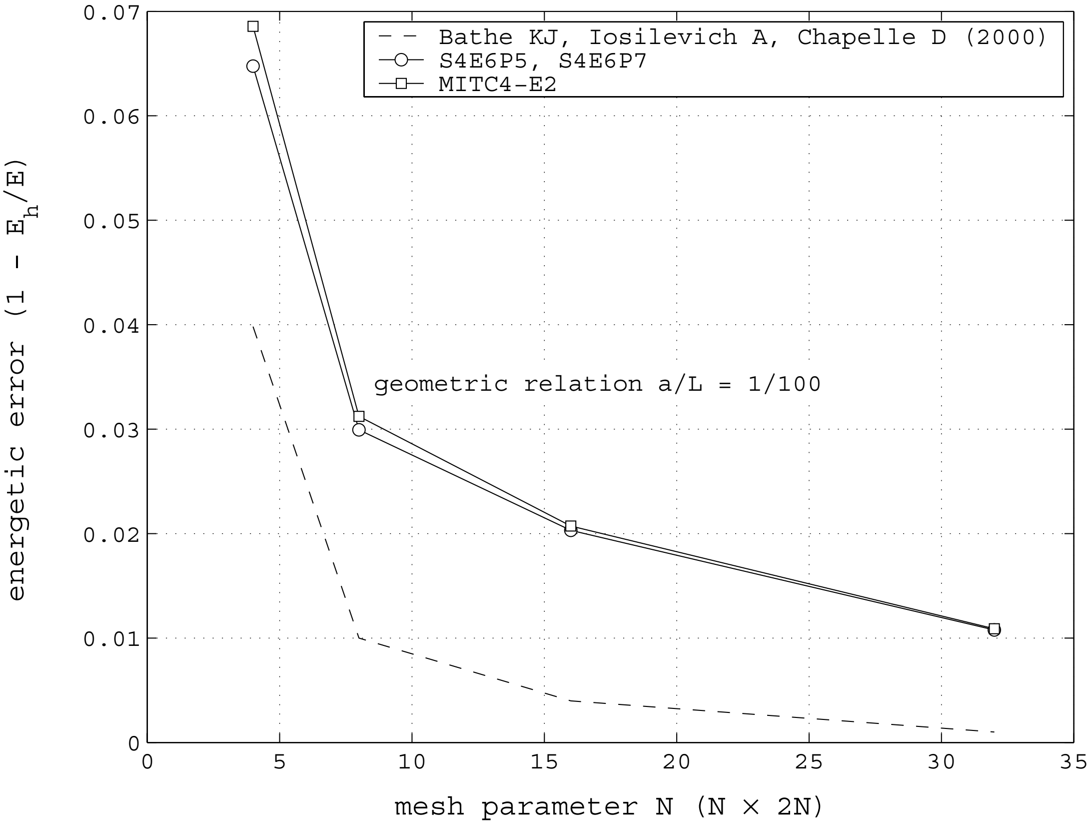

Figure 5.28: Free cylinder problem - Convergence in stain energy for a/L = 100

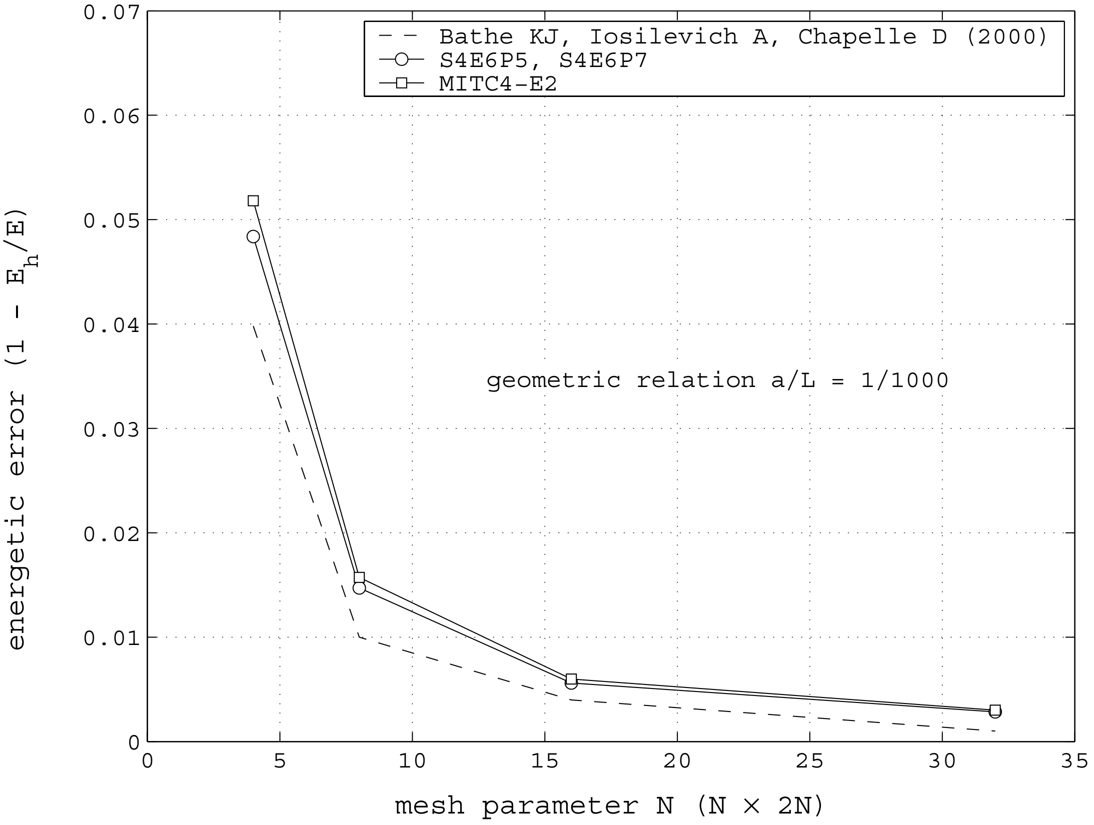

Figure 5.29: Free cylinder problem - Convergence in stain energy for $\mathsf{a}/\mathsf{L} = 1000$

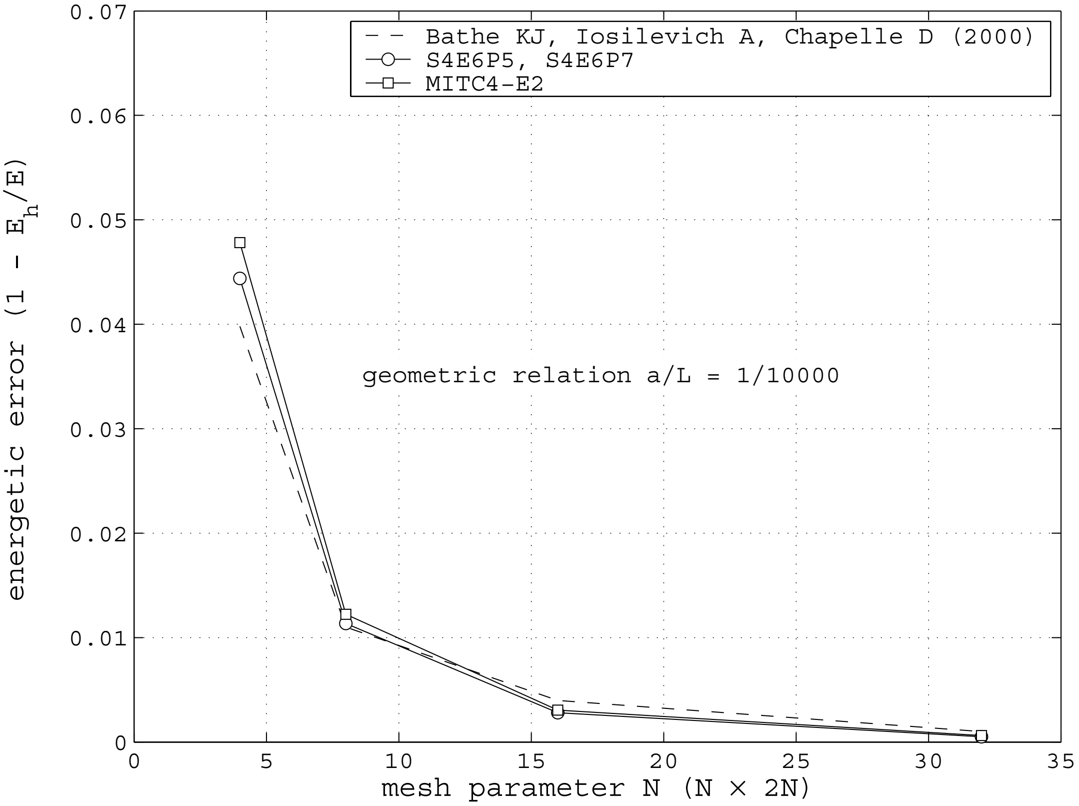

Figure 5.30: Free cylinder problem - Convergence in stain energy for $\mathsf{a}/\mathsf{L} = 10000$

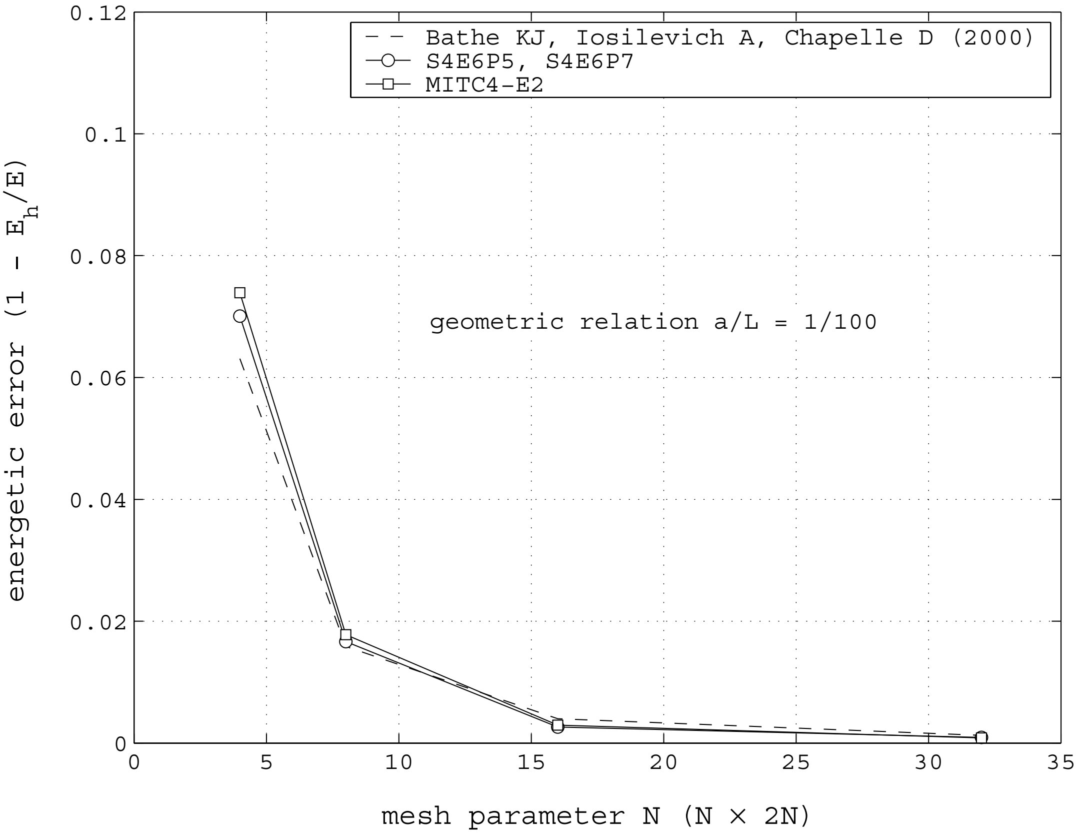

Figure 5.31: Clamped cylinder problem - Convergence in stain energy for $\mathsf{a}/\mathsf{L} = 100$

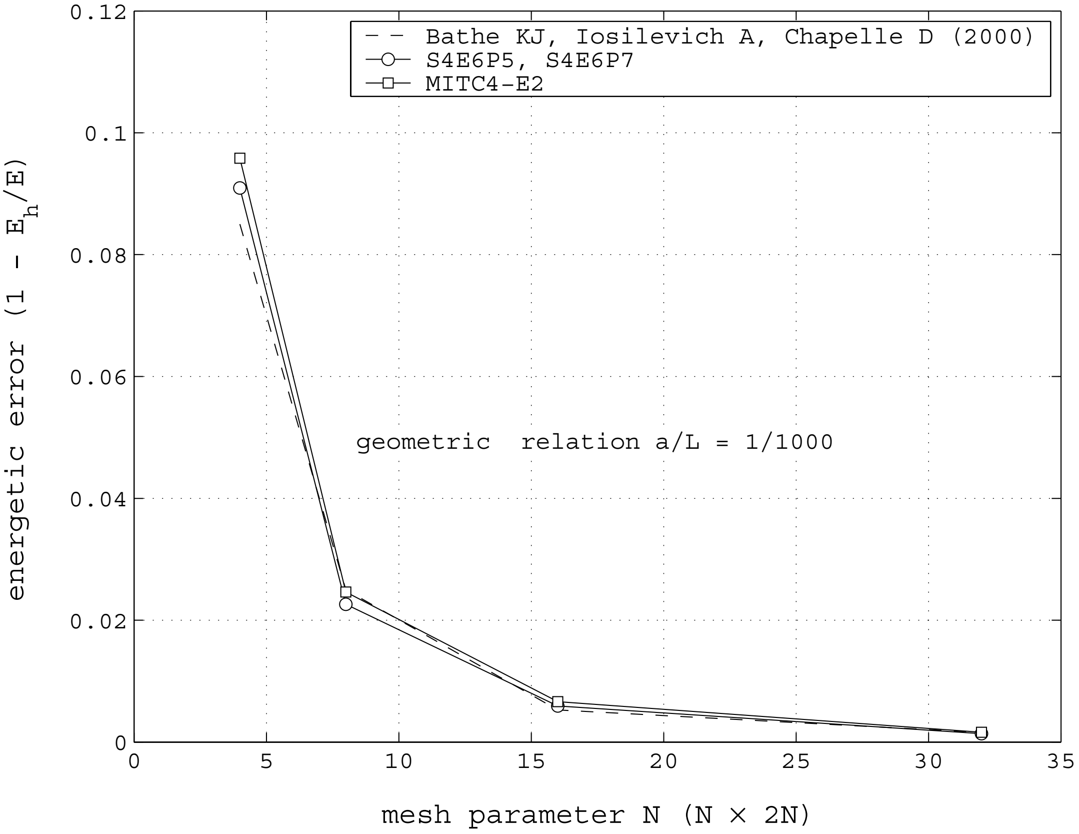

Figure 5.32: Clamped cylinder problem - Convergence in stain energy for $\mathsf{a}/\mathsf{L} = 1000$

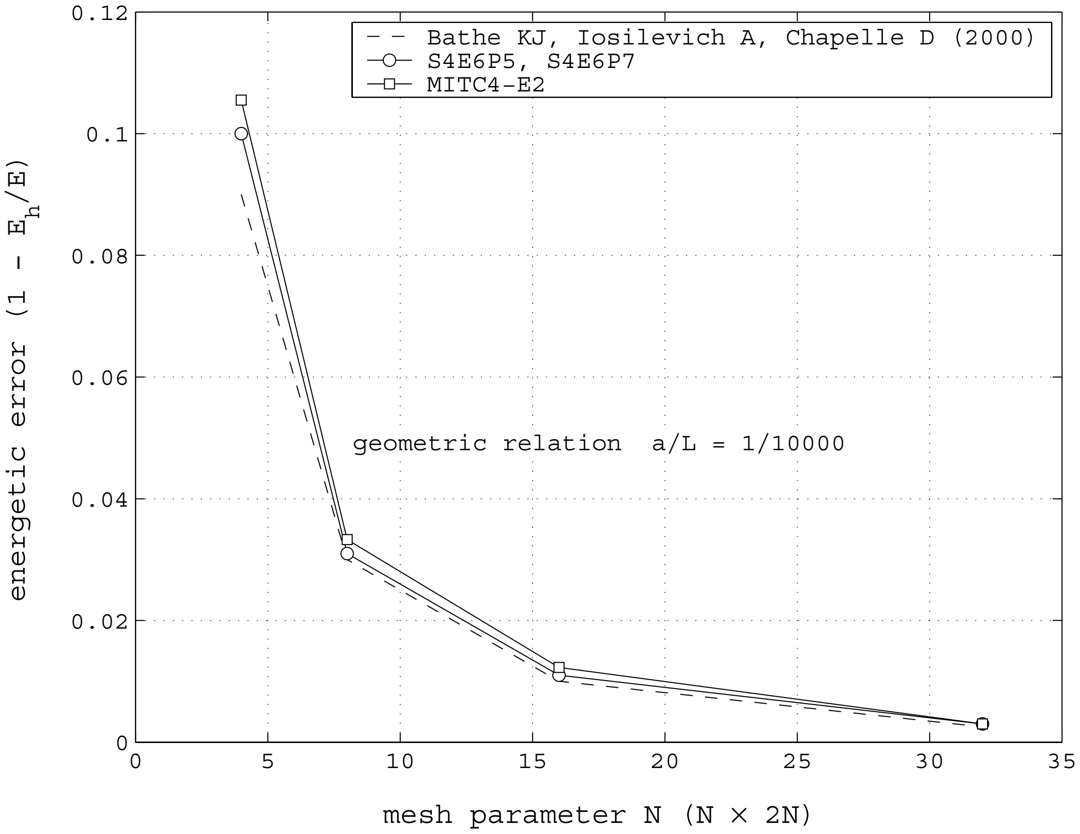

Figure 5.33: Clamped cylinder problem - Convergence in stain energy for $\mathsf{a}/\mathsf{L} = 10000$

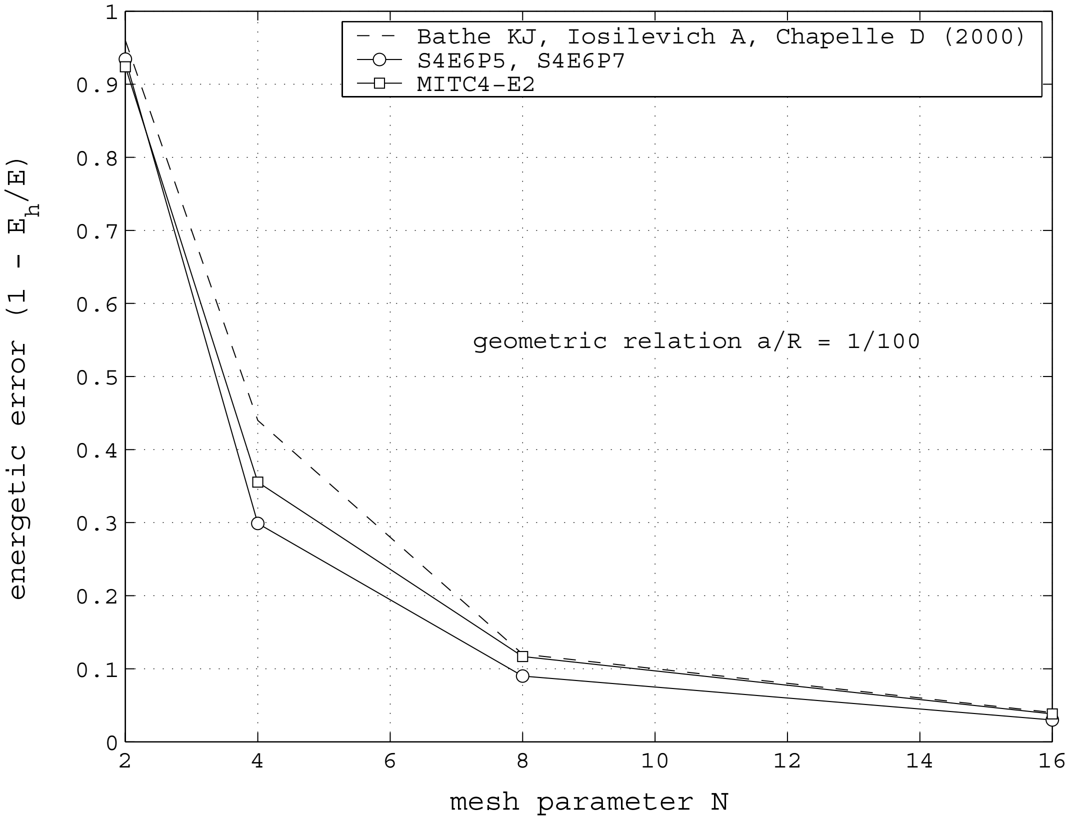

Figure 5.34: Clamped hemispherical cap problem - Convergence in stain energy for $\mathsf{a}/\mathsf{R} = 100$

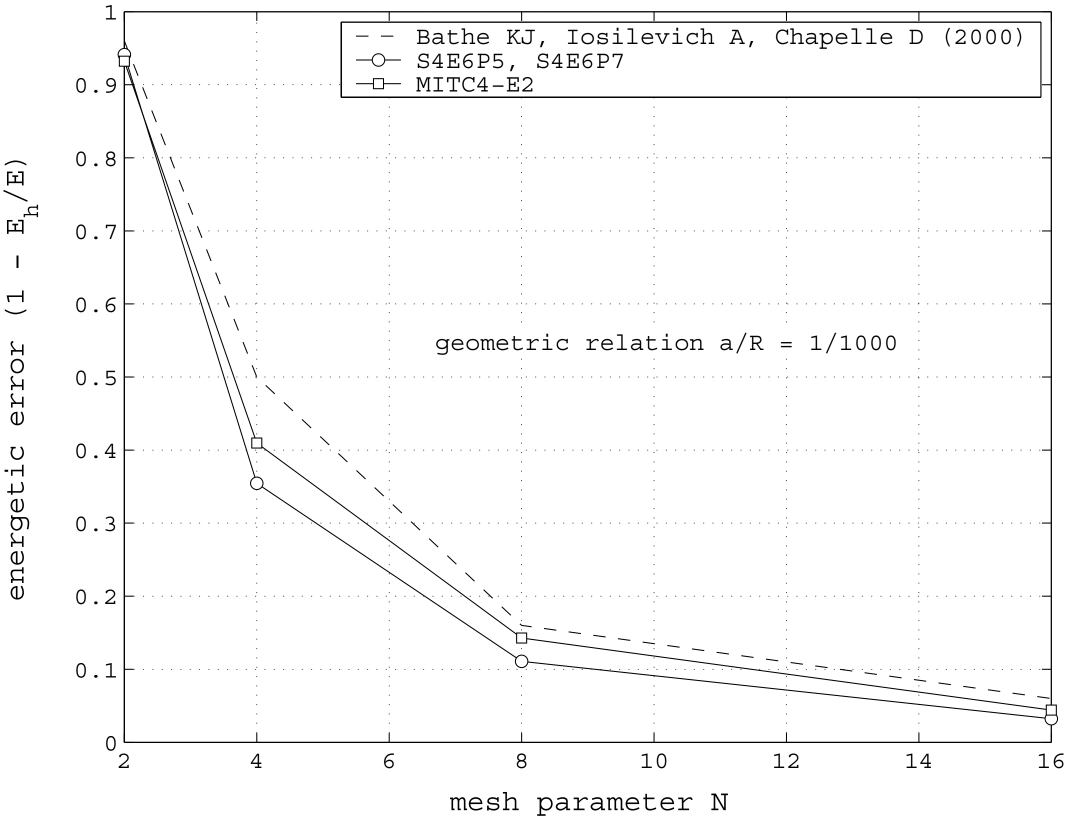

Figure 5.35: Clamped hemispherical cap problem - Convergence in stain energy for $\mathsf{a}/\mathsf{R} = 1000$

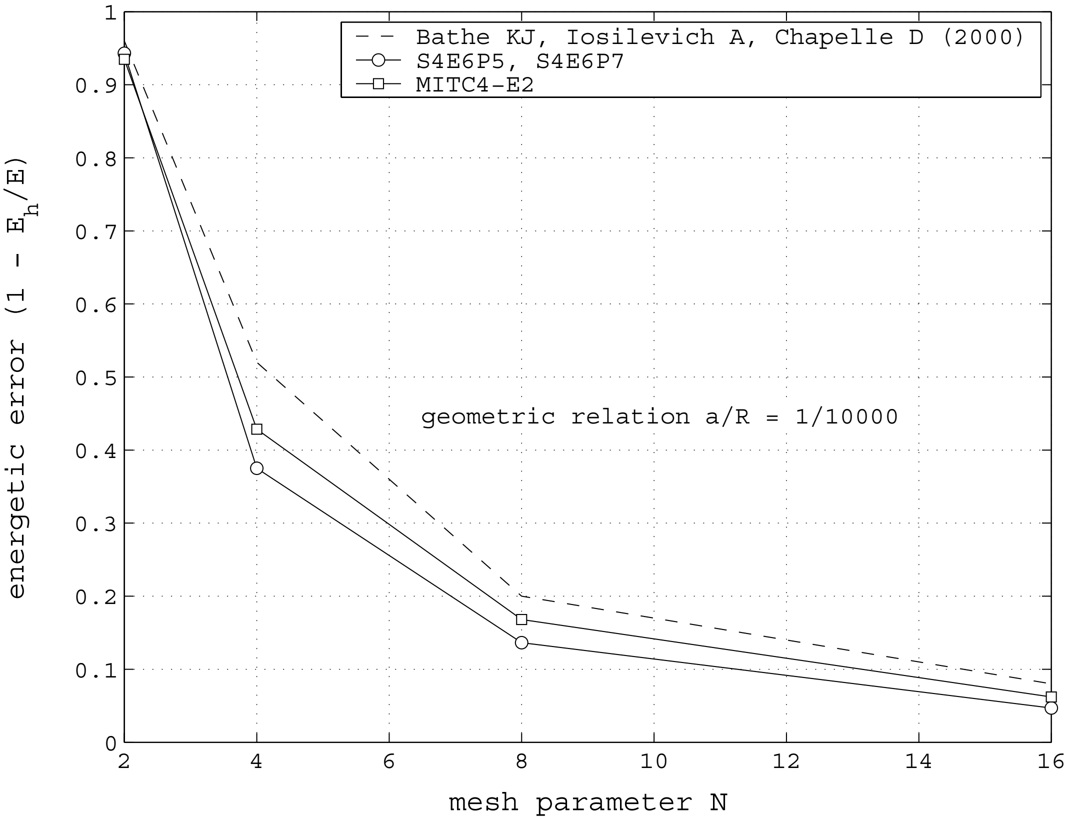

Figure 5.36: Clamped hemispherical cap problem - Convergence in stain energy for $\mathsf{a}/\mathsf{R} = 10000$

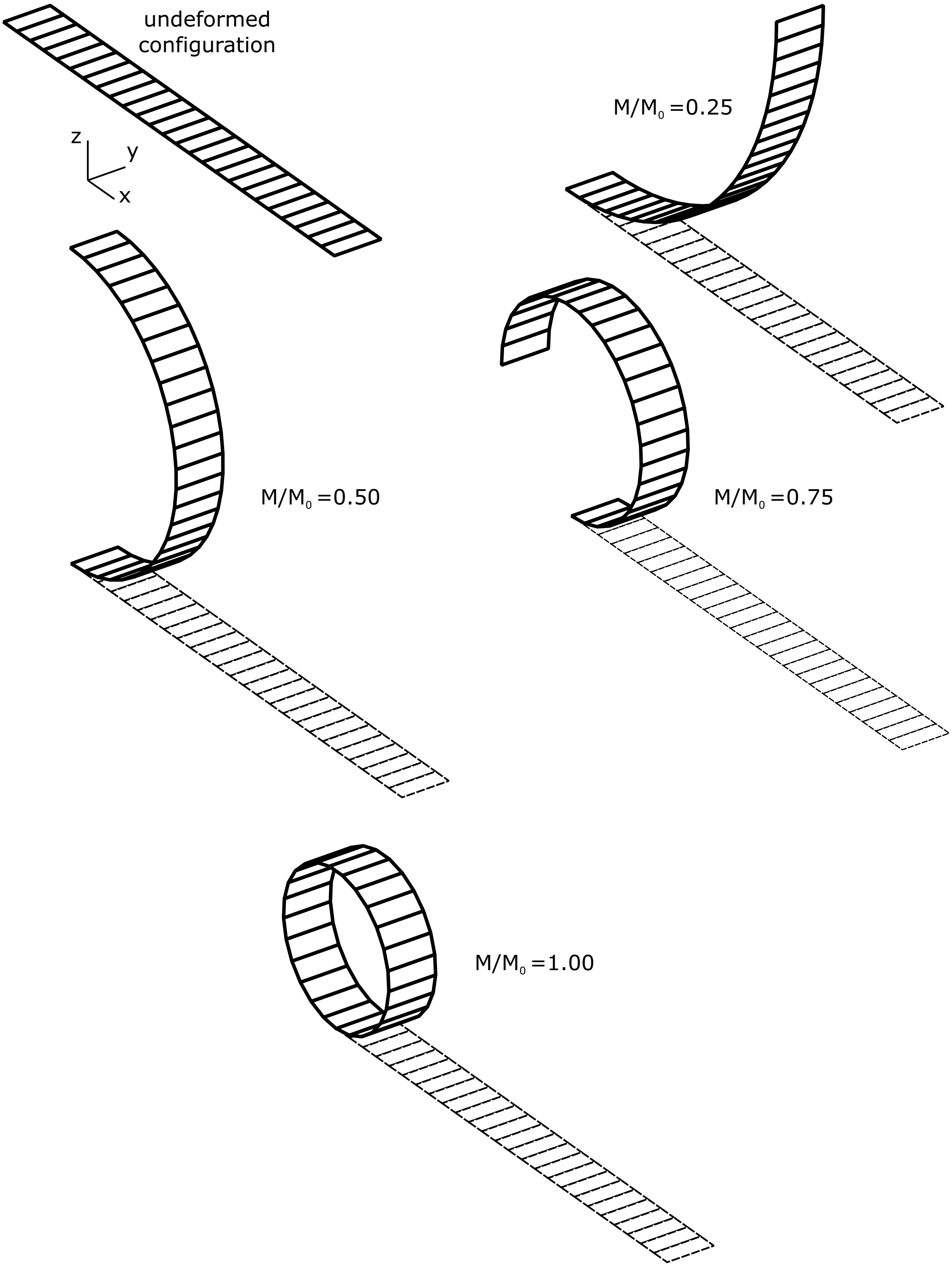

Figure 5.37: Results for the roll-up analysis of a clamped beam for various imposed (normalized) moments (M/M_0)

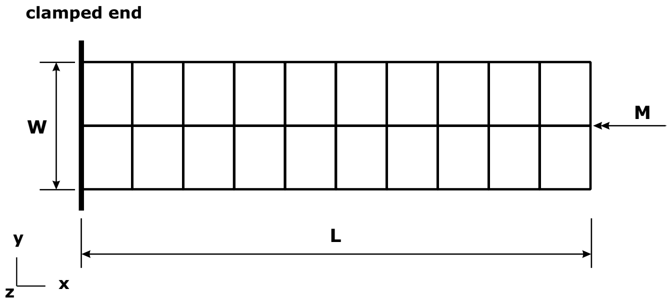

Figure 5.38: Torsion of a plate strip - Initial configuration

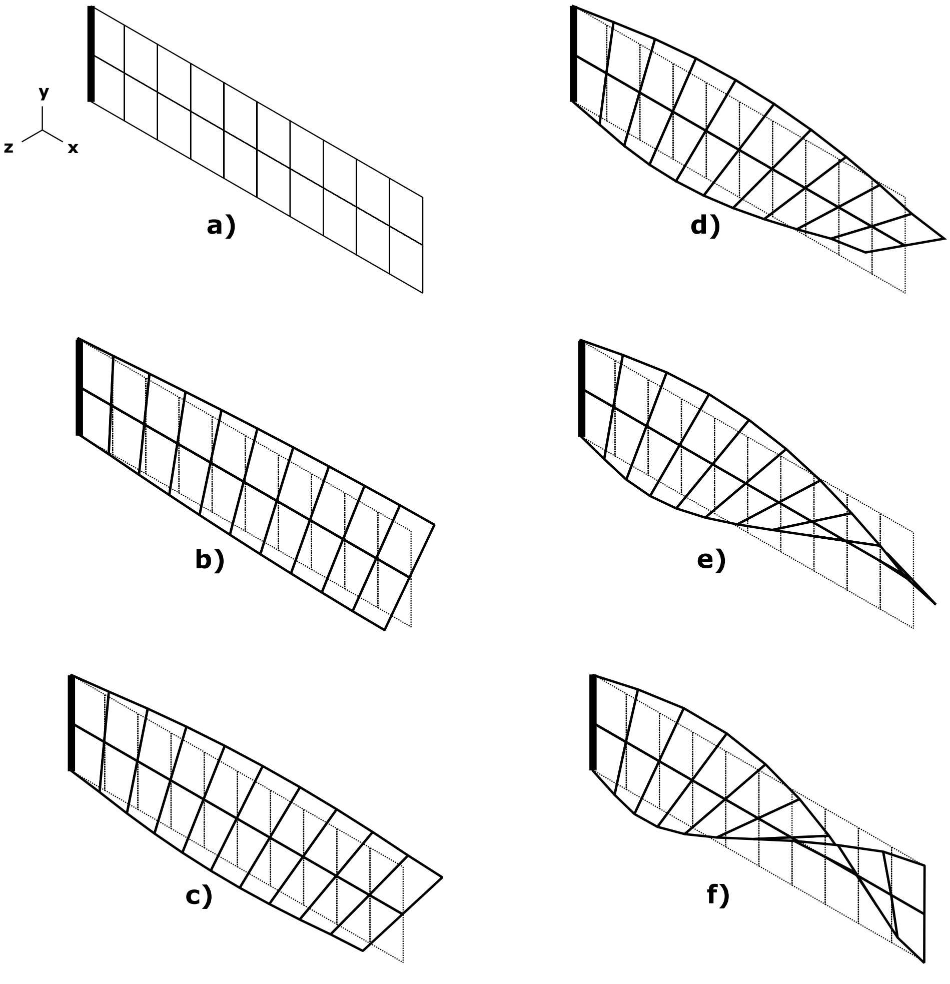

Figure 5.39: Torsion of a plate strip - 5-Step deformation sequence

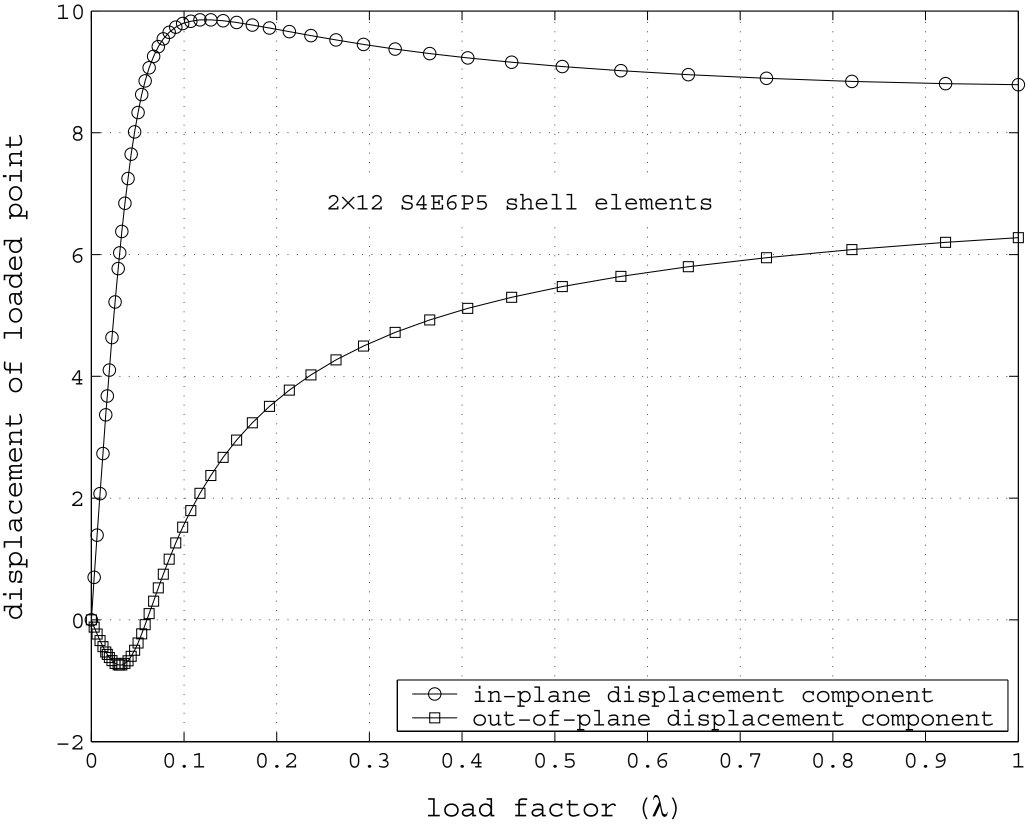

Figure 5.40: Nonlinear geometric analysis of the twisted beam (Fig. 5.12) - Results for a (combined) load level $\mathsf{F} = 250 \times \lambda$

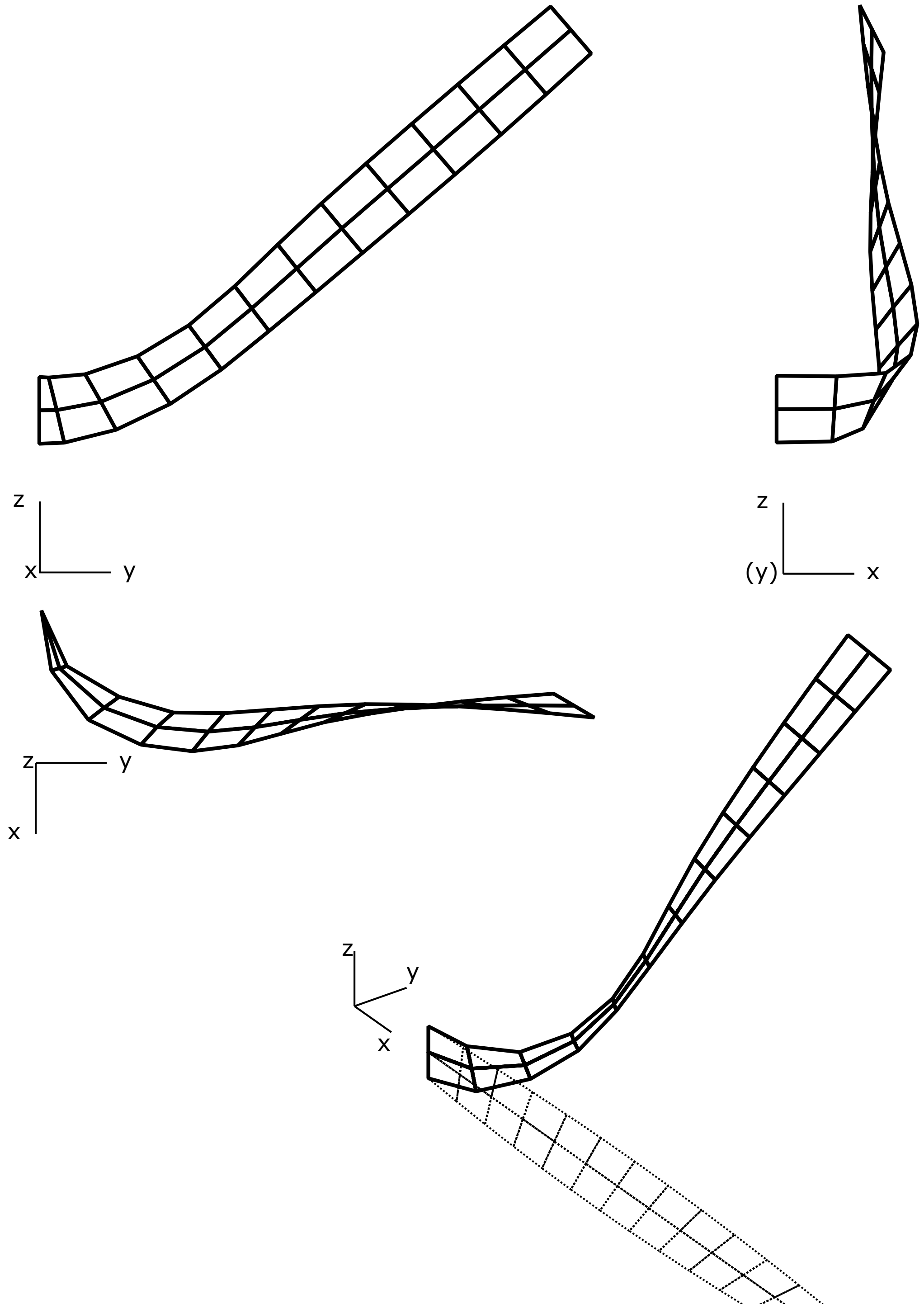

Figure 5.41: Nonlinear geometric analysis of the twisted beam (Fig. 5.12) - Deformed configuration for a load factor $\lambda = 1.0$

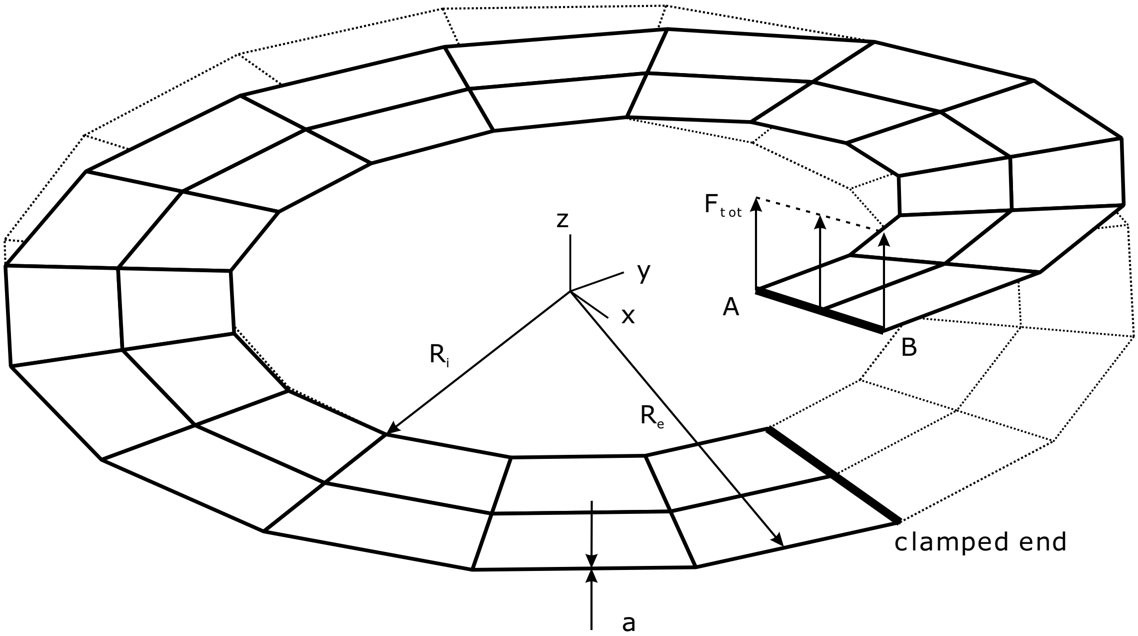

Figure 5.42: Cantilever ring - Schematic representation involving geometry, boundary and loading conditions

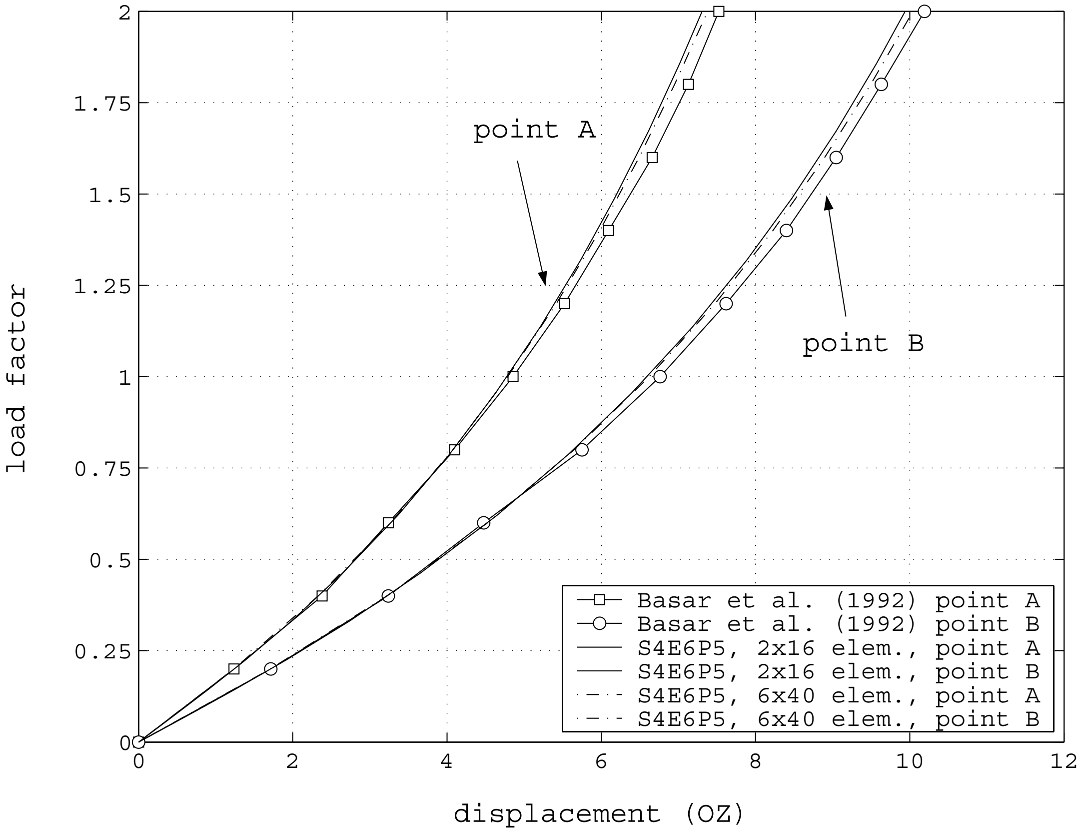

Figure 5.43: Cantilever ring - Displacements evolution for points A and B in Fig. 5.42

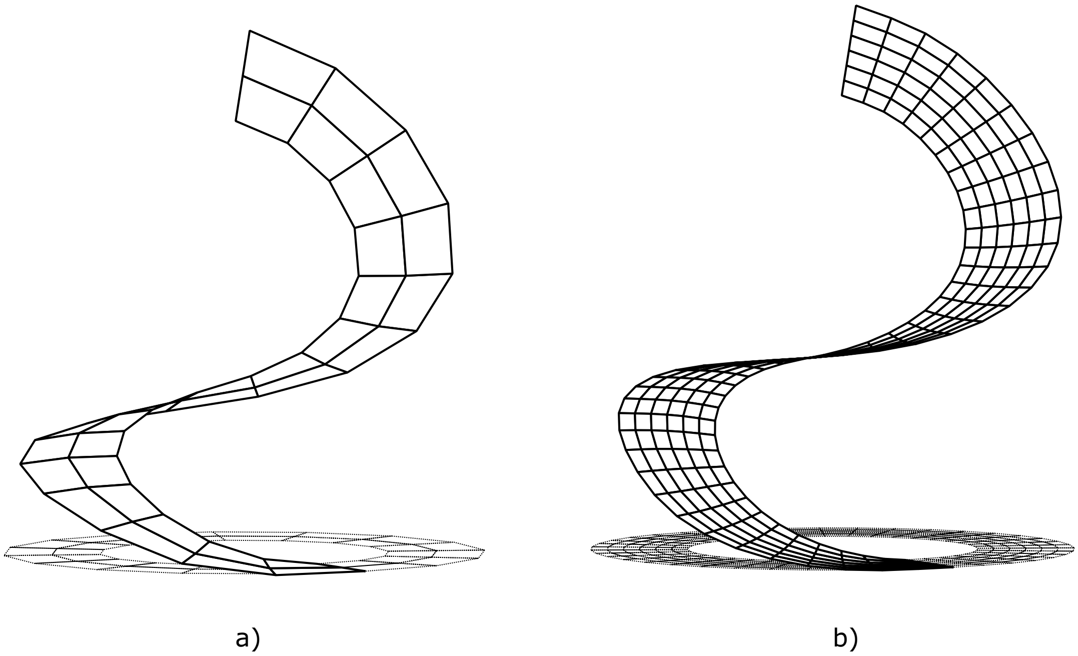

Figure 5.44: Cantilever ring - Final configuration for a load factor $\lambda = 20$. (a) 2×16 mesh; (b) 6×40 mesh

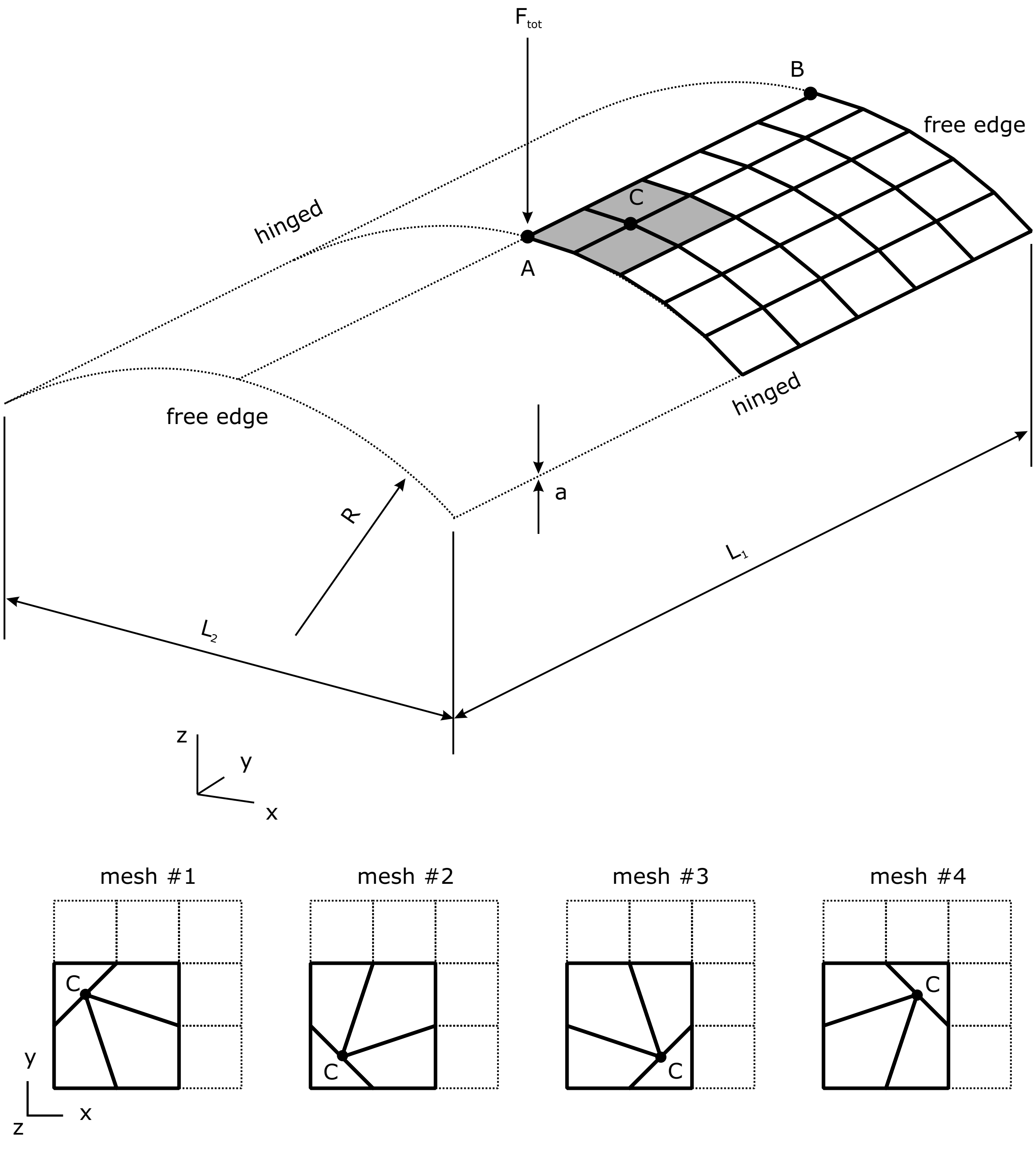

Figure 5.45: Snap-through and snap-back analysis - Shallow shell model with regular mesh and details of distorted mesh areas

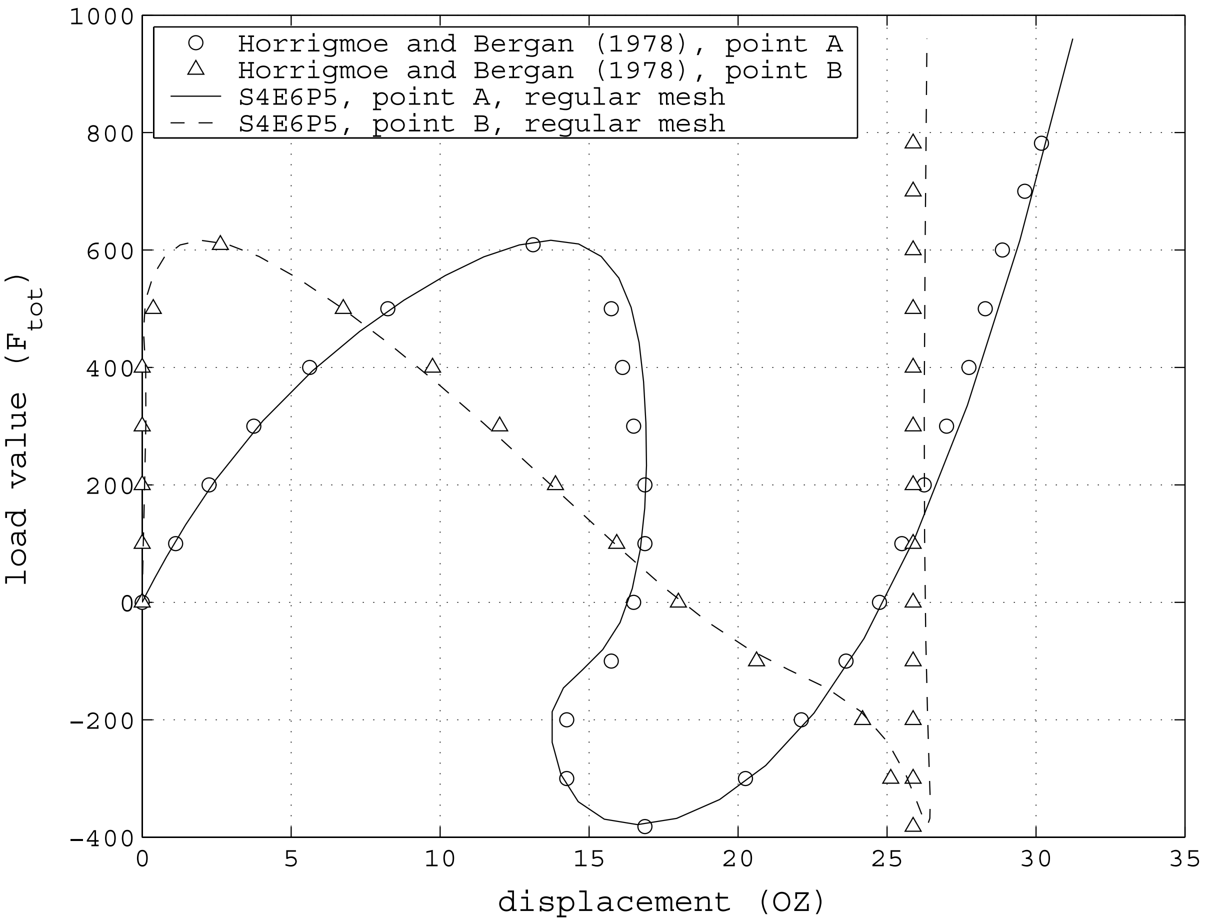

Figure 5.46: Snap-through and snap-back analysis - Results for the regular 5 × 5 mesh

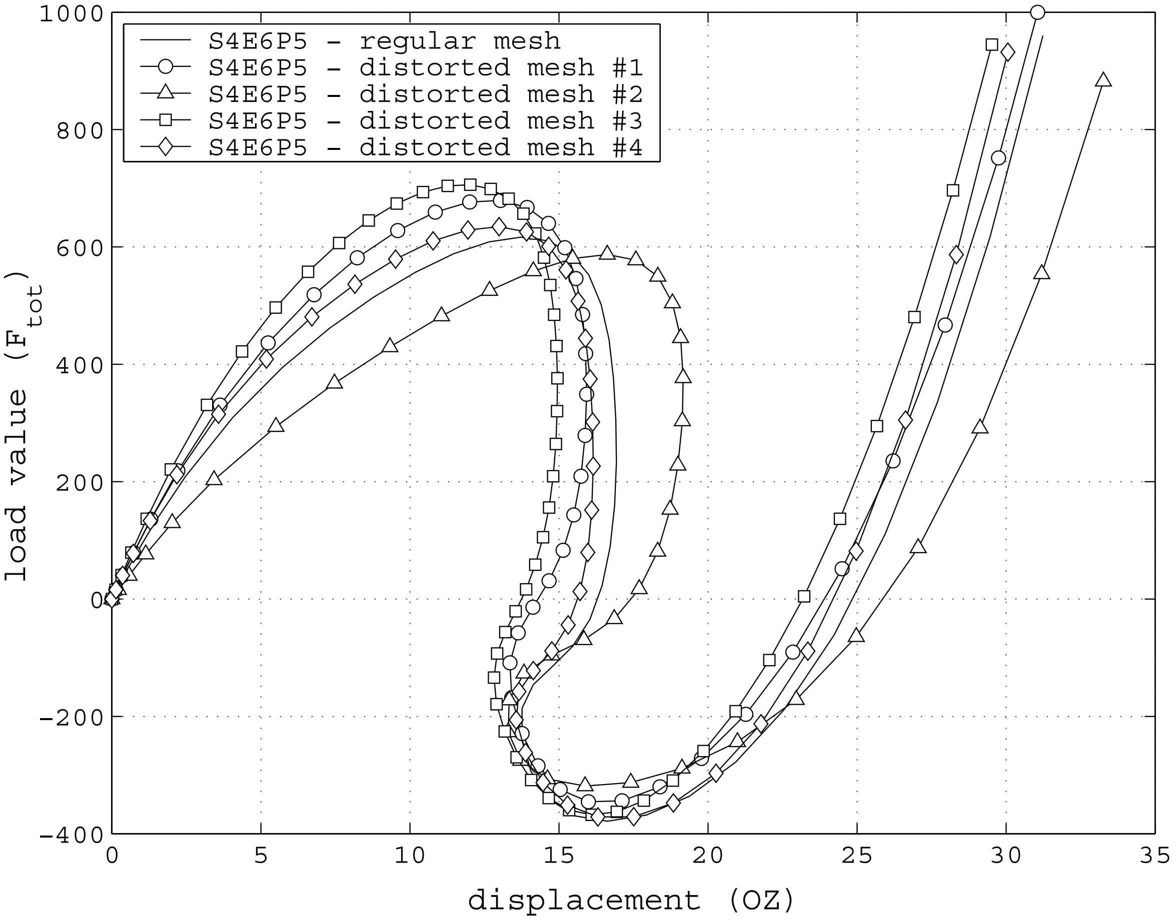

Figure 5.47: Snap-through and snap-back analysis - Results for point A (distorted meshes)

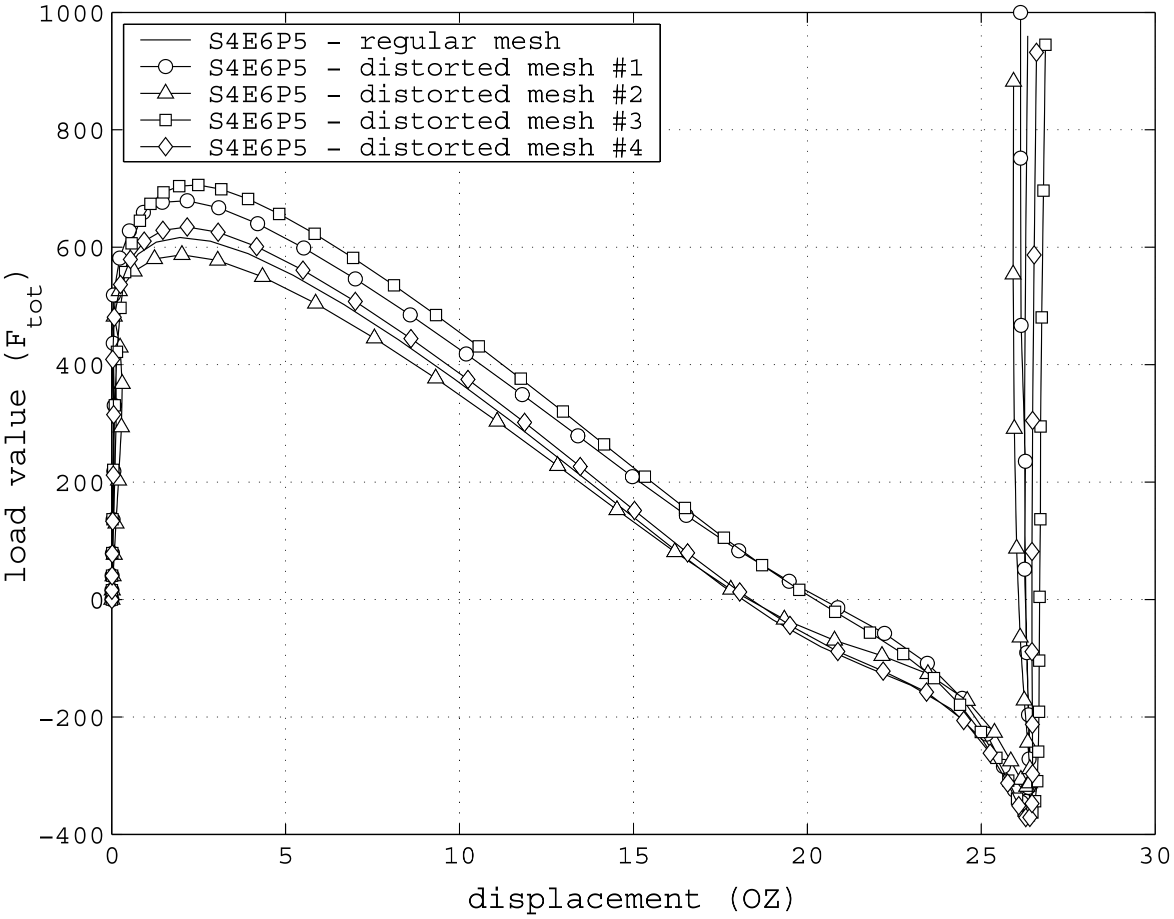

Figure 5.48: Snap-through and snap-back analysis - Results for point B (distorted meshes)

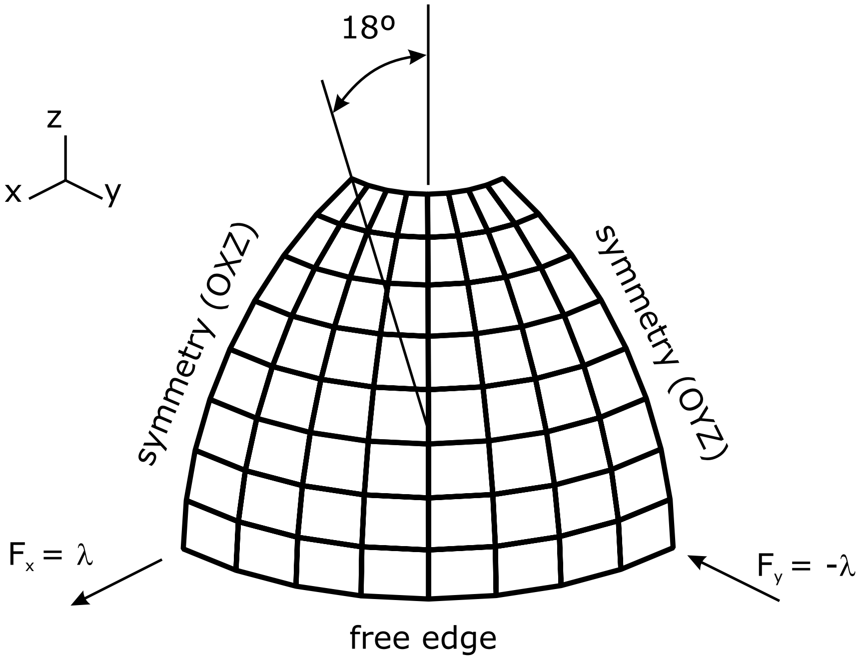

Figure 5.49: Pinched hemisphere with an 18º hole - Mesh, loading and boundary conditions (one quadrant represented)

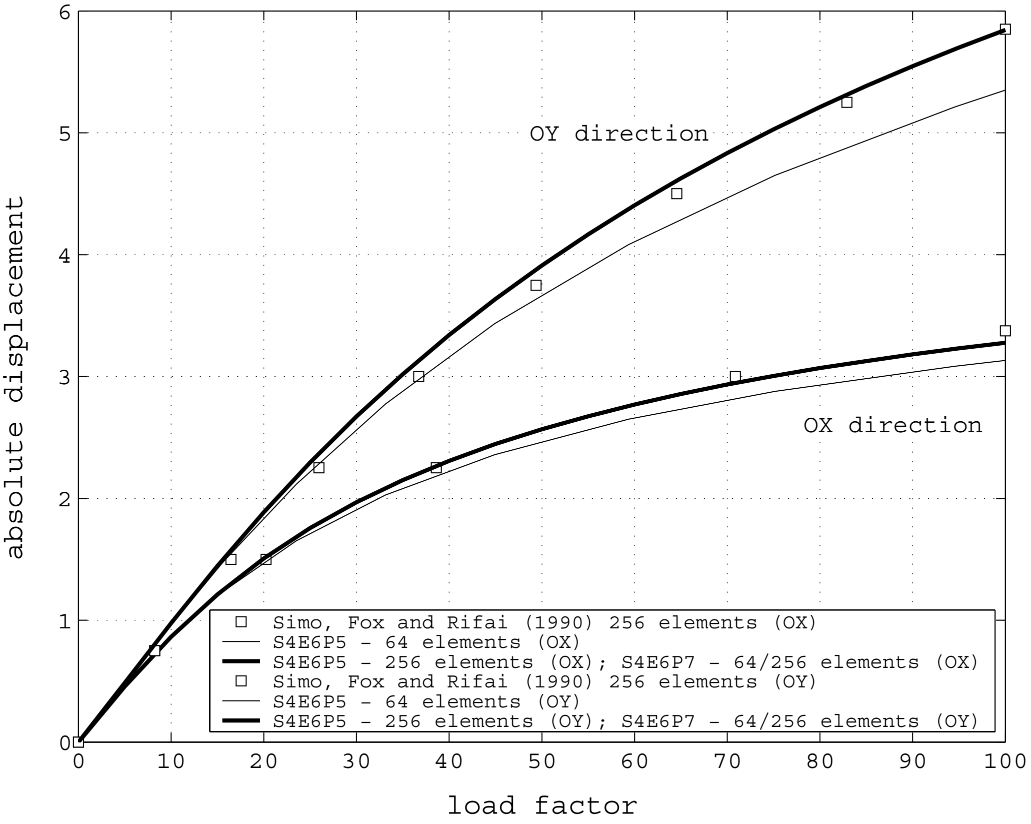

Figure 5.50: Pinched hemisphere with an 18° hole - Results for various mesh configurations

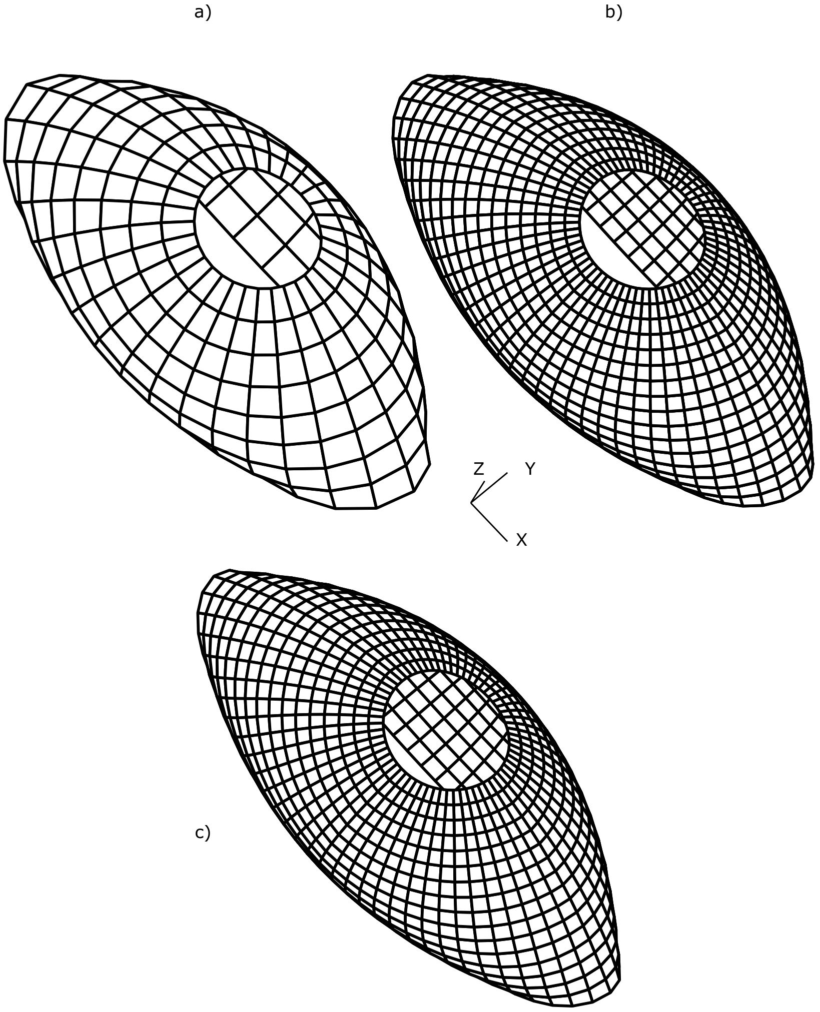

Figure 5.51: Pinched hemisphere with an 18° hole - Final configurations for: (a) 8 × 8 elements mesh and a load factor $\lambda = 100.0$; (b) 16 × 16 elements mesh and a load factor $\lambda = 100.0$; (c) 16 × 16 elements mesh and a load factor $\lambda = 200.0$

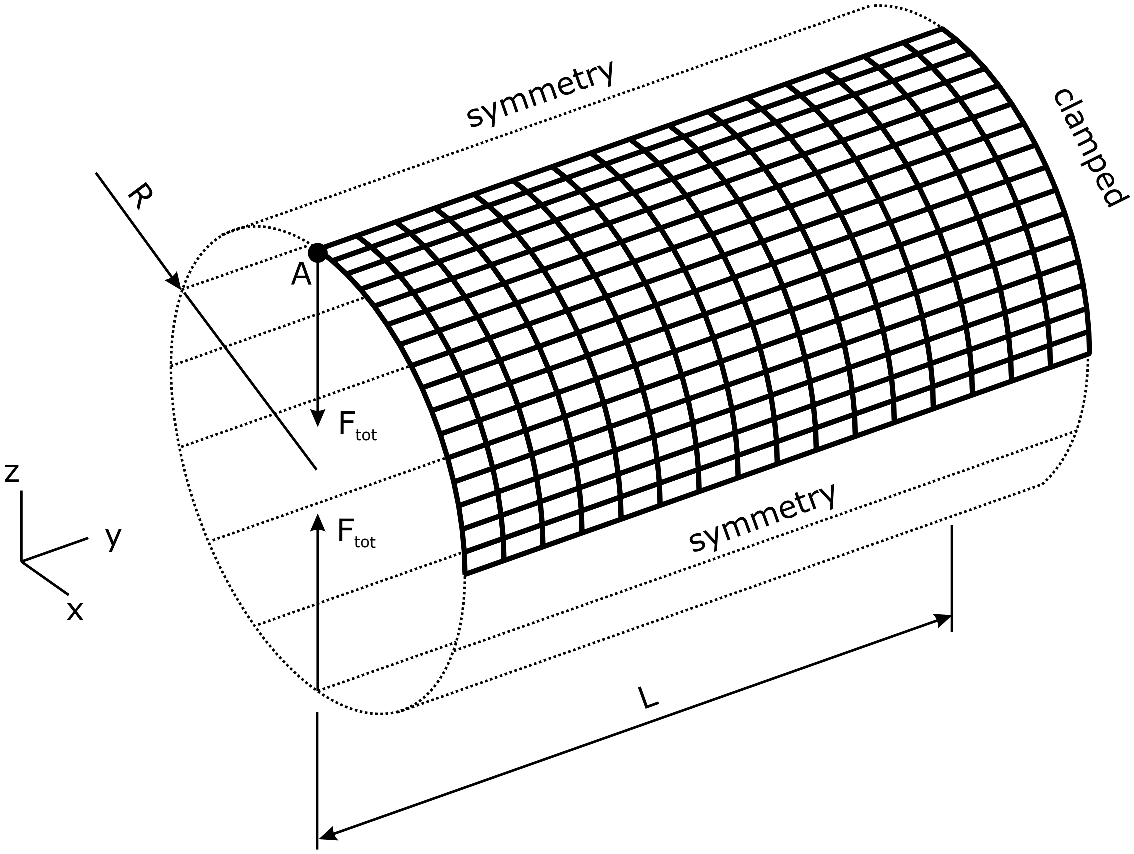

Figure 5.52: Clamped cylindrical shell problem - Mesh, loading and boundary conditions

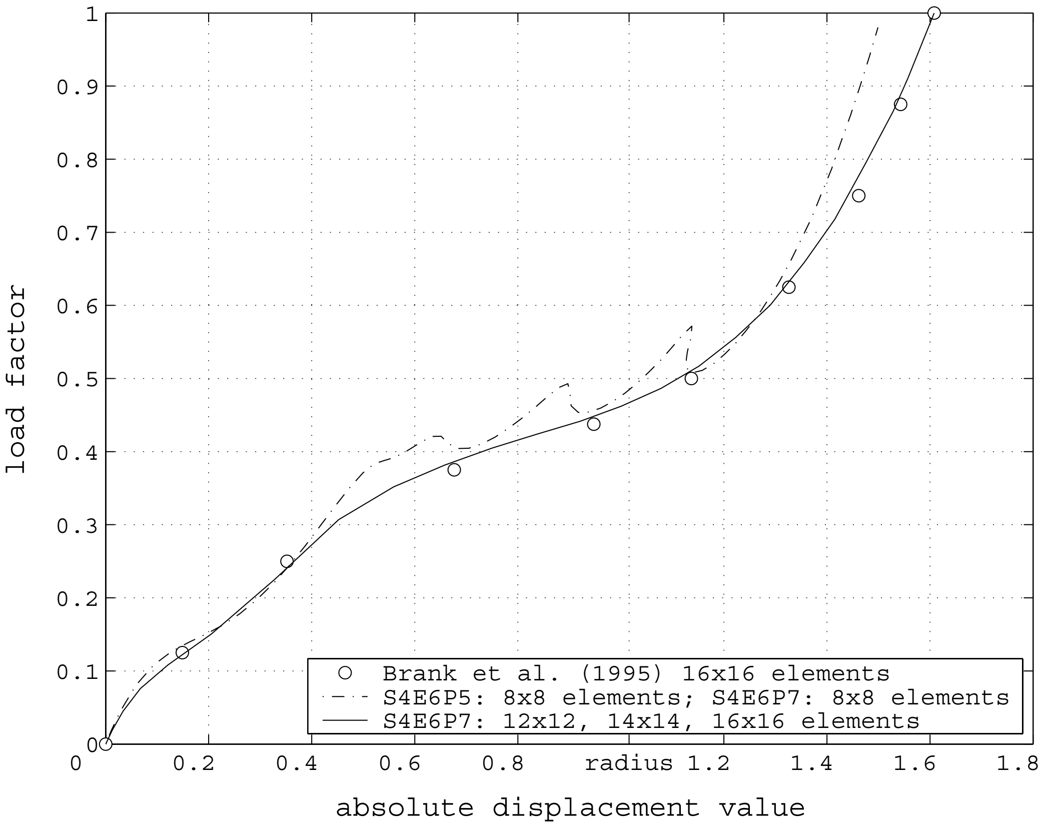

Figure 5.53: Clamped cylindrical shell problem - Results for point A in Fig. 5.52 with an 8 × 8 elements mesh

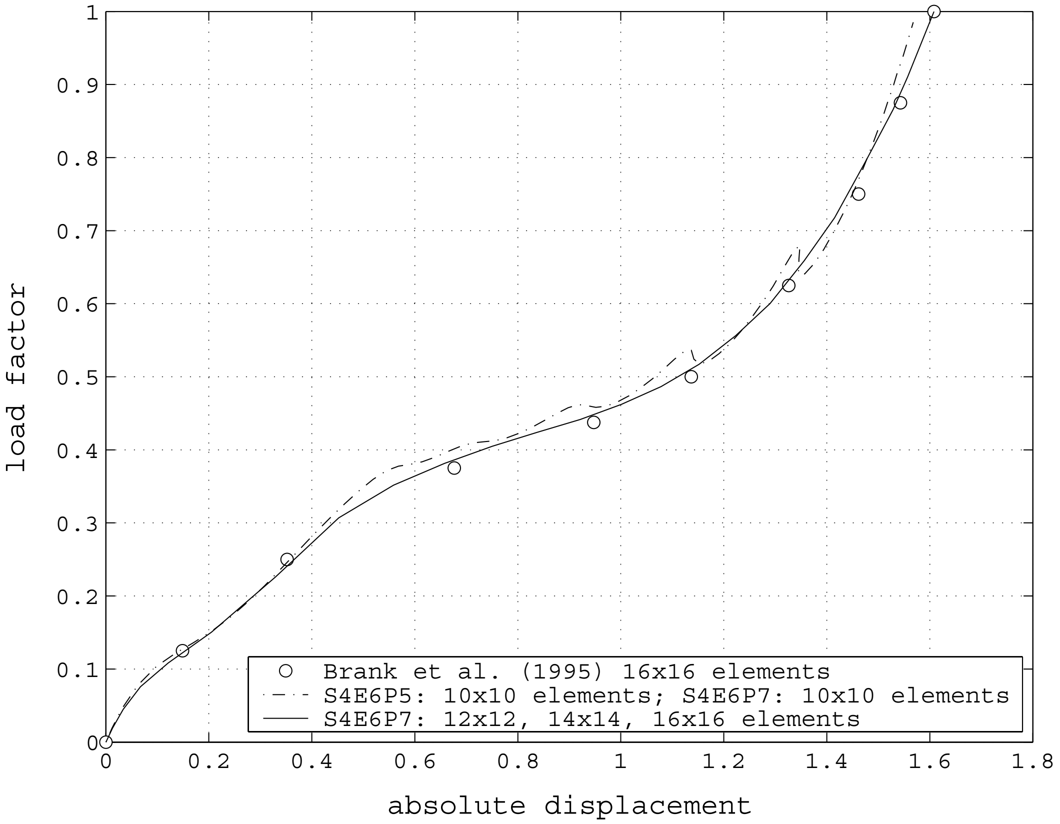

Figure 5.54: Clamped cylindrical shell problem - Results for point A in Fig. 5.52 with an 10×10 elements mesh

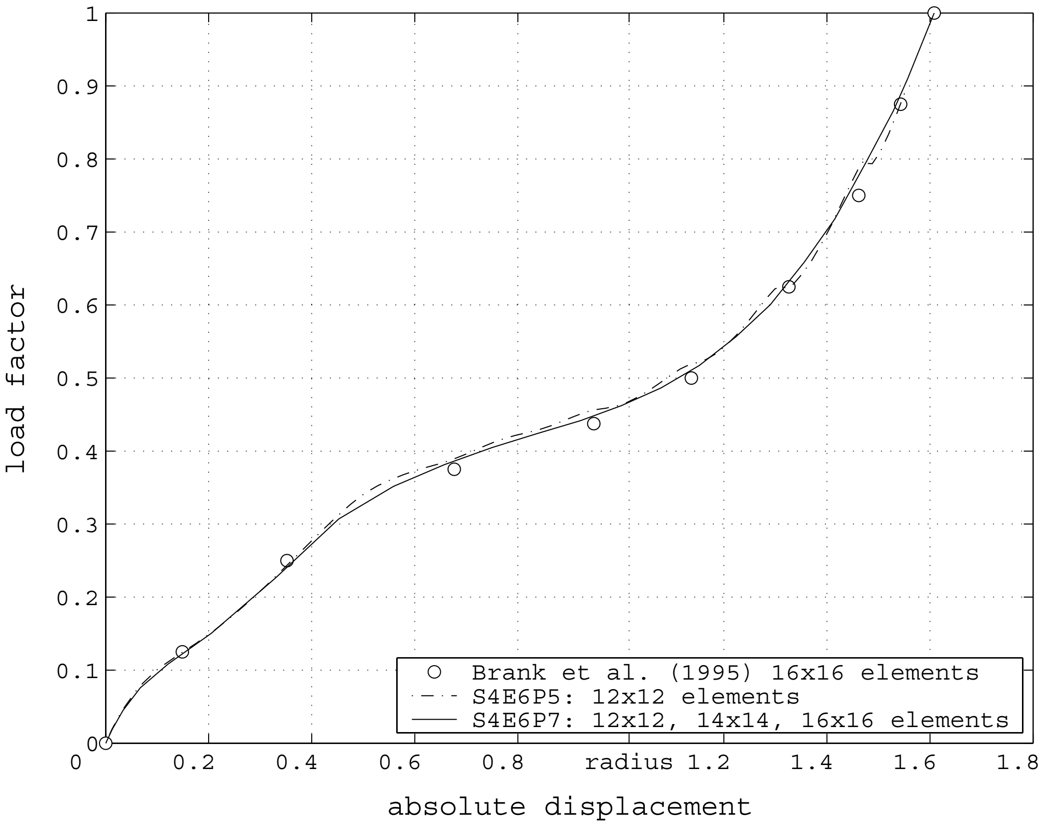

Figure 5.55: Clamped cylindrical shell problem - Results for point A in Fig. 5.52 with an 12 × 12 elements mesh

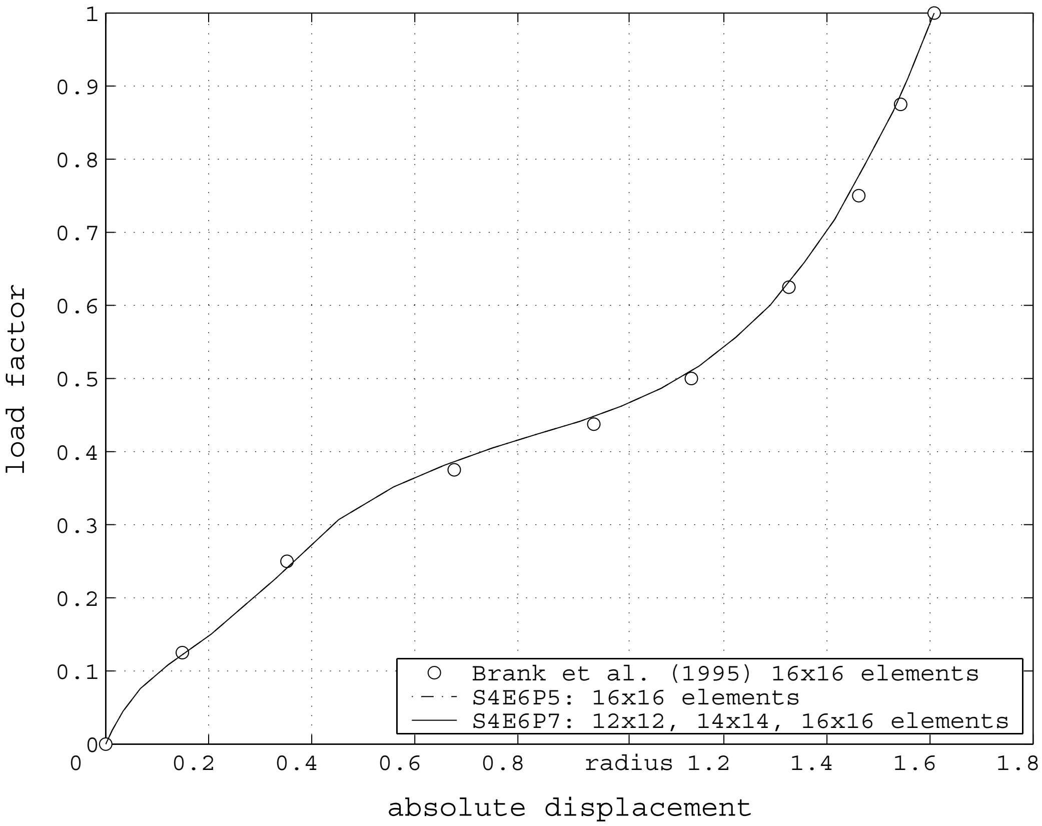

Figure 5.56: Clamped cylindrical shell problem - Results for point A in Fig. 5.52 with an 16 × 16 elements mesh

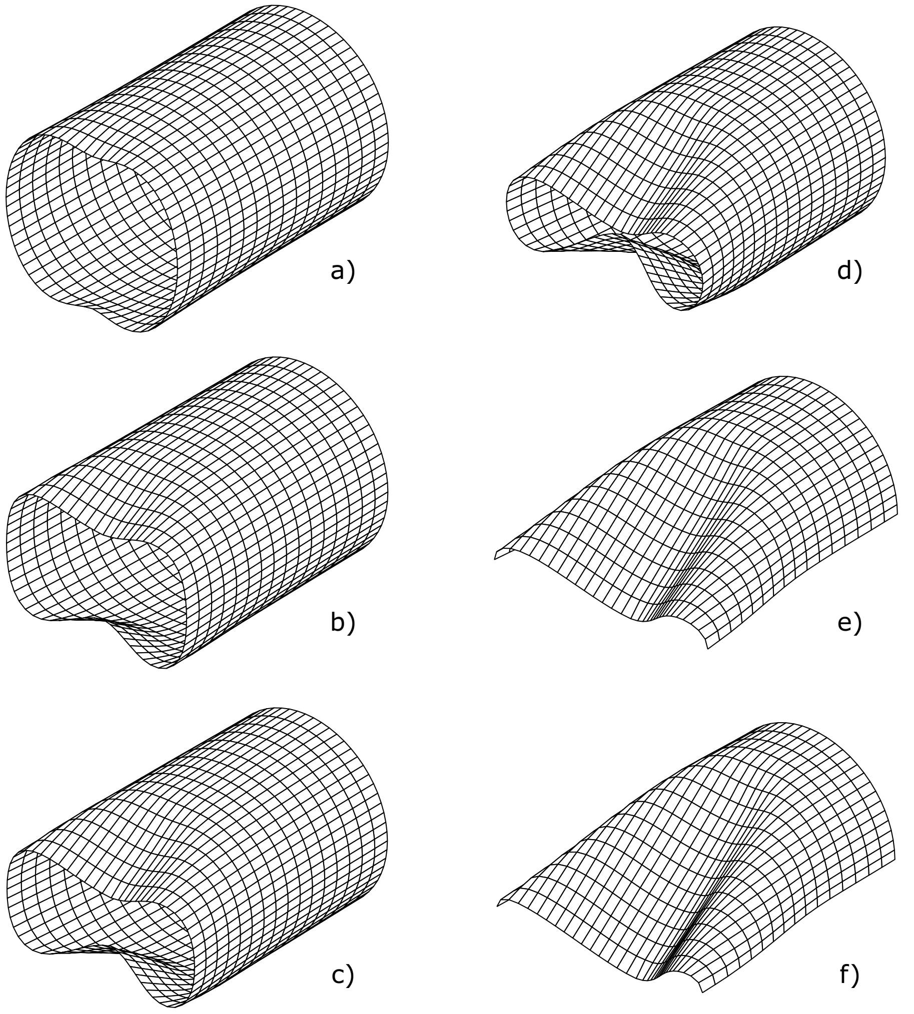

Figure 5.57: Clamped cylindrical shell problem - Sequence of deformed configurations, for the 16×16 elements, and displacements of: (a) 0.202R, (b) 0.550R, (c) 0.739R, (d) 0.985R, (e) 1.335R, (f) 1.584R

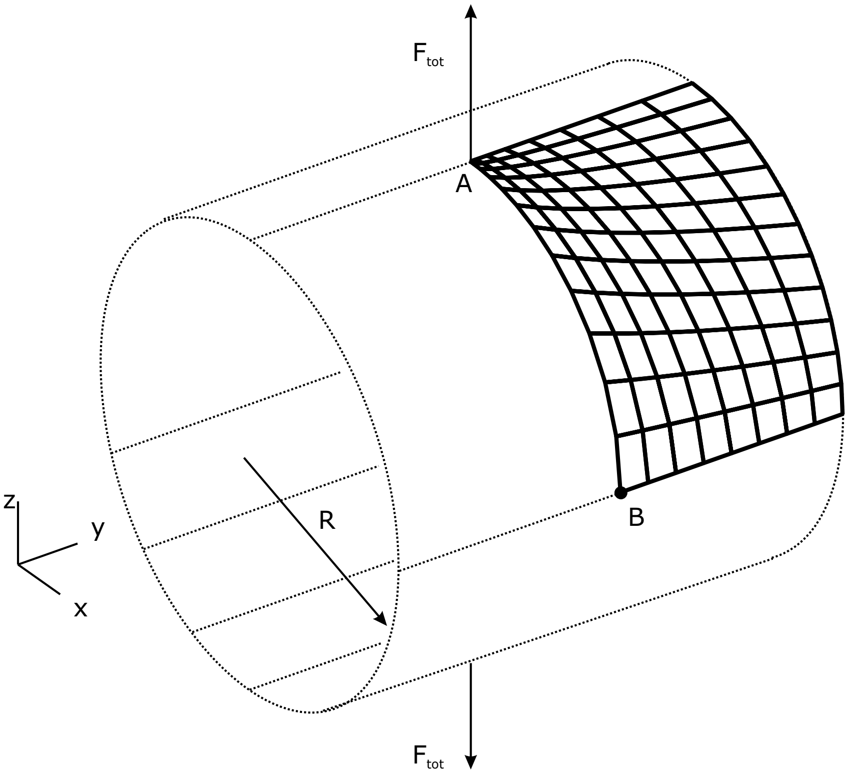

Figure 5.58: Stretching of a free cylinder - Model for simulation with 12×8 elements in a distorted mesh

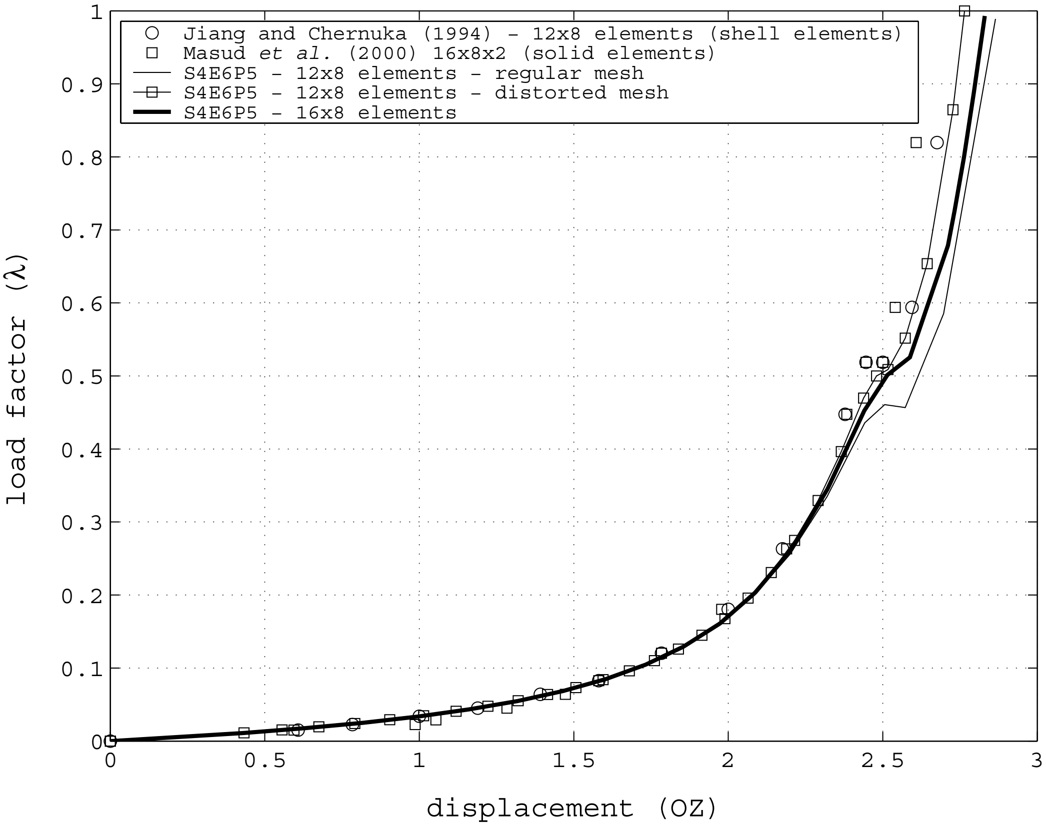

Figure 5.59: Stretching of a free cylinder - Results for point A in Fig. 5.58

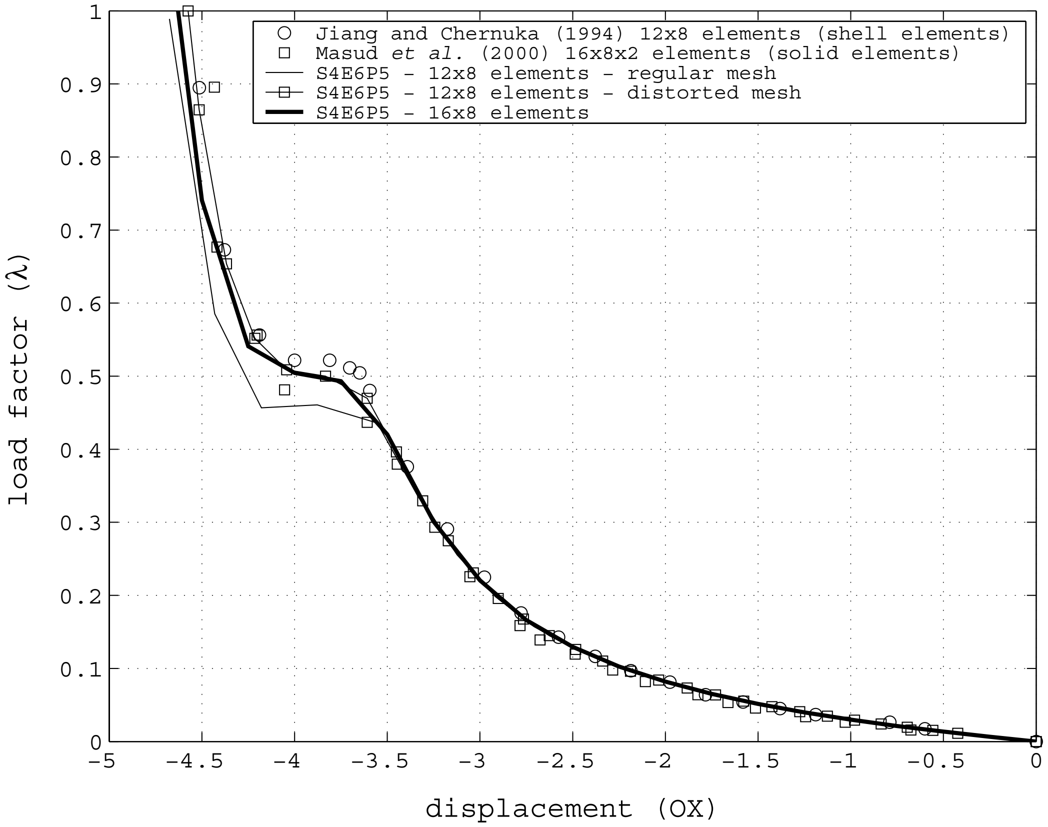

Figure 5.60: Stretching of a free cylinder - Results for point B in Fig. 5.58

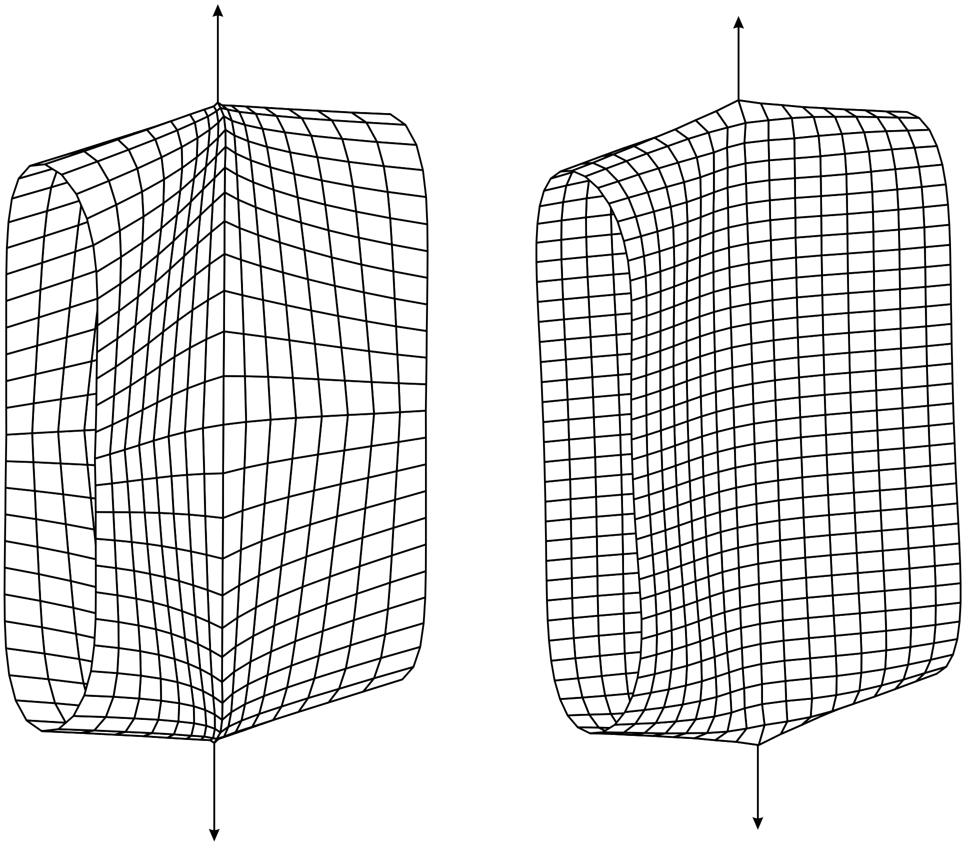

Figure 5.61: Stretching of a free cylinder - Final configuration ($\lambda = 1.0$) for the distorted (12×8) and regular (16×8) meshes

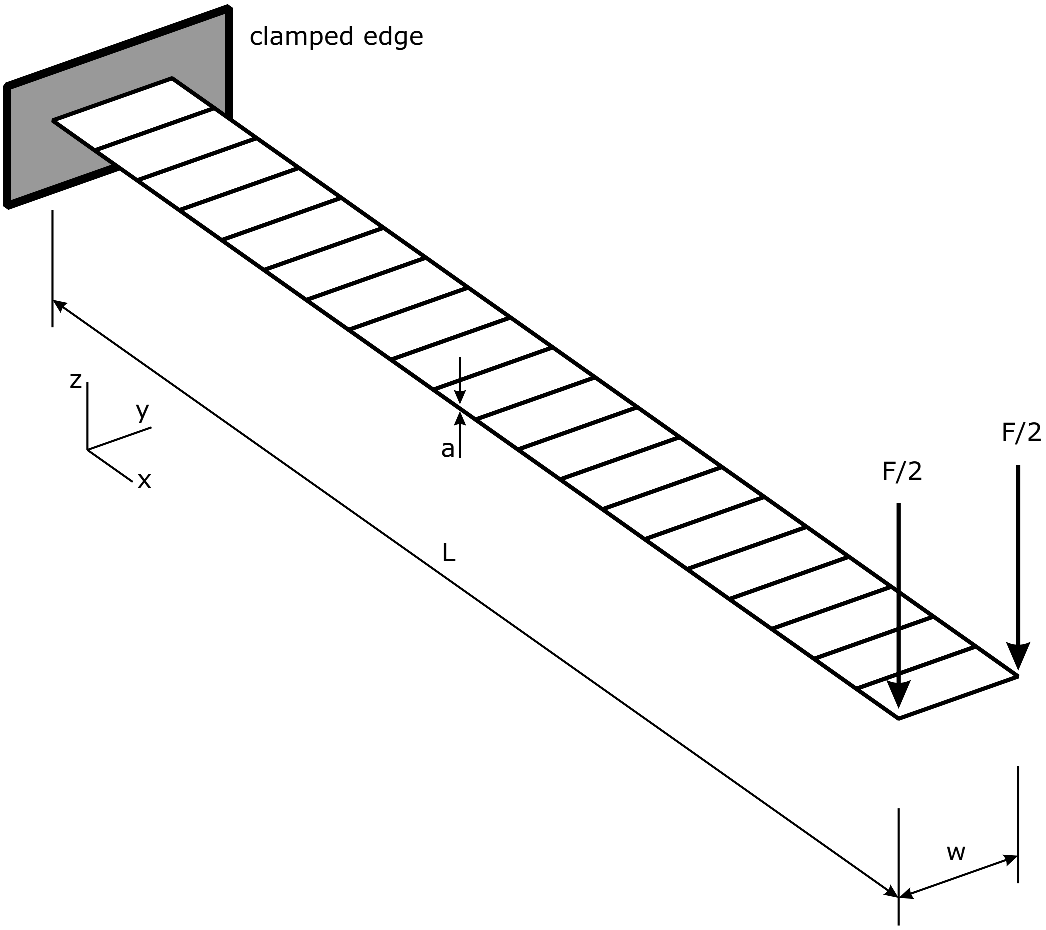

Figure 5.62: Elasto-plastic cantilever beam - Geometry and boundary conditions

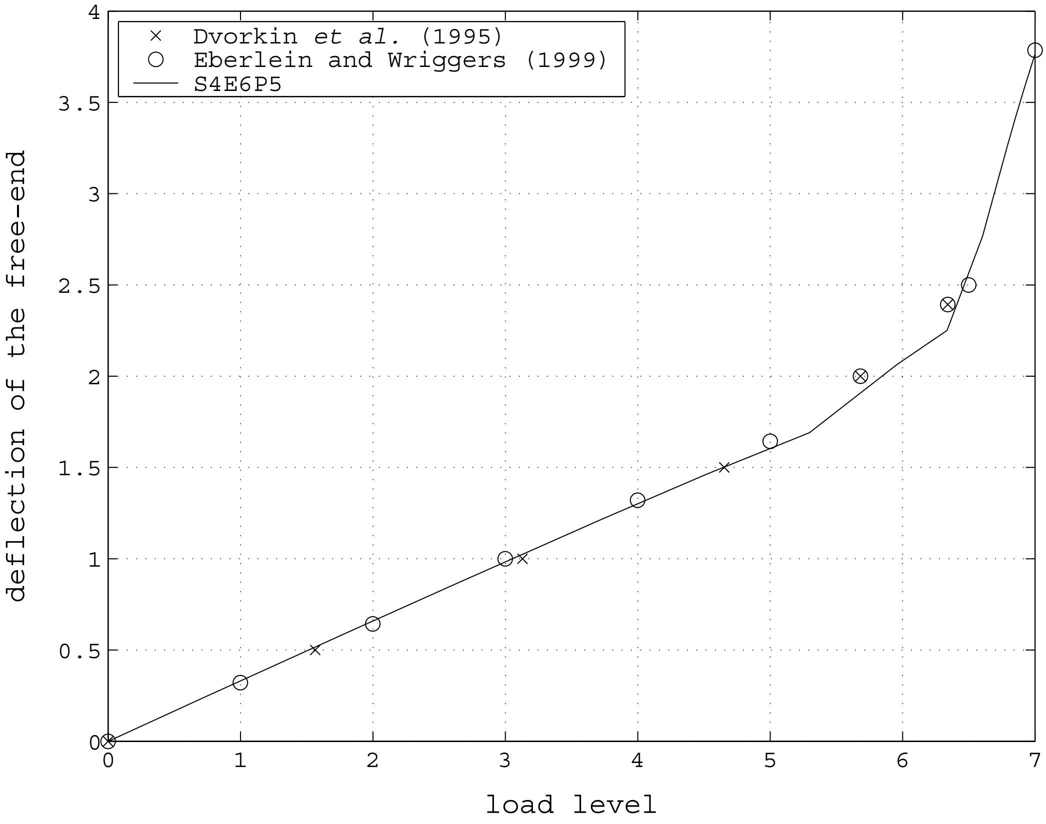

Figure 5.63: Elasto-plastic cantilever beam - Deflection values following the evolution of the load level F

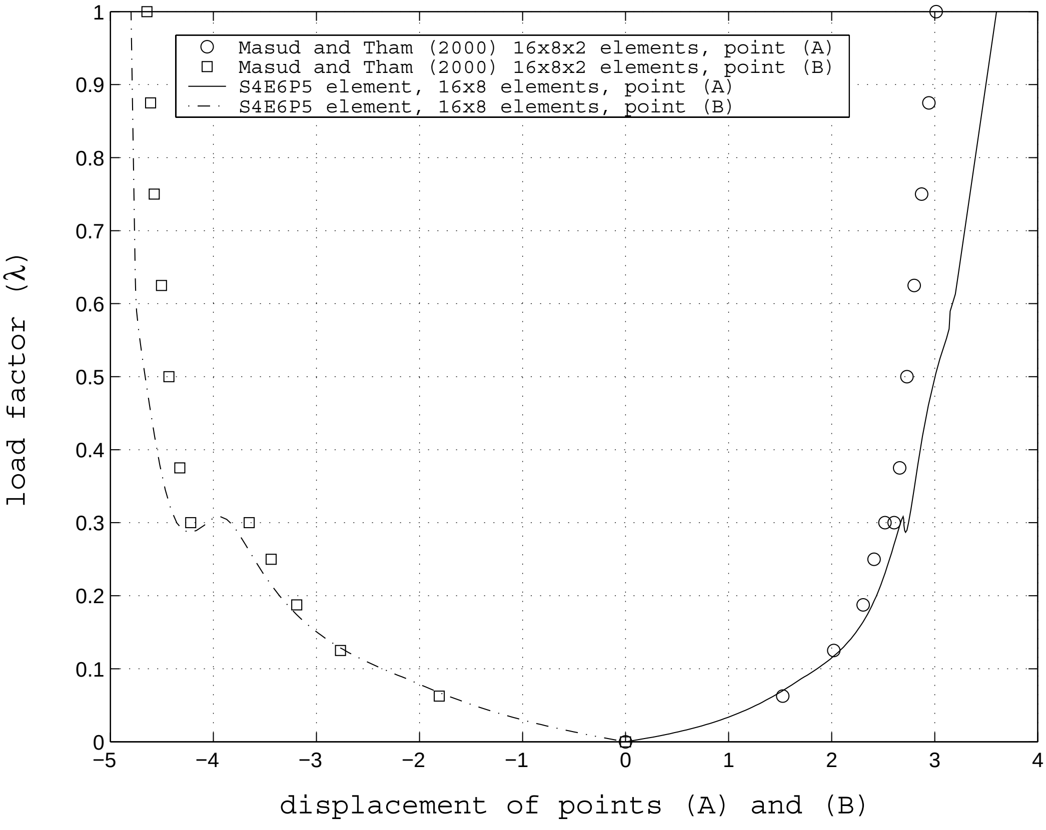

Figure 5.64: Free cylindrical shell - Displacement of points A and B in Fig. 5.58 for a given load factor (λ)

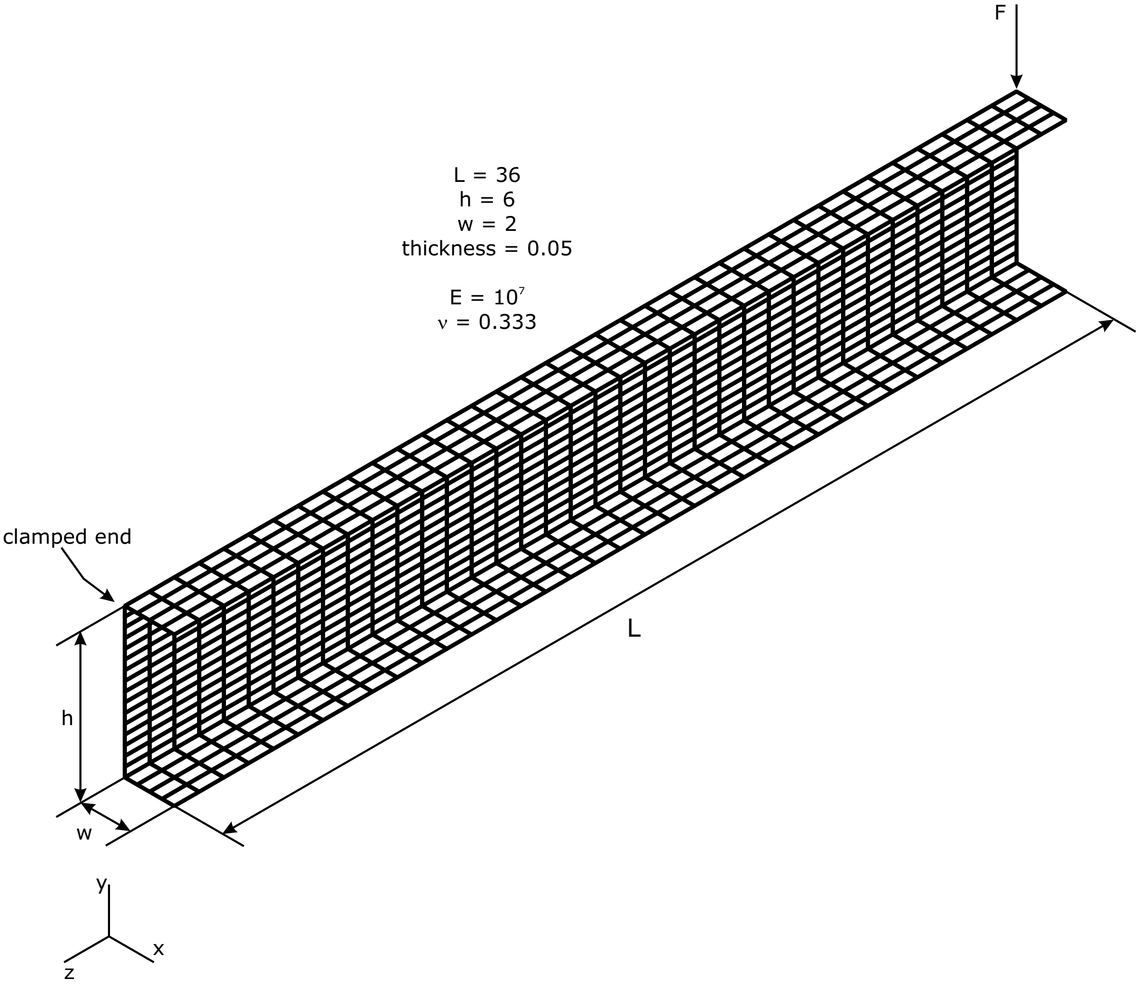

Figure 5.65: Channel-section beam - Model with a mesh of 24 × 36 elements, including geometric, boundary and loading conditions

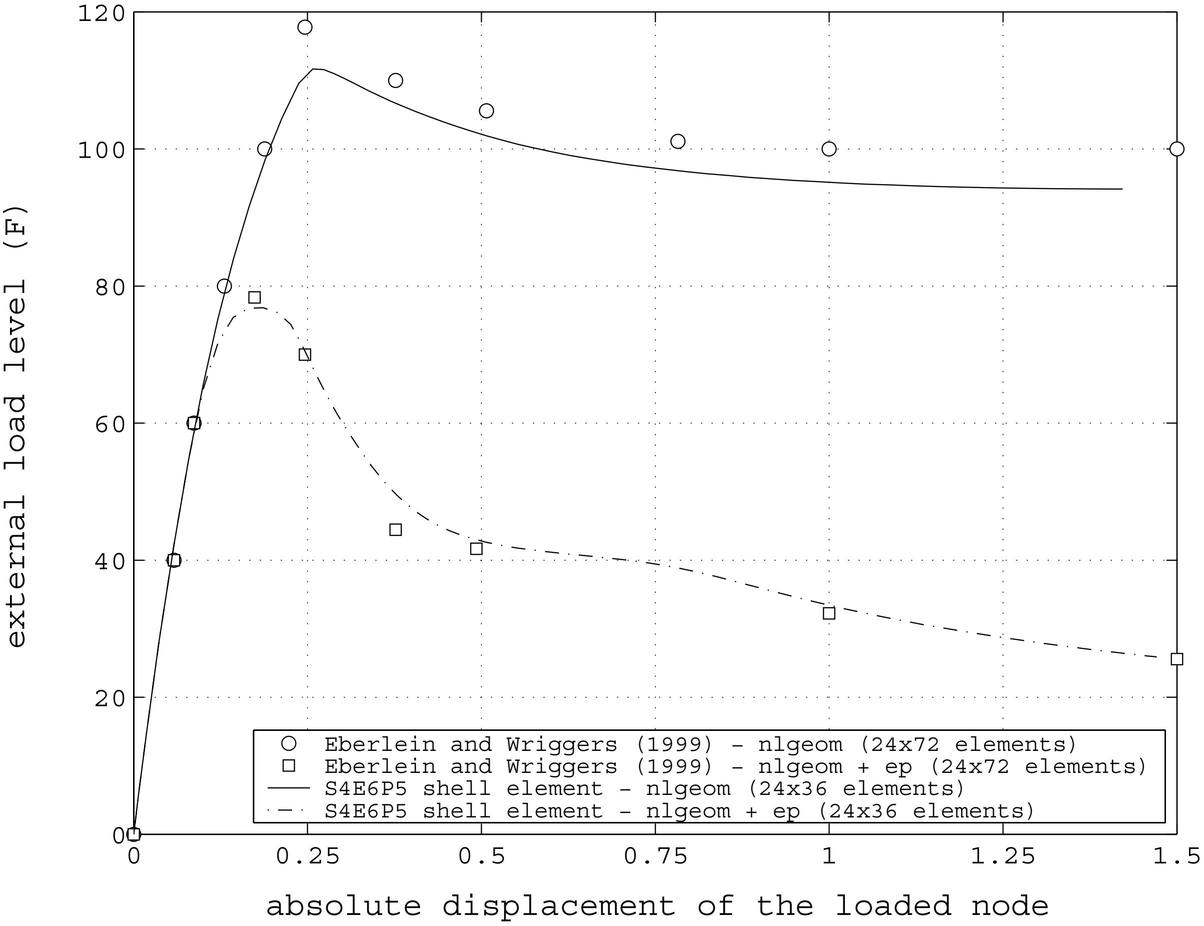

Figure 5.66: Channel-section beam - Deflection curves for the loaded node

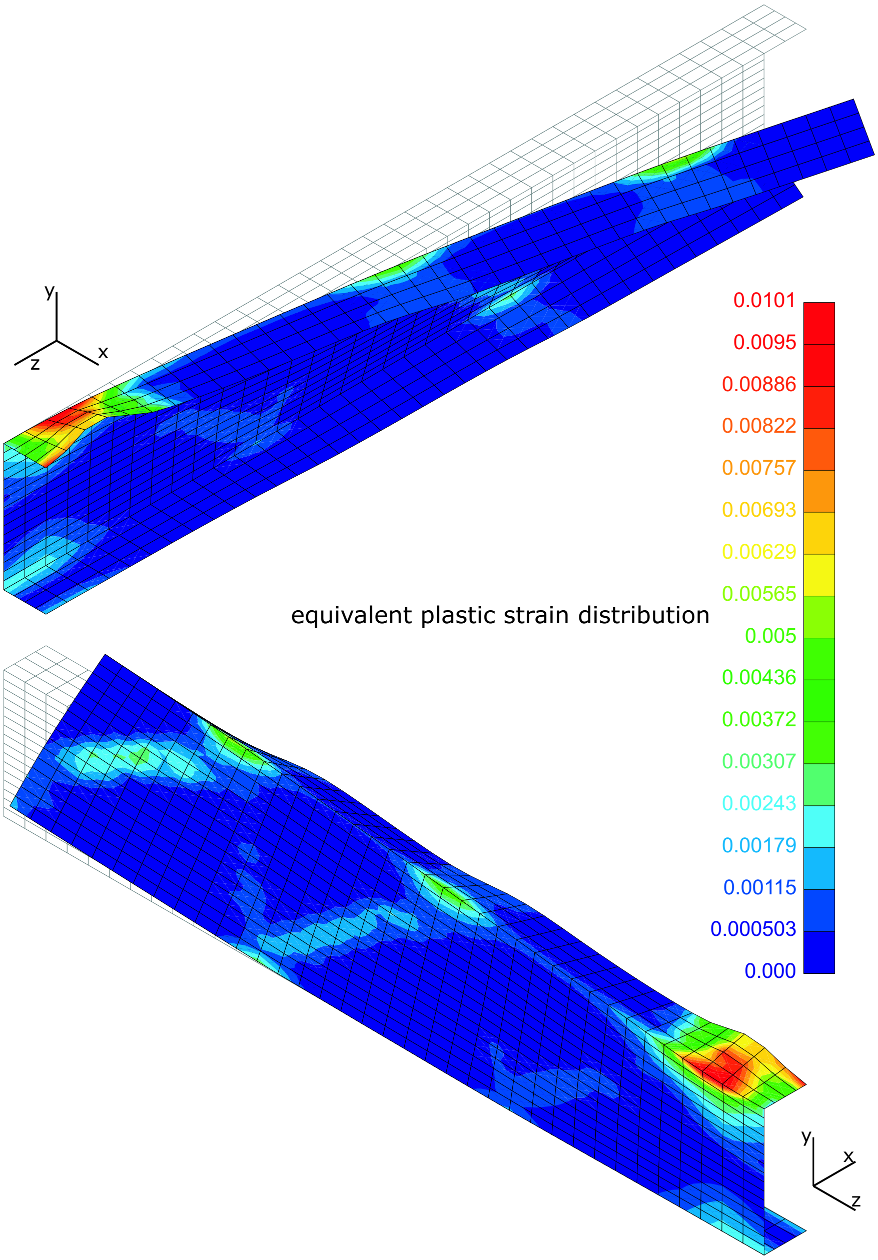

Figure 5.67: Channel-section beam - Deformed configuration and equivalent plastic strain for a displacement value of 1.471

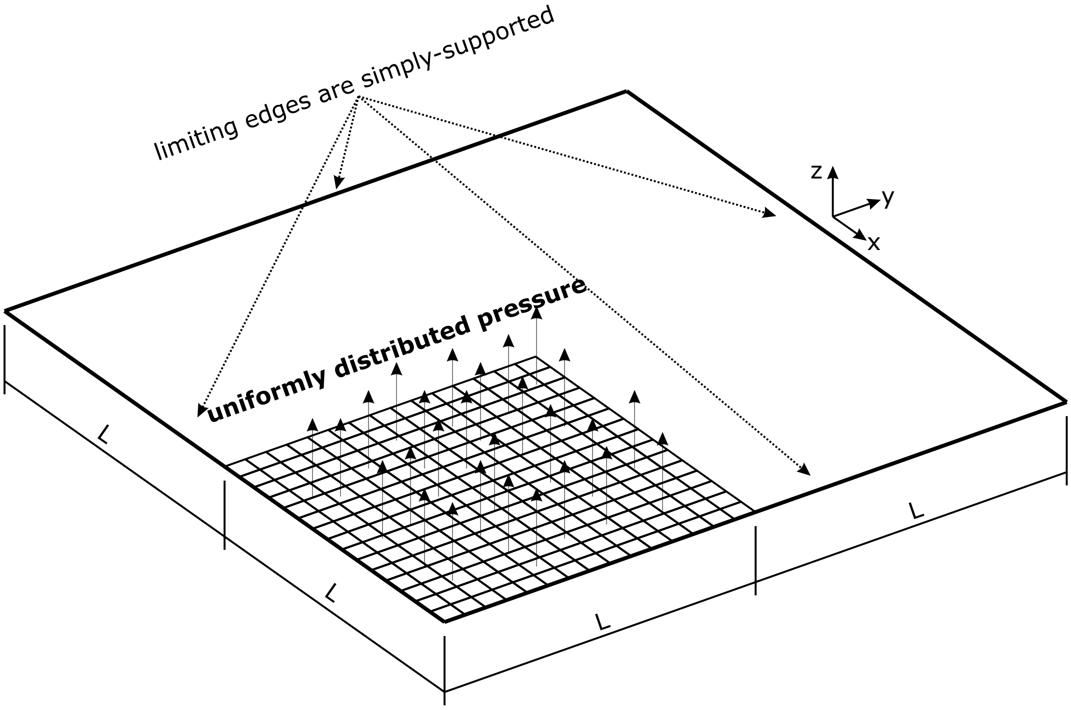

Figure 5.68: Simply-supported plate - Problem definition with a representative regular mesh of 15 × 15 elements

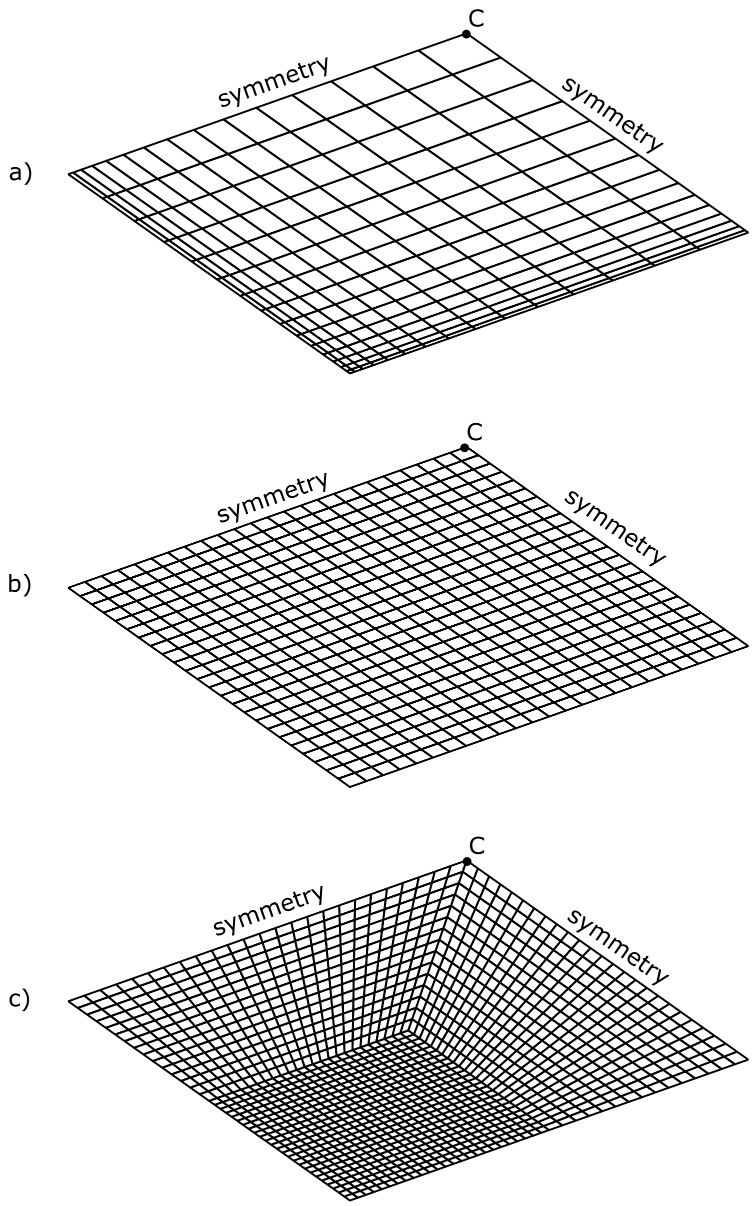

Figure 5.69: Simply-supported plate - Adopted meshes with: a) 15 × 15; b) 24 × 24; c) 1375 shell elements

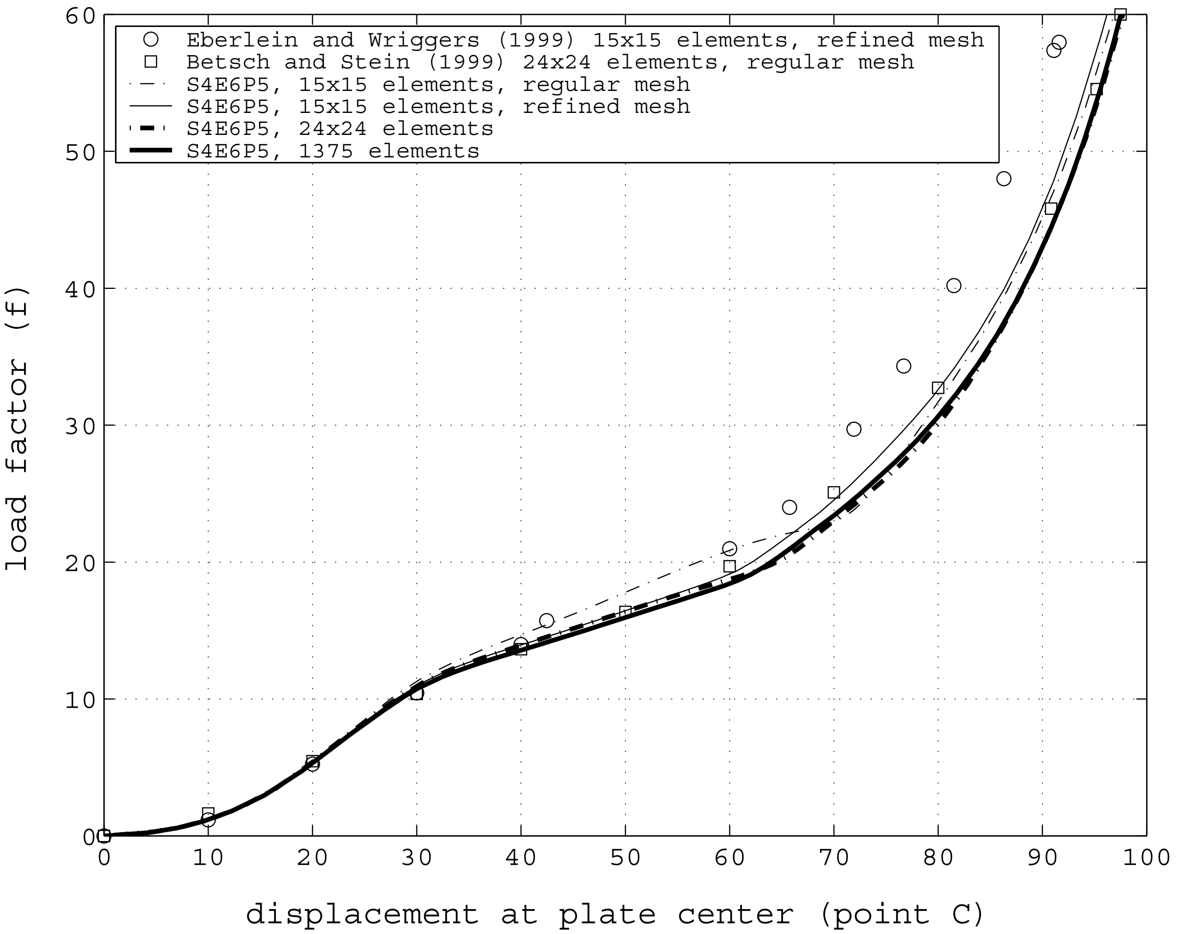

Figure 5.70: Simply-supported plate - Load-deflection curves for a limit load factor f = 60

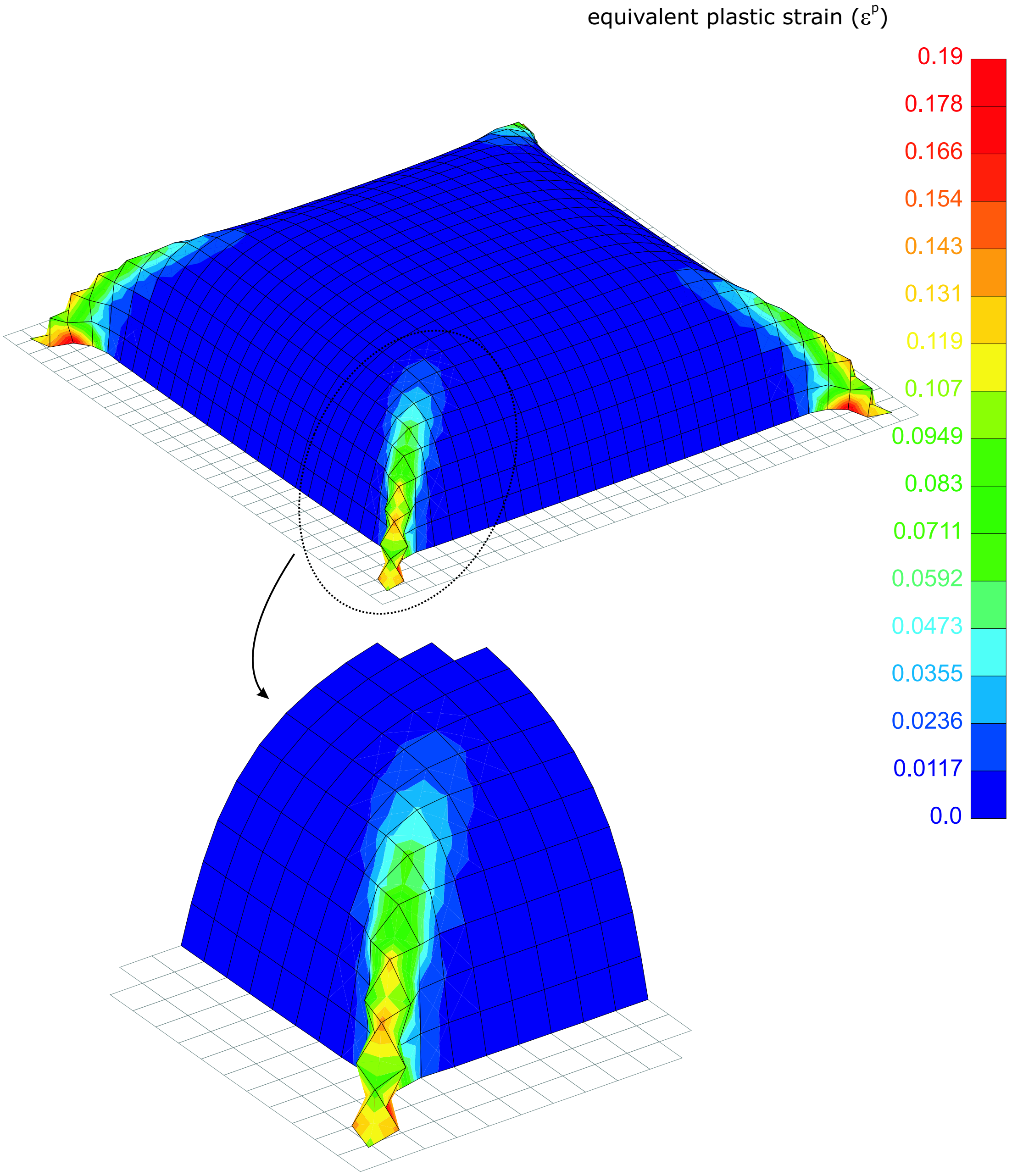

Figure 5.71: Simply-supported plate - Deformed configuration for the 15×15 regular mesh with a load factor $\mathsf{f} = 60$

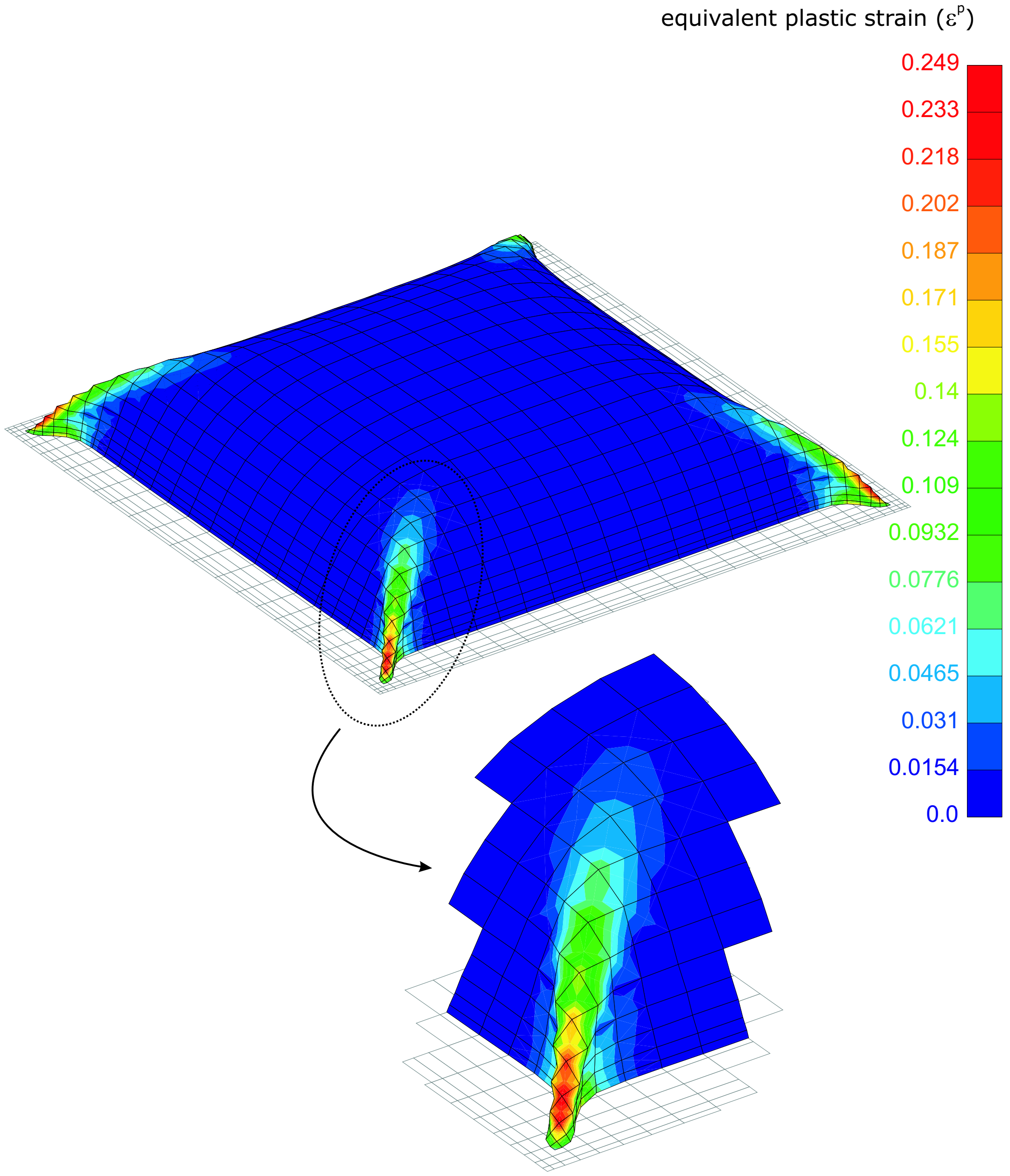

Figure 5.72: Simply-supported plate - Deformed configuration for the 15×15 mesh (refined at the corners) with a load factor $\mathsf{f} = 60$

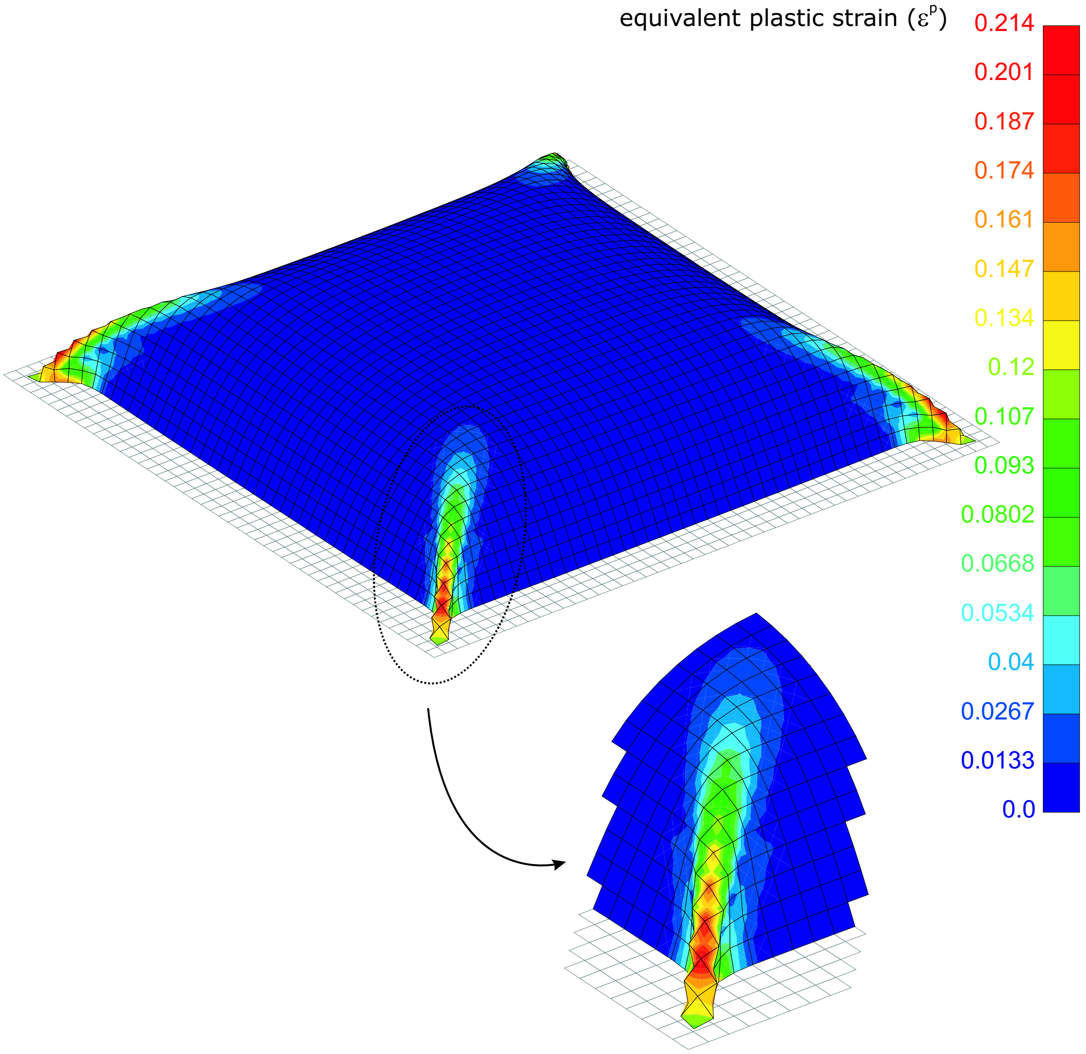

Figure 5.73: Simply-supported plate - Deformed configuration for the 24 × 24 mesh for a load factor $\mathsf{f} = 60$

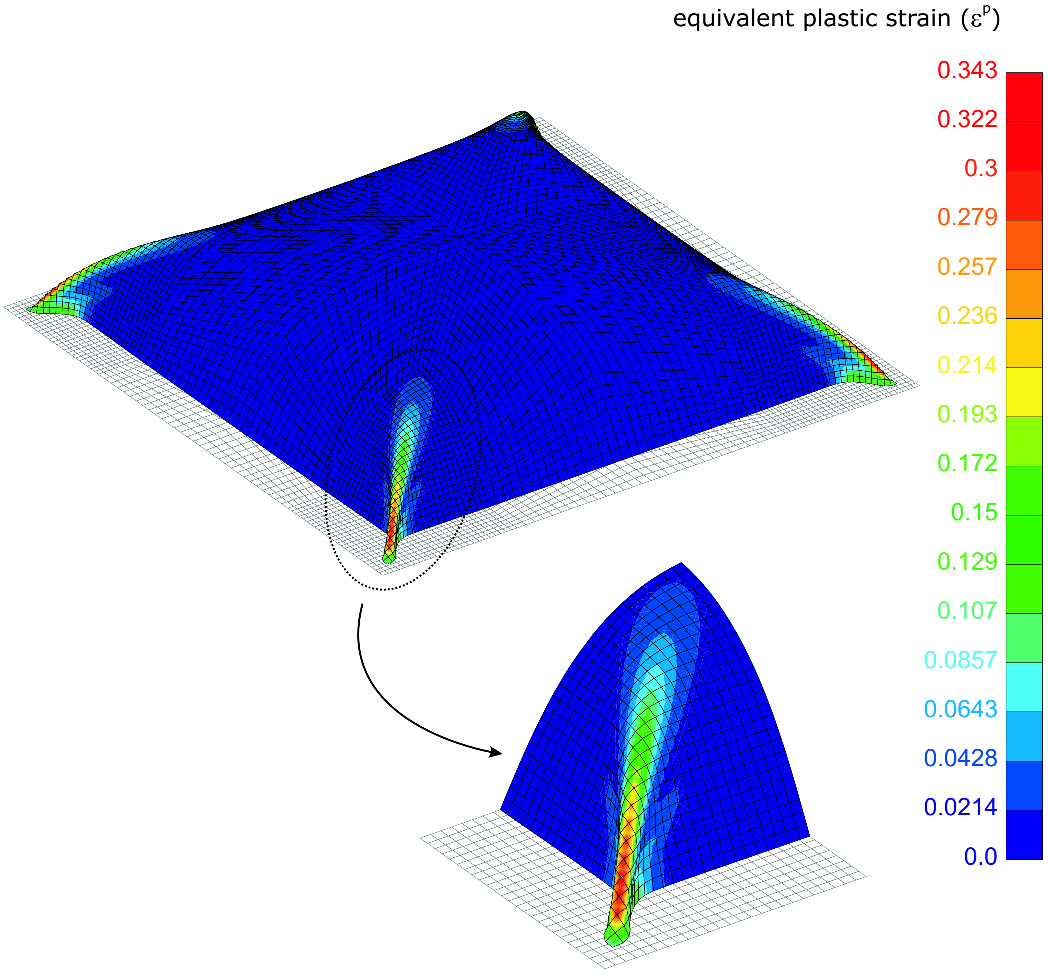

Figure 5.74: Simply-supported plate - Deformed configuration for the mesh with 1375 elements for a load factor $\mathsf{f} = 60$

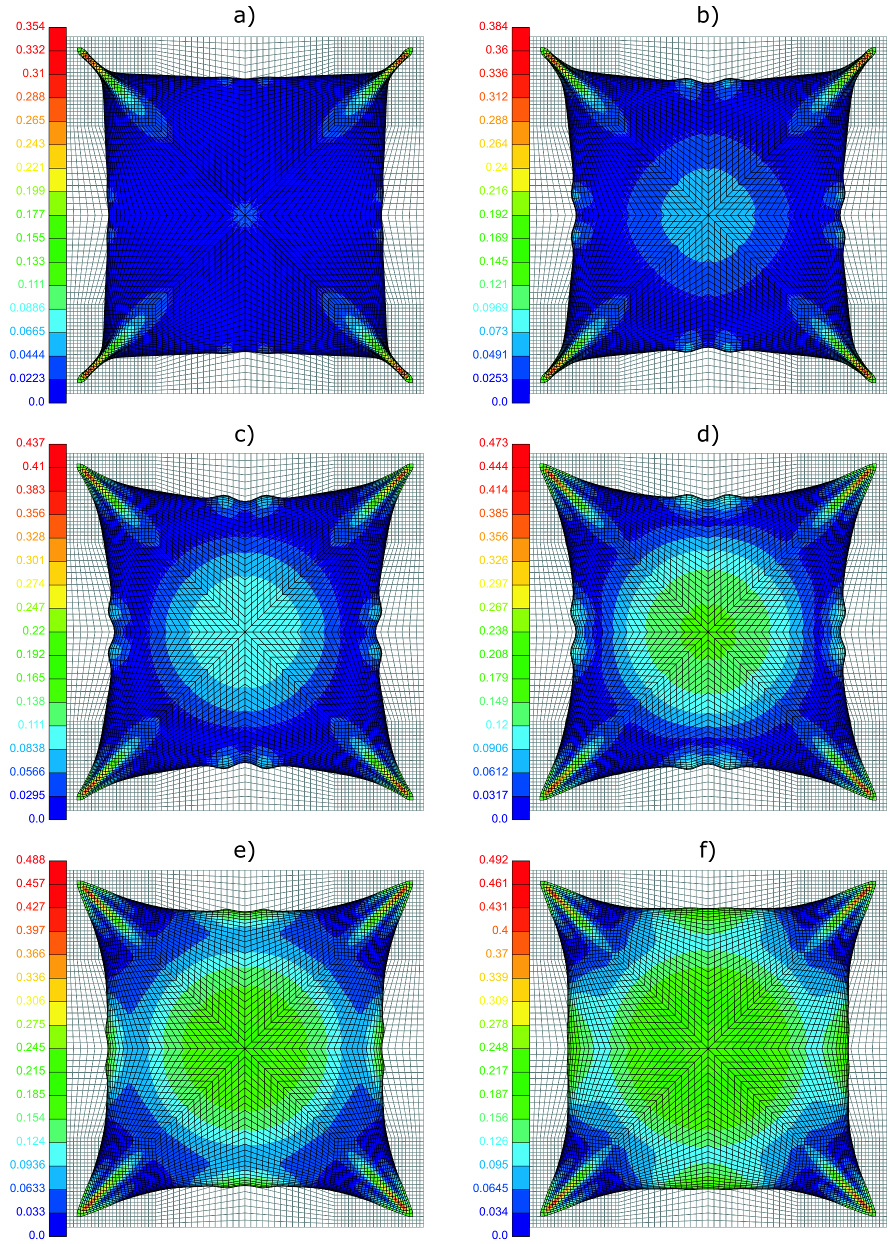

Figure 5.75: Simply-supported plate - Deformed configurations (top view) for load factors a) f = 285.4; b) f = 386.8; c) f = 479.9; d) f = 557.6; e) f = 600.7; f) f = 635.5; with equivalent plastic strain contours

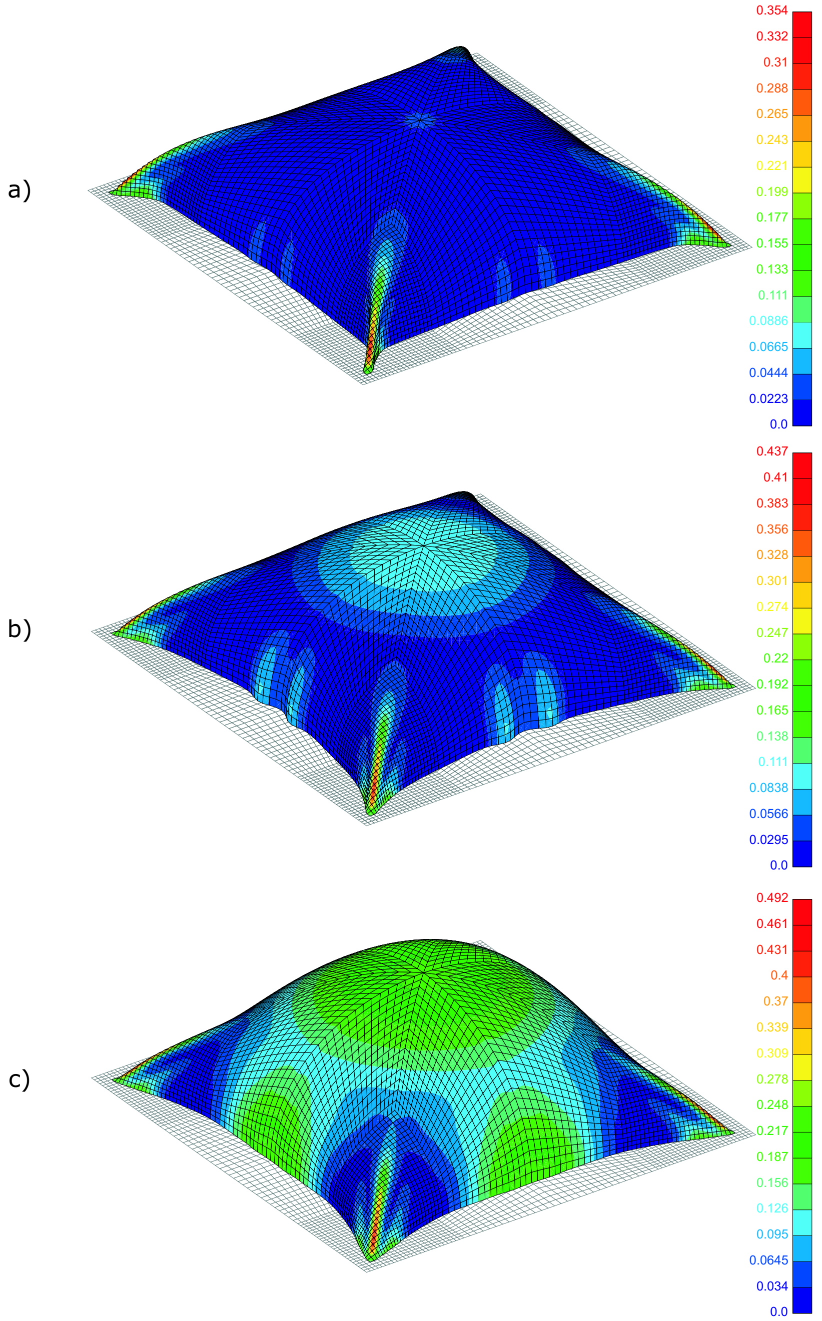

Figure 5.76: Simply-supported plate - Deformed configurations (dimetric perspective) and equivalent plastic strain for load factors: a) f = 285.4; b) f = 479.9; c) f = 635.5

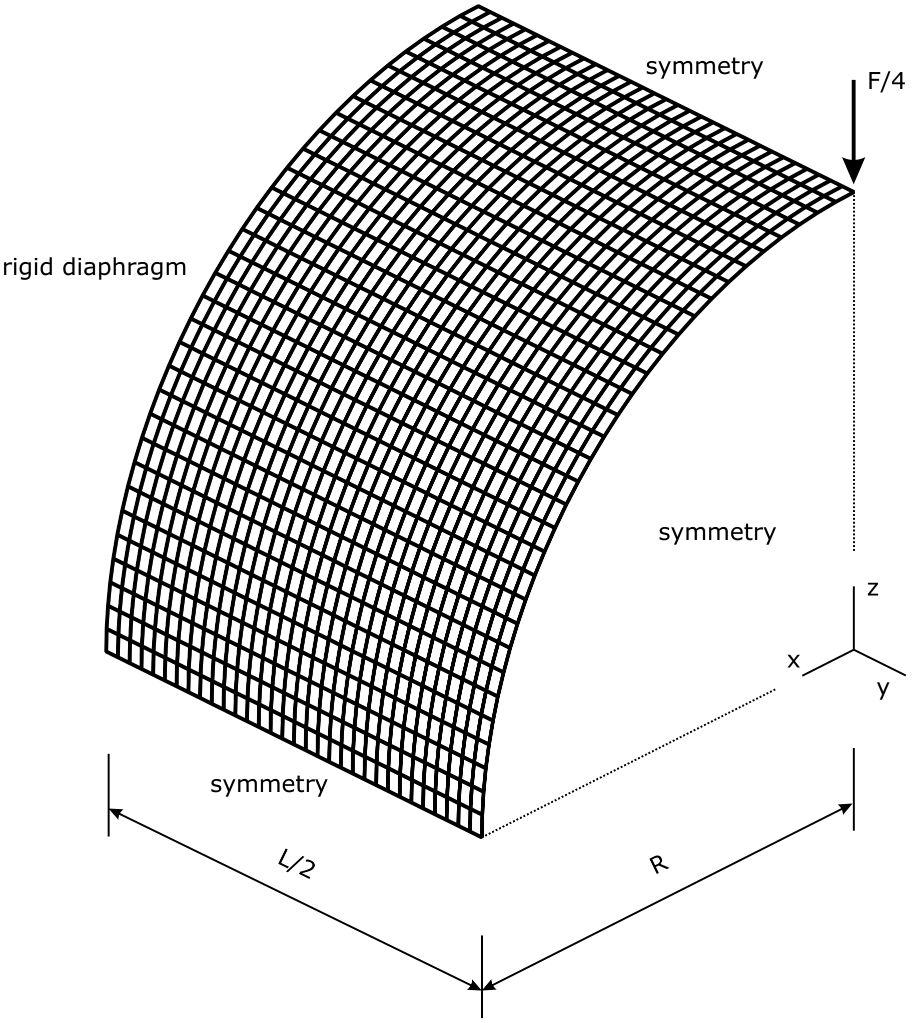

Figure 5.77: Pinched Cylinder - Initial configuration with geometry, loading and boundary conditions.

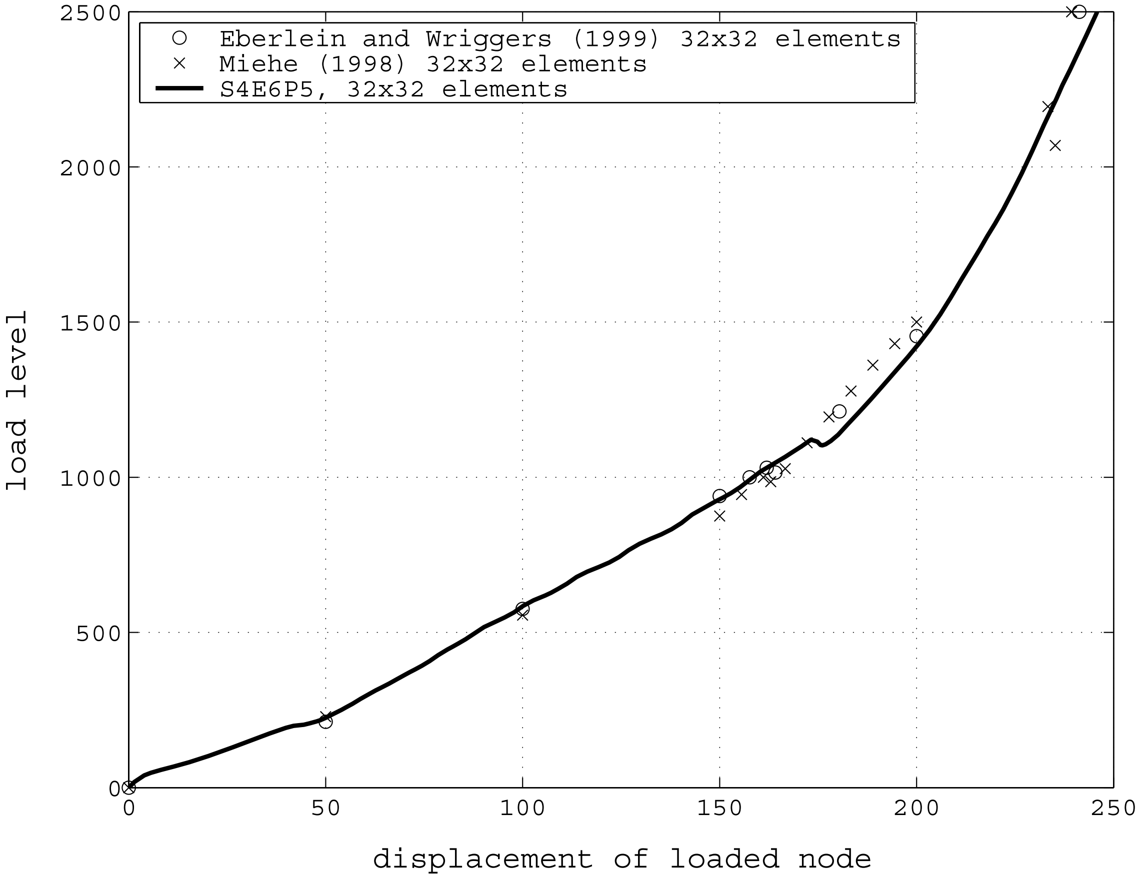

Figure 5.78: Pinched Cylinder - Deflection of the loaded node as a function of the external force F.

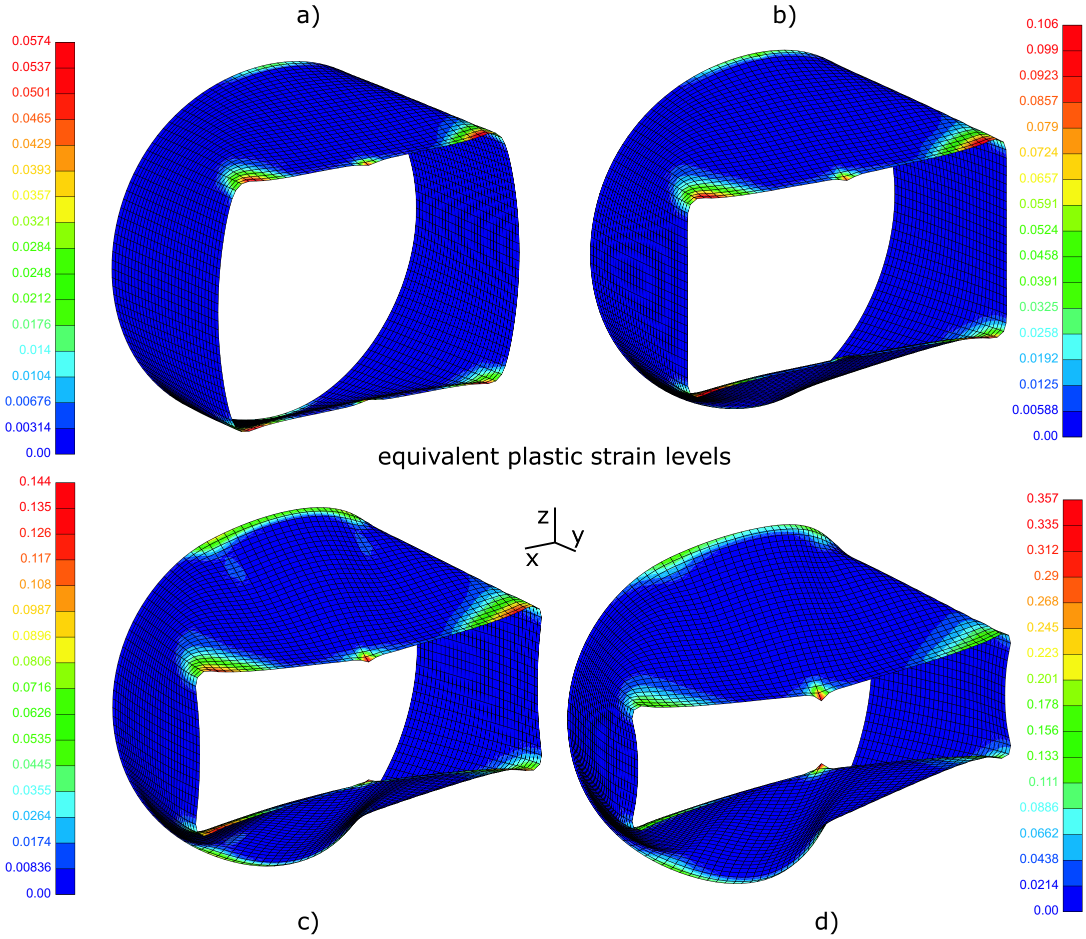

Figure 5.79: Pinched Cylinder - Equivalent plastic strain levels for displacement values of: a) 101.2; b) 151.3; c) 200.0; d) 246.8 consistent unities

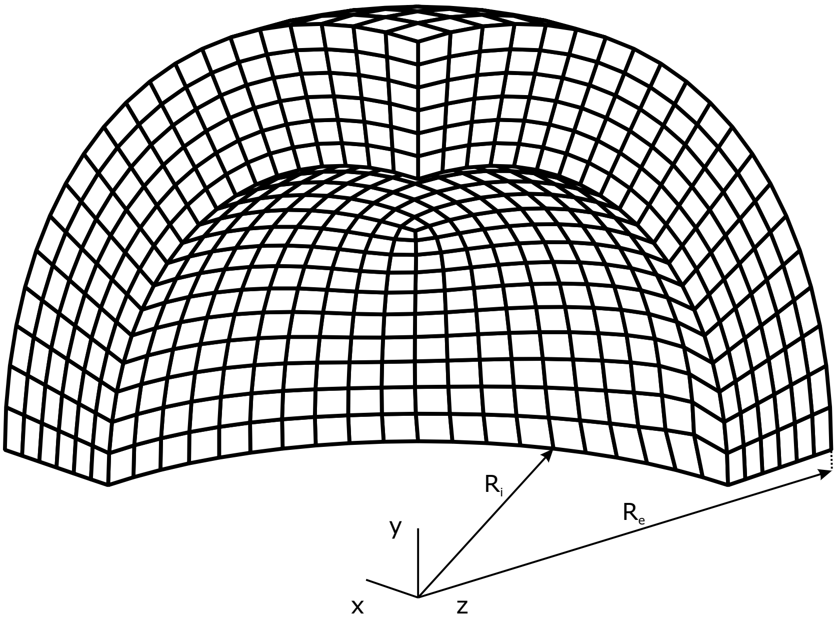

Figure 5.80: Nonlinear geometric thick-wall sphere - Finite elements' mesh adopted, with a total of 2100 solid-shell elements

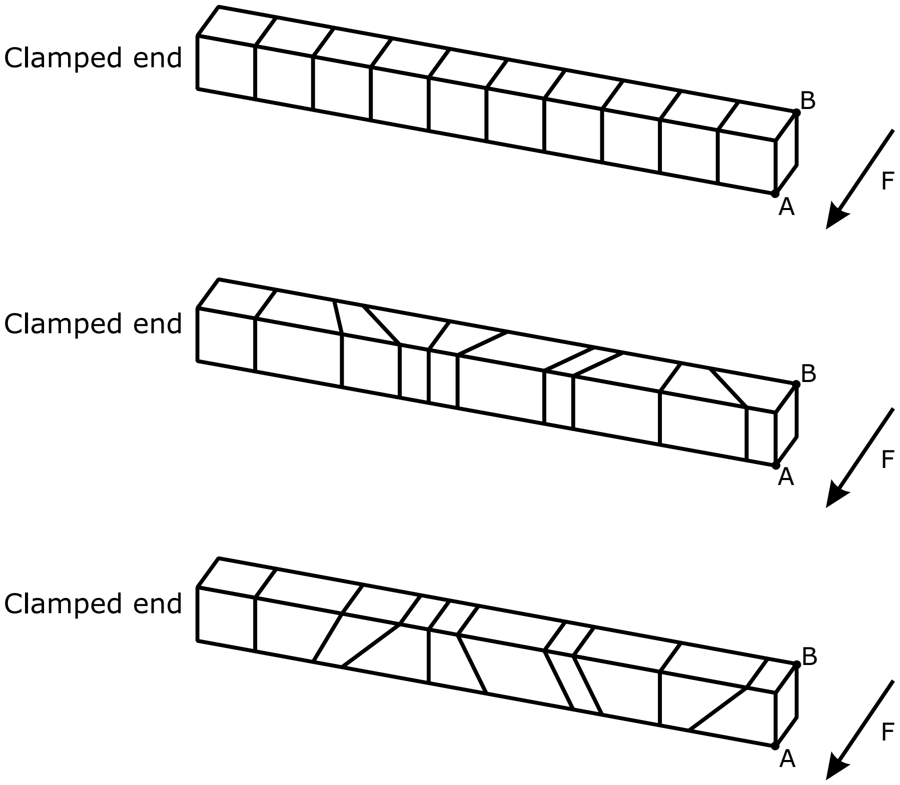

Figure 5.81: Membrane (in-plane) bending benchmark - Initial configurations for 3 different meshes

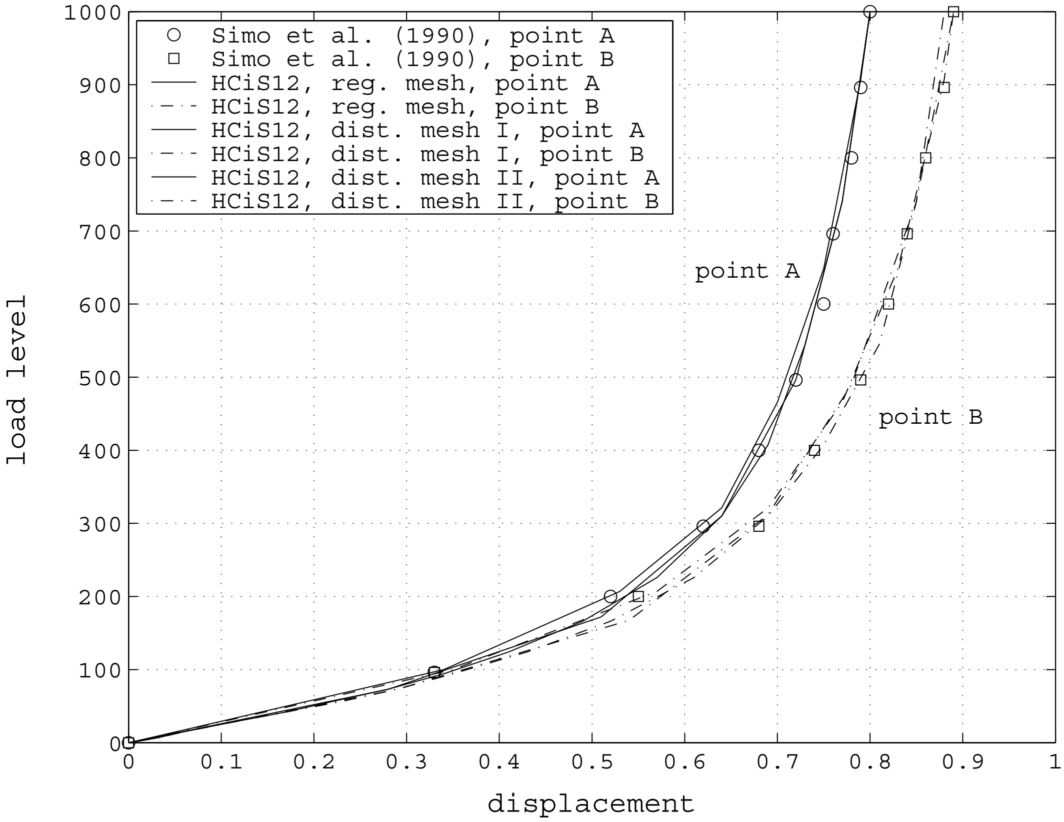

Figure 5.82: Membrane (in-plane) bending benchmark - Evolution of displacements (in the load direction) with load-level for points A and B

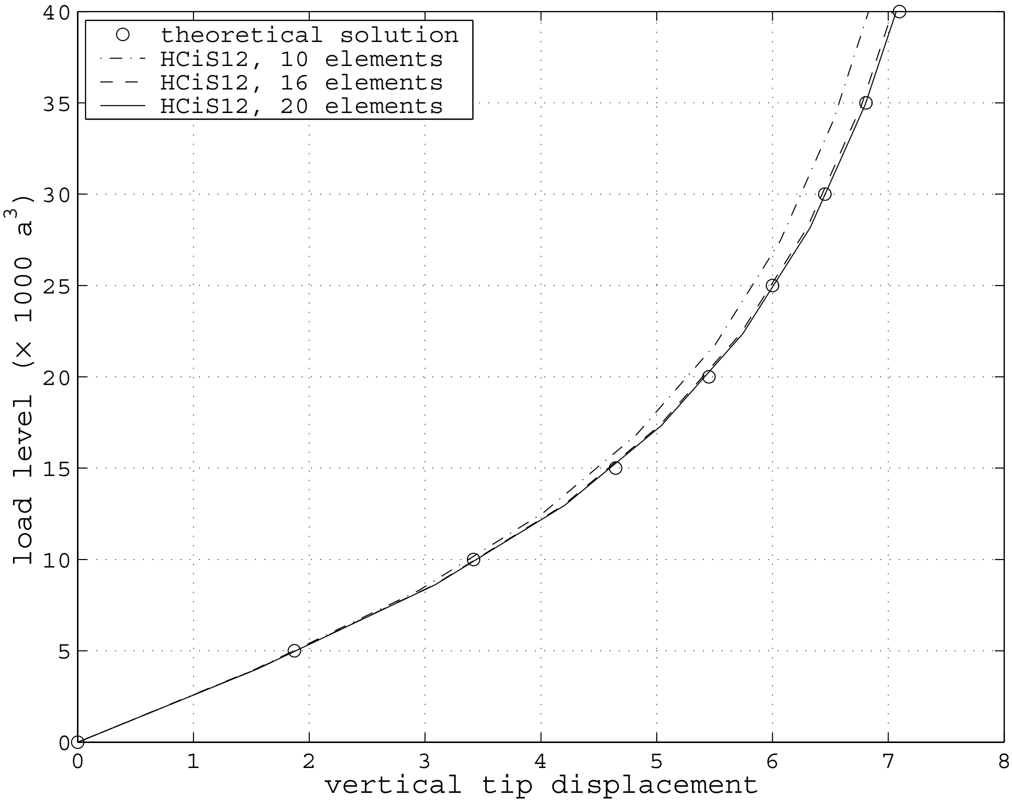

Figure 5.83: Out-of-plane bending benchmark - Evolution of displacements with load level for different meshes and $\nu = 0.3$

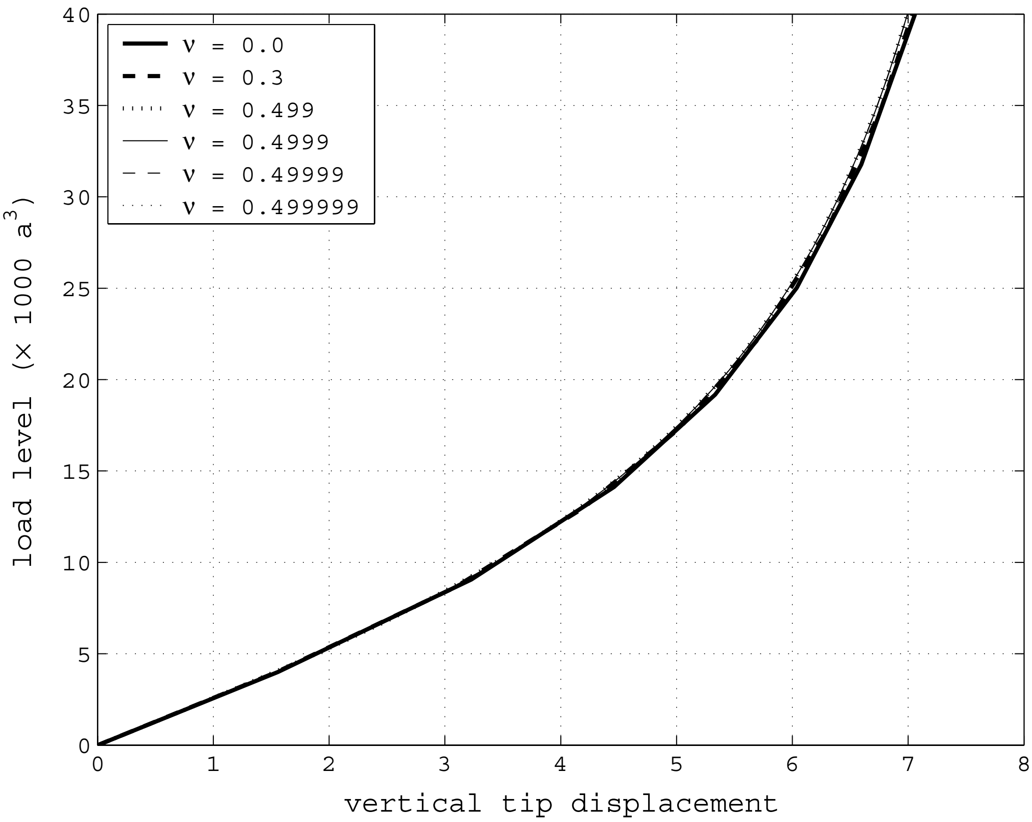

Figure 5.84: Out-of-plane bending benchmark - Influence of Poisson's coefficient on the deflection of 16×1×1 mesh

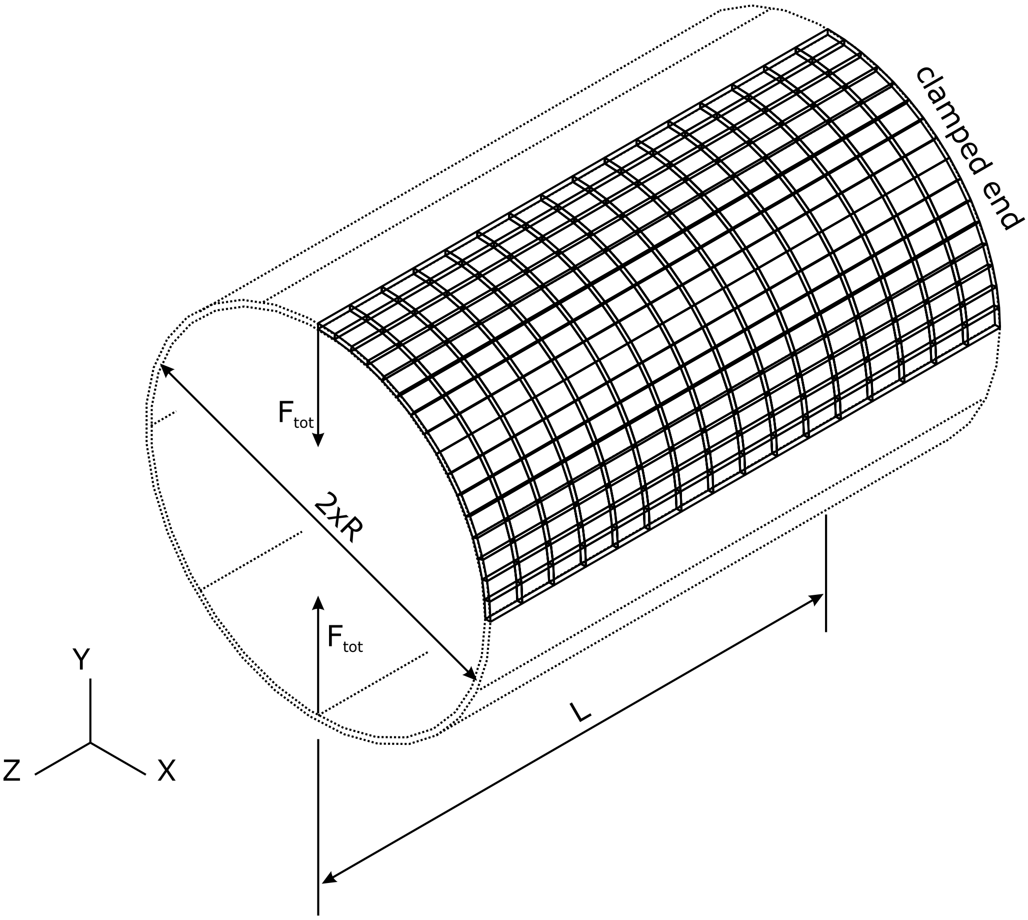

Figure 5.85: Clamped cylinder problem - Mesh, loading and boundary conditions

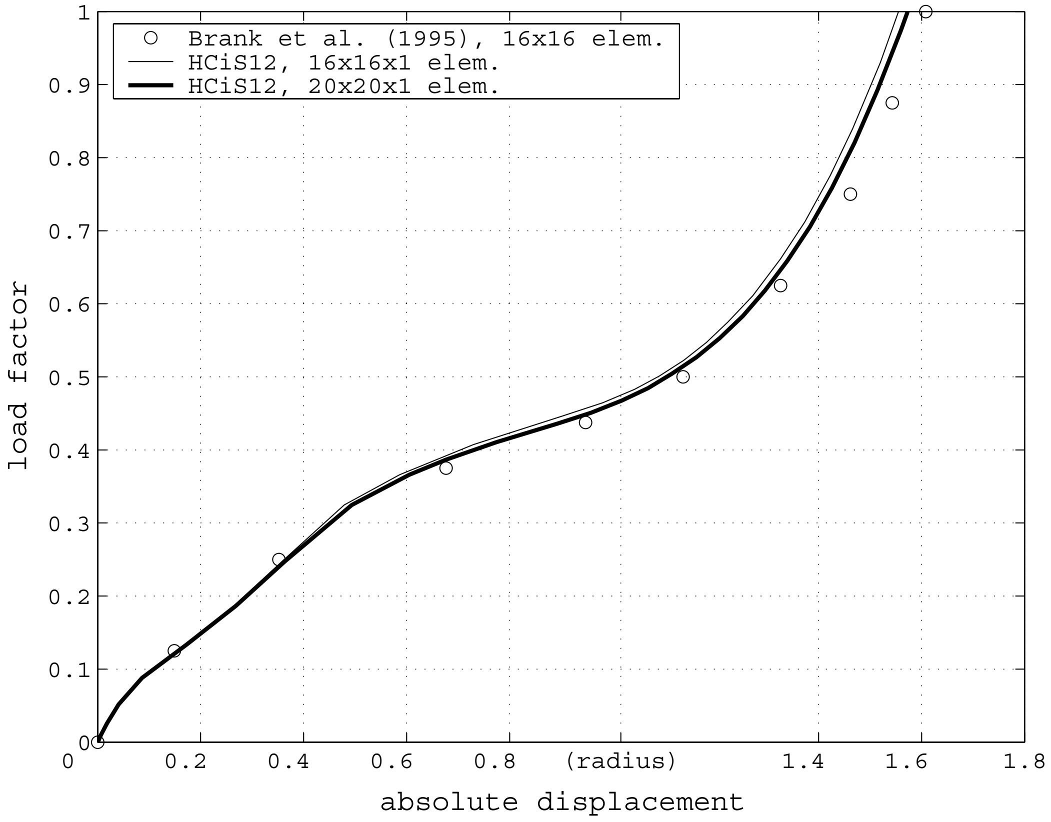

Figure 5.86: Clamped cylinder problem - Deflection curve for loaded point

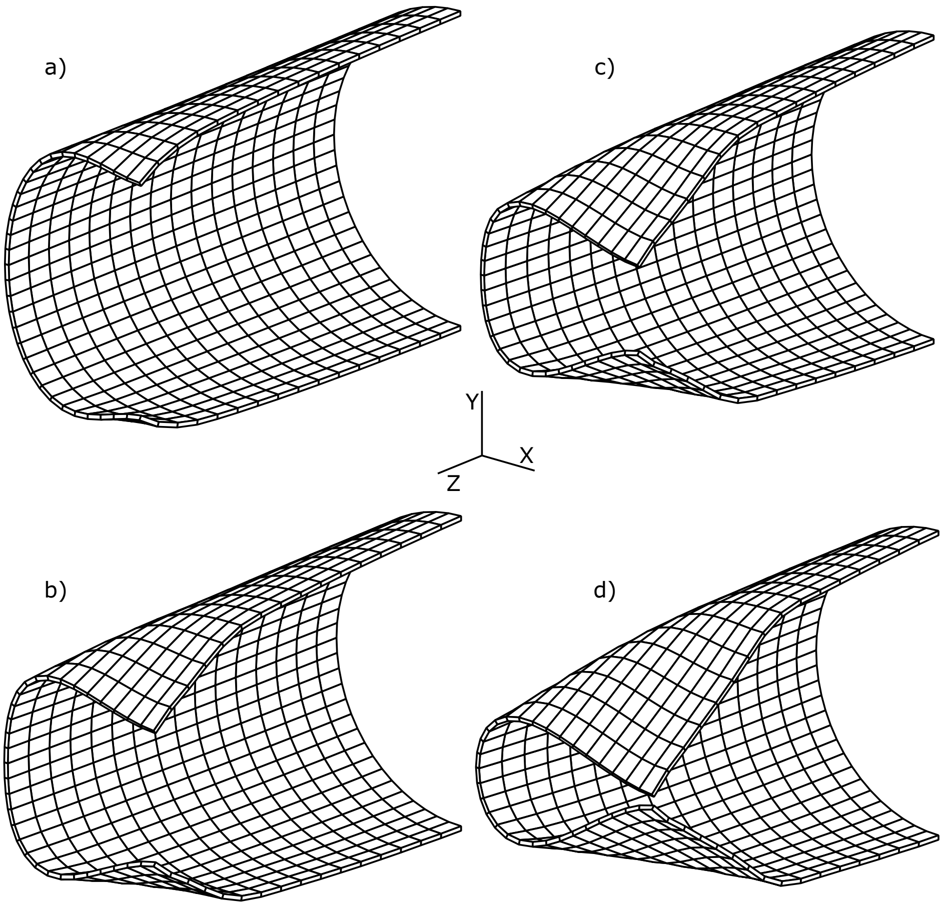

Figure 5.87: Clamped cylinder problem - Sequence of deformed configurations for displacements of: a) 0.26 R, b) 0.58 R, c) 0.72 R, d) 0.97 R

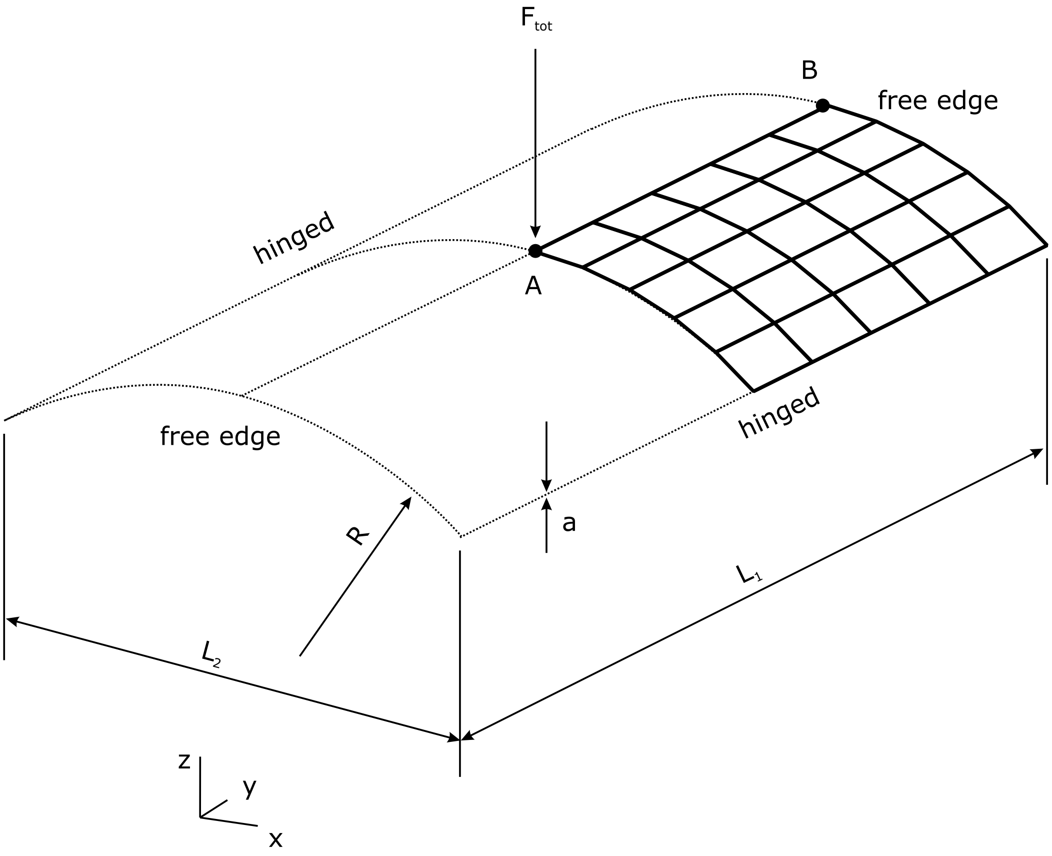

Figure 5.88: Shallow roof problem - Geometric model with load and boundary conditions

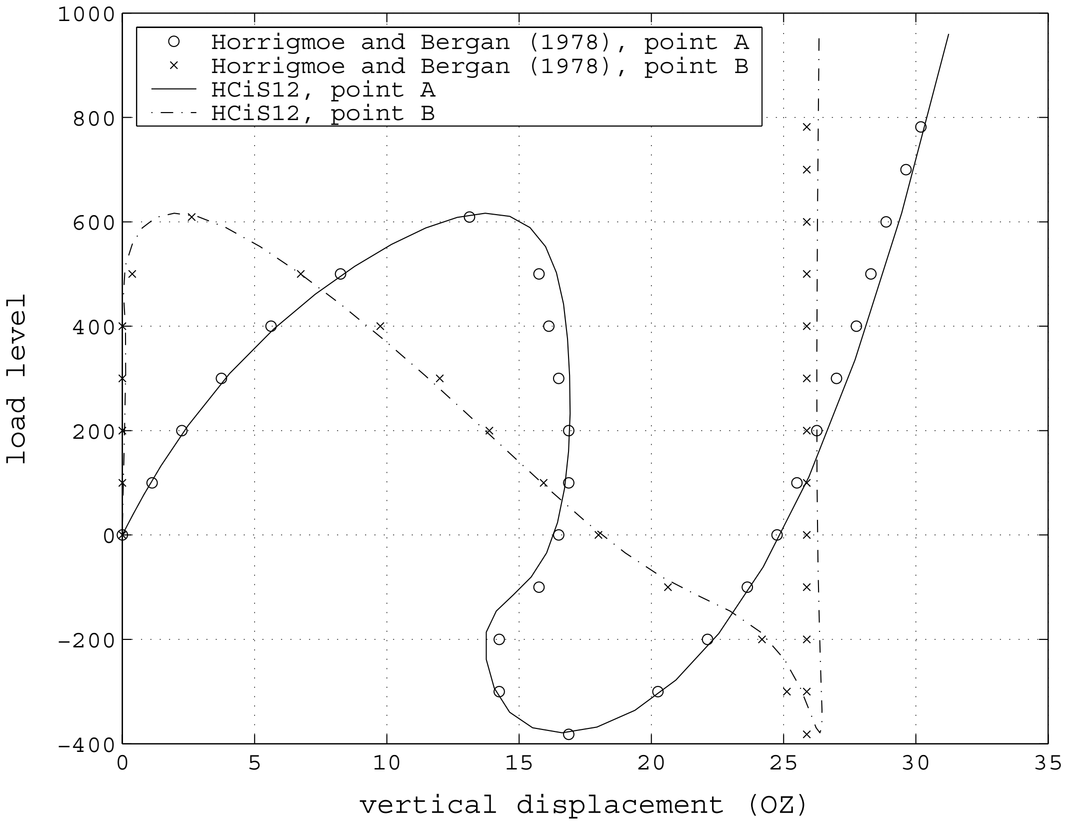

Figure 5.89: Shallow roof problem - Results for points A and B

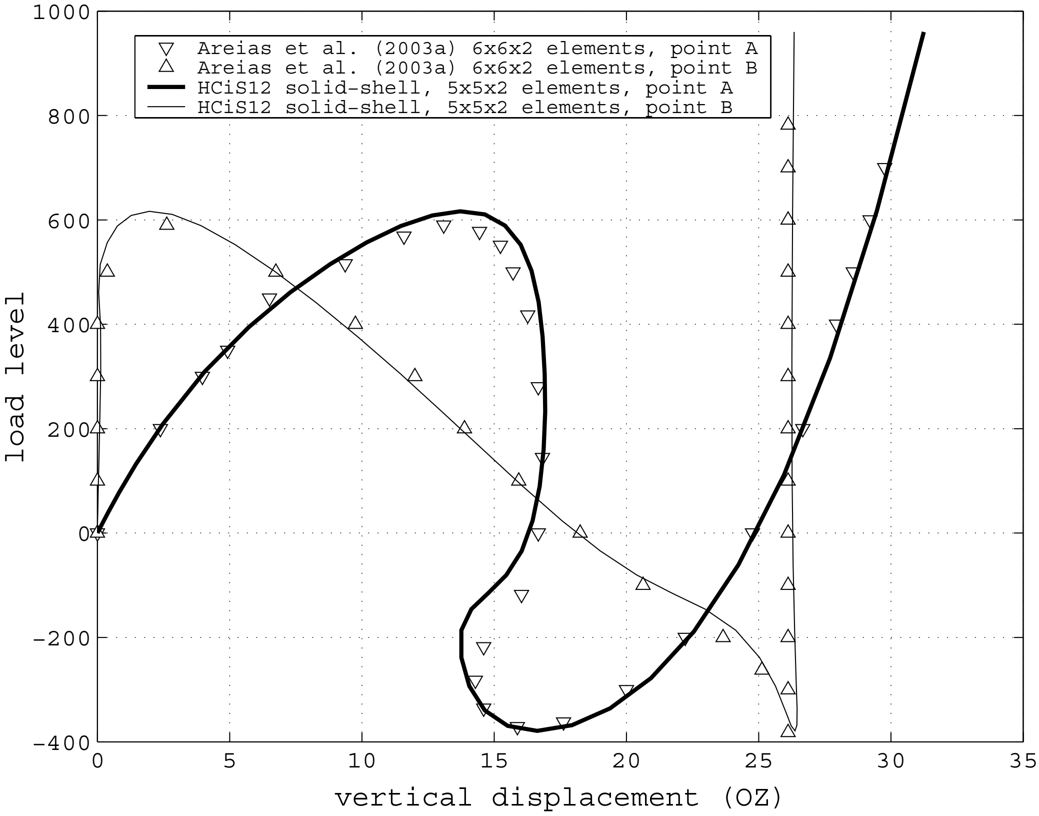

Figure 5.90: Shallow roof problem - Results for points A and B for solid-shell formulations

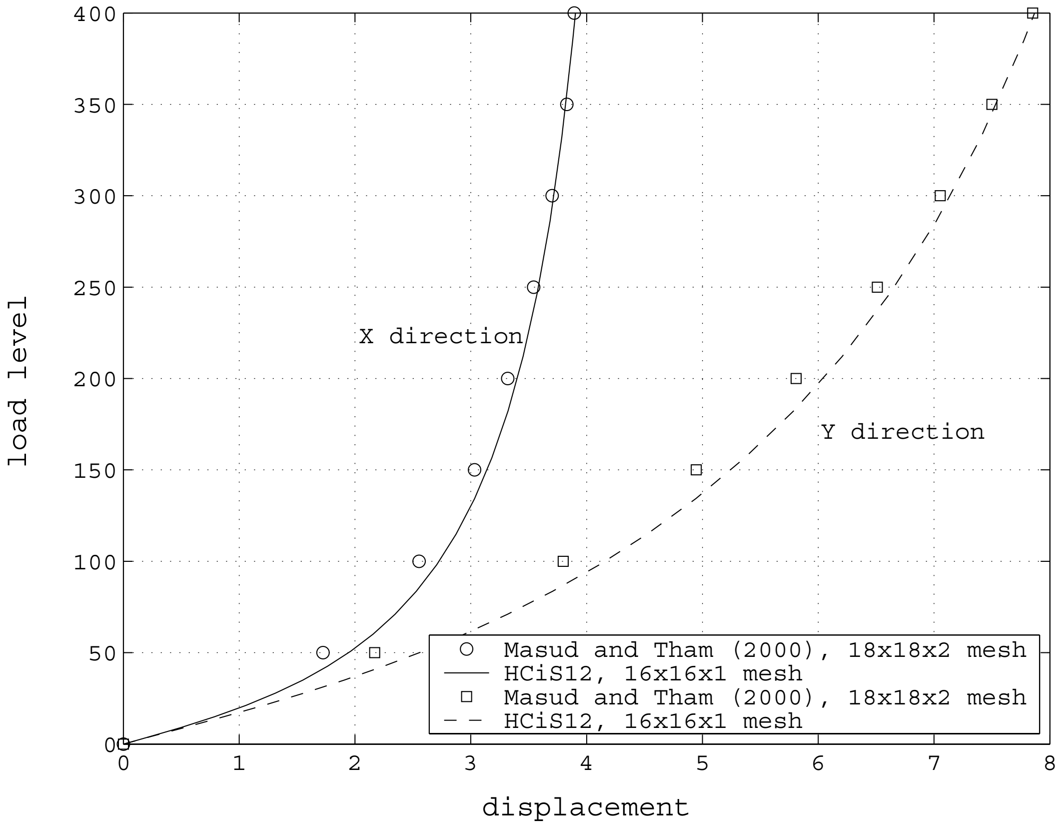

Figure 5.91: Elastoplastic pinched hemispherical shell - Load-deflection diagram

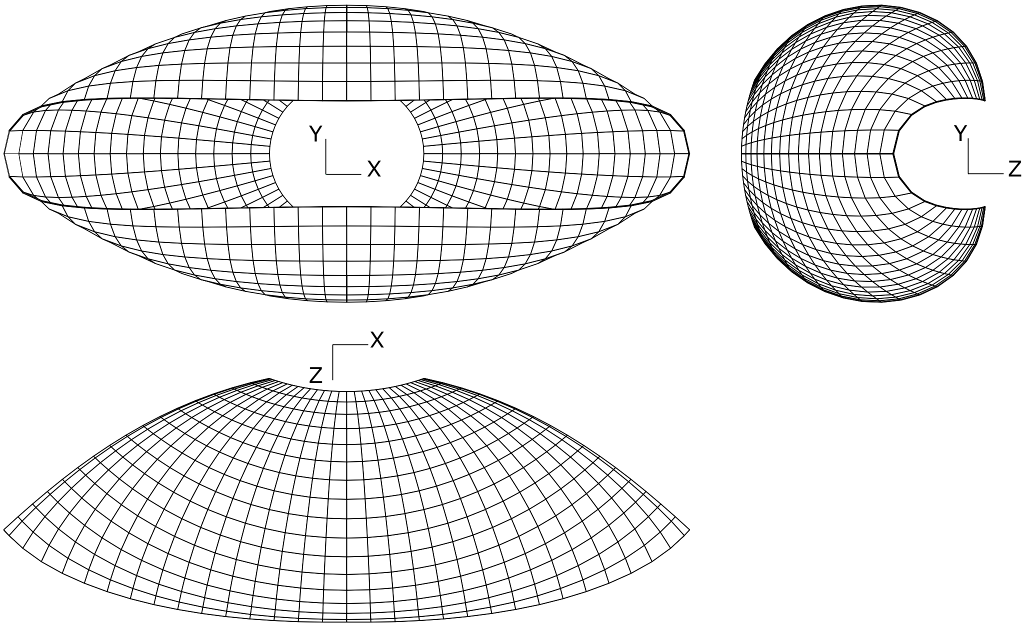

Figure 5.92: Elastoplastic pinched hemispherical shell - Orthogonal views of deformed geometry

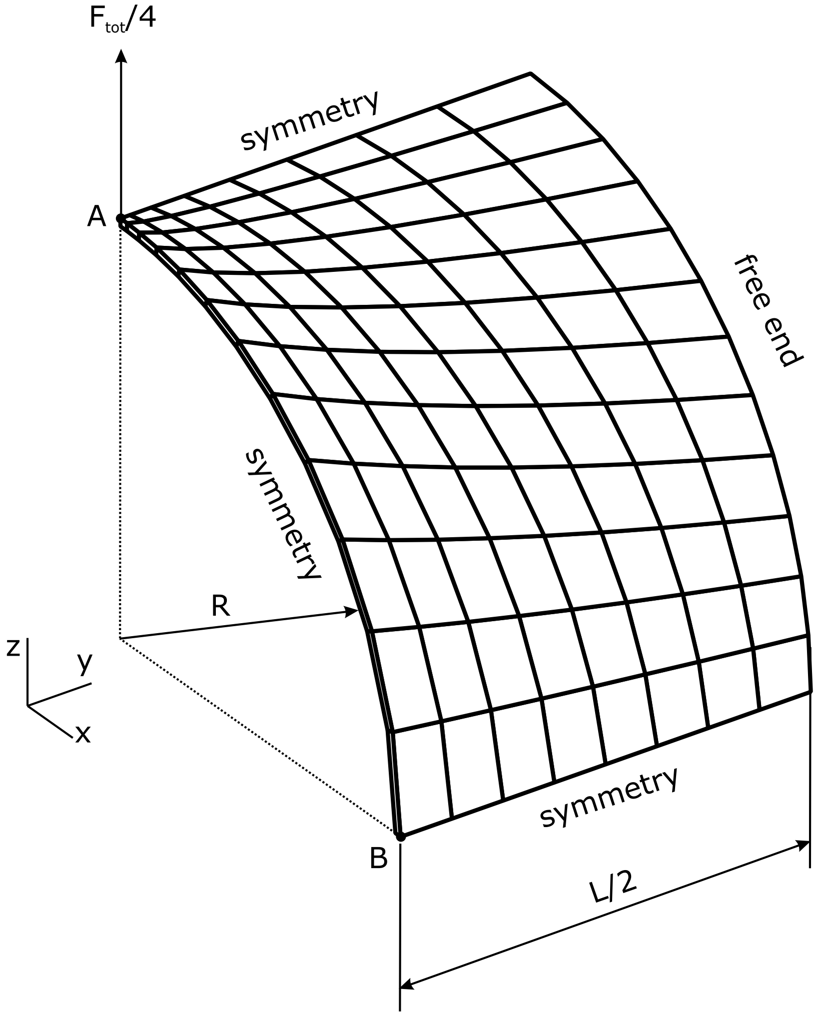

Figure 5.93: Stretching of a cylinder - Schematic view (one octant) with 12×8×1 elements in a distorted mesh

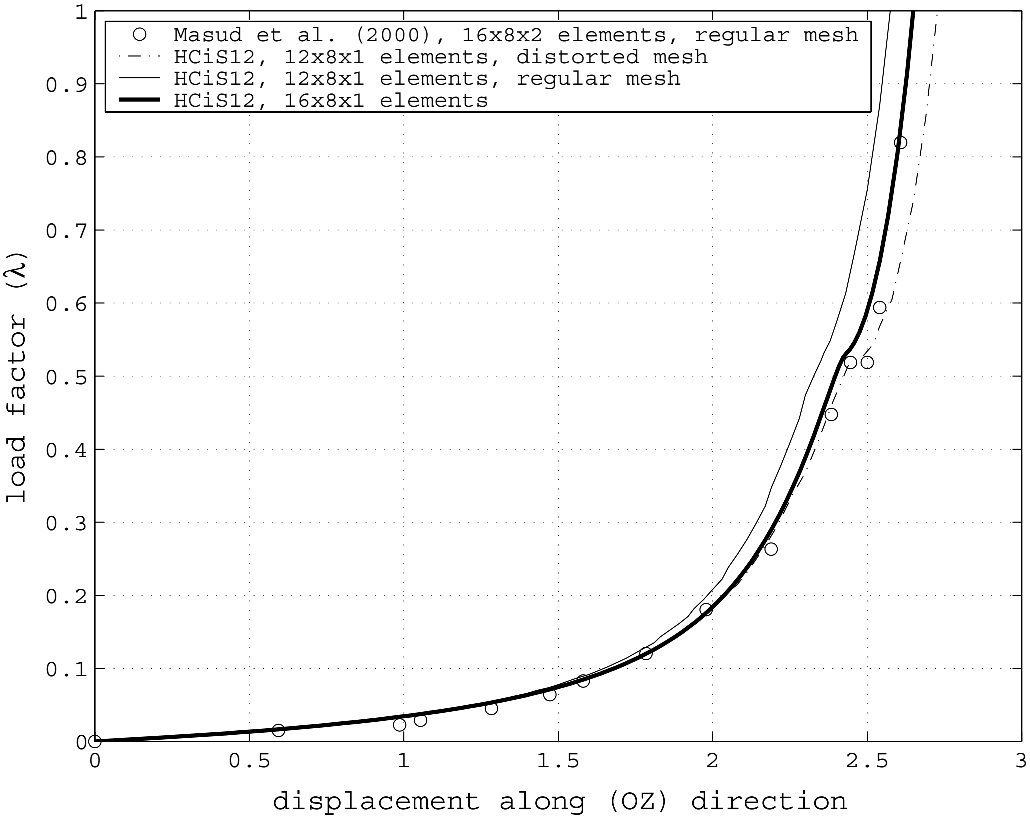

Figure 5.94: Stretching of a cylinder - Results for point A, elastic case

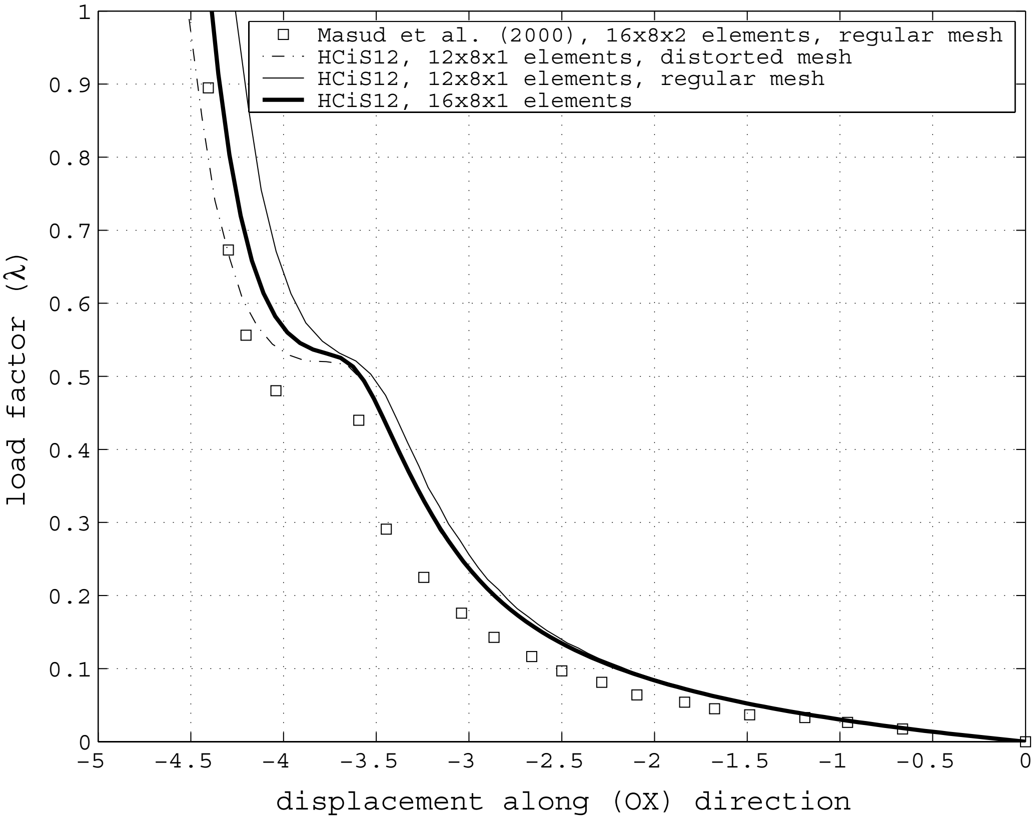

Figure 5.95: Stretching of a cylinder - Results for point B, elastic case

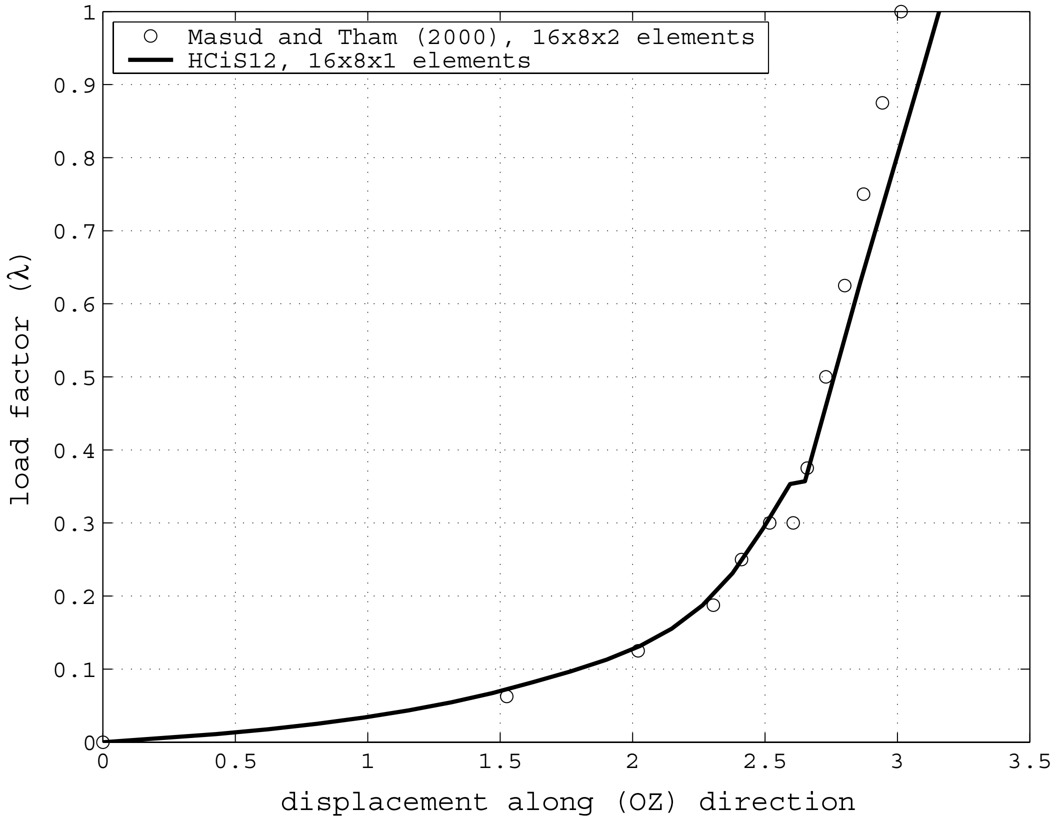

Figure 5.96: Stretching of a cylinder - Results for point A, elasto-plastic case

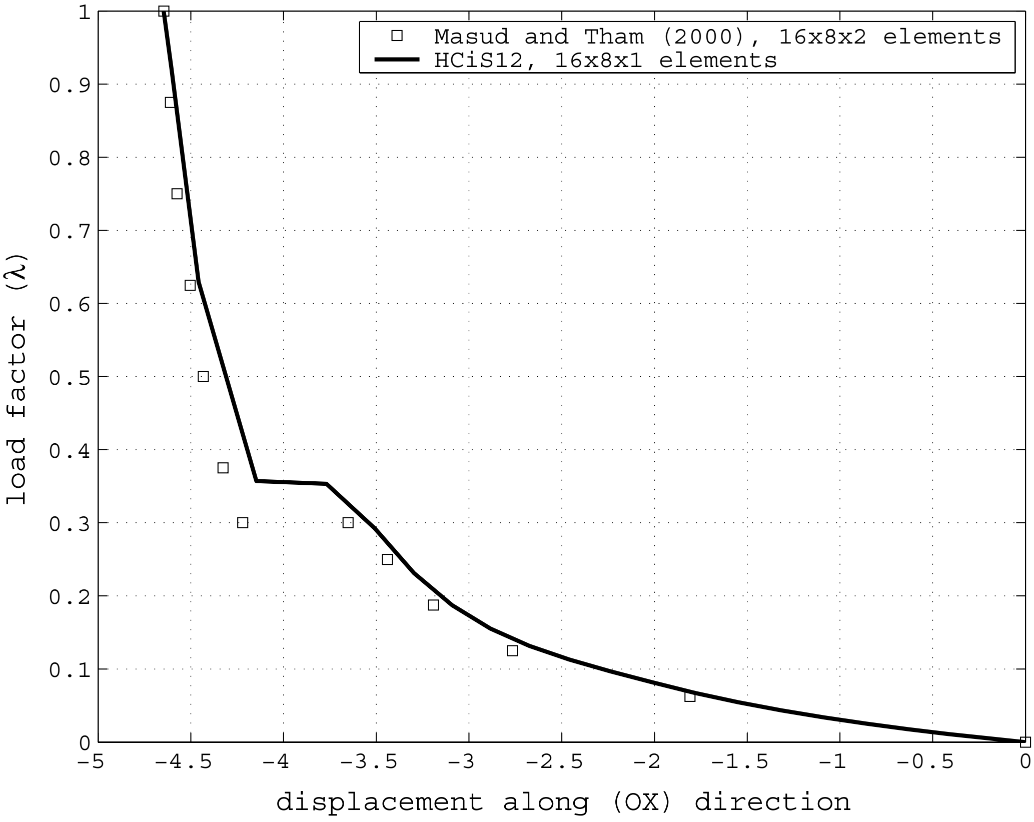

Figure 5.97: Stretching of a cylinder - Results for point B, elasto-plastic case

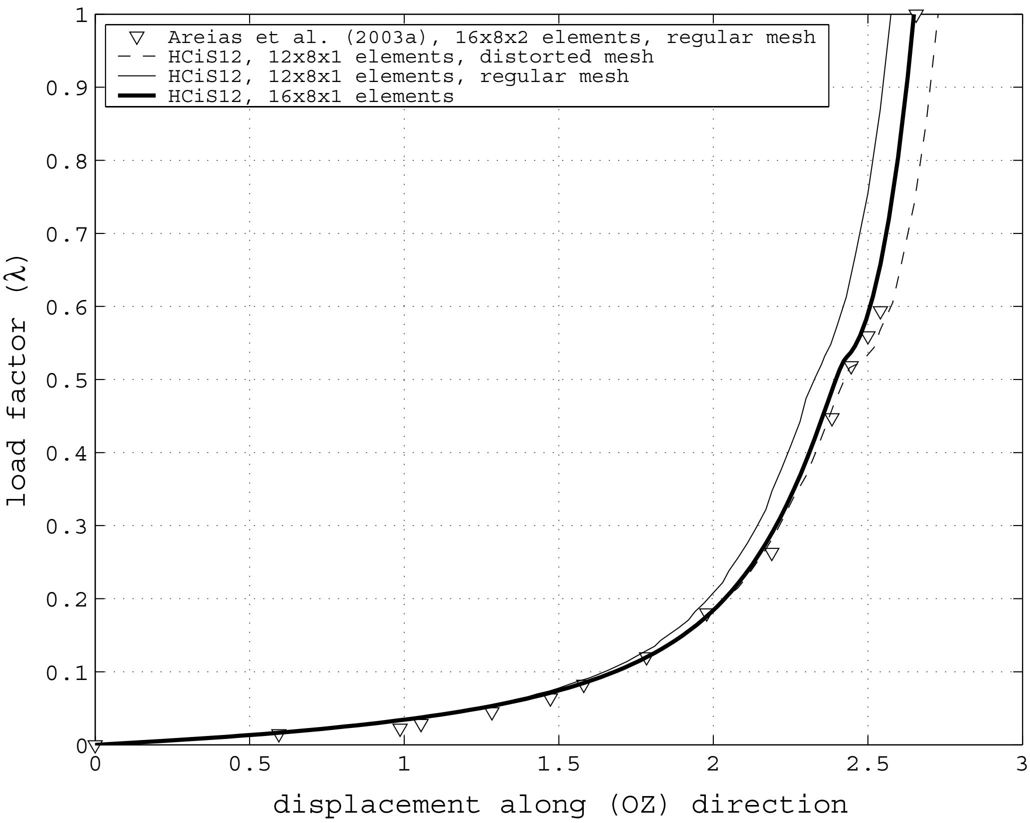

Figure 5.98: Stretching of a cylinder - Results for point A (elastic case) coming from solid-shell formulations

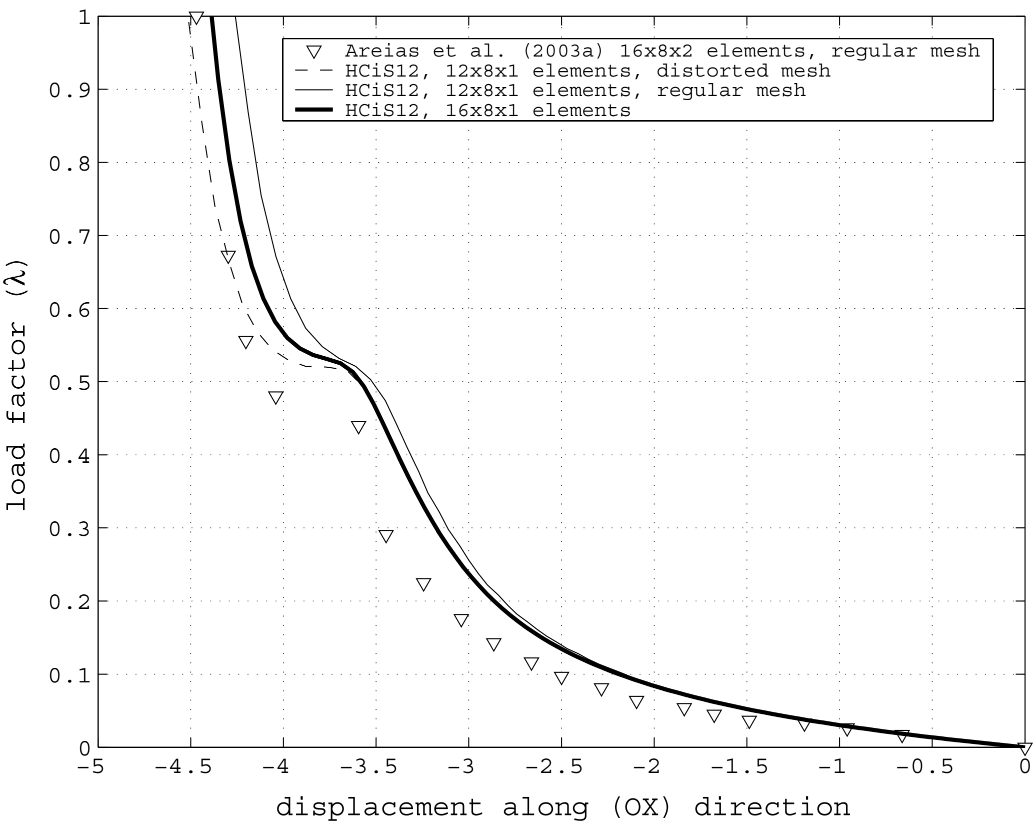

Figure 5.99: Stretching of a cylinder - Results for point B (elastic case) coming from solid-shell formulations

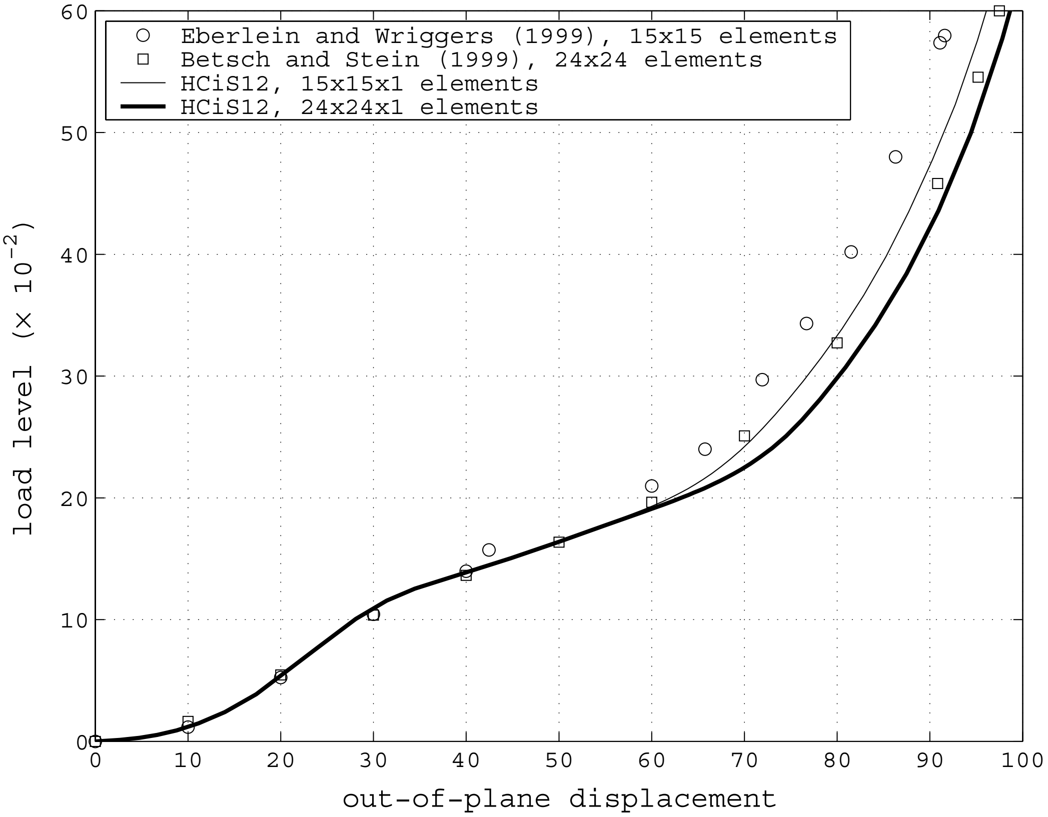

Figure 5.100: Simply supported plate - Results for the out of plane deflection of the center node

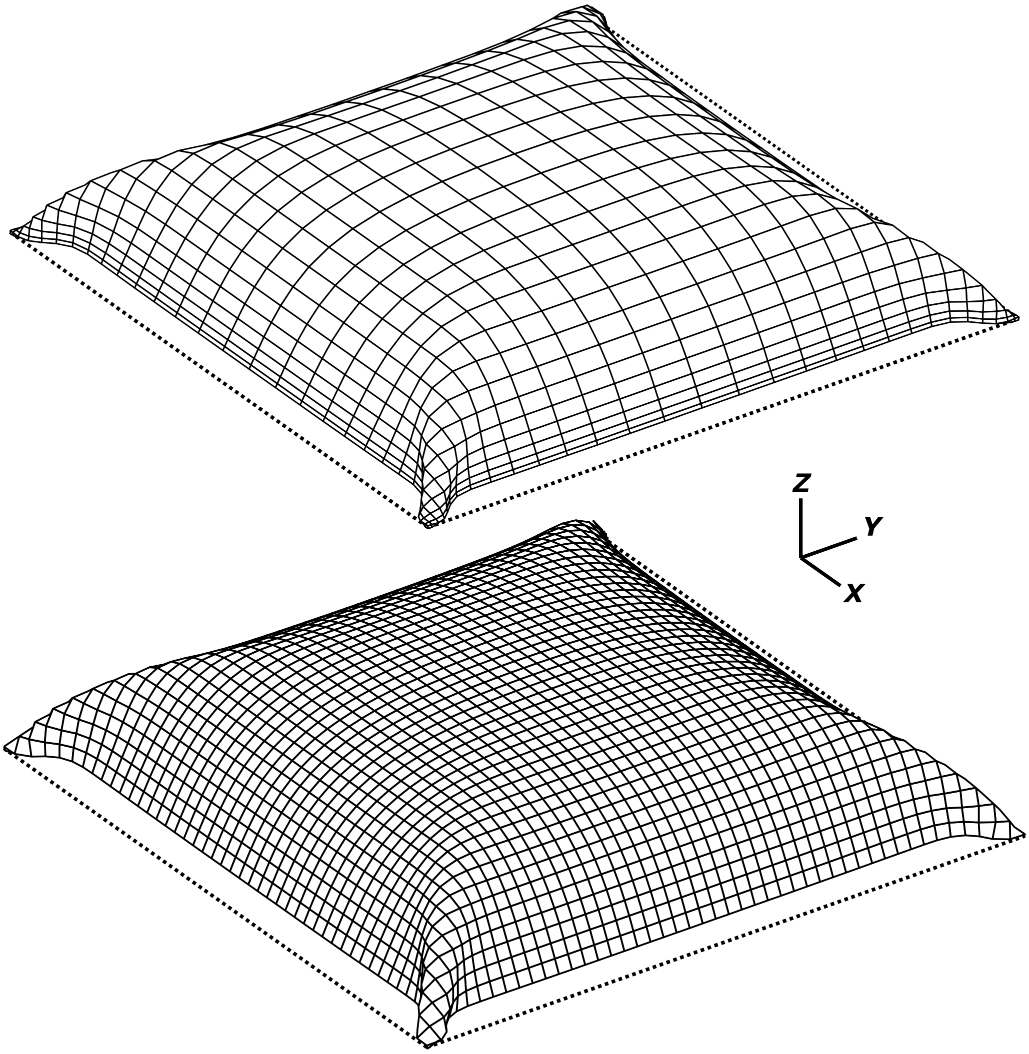

Figure 5.101: Simply supported plate - Deformed configurations for the analyzed meshes at full load

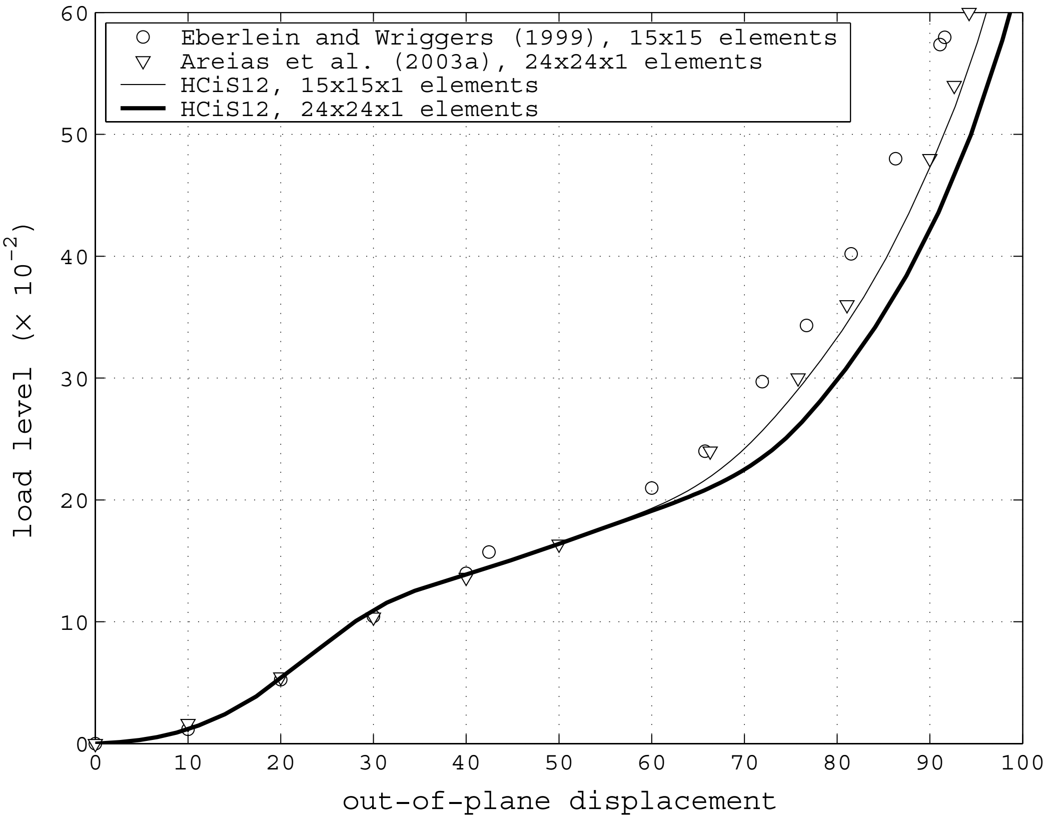

Figure 5.102: Simply supported plate - Results for the out of plane deflection of the center node, coming from the comparison of solid-shell formulations

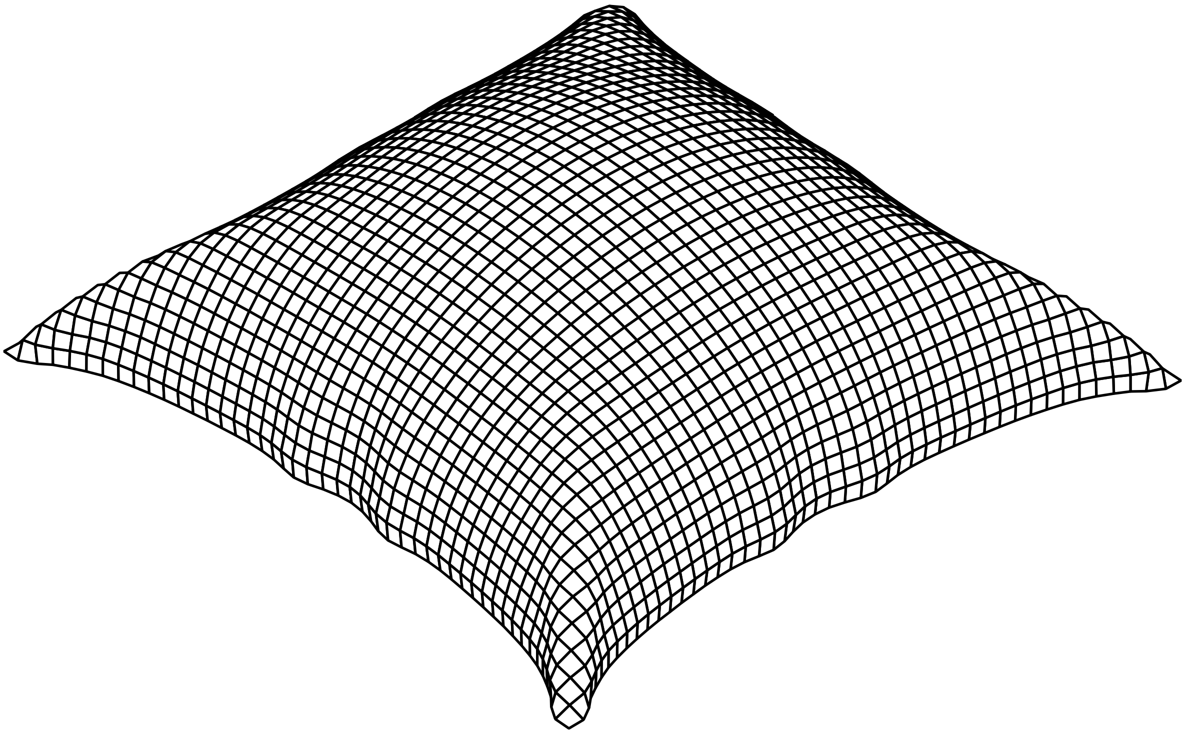

Figure 5.103: Simply supported plate - Deformed configuration at the onset of wrinkling in the mid-sides ($\mathsf{p} = 4.06$) for the $24 \times 24 \times 1$ mesh

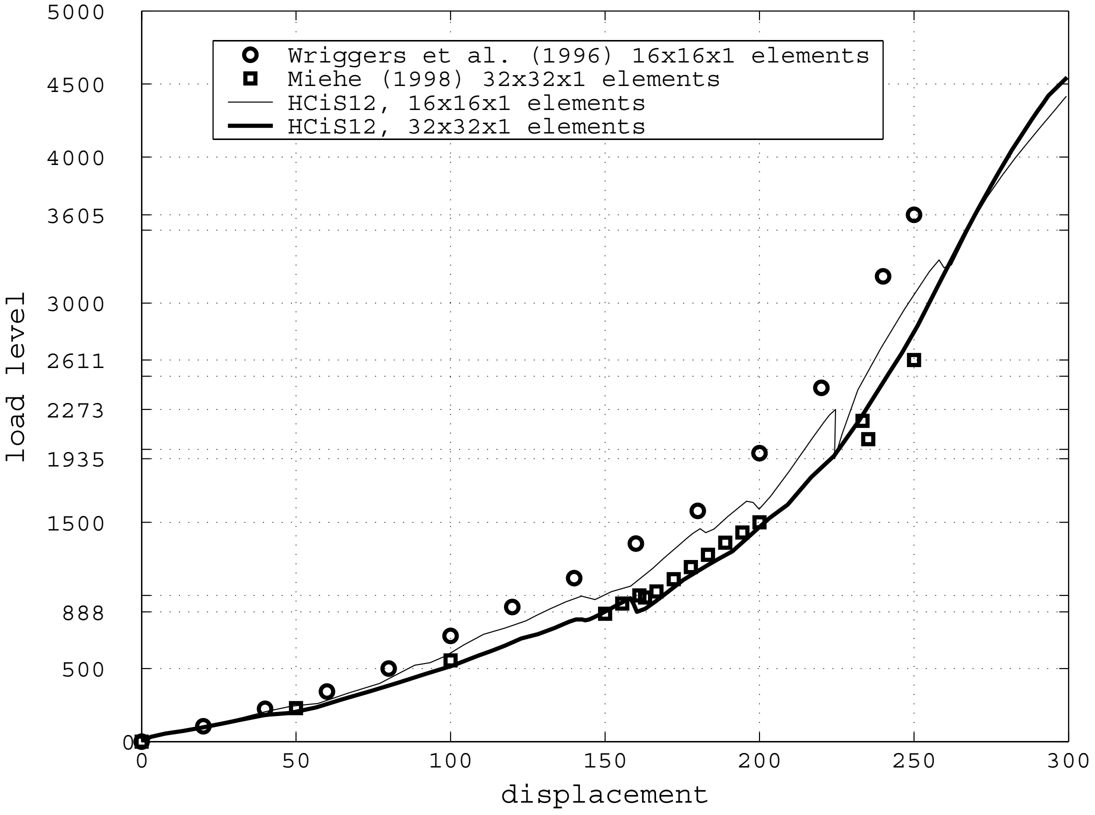

Figure 5.104: Pinched cylinder problem - Load deflection curve for the loaded point

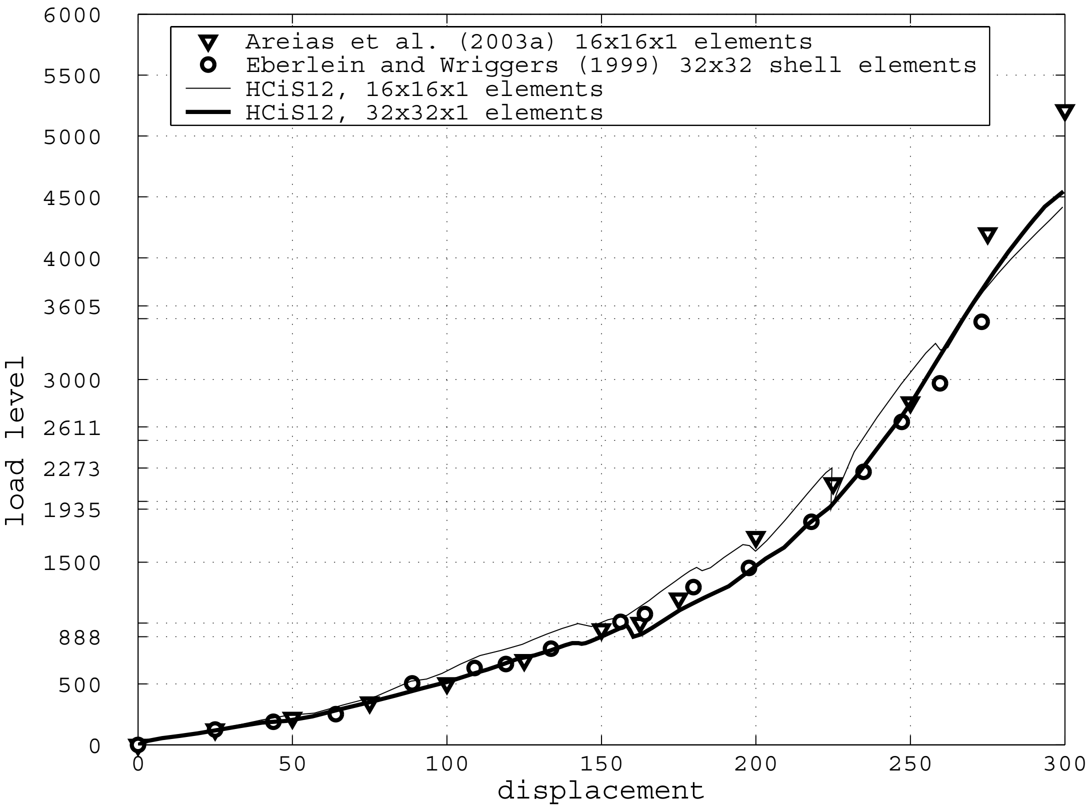

Figure 5.105: Pinched cylinder problem - Load deflection curves for the loaded point for *EAS*-based solid, solid-shell and shell finite elements' formulations

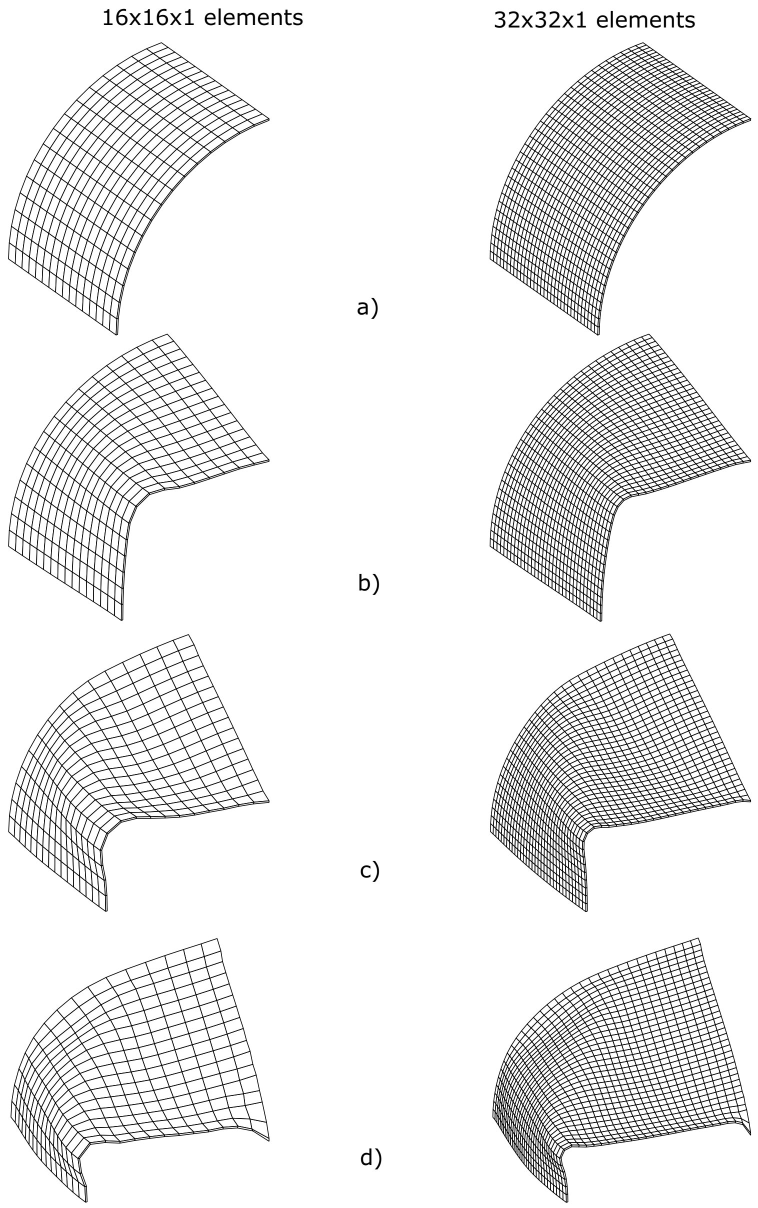

Figure 5.106: Pinched cylinder problem - Sequence of deformed configurations for both meshes. (a) Initial configurations; Deformed meshes at (b) $w \approx 100$, (c) $w \approx 200$, (d) $w \approx 300$

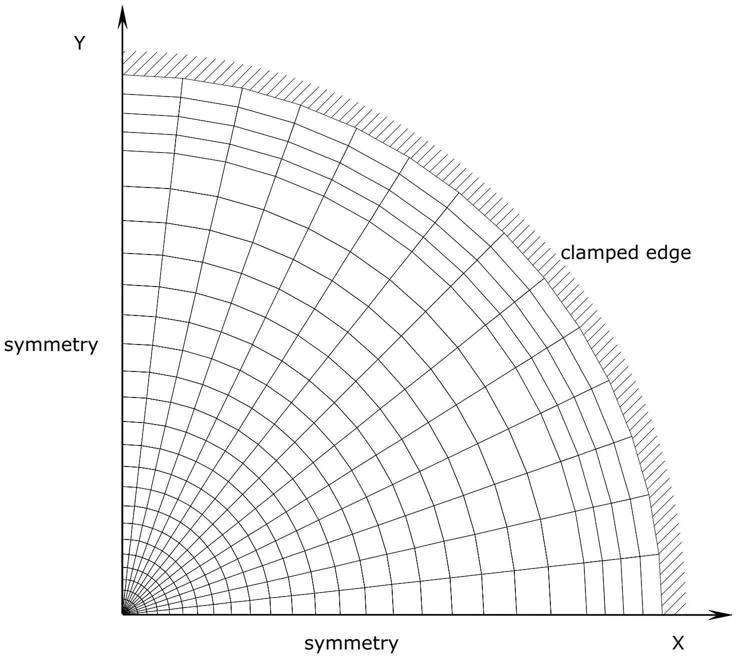

Figure 5.107: Hydro-bulge forming - Mesh and boundary conditions adopted

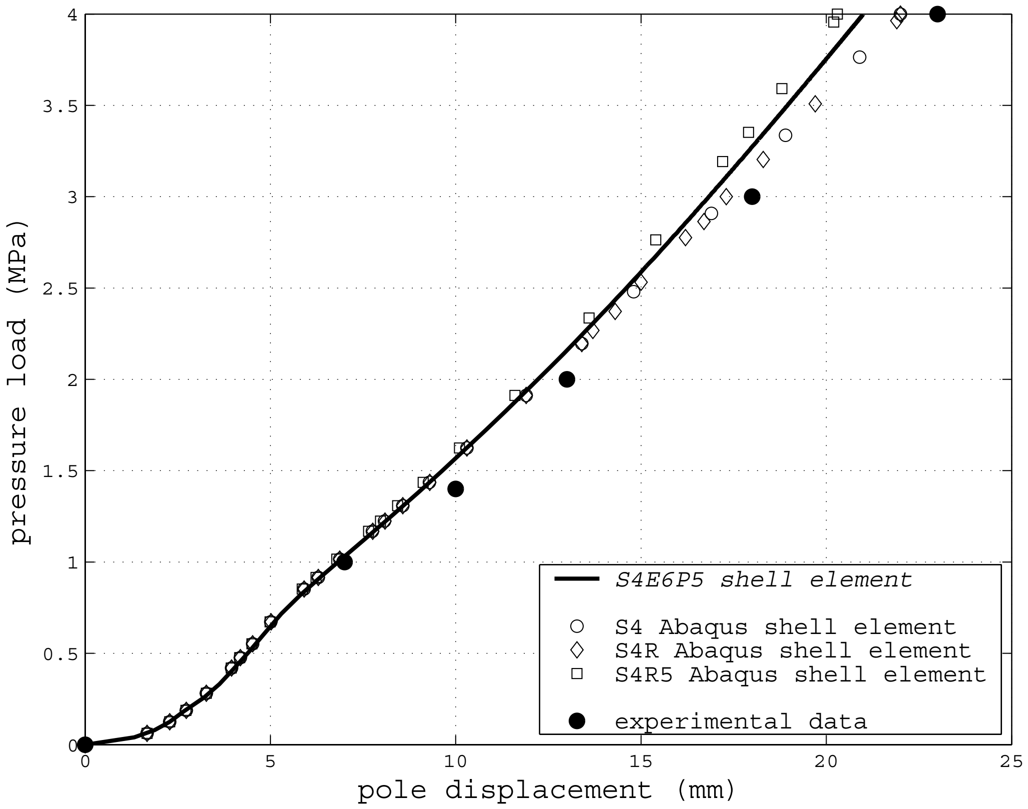

Figure 5.108: Hydro-bulge forming - Results for shell elements under isotropic constitutive evolution

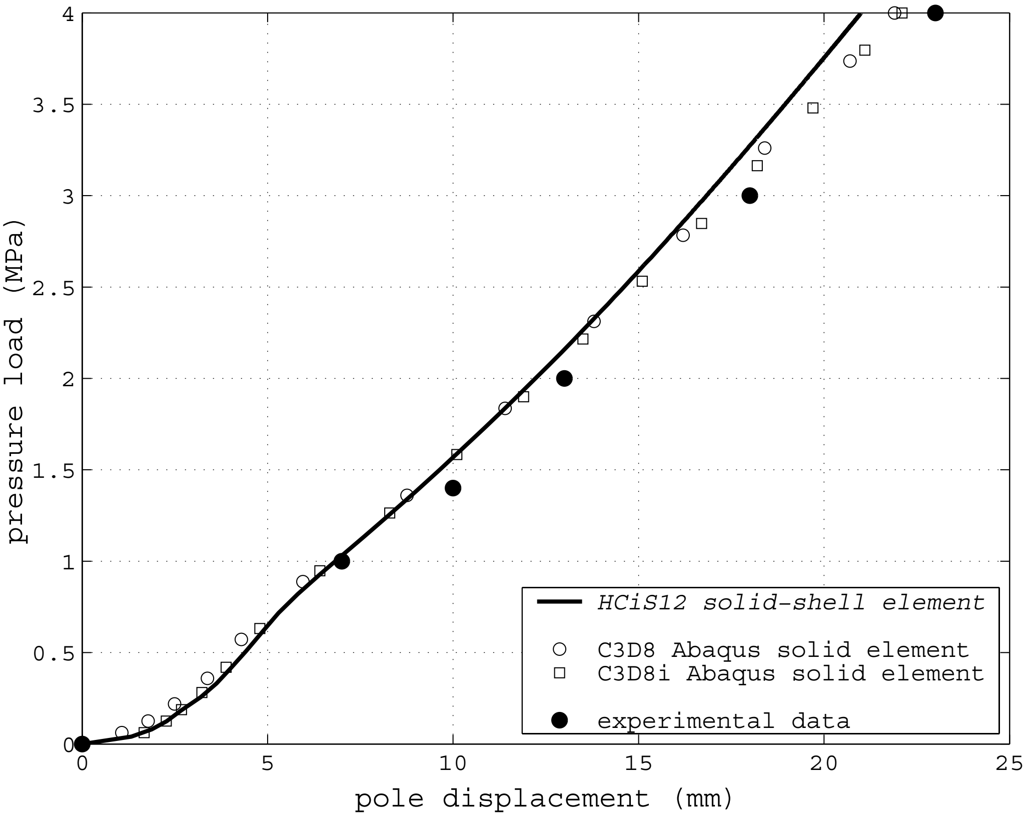

Figure 5.109: Hydro-bulge forming - Results for solid-shell elements under isotropic constitutive evolution

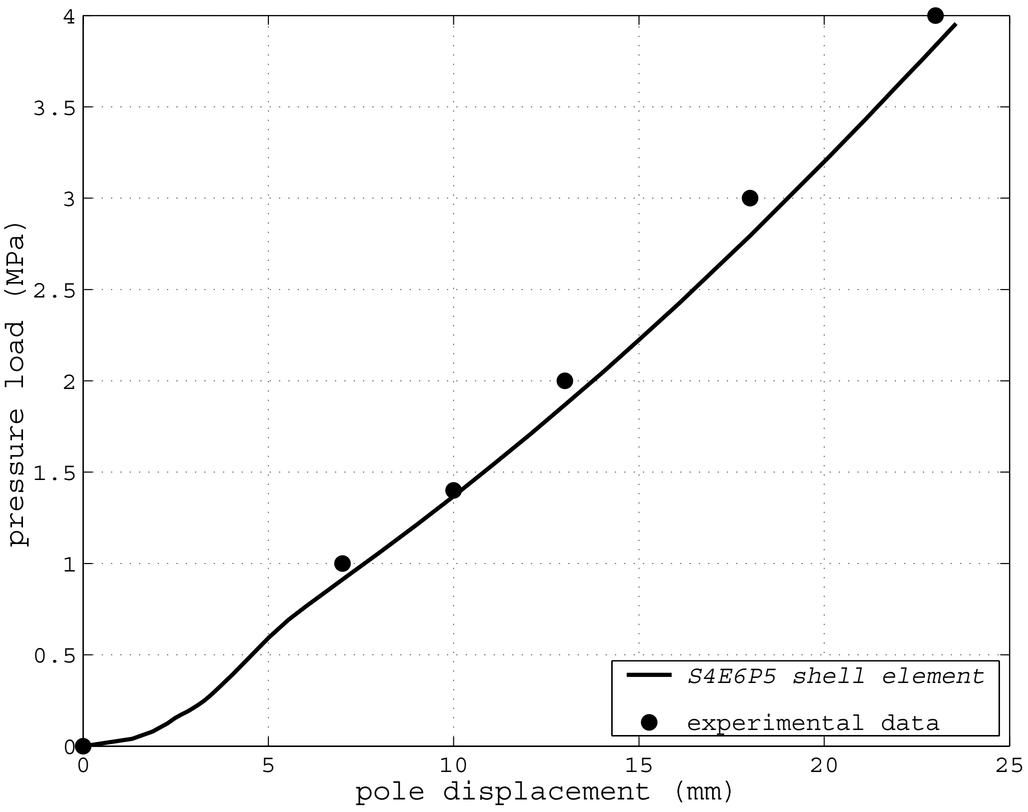

Figure 5.110: Hydro-bulge forming - Results for the enhanced assumed strain shell element, considering the anisotropic yield criterion of Barlat *et al.* (1991)

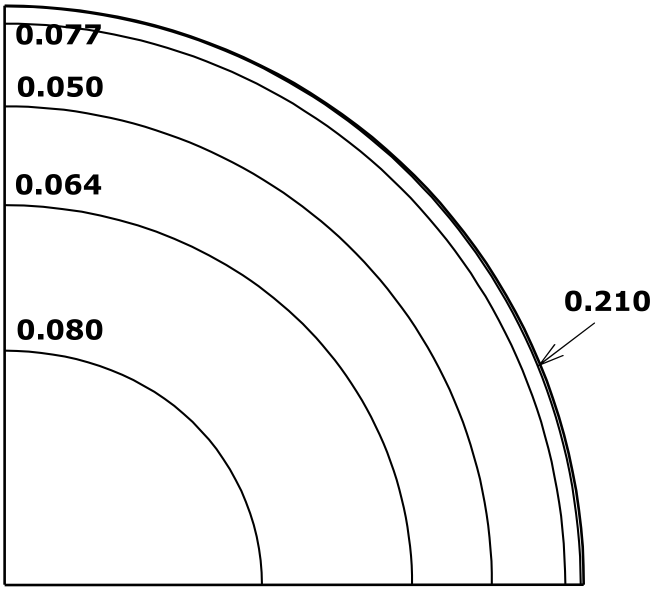

Figure 5.111: Hydro-bulge forming - Equivalent plastic strain distribution for a rolling direction at 0°, considering the anisotropic yield criterion of Barlat *et al.* (1991) (pressure level of 4 MPa)

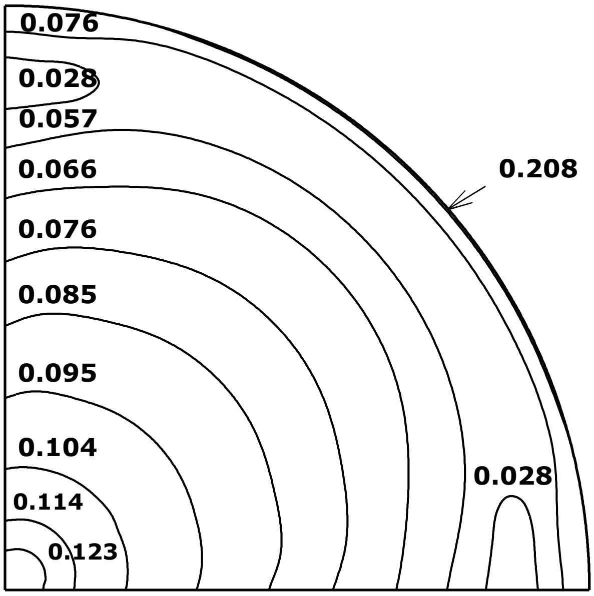

Figure 5.112: Hydro-bulge forming - Equivalent plastic strain distribution for a rolling direction at 45°, considering the anisotropic yield criterion of Barlat *et al.* (1991) (pressure level of 4 MPa)

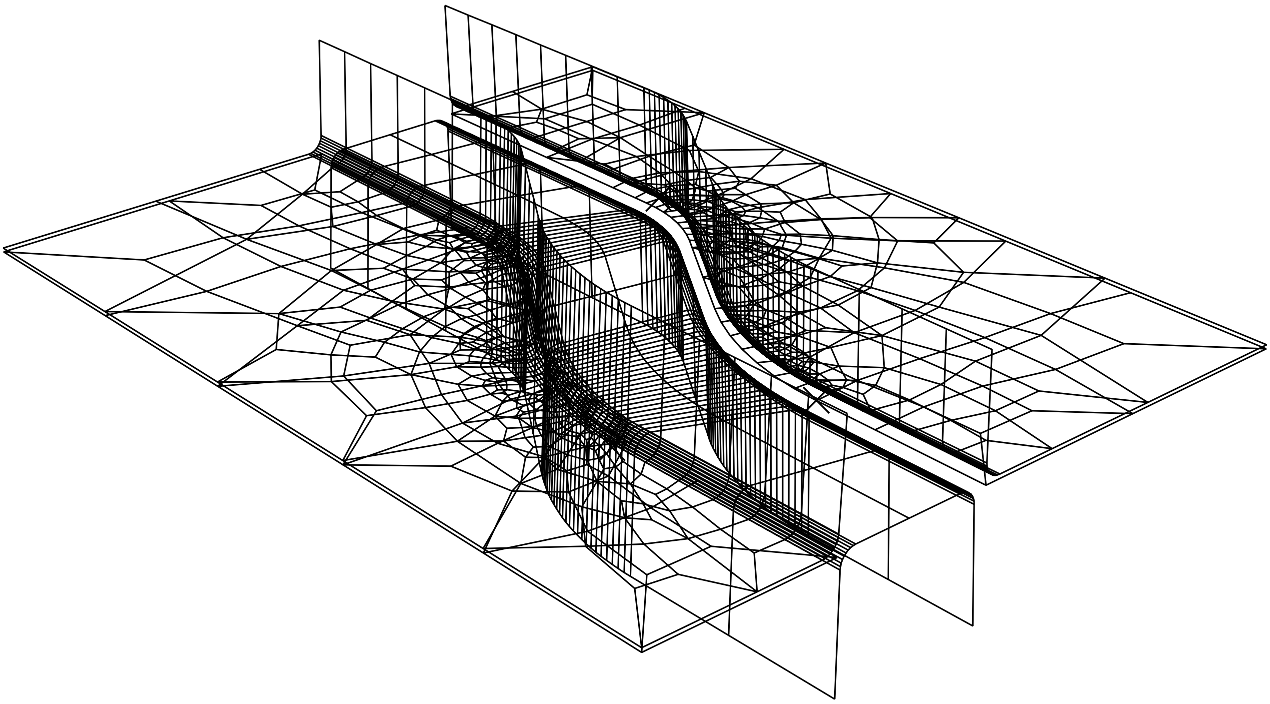

Figure 5.113: S-Rail problem - Definition of tools

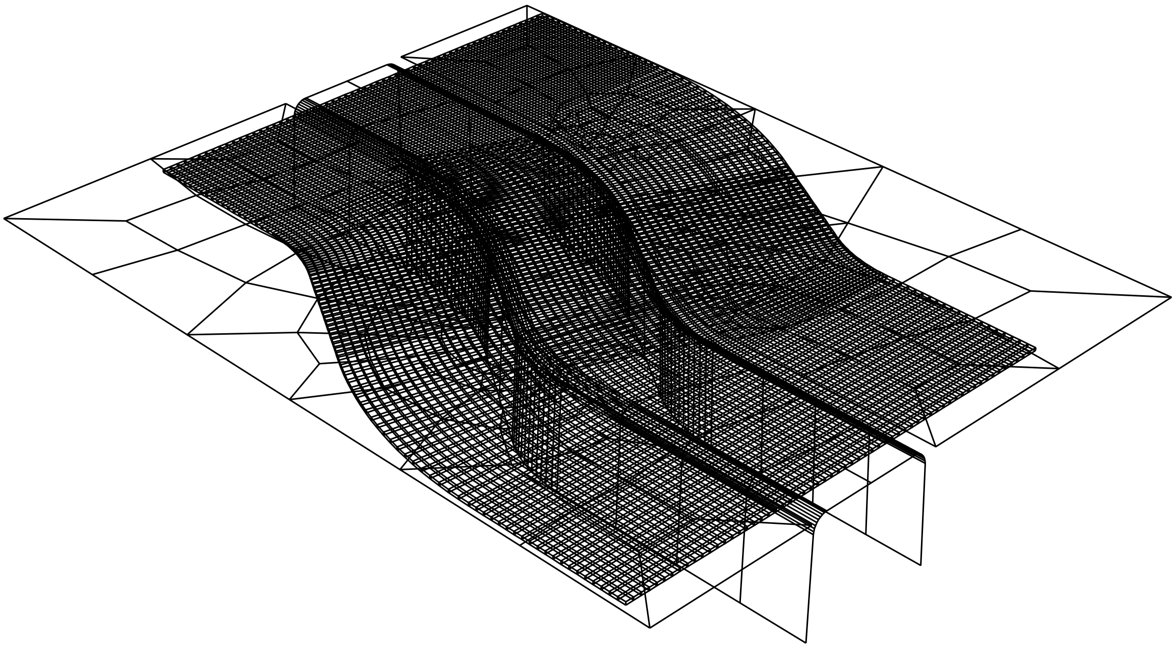

Figure 5.114: S-Rail problem - Detail of the finite element mesh over the undeformed plate, consisting of 6000 solid-shell elements

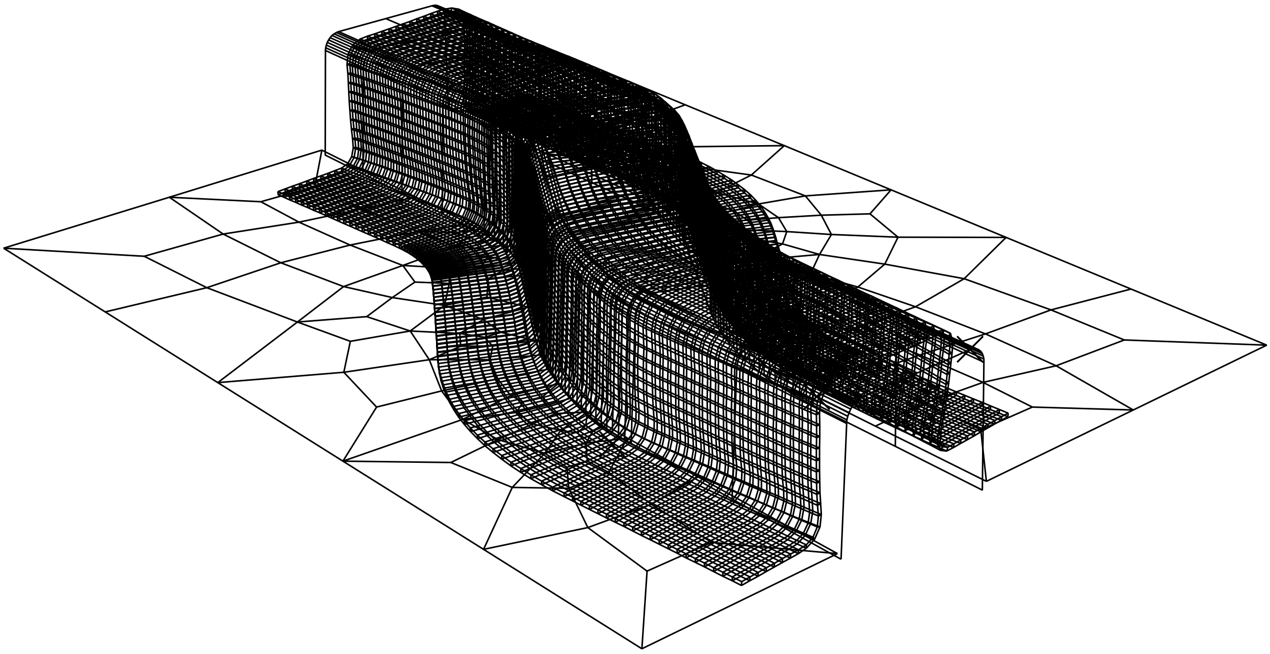

Figure 5.115: S-Rail problem - Deformed configuration

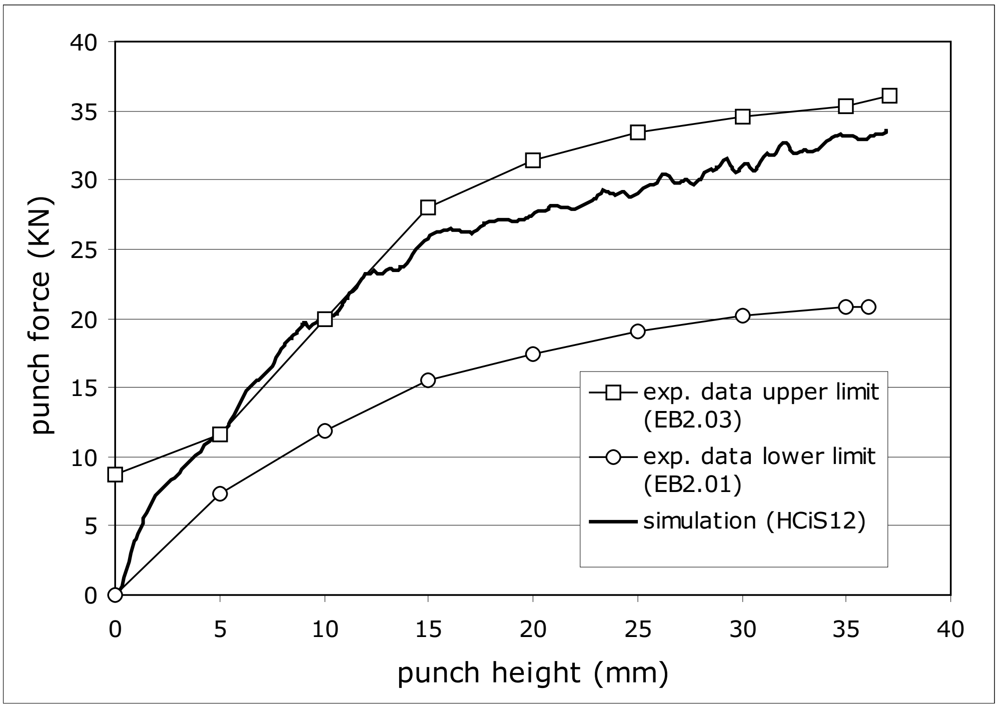

Figure 5.116: S-Rail problem - Comparison between present simulation results and upper and lower bounds of experimental results

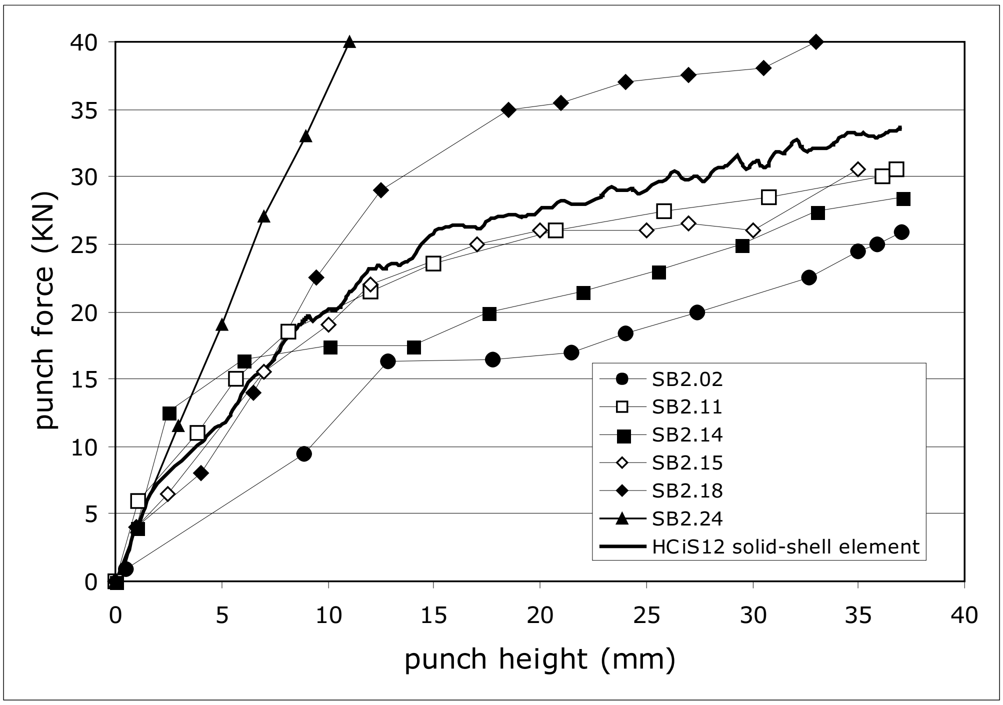

Figure 5.117: S-Rail problem - Comparison between present results and simulation (implicit) results presented in NUMISHEET (1996)

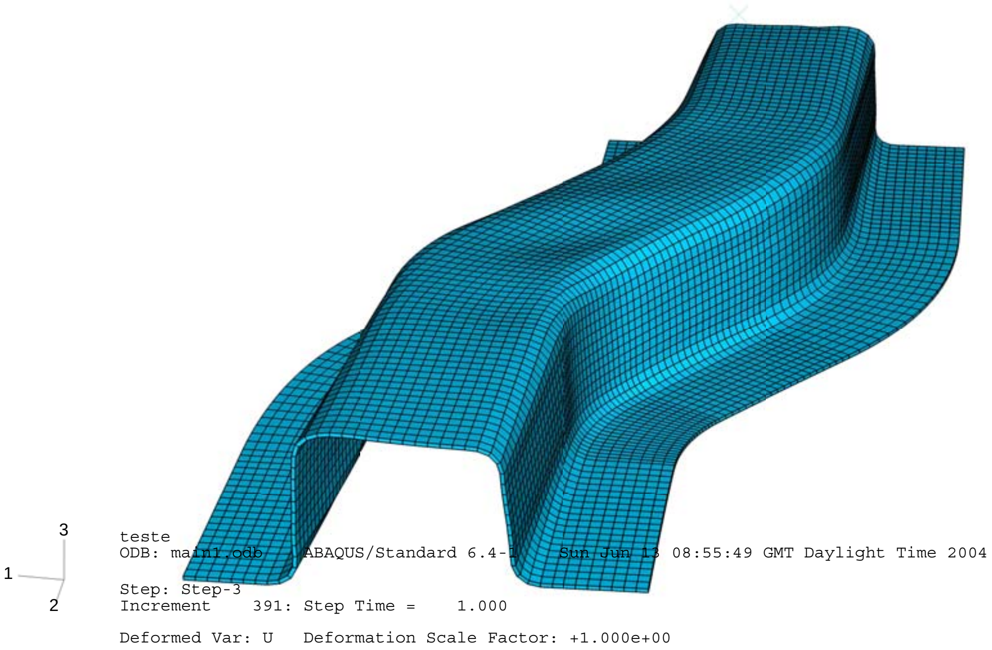

```
teste
ODB: main1.odb    ABAQUS/Standard 6.4-1    Sun Jun 13 08:55:49 GMT Daylight Time 2004

Step: Step-3
Increment    391: Step Time =    1.000

Deformed Var: U   Deformation Scale Factor: +1.000e+00
```

Figure 5.118: S-Rail problem - Overview of the deformed configuration, being noticeable the onset of wrinkles

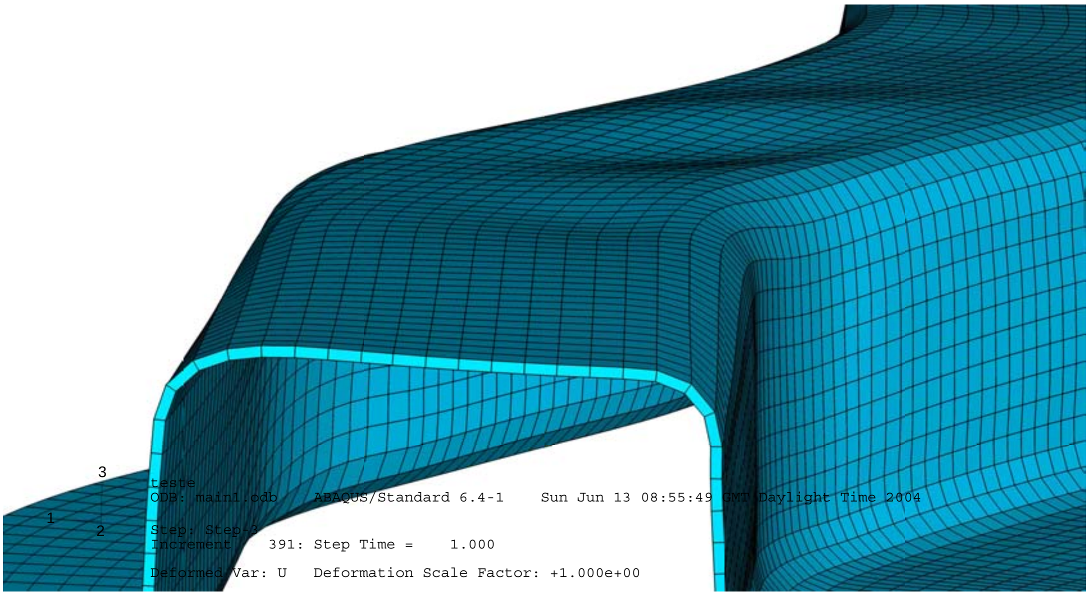

Figure 5.119: S-Rail problem - Detailed representation of the deformed model, focusing on the presence of wrinkles (top view)

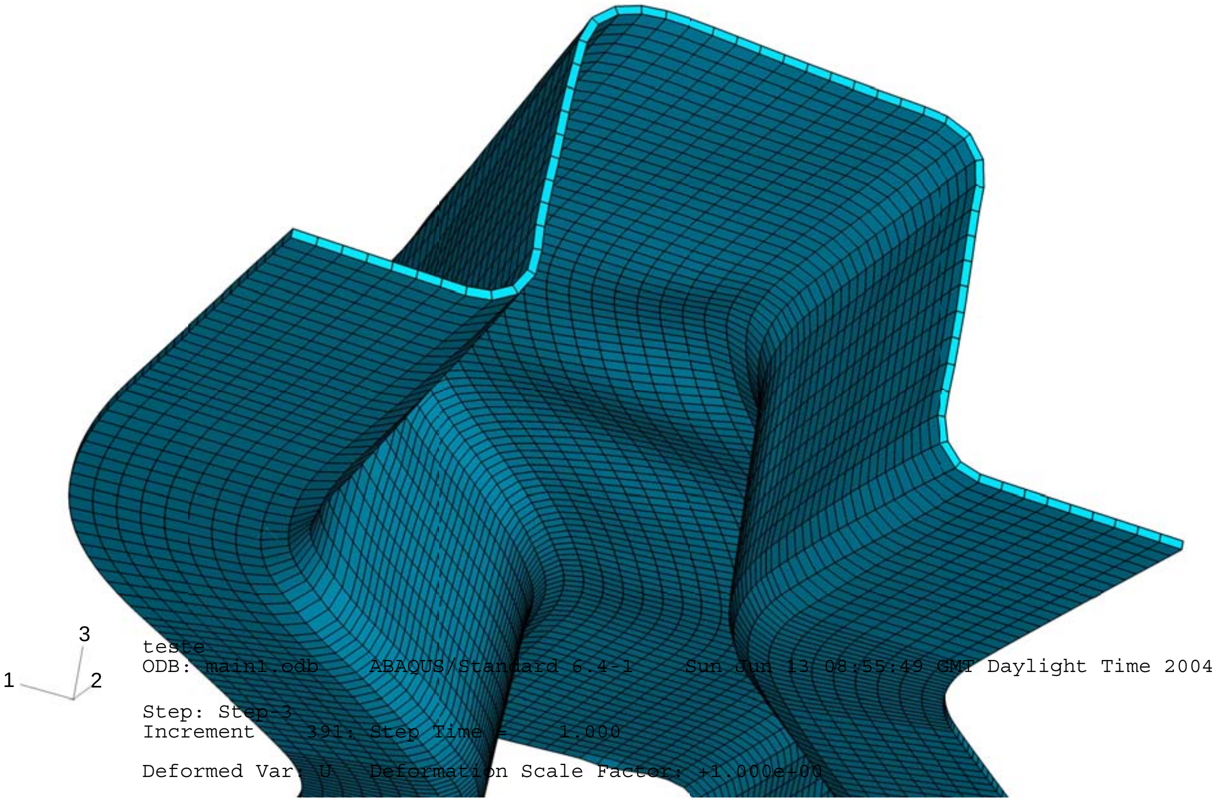

Figure 5.120: S-Rail problem - Detailed representation of the deformed model, focusing on the presence of wrinkles (bottom view)

Chapter 6

Conclusions and Future Works

In this work a new class of shell and solid-shell finite elements for the simulation of shell structures was formulated and presented. The elements are based on the Enhanced Assumed Strain (*EAS*) method, and are suited for the treatment of numerical pathologies such as the transverse shear locking and volumetric locking, arising either in the linear and nonlinear ranges (either material and/or geometric). The distinguishing point of the present finite elements relies on the fact that just the *EAS* approach is used, together with the conventional, displacement-based, formulation.

The studied shell elements (Chapter 2), for instance, do not make use of other mixed techniques, such as the Mixed Interpolation of Tensorial Components formulation (adopted by almost all well-established formulations in the literature). Therefore, the solely use of a enhanced strain field was enough to completely eliminate the transverse shear locking for thin shells, irrespective of curvature values. This behavior proved successful either in regular and distorted meshes, which very often poses severe problems for enhanced-based formulations. At the end, a fully integrated four-node, bilinear shell element was achieved, proving to be robust and reliable in linear as well as nonlinear demanding numerical benchmarks.

For the solid-shell formulations (Chapter 3), the main goal was to achieve a simpler formulation (and implementation), altogether with a higher generality, when compared to the referred shell elements. This is particular true for the fact that solid-shell elements deals exclusively with (additive-type) degrees-of-freedom – thus skipping particular treatment of rotation nodal variables, present in shell elements – and also that, with solid-shell elements, full 3D material laws can be included directly into the constitutive models – avoiding the *ad hoc* consideration of plane-stress hypothesis at each Gauss point level, characteristic of shell elements. The presented solid-shell elements use the Enhanced Assumed Strain method to overcome parasitic phenomena such as the volumetric locking (arising when dealing with computational plasticity) and the transverse shear locking, for low thickness values. The resulting hexahedral element revealed a high level of predicability, although employing a minimum set of internal (element-wise) variables, when compared to well-known solid-shell formulations in the literature. Additionally, and in contrast to what is common in published papers, the present formulation makes use of just the *EAS* formulation.

Starting from an in-house finite element code prepared for 2D finite elements, this thesis involved the study and implementation of the referred shell elements (linear and nonlinear) as well as the solid-shell elements, in the nonlinear range. The particular implementation adopted for the *EAS* method for nonlinear problems (Chapter 4) turned to be a straightforward and efficient choice, mainly because the same theoretical structure of the original *EAS* approach for linear problems was kept unaltered, which results in small computational effort for the very same final performance. This can be attested from the overall quality of results obtained in the nonlinear geometric range, in problems with or without numerical instabilities (Chapter 5). On the other side, accounting for the integration of the constitutive equations within a local frame, rigidly moving with each finite element, has allowed for a simplified computational treatment of nonlinear material problems, ending up with a constitutive update procedure which is totally equivalent to the one commonly used in small deformation problems. Both shell and solid-shell elements have led to a series of publications within the research group of the author, such as the references César de Sá *et al.* (2002); Alves de Sousa *et al.* (2002, 2003a,b); Fontes Valente *et al.* (2003, 2004a,b,c), in chronological order.

The implementation of the proposed *EAS*-based elements in Abaqus commercial code (as user-elements) have allowed for the treatment of more demanding problems, namely involving contact nonlinearities. Preliminary results were also presented in this work, while further improvements and testing are still on course.

In the meanwhile, extensions to this work are being carried out within the group the author is involved with. First of all, it is on course the extension of the present formulation to problems accounting for anisotropic material effects, either applied to shell (Fontes Valente *et al.*, 2004b) and solid-shell (Parente *et al.*, 2004) finite elements. Also, some developments were already achieved in the modelling of cyclic load effects in aluminum alloy parts, including material anisotropy, which have involved the formulation and implementation of kinematic hardening constitutive models, and whose initial numerical results were recently presented (Yoon *et al.*, 2003).

Another ongoing research field still relies on finite element technology. Seeking for an enhanced strain solid-shell element computationally more cost-effective than the one shown in the present work, it is now under study the conjunction between the *EAS* methodology and reduced integrated techniques. Although the formulation here introduced proved to be reliable and effective, the account for reduced integration procedures would at least improve the computational economy of the solid-shell element for large-scale (industrial) problems. Some encouraging results for geometrically linear problems were already achieved (Alves de Sousa *et al.*, 2004), while the fully nonlinear study is being carried out at the present.

Finally, application of the described concepts into composite analysis and simulation, as well as in the biomechanical description of the behavior of soft tissues, are in the initial stages. Furthermore, an extensive insight into the proposed shell element *MITC4–E2* is still needed, and will be dealt with in the near future.

Bibliography

ABAQUS (2002a) Theory Manual, Version 6.3. Hibbitt, Karlsson & Sorensen, Inc. Rhode-Island USA

ABAQUS (2002b) Benchmarks Manual, Version 6.3. Hibbitt, Karlsson & Sorensen, Inc. Rhode-Island USA

el-Abbasi N, Meguid SA (2000) A new shell element accounting for through-thickness deformation. Computer Methods in Applied Mechanics and Engineering 189: 841–862

Ahmad S, Irons BM, Zienkiewicz OC (1970) Analysis of thick and thin shell structures by curved finite elements. International Journal for Numerical Methods in Engineering 2: 419–451

Alves de Sousa RJ, Natal Jorge RM, Fontes Valente RA, César de Sá JMA (2002) Low Order Elements for 3D Analysis. Mang HA, Rammerstorfer FG, Eberhardsteiner J (eds.) Proceedings of the Fifth World Congress on Computational Mechanics – WCCM V. Vienna, Austria

Alves de Sousa RJ, Natal Jorge RM, Fontes Valente RA, César de Sá JMA (2003a) A new volumetric and shear locking-free 3D enhanced strain element. Engineering Computations 20: 896–925

Alves de Sousa RJ, Natal Jorge RM, Fontes Valente RA, César de Sá JMA (2003b) Formulation of EAS solid elements for incompressibility and thin shell applications in non-linear range. Owen DRJ, Onate E, Suarez B (eds.) Proceedings of the Seventh Congress on Computational Plasticity – COMPLAS VII. Barcelona, Spain

Alves de Sousa RJ (2003c) Modelling of Three-Dimensional Incompressible Problems with the Enhanced Assumed Strain Method. MSc Thesis (in Portuguese). Faculty of Engineering, University of Porto

Alves de Sousa RJ, Cardoso RPR, Fontes Valente RA, Yoon JW, Grácio JJ, Natal Jorge RM (2004) A new one-point quadrature Enhanced Assumed Strain solid-shell element with multiple integration points along thickness. Part I – Geometrically linear applications. International Journal for Numerical Methods in Engineering (submitted)

Andelfinger U, Ramm E (1993) EAS-Elements for two-dimensional, three-dimensional, plate and shells and their equivalence to HR-elements. International Journal for Numerical Methods in Engineering 36: 1413–1449

Areias PMA, César de Sá JMA, Conceição António CA, Fernandes AA (2003a) Analysis of 3D problems using a new enhanced strain hexahedral element. International Journal for Numerical Methods in Engineering 58: 1637–1682

Areias PMA (2003b) Finite Element Technology, Damage Modeling, Contact Constraints and Fracture Analysis. PhD Thesis. Faculty of Engineering, University of Porto

Argyris J, Dunne P, Angelopoulus T, Bichat B (1974) Large natural strains and some special difficulties due to nonlinearity and incompressibility in finite elements. Computer Methods in Applied Mechanics and Engineering 4: 219–278

Ashwell DG (1976) Strain elements with applications to arches, rings and cylindrical shells. In: Ashwell DG, Gallagher RH (eds.) Finite Elements for Thin Shells and Curved Members. John Wiley & Sons, New York

Barbosa JAT Nonlinear Finite Element Analysis of Reinforced Plates and Shells. PhD Thesis (in Portugueses). Faculty of Engineering, University of Porto

Barlat F, Lege DJ, Brem JC (1991) A six-component yield function for anisotropic metals. International Journal of Plasticity 7: 693–712

Basar Y, Ding Y, Krätzig WB (1992) Finite-rotation shell elements via mixed formulation. Computational Mechanics 10: 289–306

Basar Y, Ding Y (1997) Shear deformation models for large-strain shell analysis. International Journal of Solids and Structures 34: 1687–1708

Basar Y, Itskov M (1999) Constitutive model and finite element formulation for large strain elasto-plastic analysis of shells. Computational Mechanics 23: 466–481

Basar Y, Weicher D (2000) Nonlinear Continuum Mechanics of Solids. Springer-Verlag, Berlin Heidelberg New York

Bathe KJ, Dvorkin EN (1983) On the automatic solution of nonlinear finite element equations. Computers & Structures 17: 871–879

Bathe KJ, Dvorkin EN (1985) A four-node plate bending element based on Mindlin/Reissner plate theory and a mixed interpolation. International Journal for Numerical Methods in Engineering 21: 367–383

Bathe KJ, Dvorkin E (1986) A formulation of general shell elements - the use of mixed interpolation of tensorial components. International Journal for Numerical Methods in Engineering 22: 697–722

Bathe KJ (1996) Finite Element Procedures. 2^{nd} edn. Prentice-Hall, New Jersey

Bathe KJ, Iosilevich A, Chapelle D (2000) An evaluation of the MITC shell elements. Computers & Structures 75:1–30

Bathe KJ, Chapelle D, Lee PS (2003) A shell problem "highly sensitive" to thickness changes. International Journal for Numerical Methods in Engineering 57: 1039–1052

Batoz JL, Dhatt G (1979) Incremental displacement algorithms for non-linear problems. International Journal for Numerical Methods in Engineering 14: 1262–1266

Batoz JL, Dhatt G (1992) Modélisation des Structures par Éléments Finis. Volume 3 – Coques. Hermès, Paris

Belleni PX, Chulya A (1987) An improved automatic incremental algorithm for the efficient solution of nonlinear finite element equations. Computers & Structures 26: 99–110

Belytschko T, Tsay C (1983) A stabilization procedure for the quadrilateral plate element with one-point quadrature. International Journal for Numerical Methods in Engineering 19: 405–419

Belytschko T, Stolarski H, Liu WK, Carpenter N, Ong JSJ (1985) Stress projection for membrane and shear locking in shell finite elements. Computer Methods in Applied Mechanics and Engineering 51: 221–258

Belytschko T, Bindeman LP (1993) Assumed strain stabilization of the eight node hexahedral element. Computer Methods in Applied Mechanics and Engineering 105: 225–260

Belytschko T, Leviathan I (1994) Physical stabilization of the 4-node shell element with one point quadrature. Computer Methods in Applied Mechanics and Engineering 113: 321–350

Belytschko T, Liu WK, Moran B (2000) Nonlinear Finite Elements for Continua and Structures. John Wiley & Sons, West Sussex, England

Bernadou M (1996) Finite Element Methods for Thin Shell Problems. John Wiley & Sons, West Sussex, England

Betsch P, Stein E (1995) An assumed strain approach avoiding artificial thickness straining for a nonlinear 4-node shell element. Communications in Numerical Methods in Engineering 11: 899–909

Betsch P, Gruttmann F, Stein E (1996) A 4-node finite shell element for the implementation of general hyperelastic 3D-elasticity at finite strains. Computer Methods in Applied Mechanics and Engineering 130: 57–79

Betsch P, Stein E (1996) A nonlinear extensible 4-node shell element based on continuum theory and assumed strain interpolations. Journal of Nonlinear Science 6: 169–199

Betsch P, Manzel A, Stein E (1998) On parametrization of finite rotations in computational mechanics. A classification of concepts with application to smooth shells. Computer Methods in Applied Mechanics and Engineering 155: 273–305

Betsch P, Stein E (1999) Numerical implementation of multiplicative elasto-plasticity into assumed strain elements with application to shells at large strains. Computer Methods in Applied Mechanics and Engineering 179: 215–245

Bischoff M, Ramm E (1997) Shear deformable shell elements for large strains and rotations. International Journal for Numerical Methods in Engineering 40: 4427–4449

Boër CR, Rebelo N, Rydstad H, Schröder G (1986) Process Modelling of Metal Forming and Thermomechanical Treatment. Springer-Verlag, Berlin Heidelberg New York

de Borst R, Groen AE (1999) Towards efficient and robust elements for 3D-soil plasticity. Computers & Structures 70: 23-34

Brank B, Peric D, Damjanic FB (1995) On implementation of a nonlinear four node shell finite element for thin multilayered elastic shells. Computational Mechanics 16: 341–359

Brank B, Peric D, Damjanic FB (1997) On large deformations of thin elasto-plastic shells: implementation of a finite rotation model for a quadrilateral shell element. International Journal for Numerical Methods in Engineering 40: 689–726

Brank B, Korelc J, Ibrahimbegović A (2002) Nonlinear shell problem formulation accounting for through-the-thickness stretching and its finite element interpolation. Computers & Structures 80: 699–717

Braun M, Bischoff M, Ramm E (1994) Nonlinear shell formulations for complete three-dimensional constitutive laws including composites and laminates. Computational Mechanics 15: 1–18

Bucalem ML, Bathe KJ (1993) Higher-order MITC general shell elements. International Journal for Numerical Methods in Engineering 36: 3729–3754

Bucalem ML, Bathe KJ (1997) Finite element analysis of shell structures. Archives of Computational Methods in Engineering 4: 3–61

Büchter N, Ramm E (1992) Shell theory versus degeneration - A comparison in large rotation finite element analysis. International Journal for Numerical Methods in Engineering 34: 39–59

Büchter N, Ramm E, Roehl D (1994) Three-dimensional extension of nonlinear shell formulation based on the enhanced assumed strain concept. International Journal for Numerical Methods in Engineering 37: 2551–2568

Cardoso RPR, Yoon JW, Grácio JJA, Barlat F, César de Sá JMA (2002) Development of a one point quadrature shell element for nonlinear applications with contact and anisotropy. Computer Methods in Applied Mechanics and Engineering 191: 5177–5206

Cardoso RPR (2002) Development of one point quadrature shell elements with anisotropic material models for sheet metal forming analysis. PhD Thesis, Mechanical Engineering Department, University of Aveiro

César de Sá JMA, Owen DRJ (1986) The imposition of the incompressibility constraint in finite elements - A review of methods with a new insight to the locking phenomenon. In: Taylor, C *et al.* (eds) Proceedings of the 3^{rd} International Conference on Numerical Methods for Non-Linear Problems. Pineridge Press Ltd, Swansea

César de Sá JMA (1986) Numerical Modelling of Incompressible Problems in Glass Forming and Rubber Technology. PhD Thesis, C/Ph/91/86, University of Wales, Swansea, UK

César de Sá JMA, Natal Jorge RM (1999) New enhanced strain elements for incompressible problems. International Journal for Numerical Methods in Engineering 44: 229–248

César de Sá JMA, Areias PMA, Natal Jorge RM (2001) Quadrilateral elements for the solution of elasto-plastic finite strain problems. International Journal for Numerical Methods in Engineering 51: 883–917

César de Sá JMA, Natal Jorge RM, Fontes Valente RA, Areias PMA (2002) Development of shear locking-free shell elements using an enhanced assumed strain formulation. International Journal for Numerical Methods in Engineering 53: 1721–1750

Chadwick P (1999) Continuum Mechanics – Concise Theory and Problems. Dover Publications, New York

Chapelle D, Bathe KJ (1998) Fundamental considerations for the finite element analysis of shell structures. Computers & Structures 66: 19–36

Chapelle D, Bathe KJ (2000) The mathematical shell model underlying general shell elements. International Journal for Numerical Methods in Engineering 48: 289–313

Chapelle D, Bathe KJ (2003) The Finite Element Analysis of Shells – Fundamentals. Springer-Verlag Berlin Heidelberg New York

Cho C, Park HC, Lee SW (1998) Stability analysis using a geometrically nonlinear assumed strain solid-shell element model. Finite Elements in Analysis and Design 29: 121–135

Choi CK, Lee TY (2003) Efficient remedy for membrane locking of 4–node flat shell elements by non-conforming modes. Computer Methods in Applied Mechanics and Engineering 192: 1961–1971

Chroscielewski J, Makowski J, Stumpf H (1992) Genuinely resultant shell finite elements accounting for geometric and material non-linearities. International Journal for Numerical Methods in Engineering 35: 63–94

Clarke MJ, Hancock GJ (1990) A study of incremental-iterative strategies for nonlinear analysis. International Journal for Numerical Methods in Engineering 29: 1365–1391

Crisfield MA (1981) A fast incremental/iterative solution procedure that handles "snap-through". Computers & Structures 13: 55–62

Crisfield MA (1983) An arc-length method including line searches and accelerations. International Journal for Numerical Methods in Engineering 19: 1269–1289

Crisfield MA, Peng X (1996) Short communication: Instabilities induced by coarse meshes for a nonlinear shell problem. Engineering Computations 13: 110–114

Crisfield MA (1997) Non-Linear Finite Element Analysis of Solids and Structures, Vol. 1: Essentials, Vol. 2: Advanced Topics. John Wiley & Sons, West Sussex

Dhondt G (2004) The Finite Element Method for Three-Dimensional Thermomechanical Applications. John Wiley & Sons, West Sussex

Dienes JK (1979) On the analysis of rotation and stress rate in deforming bodies. Acta Mechanica 32: 271–232

Doghri I (2000) Mechanics of Deformable Solids - Linear, Nonlinear, Analytical and Computational Aspects. Springer-Verlag, Berlin Heidelberg New York

Doll S, Schweizerhof K, Hauptmann R, Freischläger C (2000) On volumetric locking of low-order solid and solid-shell elements for finite elastoviscoplastic deformations and selective reduced integration. Engineering Computations 17: 874–902

Doyle JF (2001) Nonlinear Analysis of Thin-Walled Structures – Statics, Dynamics and Stability. Springer–Verlag, New York

Dvorkin E, Bathe KJ (1984) A continuum mechanics based four-node shell element for general nonlinear analysis. Engineering Computations 1: 77–88

Dvorkin EN, Pantuso D, Repetto EA (1995) A formulation of the MITC4 shell element for finite strain elastoplastic analysis. Computer Methods in Applied Mechanics and Engineering 125: 17–40

Eberlein R, Wriggers P (1999) Finite element concepts for finite elastoplastic strains and isotropic stress response in shells: theoretical and computational analysis. Computer Methods in Applied Mechanics and Engineering 171: 243–279

Eckstein A, Basar Y (2000) Ductile damage analysis of elasto-plastic shells at large inelastic strains. International Journal for Numerical Methods in Engineering 47: 1663–1687

Eriksson A, Pacoste C (2002) Element formulation and numerical techniques for stability problems in shells. Computer Methods in Applied Mechanics and Engineering 191: 3775–3810

Feng YT, Peric D, Owen DRJ (1996) A new criterion for determination of initial loading parameter in arc-length methods. Computers & Structures 58: 479–485

Feng YT, Owen DRJ, Peric D (1997) On the sign of the determinant of the structural stiffness matrix for determination of loading increment in arc-length algorithms. Communications in Numerical Methods in Engineering 13: 47–49

Flanagan DP, Taylor LM (1987) An accurate numerical algorithm for stress integration with finite rotations. Computer Methods in Applied Mechanics and Engineering 62: 305–320

Flügge W (1973) Stresses in Shells. Springer-Verlag, New York

Fontes Valente RA, Natal Jorge RM, Cardoso RPR, César de Sá JMA, Grácio JJ (2003) On the use of an enhanced *transverse* shear strain shell element for problems involving large rotations. Computational Mechanics 30: 286–296

Fontes Valente RA, Alves de Sousa RJ, Natal Jorge RM (2004a) An enhanced strain 3D element for large deformation elastoplastic thin-shell applications. Computational Mechanics 34: 38–52

Fontes Valente RA, Alves de Sousa RJ, Parente MPL, Natal Jorge RM, César de Sá JMA, Grácio JJ (2004b) Enhanced assumed strain shell and solid-shell elements: application in sheet metal forming processes. In: S. Ghosh (ed) The 8^{th} International Conference on Numerical Methods in Industrial Forming Processes – NUMIFORM 2004, Ohio State University, Columbus, Ohio, USA

Fontes Valente RA, Natal Jorge RM, César de Sá JMA, Grácio JJ (2004) Enhanced *transverse* shear strain shell formulation applied to large elasto-plastic deformation problems. International Journal for Numerical Methods in Engineering (submitted)

Forde BWR, Sttemer SF (1987) Improved arc-length orthogonality methods for nonlinear finite element analysis. Computers & Structures 27: 625–630

Franca LP (1989) An algorithm to compute the square root of a 3 × 3 positive definite matrix. Computers & Mathematics with Applications 18: 459–466

Freischlager C, Schweizerhof K (1996) On a systematic development of trilinear three-dimensional solid elements based on Simo's enhanced strain formulation. International Journal of Solids and Structures 33: 2993–3017

Fried I (1974) Finite element analysis of incompressible material by residual energy balancing. International Journal of Solids and Structures 10: 993–1002

Frisch-Fay R (1962) Flexible Bars, Butterworths, London

Fung YC, Tong P (2001) Classical and Computational Solid Mechanics. World Scientific, Singapore

Gambin W (2001) Plasticity and Textures. Kluwer Academic Publishers, The Netherlands

Gierlinski JT, Graves-Smith TR (1985) A variable load iteration procedure for thin-walled structures. Computers & Structures 21: 1085–1094

Groenwold AA, Slander N (1995) An efficient 4-node 24 DOF thick shell finite element with 5-point quadrature. Engineering Computations 12: 723–747

Gruttmann F, Wagner W, Wriggers P (1992) A nonlinear quadrilateral shell element with drilling degrees of freedom. Archive of Applied Mechanics 62: 474–486

Haupt P (2002) Continuum Mechanics and Theory of Materials. Springer-Verlag, Berlin Heidelberg New York

Hauptmann R, Schweizerhof K (1998) A systematic development of "solid-shell" element formulations for linear and non-linear analyses employing only displacement degrees of freedom. International Journal for Numerical Methods in Engineering 42: 49–69

Harnau M, Schweizerhof K (2002) About linear and quadratic "solid-shell" elements at large deformations. Computers & Structures 80: 805–817

Hauptmann R, Schweizerhof K, Doll S (2000) Extension of the solid-shell concept for application to large elastic and large elastoplastic deformations. International Journal for Numerical Methods in Engineering 49: 1121–1141

Hellweg HB, Crisfield MA (1998) A new method for handling sharp snap-backs. Computers & Structures 66: 705–709

Horrigmoe G, Bergan PG (1978) Nonlinear analysis of free-form shells by flat finite elements. Computer Methods in Applied Mechanics and Engineering 16: 11–35

Huang BZ, Atluri SN (1995) A simple method to follow post-buckling paths in finite element analysis. Computers & Structures 57: 477–489

Huang HC, Hinton E (1986) A new nine node degenerated shell element with enhanced membrane and shear interpolation. International Journal for Numerical Methods in Engineering 22: 73–92

Huang HC (1989) Static and Dynamic Analyses of Plates and Shells – Theory, Software and Applications. Springer-Verlag, Berlin Heidelberg New York

Huettel C, Matzenmiller A (1999) Consistent discretization of thickness strains in thin shells including 3d-material models. Communications in Numerical Methods in Engineering 15: 283–293

Hughes TJR (1977) Equivalence of finite elements for nearly incompressible elasticity. Journal of Applied Mechanics 44: 181–183

Hughes TJR, Cohen M, Haroun M (1978) Reduced and selective integration techniques in finite element analysis of plates. Nuclear Engineering and Design 46: 203–222

Hughes TJR (1980) Generalisation of selective integration procedures to anisotropic and nonlinear media. International Journal for Numerical Methods in Engineering 15: 1413–1418

Hughes TJR, Liu WK (1981) Nonlinear finite element analysis of shells: Part I. Three-dimensional shells. Computer Methods in Applied Mechanics and Engineering 26: 331–362

Hughes TJR, Tezduyar TE (1981) Finite elements based upon Mindlin plate theory with particular reference to the four-node bilinear isoparametric element. Journal of Applied Mechanics 48: 587–596

Hughes TJR, Carnoy E (1983) Nonlinear finite shell element formulation accounting for large membrane strains. Computer Methods in Applied Mechanics and Engineering 39: 69–82

Hughes TJR (1984) Numerical implementation of constitutive models: rate independent deviatoric plasticity. In: Nemat-Nasser S *et al.* (eds.), Theoretical Foundations for

Large-Computations for Non-Linear Material Behavior. Martinus Nijhoff Publishers, Dordrecht, The Netherlands

Hughes TJR (2000) The Finite Element Method: Linear Static and Dynamic Finite Element Analysis. 2^{nd} edn. Dover Editions, Toronto

Ibrahimbegović A, Taylor RL, Wilson EL (1990) A robust quadrilateral membrane finite element with drilling degrees of freedom. International Journal for Numerical Methods in Engineering 30: 445–457

Ibrahimbegović A, Brank B, Courtois P (2001) Stress resultant geometrically exact form of classical shell model and vector-like parameterization of constrained finite rotations. International Journal for Numerical Methods in Engineering 52: 1235–1252

Ibrahimbegović A, Frey F (1994) Stress resultant geometrically nonlinear shell theory with drilling rotations – Part II: Computational aspects. Computer Methods in Applied Mechanics and Engineering 188: 285–308

Jiang L, Chernuka MW (1994a) A simple four-noded corotational shell element for arbitrarily large rotations. Computers & Structures 53: 1123–1132

Jiang L, Chernuka MW (1994b) A co-rotational, updated lagrangean formulation for geometrically nonlinear finite element analysis of shell structures. Finite Elements in Analysis and Design 18: 129–140

Kasper EP, Taylor RL (2000) A mixed-enhanced strain method. Part I: Geometrically linear problems. Computers & Structures 75: 237–250

Kemp BL, Cho C, Lee SW (1998) A four-node solid shell element formulation with assumed strain. International Journal for Numerical Methods in Engineering 43: 909–924

Key SW (1969) A variational principle for incompressible and nearly incompressible anisotropic elasticity. International Journal of Solids and Structures 5: 951–964

Key SW, Krieg RD (1982) On the numerical implementation of inelastic time dependent and time independent finite strain constitutive equations in structural mechanics. Computer Methods in Applied Mechanics and Engineering 33: 439–452

Khan AS, Huang S (1995) Continuum Theory of Plasticity. John Wiley & Sons, New York

Kim JH, Kim YH (2001) A predictor-corrector method for structural nonlinear analysis. Computer Methods in Applied Mechanics and Engineering 191: 959–974

Klinkel S, Wagner W (1997) A geometrical nonlinear brick element based on the eas-method. International Journal for Numerical Methods in Engineering 40: 4529–4545

Klinkel S, Gruttman F, Wagner W (1999) A continuum based 3d-shell element for laminated structures. Computers & Structures 71: 43–62

Knight NF (1997) The Raasch Challenge for Shell Elements. AIAA Journal 35: 375–381

Korelc J, Wriggers P (1996) Consistent gradient formulation for a stable enhanced strain method for large deformations. Engineering Computations 13: 103–123

Kui LX, Liu GQ, Zienkiewicz OC (1985) A generalized displacement method for the finite element analysis of thin shells. International Journal for Numerical Methods in Engineering 21: 2145–2155

Lautersztajn-S N, Samuelsson A (2000) Further discussion on four-node isoparametric quadrilateral elements in plane bending. International Journal for Numerical Methods in Engineering 47: 129–140

Legay A, Combescure A (2003) Elastoplastic stability analysis of shells using the physically stabilized finite element *SHB8PS*. International Journal for Numerical Methods in Engineering 57: 1299–1322

Li M (2000) The finite deformation of beam, plate and shell structures. Part IV: The FE formulation of Mindlin plate and shell based on Green-Lagrangian strains. Computer Methods in Applied Mechanics and Engineering 182: 187–203

Li M, Zhan F (2000) The finite deformation theory for beam, plate and shells. Part V: The shell element with drilling degrees of freedom based on biot strain. Computer Methods in Applied Mechanics and Engineering 189: 743–759

Lindberg GM, Olson MD, Cowper GR (1969) New developments in the finite element analysis of shells. National Research Council of Canada. Quartely Bulletin of the Division of Mechanical Engineering and the National Aeronautical Establishment 4: 1–38

Liu J, Riggs HR, Tessler A (2000) A four-node, shear-deformable shell element developed via explicit Kirchhoff constraints. International Journal for Numerical Methods in Engineering 49: 1065–1086

Liu WK, Guo Y, Tang S, Belytschko T (1998) A multiple-quadrature eight-node hexahedral finite element for large deformation elasto-plastic analysis. Computer Methods in Applied Mechanics and Engineering 154: 69–132

MacNeal RH (1982) Derivation of element stiffness matrices by assumed strain distribution. Nuclear Engineering and Design 70: 3–12

MacNeal RH, Harder RL (1985) A proposed standard set of problems to test finite element accuracy. Finite Elements in Analysis and Design 1: 1–20

Malinen M, Pitkäranta J (2000) A benchmark study of reduced-strain shell finite elements: quadratic schemes. International Journal for Numerical Methods in Engineering 48: 1637–1671

Malkus DS (1976) A finite element displacement model valid for any value of the compressibility. International Journal of Solids and Structures 11: 731–738

Malkus DS, Hughes TJR (1978) Mixed finite-element methods - reduced and selective integration techniques - a unification of concepts. Computer Methods in Applied Mechanics and Engineering 15: 63–81

Marciniak Z, Duncan JL, Hu SJ (2002) Mechanics of Sheet Metal Forming, 2^{nd} edition. Butterworth Heinemann, Oxford

Marsden JE, Hughes TJR (1994) Mathematical Foundations of Elasticity. Dover Publications, New York

Massin P, al Mikdad M (2002) Nine-node and seven-node thick shell elements with large displacements and rotations. Computers & Structures 80: 835–847

Masud A, Tham CL, Liu WK (2000) A stabilized 3D co-rotational formulation for geometrically nonlinear analysis of multi-layered composite shells. Computational Mechanics 26(1): 1–12

Masud A, Tham CL (2000) Three-dimensional corotational framework for finite deformation elasto-plastic analysis of multilayered composite shells. AIAA Journal 38(9): 1–8

Miehe C (1998) A theoretical and computational model for isotropic elastoplastic stress analysis in shells at large strains. Computer Methods in Applied Mechanics and Engineering 155: 193–233

Militello C, Felippa C (1990) A variational justification of the assumed natural strain formulation of finite elements, Part I: Variational principles. Computers & Structures 34: 431–438

Moita GF, Crisfield MA (1996) A finite element formulation for 3D continua using the corotational technique. International Journal for Numerical Methods in Engineering 39: 3775–3792

Morley LSD (1963) Skew Plates and Structures. Pergamon Press London

Nagtegaal JC, Parks DM, Rice JR (1974) On numerically accurate finite element solutions in the fully plastic range. Computer Methods in Applied Mechanics and Engineering 4: 153–177

Natal Jorge RM (1998) Modeling of Incompressible Problems with the Enhanced Strain Method based on Compatible Modes. PhD Thesis (in Portuguese). Faculty of Engineering, University of Porto

Novozhilov VV (1999) Foundations of the Nonlinear Theory of Elasticity. Dover Publications, New York

NUMISHEET (1996) Proceedings of the 3rd International Conference on Numerical Simulation of Sheet Metal Forming Processes – Verification of Simulations with Experiments. Lee JK, Kinzel GL, Wagoner RH (eds.), Dearborn, Michigan, USA

Oliver J, Oñate E (1984) A total lagrangian formulation for geometrically nonlinear analysis of structures using finite elements - Part I: Two-dimensional problems: shell and plate structures. International Journal for Numerical Methods in Engineering 20: 2253–2281

Ortiz M, Popov EP Accuracy and stability of integration algorithms for elastoplastic constitutive relations. International Journal for Numerical Methods in Engineering 21: 1561–1576

Parente MPL (2003) Elasto-Plastic Anisotropic Analysis of Shell-Type Structures. MSc Thesis (in Portuguese). Faculty of Engineering, University of Porto

Parente MPL, Natal Jorge RM, Fontes Valente RA, Alves de Sousa RJ (2004) Mixed formulated solid-shell finite elements in thin shell structural problems with anisotropic behavior. In: B. H. V. Topping (ed) The Fourth International Conference on Engineering Computational Technology, Lisbon, Portugal

Park KC (1986) Improved strain interpolation for curved C^0 elements. International Journal for Numerical Methods in Engineering 22: 281–288

Park KC, Stanley GM (1986) A curved C^0 shell element based on assumed natural coordinate strains. Journal of Applied Mechanics 53: 278–290

Parisch H (1991) An investigation of a finite rotation four node assumed strain shell element. International Journal for Numerical Methods in Engineering 31: 127–150

Parisch H (1995) A continuum based shell element for non-linear applications. International Journal for Numerical Methods in Engineering 38: 1855–1883

Peng X, Crisfield MA (1992) A consistent corotational formulation for shells using the constant stress/constant moment triangle. International Journal for Numerical Methods in Engineering 35: 1829–1847

Pian THH, Sumihara K (1985) Rational approach for assumed stress finite elements. International Journal for Numerical Methods in Engineering 20: 1685–1695

Piltner R, Joseph DS (2001) A mixed finite element for plate bending with eight enhanced strain modes. Communications in Numerical Methods in Engineering 17: 443–454

Pinsky PM, Ortiz M, Pister KS (1983) Numerical integration of rate constitutive equations in finite deformation analysis. Computer Methods in Applied Mechanics and Engineering 40: 137–158

Pitkäranta J, Leino Y, Ovaskainen O, Piila J (1995) Shell deformation states and the finite element method: A benchmark study of cylindrical shells. Computer Methods in Applied Mechanics and Engineering 128: 81–121

Powell G, Simons J (1981) Improved iterative strategy for nonlinear structures. International Journal for Numerical Methods in Engineering 17: 1455–1467

Qin Z, Chen Z (1988) Large deformation analysis of shells with finite element method based on the S–R Decomposition theorem. Computers & Structures 30: 957–961

Ramm E (1977) A plate/shell element for large deflections and rotations. In: K.J. Bathe, J.T. Oden, W. Wunderlich (eds) Formulations and Computational Algorithms in Finite Element Analysis, M.I.T. Press

Ramm E (1981) Strategies for tracing the non-linear response near limit-points. In: W. Wunderlich (ed) Finite Element Analysis in Structural Mechanics, Springer-Verlag Berlin

Ramm E (1982) The Riks/Wempner approach – An extension of the displacement control method in nonlinear analysis. In: E. Hinton *et al.*, Pineridge Press, Swansea

Ramm E, Matzenmiller A (1988) Consistent linearization in elasto-plastic shell analysis. Engineering Computations 5: 289–299

Reese S, Küssner M, Reddy BD (1999) A new stabilization technique for finite elements in non-linear elasticity. International Journal for Numerical Methods in Engineering 44: 1617–1652

Reese S, Wriggers P (2000) A stabilization technique to avoid hourglassing in finite elasticity. International Journal for Numerical Methods in Engineering 48: 79–109

Reese S (2002) On the equivalence of mixed element formulations and the concept of reduced integration in large deformation problems. International Journal of Nonlinear Sciences and Numerical Simulation 3: 1–33

Reese S (2003) On a consistent hourglass stabilization technique to treat large inelastic deformations and thermo-mechanical coupling in plane strain problems. International Journal for Numerical Methods in Engineering 57: 1095–1127

Remmers JJC, Wells GN, de Borst R (2003) A solid-like shell element allowing for arbitrary delaminations. International Journal for Numerical Methods in Engineering 58: 2013–2040

Riks E (1972) The application of Newton's method to the problem of elastic stability. Journal of Applied Mechanics 39: 1060–1066

Riks E (1979) An incremental approach to the solution of snapping and buckling problems. International Journal of Solids and Structures 15: 529–551

Riks E (1992) On formulations of path-following techniques for structural stability analysis. In: P. Ladeveze and O. C. Zienkiewicz, New Advances in Computational Structural Mechanics, Elsevier

Roehl D, Ramm E (1996) Large elasto-plastic finite element analysis of solids and shells with the enhanced assumed strain concept. International Journal of Solids and Structures 33: 3215–3237

Sabir AB, Lock AC (1972) The application of finite elements to the large-deflection geometrically non-linear behaviour of cylindrical shells. Proceedings of the International Conference on Variational Methods in Engineering. Southampton University, UK

Saleeb AF, Chang TY (1987) An efficient quadrilateral element for plate bending analysis. International Journal for Numerical Methods in Engineering 24: 1123–115

Saleeb AF, Chang TY, Graf W (1987) A quadrilateral shell element using a mixed formulation. Computers & Structures 26: 787–803

Saleeb AF, Chang TY, Graf W, Yingyeunyong S (1990) A hybrid/mixed model for non-linear shell analysis and its applications to large-rotation problems. International Journal for Numerical Methods in Engineering 29: 407–446

Sansour C, Bufler H (1992) An exact finite rotation shell theory, its mixed variational formulation and its finite element implementation. International Journal for Numerical Methods in Engineering 34: 73–115

Sansour C (1995) A theory and finite element formulation of shells at finite deformations including thickness change: Circunventing the use of a rotation tensor. Archive of Applied Mechanics 65: 194–216

Sansour C, Bocko J (1998) On hybrid stress, hybrid strain and enhanced strain finite element formulations for a geometrically exact shell theory with drilling degrees of freedom. International Journal for Numerical Methods in Engineering 43: 175–192

Sansour C, Kollmann FG (2000) Families of 4–node and 9-node finite elements for a finite deformation shell theory: An assessment of hybrid stress, hybrid strain and enhanced strain elements. Computational Mechanics 24: 435–447

Schweizerhof K, Wriggers P (1986) Consistent linearization for path following methods in nonlinear finite element analysis. Computer Methods in Applied Mechanics and Engineering 59: 261–279

Scordelis AC, Lo KS (1964) Computer analysis of cylindrical shells. Journal of the American Concrete Institute 61: 539–562

Simo JC, Taylor RL (1982) Penalty-function formulations for incompressible non-linear elastostatics. Computer Methods in Applied Mechanics and Engineering 35: 107–118

Simo JC, Wriggers P, Schweizerhof K, Taylor RL (1984) Finite deformation post-buckling analysis involving inelasticity and contact constraints. In: W. K. Liu *et al.* (eds), Innovative Methods for Nonlinear Problems, Pineridge Press, Swansea

Simo JC, Taylor RL, Pister KS (1985) Variational and projection methods for the volume constraint in finite deformation elasto-plasticity. Computer Methods in Applied Mechanics and Engineering 51: 177–208

Simo JC, Fox DD, Rifai MS (1989a) On a stress resultant geometrically exact shell model. Part I: Formulation and optimal parametrization. Computer Methods in Applied Mechanics and Engineering 72: 267–304

Simo JC, Fox DD, Rifai MS (1989b) On a stress resultant geometrically exact shell model. Part II: The linear theory – computational aspects. Computer Methods in Applied Mechanics and Engineering 73: 53-92

Simo JC, Rifai MS (1990) A class of mixed assumed strain methods and the method of incompatible modes. International Journal for Numerical Methods in Engineering 29: 1595–1638

Simo JC, Fox DD, Rifai MS (1990a) On a stress resultant geometrically exact shell model. Part III: Computational aspects of the nonlinear theory. Computer Methods in Applied Mechanics and Engineering 79: 21–70

Simo JC, Fox DD, Rifai MS (1990b) On a stress resultant geometrically exact shell model. Part IV: Variable thickness shells with through-the-thickness stretching. Computer Methods in Applied Mechanics and Engineering 81: 91–126

Simo JC, Armero F (1992) Geometrically non-linear enhanced strain mixed methods and the method of incompatible modes. International Journal for Numerical Methods in Engineering 33: 1413–1449

Simo JC, Kennedy JG (1992) On a stress resultant geometrically exact shell model. Part V: Nonlinear plasticity - formulation and integration algorithms. Computer Methods in Applied Mechanics and Engineering 96: 133–171

Simo JC, Armero F, Taylor RL (1993) Improved versions of assumed enhanced strain tri-linear elements for 3D finite deformation problems. Computer Methods in Applied Mechanics and Engineering 110: 359–386

Slavković R, Miroslav Z, Kojić M (1994) Enhanced 8-node three-dimensional solid and 4–node shell elements with incompatible generalized displacements. Communications in Numerical Methods in Engineering 10: 699–709

Sorić J, Montag U, Krätzig WB (1997) An efficient formulation of integration algorithms for elastoplastic shell analysis based on layered finite element approach. Computer Methods in Applied Mechanics and Engineering 148: 315–328

de Souza Neto EA, Feng YT (1999) On the determination of the path direction for arc-length methods in the presence of bifurcations and "snap-backs". Computer Methods in Applied Mechanics and Engineering 179: 81–89

Stander N, Matzenmiller A, Ramm E (1989) An assessment of assumed strain methods in finite rotation shell analysis. Engineering Computations 6: 58–66

Stanley GM, Park KC, Hughes TJR (1986) Continuum-based resultant shell elements. In: T.J.R. Hughes, E. Hinton (eds) Finite Element Methods for Plate and Shell Structures, Pineridge Press, Swansea, pp 1–45

Surana KS (1983) Geometrically non-linear formulation for the curved shell elements. International Journal for Numerical Methods in Engineering 19: 581–615

Sze KY, Sim YS, Soh AK (1997) A hybrid stress quadrilateral shell element with full rotational degrees-of-freedom. International Journal for Numerical Methods in Engineering 40: 1785–1800

Sze KY, Liu XH, Lo SH (2004) Popular benchmark problems for geometrically nonlinear analysis of shells. Finite Elements in Analysis and Design 40: 1551–1569

Szyszkowski W, Husband JB (1999) Curvature controlled arc-length method. Computational Mechanics 24: 245–257

Taylor RL, Pister KS, Herrmann LR (1968) On a variational theorem for incompressible and nearly incompressible orthotropic elasticity. International Journal of Solids and Structures 4: 875–883

Taylor RL, Beresford PJ, Wilson EL (1976) A non-conforming element for stress analysis. International Journal for Numerical Methods in Engineering 10: 1211–1219

Taylor RL (2003) FEAP – A Finite Element Analysis Program – Theory Manual (version 7.5). Department of Civil and Environmental Engineering, University of California at Berkeley

Truesdell C, Noll W (1965) The Non-Linear Field Theories of Mechanics. In: Flügge S (editor) Encyclopedia of Physics, Springer-Verlag, New York

Ugural AC (1981) Stresses in Plates and Shells. McGraw-Hill New York

Vila A, Rodriguez-Ferran A, Huerta A (1995) Nonlinear Finite Element Techniques using an Object-Oriented Code. Monograph CIMNE n^o 31. CIMNE, Barcelona, Spain

Vu-Quoc L, Tan XG (2003) Optimal solid shells for non-linear analysis of multilayer composites. Part I: Statics. Computer Methods in Applied Mechanics and Engineering 192: 975–1016

Wagner W, Klinkel S, Gruttmann F (2002) Elastic and plastic analysis of thin-walled structures using improved hexahedral elements. Computers & Structures 80: 857–869

Wang L, Thierauf G (2001) Finite rotations in non-linear analysis of elastic shells. Computers & Structures 79: 2357–2367

Watson LT, Holzer SM (1983) Quadratic convergence of Crisfield's method. Computers & Structures 17: 69-72

Wempner GA (1971) Discrete approximations related to nonlinear theories of solids. International Journal of Solids and Structures 7: 1581–1599

Widjaja BR (1998) Path-following techniques based on residual energy suppression for nonlinear finite element analysis. Computers & Structures 66: 201–209

Wriggers P, Gruttmann F (1993) Thin shells with finite rotations formulated in Biot stresses: Theory and finite element formulation. International Journal for Numerical Methods in Engineering 36: 2049–2071

Wriggers P, Eberlein R, Reese S (1996) A comparison of three-dimensional continuum and shell elements for finite plasticity. International Journal of Solids and Structures 33: 3309–3326

Wriggers P, Reese S (1996) A note on enhanced strain methods for large deformations. Computer Methods in Applied Mechanics and Engineering 135: 201–209

Yang HTY, Saigal S, Masud A, Kapania RK (2000) A survey of recent shell finite elements. International Journal for Numerical Methods in Engineering 47: 101–127

Yoon JW (1996) Finite element formulation based on incremental deformation theory for sheet metal forming of planar anisotropic materials. PhD Dissertation. Korea Advanced Institute of Science and Technology (KAIST), South Korea

Yoon JW, Yang DY, Chung K (1999) Elasto-plastic finite element method based on incremental deformation theory and continuum based shell elements for planar anisotropic sheet materials. Computer Methods in Applied Mechanics and Engineering 174: 23–56

Yoon JW, Cardoso RPR, Fontes Valente RA, Grácio JJ (2003) Nonlinear kinematic hardening model for general non-quadratic anisotropic yield functions. In: E. Oñate and D. R. J. Owen (eds) Proceedings of the 7^{th} International Conference on Computational Plasticity – COMPLAS VII, CIMNE, Barcelona, Spain

Yunhua L, Eriksson A (1999) An alternative assumed strain method. Computer Methods in Applied Mechanics and Engineering 178: 23–37

Zhu Y, Zacharia T (1996) A new one-point quadrature, quadrilateral shell element with drilling degrees of freedom. Computer Methods in Applied Mechanics and Engineering 136: 165–203

Zienkiewicz OC, Taylor RL, Too JM (1979) Reduced integration techniques in general analysis of plates and shells. International Journal for Numerical Methods in Engineering 3: 275–290